DRELL-YAN STUDY IN CMS EXPERIMENT AT LARGE HADRON COLLIDER

A THESIS

Submitted to the

FACULTY OF SCIENCE

PANJAB UNIVERSITY, CHANDIGARH

for the degree of

DOCTOR OF PHILOSOPHY

2011

Monika Jindal

DEPARTMENT OF PHYSICS

CENTRE OF ADVANCED STUDY IN PHYSICS

PANJAB UNIVERSITY, CHANDIGARH

INDIA

Dedicated to my family and friends

Acknowledgments

Preparing a Ph.D. thesis is a unique experience for everyone who would like to undertake a scientific career. Having the task to solve a specific research problem in the most fine details is an occasion of personal and professional growth of great value. However, such a growth could not be achieved and the problem be solved, without the essential support of many people. I would like to thank many people with whom I had the pleasure to interact during the development of the work presented herein.

First of all, I would like to thank my Supervisor Prof. J.B. Singh for giving me the possibility of working in such a stimulating environment such as the CMS collaboration and CERN. Without him, I could not become one of the member of High-Energy Group at Panjab University. His accurate, enlightening, still practical advices and suggestions, pointing to the core of the problems, have been a greatly valued guidance. In addition, he helped me getting the opportunity to study at Tata Institute of Fundamental Research in Mumbai, where I finished most content of this thesis. I am also thankful to my Co-Supervisor at Panjab University Dr. Vipin BhatNagar, for his constant presence and his invaluable suggestions and the care he put in revising this thesis. It was a great experience to learn many new ideas from him and solve many problems with him.

I sincerely express my thanks and gratitudes to Prof. Kajari Mazumdar, who invited me and supervised me at TIFR. Prof. Kajari is a quite erudite master on high energy physics. She gave me a lot of fruitful suggestions on the Drell-Yan and Underlying Events analysis, including some crucial ones. Her involvement with her originality has triggered and nourished my intellectual maturity that I will benefit from, for a long time to come.

Many thanks goes to Prof. S. Beri and Prof. M. Kaur for their continuous support and efforts to provide us adequate facility in PUHEP lab. I would like to thanks INDIA-CMS collaboration for providing us platform to discuss our work by arranging regular collaboration meetings.

I would like to thank many people from the Electroweak group have also helped me along the way. Particularly, I would like to thank Prof. Dmitri Bourilkov (University of Florida), who gave me guidance and suggestions for the improvement of Drell-Yan analysis. I am also thankful to Dr. Hwidong Yoo (Purdue University), who gave me suggestions and input that was very important to get a clear understanding of the Drell-Yan analysis. It was a great experience working with all the members of the Drell-Yan analysis at CMS.

My sincere thanks goes to the Dr. Paolo Bartalini (NTU, Taiwan) and all the members of the track jet analysis in the low p_T QCD group at CMS, working with whom during the Underlying Events analysis was very valuable for me.

I am thankful to Chairman, Department of Physics, Panjab University for providing adequate facilities to work in the department.This research has been supported by various organizations including Council of Scientific Instrument and Research (CSIR) and Department of Science and Technology (DST). I am thankful to all of them for their confidence in me.

I am deeply thankful to all my friends in Physics department and in High-Energy Physics lab at university, Archana didi, Nishu, Manuk, Jyoti, Richa, Sonam, Bhawan, Nitish, Anil Sir, Lovedeep, Suneel, Sumali and Kriti who were always present for helping me out from all kind of problems with their suggestions, discussions and creating enjoyable environment during my stay in Chandigarh.

I would like to thank my friends Isha and Supreet, for their all time support and help. They are the ones to whom I can look up during any difficult time.

I would like to thank Mr. V. K. Bhandari, Mr. Baljinder Singh, Mr. Gyan, Mr. Sohan, Mr. Subhash, Mr. Udham Singh, Mr. Rooplal and all the members of

purchase section in the department who were always there to help me in my official works.

I am heartily thankful to my friends in TIFR Neeraj, Venus, Sandeep, Ashish, Gaurav, Jasmine and Thomas who made my stay at TIFR very comfortable and enjoyable.

I would like to thank all my friends Sudha, Shilpi, Sandhya, Shivali and Arun from Delhi University with whom I have spent a great time during my stay at CERN.

I can't forget to express my thankfulness to the greatest search engine Google, without whom it was impossible to do the research work. It is the one, who always give me a solution or idea for any problem.

Now a thought to my dear friends who have made my life so pleasant. Manie and Sherry, they are the ones with whom I have shared almost everything about my life. When I first met them during our post-graduation, I had never thought that this friendship will grow into such a warm and everlasting bond. Laughing at the loudest, fighting with each other, making faces, pizza or parantha parties at hostel and the dance parties without any reason, are few of the so many uncountable and unforgettable moments, we have shared together.

Inderpal, like a brother figure for me, is a person with a golden heart, who has never minded to make his friends laugh by making fun of himself. I would like to congratulate and wish both Inderpal and Sherry, who are going to tie a knot very soon, a very Happy and blessed life.

Vishal, a very dear friend of mine, is also like a brother-figure for me. His constant encouragement and suggestions has always helped me to handle every difficult situation with an ease.

I would like to thank Sandy and Sujeet for being a part of my life. Sandy, is my one of those friends upon whom I can rely for anything.

The most special thanks goes to my best partner, my best friend, my mentor, my husband Sunil, who gave me unconditional love and support through all this long process. He forms the backbone and the origin of my happiness. His love and support without any complaint or regret has enabled me to complete this Ph.D. project. Sunil, you are my deepest strength, without your support and love I could not have even think about finishing this task. I have no words to say thanks to GOD for blessing me with a friend and husband like you. Te Amo.

I would like to pay my regards to my in-laws. My father-in-law, Late Sh. Madan Lal, who is no longer with us, but is forever remembered. I would also like to thank my mother-in-law Smt. Santosh Devi, whose understanding and love encouraged me to continue pursuing Ph.D. project ever after marriage. My brother-in-law, Mr. Kamal Bansal and Bhabhi Mrs. Madhu Bansal always take care of me and supported me to complete my work. Their little son Jony makes my stay at home very enjoyable.

Now I would like to express my deepest gratitude for my family, for their unflagging love and support throughout my life. This dissertation is simply impossible without them. I have no words to thank my Father, Late Sh. Vijay Kumar Jindal, who had supported me and loved me so much throughout my life. Inspite of being not present physically in this world, I know he is continuously providing me the strength to grow stronger and stronger everytime to achieve my goal. ThankYou Papa. Love you and miss you so much.

My mother Smt. Brij Bala, is simply perfect. Her unconditional love and care always encouraged me to work harder in my life and to do my best. She has also been there to listen to me as a friend as well. Her firm and kind-hearted personality has taught me to never bend to difficulty.

My elder sister Rishu and my jiju Rahul, are my all time favourites. Their support, love and their suggestions has always helped me a lot to fight with any difficult situation which I had to face in my life. The innocent and the cute smile of their three little daughters, Disha, Shreya and Kavya always take away all my sadness and makes life so beautiful for me.

The love and the support of my younger sister Nisha and younger brother Puneet has helped me to achieve my goal. They supported me and gave me the strength to join Ph.D. It was their firm belief that, I can adopt research field as my career. I wish Nisha, who is going to begin her new life with Deepak very soon, a very beautiful and happy life. May GOD bless all of them with all kind of happiness in their life.

I am also thankful to my grandmother Smt. Satyawati, my chachaji, chachiji, my cousions Vinny, Raghav and Vivek for their everlasting love and support.

Last but not least, my greatest regards to the Almighty God for bestowing upon me the courage to face the complexities of life and complete this project successfully. There are still many more people I have to thank. I am grateful to all of those friends and colleagues who helped me finish my research work.

Dated: *Monika Jindal*

Abstract

The proton-proton collisions at the Large Hadron Collider (LHC) is the begining of a new era in the high energy physics. It enables the possibility of the discoveries at high-energy frontier and also allows the study of Standard Model physics with high precision. The new physics discoveries and the precision measurements can be achieved with highly efficient and accurate detectors like Compact Muon Solenoid.

In this thesis, we report the measurement of the differential production cross-section of the Drell-Yan process, $q\bar{q} \rightarrow Z/\gamma^* \rightarrow \mu^+\mu^-$ in proton-proton collisions at the center-of-mass energy $\sqrt{s} = 7$ TeV using CMS experiment at the LHC. This measurement is based on the analysis of data which corresponds to an integrated luminosity of $\int Ldt = 36.0 \pm 1.4$ pb^{-1}. The measurement of the production cross-section of the Drell-Yan process provides a first test of the Standard Model in a new energy domain and may reveal exotic physics processes. The Drell-Yan process which is understood with high precision, up to next-to-next leading order accuracy, is an important handle for the detector calibration and alignment. Also the Drell-Yan process is an important background for the Higgs searches and other exotica searches i.e. SUSY, large extra dimensions, etc. and hence it is essential to understand the Drell-Yan production very accurately with the LHC data available recently. In the present analysis, the Drell-Yan production cross-section has been measured in the invariant mass range of 15-600 GeV/c^2. The measured cross-section is corrected for the detector effects, selection efficiencies and effects of Final State Radiation. In order to reduce the systematic uncertainty due to the luminosity, the corrected cross-section is then normalized to the cross-section of the Z-mass peak region defined in the mass window 60-120 GeV/c^2. In this analysis the cross-section of the Z-mass peak region has been measured to be 923 $\pm$ 5 (stat) $\pm$ 6 (syst) $\pm$(4%) lumi pb and is consistent with the CMS measurement of the Z-mass peak cross-section which is 974 $\pm$0.7 (stat) $\pm$0.7 (syst) $\pm$ 4% (lumi) pb. Thus the final results in this analysis are presented in the form of this ratio of cross-sections and found to be in good agreement with the theoretical predictions at next-to-leading order.

This thesis also reports the measurement of the Underlying Event using the Drell-Yan process, $q\bar{q} \rightarrow Z/\gamma^* \rightarrow \mu^+\mu^-$, in the proton-proton collisions at the center-of-mass energy of $\sqrt{s} = 7$ TeV using CMS experiment at the LHC. This analysis also uses data which corresponds to an integrated luminosity of $\int Ldt = 36.0 \pm 1.4$ pb^{-1}. The Drell-Yan process provides an excellent way to study the Underlying Event activity by separating the hard interaction from the soft component. Good understanding of the Underlying Event is important for the precision measurements of SM processes and the search for new physics. Some of the examples where the UE plays crucial roles are the determination of the losses of events due to isolation criteria in lepton identification, computation of missing transverse energy, or the computation of reconstruction efficiency for processes, like $H \rightarrow \gamma\gamma$ where the vertex is given by the Underlying Event. In the present analysis, Underlying Event activity is measured along, transverse and opposite to the direction of muons pair in a plane transverse to the beam direction. The experimental results are corrected for the detector effects and selection efficiencies and compared with the predictions of various models for soft interactions. The measured Underlying Event activity is not fully described by any of the existing models and hence requires further tuning of the theoretical models.

Contents

1 Introduction **1**

1.1 Standard Model of Particle Physics 2

1.1.1 Fundamental Forces 2

1.1.2 Fundamental Particles 4

1.1.3 Quantum Chromodynamics (QCD) 6

1.1.4 Electro-Weak Theory 7

1.2 Shortcomings of Standard Model 9

1.3 Motivation to study Drell-Yan 10

1.3.1 Historic perspective of Drell-Yan process 10

1.3.2 Importance of Drell-Yan process 13

1.3.3 Underlying Event Study using Drell-Yan 15

1.4 Thesis Organization 17

2 Large Hadron Collider and CMS Experiment **19**

2.1 Layout of Large Hadron Collider 21

2.1.1 Accelerator systems and Injector complex 22

2.1.2 Luminosity and Center-of-mass energy 24

2.1.3 Experiments at the LHC 24

2.2 Compact Muon Solenoid 26

2.2.1 CMS Co-ordinate system 28

2.2.2 SuperConducting Magnet 28

2.2.3 Inner Tracking System 29

2.2.4 Electromagnetic Calorimeter 34

2.2.5 Hadron Calorimeter 36

2.2.6 Outer Hadron Calorimeter 39

2.2.7 Muon System 39

2.2.8 Trigger system 48

2.3 Particle Detection through interaction with detector Material 51

3 Event Reconstruction and Monte Carlo Samples **57**

3.1 Event Generators . . . 58

3.1.1 Pythia-6 . . . 59

3.1.2 Pythia-6 Tunes . . . 61

3.1.3 Pythia-8 . . . 65

3.1.4 POWHEG . . . 65

3.1.5 TAUOLA . . . 67

3.2 CMS Detector Simulation . . . 67

3.3 Particle Object Reconstruction . . . 68

3.3.1 Beam Spot reconstruction . . . 69

3.4 Vertex Reconstruction . . . 71

3.5 Track Reconstruction . . . 72

3.6 Muon Reconstruction . . . 74

3.6.1 Local Muon Reconstruction . . . 75

3.6.2 Standalone Muon Reconstruction . . . 76

3.6.3 Global Muon Reconstruction . . . 77

3.7 Monte-Carlo Samples Analyzed . . . 79

3.7.1 Monte-Carlo Samples for the Study of Drell-Yan process . . . 79

3.7.2 Monte-Carlo samples for the Study of Underlying Event using Drell-Yan process . . . 82

4 Study of Drell-Yan Process with CMS **85**

4.1 Drell-Yan Signal and Potential Backgrounds . . . 86

4.1.1 Drell-Yan Signal . . . 86

4.1.2 Background Processes . . . 87

4.2 Drell-Yan Event Selection . . . 88

4.2.1 Muon Isolation Optimization . . . 89

4.3 Event Selection . . . 92

4.4 Drell-Yan Event Selection Efficiencies estimated using Monte-Carlo Cut-based Method . . . 98

4.5 Data-Driven estimation of the single muon efficiencies using TagAnd-Probe Method . . . 103
4.5.1 Single Muon Efficiency Factorization . . . 106
4.6 Drell-Yan Signal and Background Yields . . . 113
4.6.1 Estimation of dimuon background using data driven $e\mu$ method 114
4.6.2 $e\mu$ event selection . . . 117
4.6.3 Results of $e\mu$ method . . . 119
4.7 Detector Acceptance and FSR correction . . . 124
4.7.1 Detector Acceptance . . . 126
4.7.2 FSR correction . . . 127
4.8 Experimental Results . . . 129
4.8.1 Unfolding of Experimental Distributions . . . 129
4.8.2 Response Matrix . . . 130
4.8.3 Systematic Uncertainties . . . 137
4.9 Results and Discussions . . . 140

5 Underlying Event Study using Drell-Yan 145
5.1 Introduction . . . 145
5.2 Methodology . . . 146
5.3 Event Selection . . . 148
5.3.1 Event Trigger selection . . . 148
5.3.2 Event Vertex Selection . . . 149
5.3.3 Drell-Yan Event Reconstruction . . . 149
5.4 Track Selection for Underlying Event . . . 152
5.5 Underlying Event Measurements . . . 160
5.6 Unfolding of Underlying Event Observables . . . 161
5.7 Study of Systematics in Experimental Results . . . 166
5.7.1 Systematics due to background processes . . . 166
5.7.2 Systematics due to different models of soft interactions . . . 171
5.7.3 Systematics due to event trigger selection . . . 171

5.7.4 Systematics due to event pile-up 173
5.7.5 Systematics due to lepton isolation criteria on UE variables . . 174
5.7.6 Systematics due to track selection 175
5.7.7 Systematics due to fake tracks 177
5.8 Underlying Event Results and Discussion 177

6 Summary and Conclusions **187**
6.1 Study of Drell-Yan process with CMS 187
6.2 Underlying Event Study using Drell-Yan 189

Publications/Conferences **201**

List of Figures With Captions

1.1 Building blocks of Standard Model. 3

1.2 The dilepton cross-section as measured by Christenson *et al.* at Brookhaven National Laboratory [12]. 11

1.3 Feynman diagram of the Drell-Yan lepton pair production. 12

1.4 Parton Distribution Functions as a function of x for up and down valence, and charm and strange sea quarks and gluons for a Q^2=10 GeV^2 (left) and $Q^2 = 10^4$ GeV^2 (right). The PDFs shown are MSTW2008 NLO PDF set [18] 13

1.5 The various components of the proton-proton collision at hadron collider. 15

2.1 A beautiful 7 TeV E_{cm} pp collision event seen in CMS, from the very first minutes this regime was established. 20

2.2 Graph of total integrated luminosity collected at CMS during (left) 2010 and (right) 2011 run. 21

2.3 Schematic layout of the LHC 22

2.4 The Large Hadron Collider's (LHC) accelerator complex, in Geneva (Switzerland). 23

2.5 The Compact Muon Solenoid at the LHC. 27

2.6 (Left) Transverse or cross-sectional view and (right) longitudinal view of the CMS detector 28

2.7 Artistic view of CMS solenoidal magnet. 29

2.8 Schematic view of the CMS inner tracking system. 31

2.9 Pixel detector of CMS inner tracking system. 32

2.10 Measured resolution of the track transverse (left) and longitudinal impact parameter as a function of the track transverse momentum. Only central tracks with $|\eta| < 0.4$ are considered. Black and red points are data and MC simulation respectively. 32

2.11 Primary vertex resolution in x (top left), y (top right) and z (bottom) as function of the number of tracks used in the fitted vertex. 33

2.12 Electromagnetic calorimeter of the CMS detector. 35

2.13 Longitudinal cross-section of the quarter of the CMS detector showing the positions of the hadronic calorimeter barrel (HB), hadronic calorimeter endcap (HE), forward hadronic calorimeter (HF) and outer hadronic calorimeter (HO). 38

2.14 Number of interaction lengths till the last sampling layer of the hadron calorimeter as a function of η. The two shaded regions correspond to the setups with or without the outer hadron calorimeter. 40

2.15 Material thickness in interaction lengths at various depths, as a function of pseuodorapidity. 41

2.16 Layout of the one quadrant of the CMS (left) and a display of the collision event with a muon crossing the DT and CSC chambers in the overlap region between barrel and endcap (right). 42

2.17 Layout of the CMS barrel muon DT chambers in one of the 5 wheels. The chambers in each wheel are identical with the exception of wheels -1 and +1 where the presence of cryogenic chimneys for the magnet shortens the chamber in 2 sectors. Note that in sectors 4 (top) and 10 (bottom) the MB4 chambers are cut in half to simplify the mechanism assembly and the global chamber layout. 43

2.18 The layout of muon cathode strip chambers (CSC) in one quarter of the CMS. Most of the cathode strip chambers are highlighted in dark-red, the ME4/2 chamber is not highlighted, because it was thought that it would not be installed at the start-up of the LHC, but delays in the LHC start-up allowed for it to be installed for the first data. . 44

2.19 Transverse view of the muon system layout in the barrel region, showing the positions of the DT and RPC stations. 46

2.20 Resolution on transverse momentum as measured with$\sim$ 40 nb^{-1} of integrated luminosity (black line) compared to the Monte Carlo resolution computed from Monte Carlo truth (red points) and from the fit as described in Section 4.2 (black squares). The gray band in data represents the error on the fitted function for data computed from the errors on the parameters. 47

2.21 Architecture of Level-1 trigger 49

2.22 Architecture of Data Acquisition system 50

2.23 Schematic view of an electromagnetic shower. 52

2.24 Fractional energy loss of electron per radiation length in lead as function of electron energy. 53

2.25 Slice of CMS detector showing interactions of various particles in subdetectors of CMS. 55

3.1 Basic steps in event generation, simulation and data analysis. 58

3.2 Shows two tracks originating from a displaced beam spot. The impact parameters d_{xy_i} and the azimuthal angles ϕ_i of each track are measured at the point-of-closest-approach of the track to the center of CMS. . . 71

4.1 Schematic illustration of the isolation cone. The muon direction at the vertex defines the cone axis. The energy deposit ($\sum p_T$ or $\sum E_T$) in the cone is computed and the muon contribution is removed by excluding the small area around the muon (the "veto" value) from the cone. Comparison of the deposit in the cone with a pre-defined threshold determines the muon isolation. 90

4.2 Comparison of the signal (ϵ_{signal}) vs background ($\epsilon_{background}$) efficiencies (a) for $[I_{Tr}, (\frac{\sum p_T}{p_T^\mu})]$, (b) for the $[I_{TEH}, \frac{I_{TEH}}{p_T^\mu}]$ and (c) for the $[I_{TH}, \frac{I_{TH}}{p_T^\mu}]$ isolation variables. 93

4.3 Drell-Yan isolation efficiency in various bins of reconstructed dimuon mass for three different criteria of relative isolation: I_{TH} using tracker and HCAL only, I_{TEH} using tracker, ECAL and HCAL and I_{Tr} using tracker only. 94

4.4 Data and MC comparison after offline selection with a cut on the variable plotted excluded *i.e.* (N-1) cut: (left) leading muon p_T, (right) second leading muon p_T. 99

4.5 Data and MC comparison after offline selection with a cut on the variable plotted excluded *i.e.* (N-1) cut: (left) leading muon η, (right) second leading muon η. 99

4.6 Data and MC comparison after offline selection with a cut on the variable excluded *i.e.* (N-1) cut: (a) number of hits in tracker, (b) pixel hits (c) show the normalized χ^2 and (d) number of hits in the muon chamber. 100

4.7 Data and MC comparison after offline selection with a cut on the variable plotted excluded *i.e.* (N-1) cut: (a) d_{xy} of the leading muon, (b) d_{xy} of the second leading muon w.r.t the beam spot (c) $\sum \frac{(p_T(tracks)+E_T(HCAL))}{p_T^{\mu}}$ and (d) number of matches in muon segment per muon. 101

4.8 Data and MC comparison after offline selection with a cut on the variable itself excluded: (left) shows the 3D angle between the two muons and (right) shows the vertex probability distribution. 102

4.9 Data and MC comparison of the HLT_Mu9 trigger efficiency. (a) and (b) show the trigger efficiency for HLT_Mu9 using CMS data of run 2010A as a function of probe p_T and η. Figure (b) and (c) show the HLT_Mu9 trigger efficiency using CMS data of run 2010B as a function of probe p_T and η. 109

4.10 Trigger efficiency of HLT_Mu11 trigger path for the experimental corresponding to an integrated luminosity of 9.2 pb^{-1} (a) as a function of probe p_T, (b) as a function of η. Similarly figures (b) and (c) show the HLT_Mu15 trigger efficiency as function of probe p_T and η for experimental data corresponding to an integrated luminosity of 18.4 pb^{-1} respectively. 110

4.11 Data and MC comparison of the efficiency for a muon to be reconstructed as "global" muon as function of probe p_T (left) and probe η (right). The CMS data used here corresponds to an integrated luminosity of 18.4 pb^{-1}. 111

4.12 Data and MC comparison of the efficiency for a muon to be reconstructed as "tracker" muon as function of probe p_T (left) and probe η (right). The CMS data used here corresponds to an integrated luminosity of 18.4 pb^{-1}. 112

4.13 Data and MC comparison of the efficiency for a muon to be identified as a "good" muon which is passing all the muon quality cuts, as function of probe p_T (left) and probe η (right). The CMS data used here corresponds to an integrated luminosity of 18.4 pb^{-1}. 112

4.14 Data and MC comparison of the efficiency for a muon to be isolated as a function of probe p_T (left) and probe η (right). The CMS data used here corresponds to an integrated luminosity of 18.4 pb^{-1}. 113

4.15 The observed dimuon invariant mass spectra. No corrections are applied to the distributions. The points with error bars represent the data, while the various contributions from simulated events are shown as stacked histograms. The "QCD" contribution results from processes associated with QCD and could be a genuine or mis-reconstructed muons. 116

4.16 Histogram showing the "Validation test" of $e\mu$ method using MC. The line corresponds to the $\mu^+\mu^-$ distribution predicted by MC and the "red" bullets are the $\mu^+\mu^-$ events estimated from $e\mu$ method using MC . As the $e\mu$ events are MC and the detector acceptances are known exactly on a bin-by-bin and mode-by-mode basis, exact agreement is expected between the predicted $\mu^+\mu^-$ distribution and MC. 122

4.17 (Left) shows the comparison of the $e\mu$ event yield observed in experimental data with the yield of $e\mu$ events predicted in various genuine sources of $\mu^+\mu^-$ backgrounds and (right) shows the $\mu^+\mu^-$ events estimated in experimental data using $e\mu$ data. The background samples $DY \rightarrow \tau\tau$, $t\bar{t}$ and WW are stacked and compared with data. Good agreement is observed between the MC cut based predictions and the $\mu^+\mu^-$ numbers estimated using $e\mu$ in experimental data. 123

4.18 Detector acceptance of $DY \rightarrow \mu^+\mu^-$candidates as a function of the post-FSR generator level invariant mass of the DY system. 126

4.19 Effects of FSR on the Drell-Yan mass spectrum, computed with POWHEG MC in full phase-space for the dimuon channel. 129

4.20 The response matrix computed with POWHEG MC within the detector acceptance. The distribution is normalized column-wise. 132

4.21 (Left) plot shows the comparison of the "unfolded", "truth" and "measured" mass distribution from MC and (right) shows the qualitative estimate of the deviation of the "unfolded" distribution from the "truth" mass. 132

4.22 Comparison of dimuon yield for the "unfolded", "measured" distributions from data with the "truth" distribution. The "Truth" distribution has been obtained from MC. 135

4.23 Comparison of the "unfolded", "measured" cross-section in data with the "truth" cross-section obtained from MC. The cross-section reported here is not corrected for the detector acceptance and Final State Radiation correction factors. 135

4.24 Comparison of the "unfolded" cross-section with the "truth" cross-section in each invariant-mass bin. The cross-section reported here is corrected for the acceptance and the Final State Radiation correction factors. The unfolded distribution is matching well with the truth distribution. 136

4.25 Shape of the Drell-Yan mass spectrum normalized to Z-peak compared with theory predictions at NLO with CT10 PDF set. 141

5.1 Illustration of correlations in azimuthal angle $\Delta\phi$ relative to: (left) the direction of the leading jet (highest p_T jet) in the event, in high-p_T jet production and (right) the direction of the lepton-pair in Drell-Yan (DY) production. The angle $\Delta\phi = \phi - \phi_{jet}(\Delta\phi = \phi - \phi_{pair})$ is the relative azimuthal angle between charged particles and the direction of jet (lepton-pair). 147

5.2 The z separation of the vertex from the beam spot fitted with Gaussian (a) MC and (b) Data. 150

5.3 Reconstructed vertex properties: (a) separation of the z-position of the vertex from the beam spot and (b) the number of good vertices reconstructed in an event. 150

5.4 (a) Observed invariant mass and (b) transverse momentum distribution in experimental data in [60-120] GeV/c^2 mass region after all the selection cuts. All the Monte-Carlo samples are stacked and compared with experimental data. 153

5.5 (a) shows the ΔR matching and (b) shows the relative p_T difference between track and muon for experimental data and MCs. 156

5.6 Comparison of (a) relative transverse impact parameter d_0/σ, (b) relative uncertainty in the p_T of tracks and (c) relative longitudinal impact parameter d_z/σ for Data and MC with and w/o pile-up. 157

5.7 Comparison of (a) relative d_z of the tracks with respect to the closest vertex (b) relative d_z with respect to the 1^{st} vertex vs relative d_z with respect to the 2^{nd} vertex for the tracks which are closest to the 2^{nd} vertex (c) relative d_z with respect to 1^{st} vertex vs relative d_z with respect to the 3^{rd} vertex for the tracks which are closest to 3^{rd} vertex and (d) relative d_z with respect to 1^{st} vs relative d_z with respect to 4^{th} vertex for the tracks which are the closest to the 4^{th} vertex for Pythia-6 Z2 tune with pile-up events. 158

5.8 (Top left) and (top right) plots shows the fake rate as a function of track η and track p_T respectively. (Center left) and (center right) shows the shape comparison of track η and ϕ and, (bottom left) and (bottom right) shows the shape comparison of p_T and multiplicity of the tracks for experimental data and Pythia-6 Z2 tune with and w/o pile-up. . . 159

5.9 (a) shows the number of charged particles per unit pseudo-rapidity ($dN_{\rm chg}/d\eta$), (b) shows the average number of charged particles per unit pseudo-rapidity per unit $\Delta\phi$ for charged particle tracks with $p_T > 0.5$ GeV/c and $|\eta| < 2.0$. $\Delta\phi$ is the azimuthal angle between the resultant direction of the dimuon system and the charged tracks.(c) shows the average scalar sum of p_T of charged particles per unit pseudo-rapidity per unit $\Delta\phi$, for experimental data and different MC tunes as a function of $\Delta\phi$. Only tracks with $p_T > 0.5$ GeV/c and $|\eta|$ <2 are considered here.162

5.10 (Left column) shows average number of charged particles and (right column) shows the average scalar sum of the p_T of the charged particles, per unit pseudo-rapidity per unit $\Delta\phi$ from (top to bottom) in *towards*, *transverse* and *away* regions as a function of $p_T^{\mu\mu}$ for charged particle tracks with $p_T > 0.5$ GeV/c and $|\eta| < 2.0$. 163

5.11 (Left column) shows average number of charged particles and (right column) shows the average scalar sum of the p_T of the charged particles, per unit pseudo-rapidity per unit $\Delta\phi$ from (top to bottom) in *towards*, *transverse* and *away* regions as a function of $M_{\mu\mu}$ for charged particle tracks with $p_T > 0.5$ GeV/c and $|\eta| < 2.0$ 164

5.12 (a) The correlation between $p_T^{\mu\mu}$ at the generator and the reconstruction level and (b) shows the profile distribution of the average the $p_T^{\mu\mu}$ at reconstruction level as a function of $p_T^{\mu\mu}$ at generator level. 166

5.13 (Left column) shows the response factor ($\frac{Rec}{Gen}$) as a function of $p_T^{\mu\mu}$ for average number of charged particles and (right column) for the average scalar sum of the p_T of the charged particles, per unit pseudorapidity per unit $\Delta\phi$ from (top to bottom) in *towards*, *transverse* and *away* regions respectively. 167

5.14 (Left column) shows the response factor ($\frac{Rec}{Gen}$) as a function of $M_{\mu\mu}$ for average number of charged particles and (right column) for the average scalar sum of the p_T of the charged particles, per unit pseudorapidity per unit $\Delta\phi$ from (top to bottom) in *towards*, *transverse* and *away* regions respectively. 168

5.15 (Left column) shows the comparison of corrected and uncorrected experimental data as a function of $p_T^{\mu\mu}$ for the average charge particle density and (right column) for the average p_T sum density, per unit pseudorapidity per unit $\Delta\phi$ from (top to bottom) in *towards*, *transverse* and *away* regions respectively. Predictions from Pythia-6 Z2 tune MC are also overlayed for the comparison. 169

5.16 (Left column) shows the comparison of corrected and uncorrected experimental data respectively as a function of $M_{\mu\mu}$ for the average charge particle density and (right column) for the average p_T sum density, per unit pseudorapidity per unit $\Delta\phi$ from (top to bottom) in *towards*, *transverse* and *away* regions. Predictions from Pythia-6 Z2 tune MC are also overlayed for the comparison. 170

5.17 (Left) shows the relative fraction of $t\bar{t}$ as a function of $p_T^{\mu\mu}$ and (right) as a function of $M_{\mu\mu}$. The signal sample used for this estimation is Pythia-6 Z2 Tune. 171

5.18 The comparison of the number of expected pile-up events in experimental data and MC with pile-up before and after the re-weightning. 174

5.19 (Left column) shows the average scalar sum of p_T of the charged particles per unit pseudo-rapidity per unit $\Delta\phi$ and (right column) shows the ratio of MC prediction and measurement in experimental data for the same variable in the from (top to bottom) in *towards*, *transverse* and *away* regions respectively as a function of $p_T^{\mu\mu}$. The inner band indicates the statistical uncertainties and the outer band represent the statistical and systematic uncertainties added in quadrature. 182

5.20 (Left column) shows the average number of charged particles per unit pseudo-rapidity per unit $\Delta\phi$ and (right column) shows the ratio of MC prediction and measurement in experimental data, from (top to bottom) in the *towards*, *transverse* and *away* regions respectively as a function of $p_T^{\mu\mu}$. The inner band indicates the statistical uncertainties and the outer band represents the statistical and the systematic uncertainties added in quadrature. 183

5.21 (Left column) shows the average number of charged particles per unit pseudo-rapidity per unit $\Delta\phi$ and (right column) shows the ratio of MC prediction and measurement in data, from (top to bottom) in the *towards*, *transverse* and *away* regions respectively as a function of $M_{\mu\mu}$. The inner band indicates the statistical uncertainties and the outer band represents the statistical and the systematic uncertainties added in quadrature. 184

5.22 (Left column) shows the average scalar sum of p_T of the charged particles per unit pseudo-rapidity per unit $\Delta\phi$ and (right column) shows the ratio of MC prediction and measurement in experimental data for the same variable in the *away* (left), *transverse* (centre) and *towards* (right) regions as a function of $M_{\mu\mu}$. The inner error bars indicate the statistical uncertainties affecting the measurements and the outer error bars represent the statistical and systematic uncertainties added in quadrature. 185

6.1 Shape of the Drell-Yan mass spectrum normalized to Z-peak compared with theory predictions at NLO with CT10 PDF set. 189

List of Tables with Details

1.1 Details about the four fundamental forces known in nature. 4

1.2 Three generations of elementary particles. 6

3.1 Description of the parameters of Pythia-6 Tunes which control the Underlying Event activity. The first 9 parameters tune the Multiple parton interactions. PARP(62), PARP(64) and PARP(67) tune the initial-state radiation and the last three parameters set the intrinsic k_T of the partons within the incoming proton-proton 63

3.2 Parameters of various Pythia-6 Tunes which control the Underlying Event activity. 66

3.3 Summary of the Generators, cross-section and number of events of various Monte-Carlo samples used in the study of Drell-Yan process. . 80

3.4 Summary of the Generators, cross-section and QCD models of Drell-Yan signal Monte-Carlo samples used in the study of Underlying Event using Drell-Yan process. 82

4.1 Summary of the trigger paths according to the run range applied on data. 94

4.2 The efficiencies of Drell-Yan event selection cuts for the signal MC and Data. The efficiencies reported here are relative w.r.t the previous cut. 103

4.3 The efficiencies of Drell-Yan event selection cuts for the Electroweak backgrounds. The efficiencies reported here are relative w.r.t. the previous cut. 104

4.4 The efficiencies of Drell-Yan event selection cuts for QCD sample binned according to the cut on the p_T at the generator level. The efficiencies reported here are relative w.r.t the previous cut. 105

4.5 Estimation of the High-Level Trigger efficiencies for single muon trigger paths in different run ranges of 2010 data. 108

4.6 Estimation of the muon identification and isolation efficiencies for data and simulation. The total data used here corresponds to 18.4 pb^{-1} of integrated luminosity. 111

4.7 Dimuon yield observed in experimental data after all selection cuts, estimated backgrounds (MC based) and background subtracted yields in data. 115

4.8 The values of the isolation, conversion rejection and identification cuts for the electron in the barrel and endcap detector regions. 120

4.9 Total $e\mu$ and $\mu^+\mu^-$ events observed in data and predictions in MC. . 124

4.10 Bin-by-Bin estimation of $\mu^+\mu^-$ events in MC and data (from $e\mu$) method. 125

4.11 Drell-Yan acceptance for "post-FSR" muons per invariant mass bin and the FSR correction factor calculated bin-by-bin after the acceptance cuts. 128

4.12 Number of the observed and unfolded dimuon events in data. The unfolded yield is obtained after subtracting the background contribution in data. 134

4.13 Bin-by-Bin comparison of the unfolded and (acceptance*FSR) corrected cross-section (σ_{corr}) from the experimental data with the "truth" cross-section. The "truth" cross-section is obtained from the POWHEG MC sample having CT10 PDF set. The "measured" experimental cross-section *i.e.*, the cross-section before the unfolding procedure is also shown. 138

4.14 Summary of systematic uncertainties in the muon channel (in %). The "Total" is a quadratic sum of all sources without "Detector acceptance". With the exception of "Detector acceptance", the numbers correspond to the individual measurements per bin and not the ratio to the Z peak region. 139

4.15 Result of the Drell-Yan spectrum normalized to Z-peak presented bin-by-bin. The errors mentioned here are only statistical. 142

5.1 Summary of the trigger paths according to the run range applied on experimental data. 148

5.2 Track selection efficiency (%) for experimental data and PYTHIA-6 tune Z2 (with and without pile-up). For each cut, the quoted efficiency is relative to the previous cut. 156

5.3 The bin-by-bin systematic bias (%) induced due to contamination from $t\bar{t}$ background process. 172

5.4 The isolation efficiency(%) for various Pythia-6 tunes. 175

5.5 The systematic bias (%) due to muon isolation criteria on uncorrected UE observables for various tunes of Pythia-6. 175

5.6 The systematic uncertainties (%) due to different track selection criteria. The last column reports the combined uncertainty obtained by adding the individual contributions in quadrature. The numbers out of parentheses are for the study as a function of resultant transverse momentum ($p_T^{\mu\mu}$) of dimuon system and those in parentheses correspond to the study as a function of invariant mass ($M_{\mu\mu}$). 176

5.7 Summary of the systematic uncertainties (%) from different sources. The first three rows show the systematic uncertainties for the average scalar sum of p_T of the charged particles in the *towards*, *transverse* and *away* regions, whereas the last three rows report the systematic uncertainties for the average number of charged particles ($1/\mathrm{N}_{ev}$ $\Delta^2 N_{ch}/\Delta\eta\ \Delta(\Delta\phi)$) in the *towards*, *transverse* and *away* regions. The last column reports the maximum uncertainty due to ($t\bar{t}$) background. The numbers refer to study vs. $p_T^{\mu\mu}$. 178

5.8 Summary of the systematic uncertainties (%) from different sources. The first three rows show the systematic uncertainties for the average scalar sum of p_T of the charged particles ($1/\mathrm{N}_{ev}\ \Delta^2\Sigma p_T/\Delta\eta\ \Delta(\Delta\phi)$) in the *towards*, *transverse* and *away* regions, whereas the last three rows report the systematic uncertainties for the average number of charged particles in the *towards*, *transverse* and *away* regions. The last column reports the maximum uncertainty due to ($t\bar{t}$) background. The numbers refers to the study vs. $M_{\mu\mu}$. 179

1

Introduction

High energy physics aims to understand, at the deepest level the fundamental laws that control the building of matter and the physical universe. In the past century, different theories and discoveries have resulted into a remarkable picture of the fundamental structure of the matter, which is known as the Standard Model (SM) [1]. It provides an accurate description of elementary particles and their interactions. The SM summarized very briefly in the next Section, is a very successful model which explains the structure of the matter and forces acting between the fundamental particles and is well tested by different experiments at the Large Electron-Positron collider (LEP), Tevatron, B-factories, etc. However it is incomplete in many aspects and the experimental observations point to the possibilities of the major discoveries in the current and the future high energy particle colliders. In order to find new physics in these colliders, it is essential to have a very good understanding of the SM physics and that has been the motivation for the present work.

In this Chapter, an overview of the SM and the properties of the fundamental particles and the forces are given. Then the motivations for the study of the: Drell-Yan (DY) process and the measurement of the Underlying Event (UE) using the DY process has been presented.

1.1 Standard Model of Particle Physics

The Standard Model (SM) is a theoretical framework that describes how matter is composed of fundamental constituents and the various types of interactions between these constituents. Developed in the early 1970s, it has successfully explained most of the experimental results and precisely predicted a wide variety of phenomena. According to SM, all visible matter in the universe is made up of twelve basic building blocks called "fundamental particles", categorized in three generation of quarks and three generation of leptons, which interacts via four fundamental forces. The SM is a gauge invariant theory which is described by $SU(3)_C \otimes SU(2)_L \otimes U(1)_Y$, where C means color charge, L stands for weak isospin and Y represents hypercharge. The electromagnetic interactions are described by unitary group U(1). This interaction is mediated by massless particle *"photon"* and theory is called *"Quantum Electrodynamics"* (QED). Weak interaction is described in the form of continuous SU(2) group with 3 gauge bosons ($W^{\pm}$, Z^0), whereas SU(3) is the gauge group of the theory of strong interaction known as *"Quantum ChromoDynamics"* (QCD). The SU(3) group has eight generators (gauge bosons), called *"gluons"* which are massless and carry color charge. The gravity is not included in the SM because of lack of theoretical description and experimental clues of the bosons, to be known as "Graviton", which mediates the gravitational interaction. Characteristics of the four fundamental forces and the fundamental particles are briefly dicussed in the next subsection.

1.1.1 Fundamental Forces

All matter in the universe interacts via four distinct forces - gravitational, electromagnetic, strong and weak. These forces are characterized on the basis of the following four criteria: the types of particles that experience the force, the relative strength of the force, the range over which the force is effective and the nature of the particles that mediate the force. A brief insight into the basic properties of fundamental forces is described as follows:

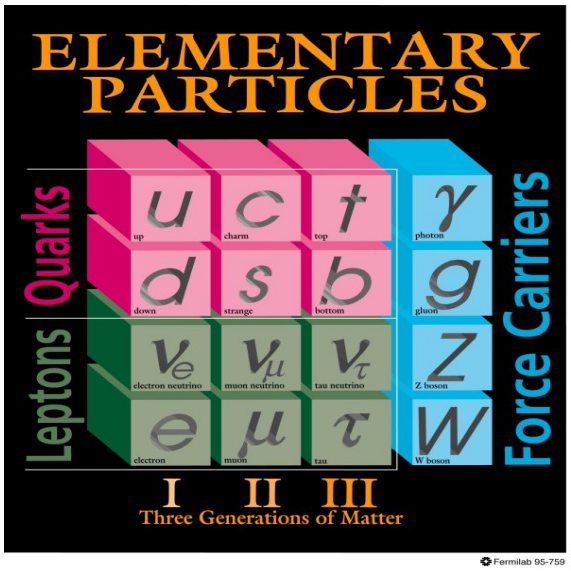

Figure 1.1: Building blocks of Standard Model.

1. **Strong Interaction**: It is responsible for holding nucleus together against the electromagnetic repulsive force due to the presence of protons inside the nucleus. Yukawa modeled the strong force as an exchange force in which the exchange particles are pions. However, it is the strongest of the four fundamental forces, but it has a very short range of the order of 1 femtometer (10^{-15} m). Strong force acts between the particles carrying color quantum number. The strong force arises from an exchange of the quanta of the strong color field known as "gluon".

2. **Electromagnetic Interaction**: Out of the four fundamental forces, this is the force which exists between all particles which have an electromagnetic charge. For example, electrons (negatively charged) bind with nucleus of an atom, due to the presence of protons (positive charge). The force is long range, in principle extending over infinite distance. The electromagnetic force is carried by the exchange of photon, which is a massless particle.

3. **Weak Interaction**: The weak force is responsible for the radioactive decay of unstable nuclei and for the interactions of neutrinos and other leptons with

Force	Mediating boson	Charge	Spin	Mass (GeV/c^2)	Range (m)	Relative Strength
Strong	8 gluons(g)	0	1	0	10^{-15}	1
EM	Photon(γ)	0	1	0	∞	10^{-2}
Weak	$W^{\pm}$	±1	1	80.403±0.029	10^{-18}	10^{-6}
	Z^0	0	1	91.187±0.002		
Gravity	graviton	0	2	0	∞	10^{-38}

Table 1.1: Details about the four fundamental forces known in nature.

matter. It arises from an exchange of intermediate vector bosons $W^{\pm}$ and Z^0, which are very massive.

4. **Gravitational Interaction**: It is the weakest in magnitude and has infinite range. This force is mediated by gauge boson called "graviton" which is experimentally not observed. This force is extremely weak, has a relative strength of 10^{-38} times that of the strong force. It is a purely attractive force which reaches through even the empty void of space to attract the two masses towards each other. It keeps the planets in orbit around the sun and the moon in orbit around the Earth.

A comparison of the relative strengths of the four forces is given in Table 1.1

1.1.2 Fundamental Particles

The Standard Model (SM) for elementary particle physics [2] views "*quarks*" and "*leptons*" as the fundamental particles, which appear to be pointlike when probed at the shortest distance scales accessible to current accelerators. The quarks are fractionally charged, spin -$\frac{1}{2}$ and strongly interacting objects which are known to form the composites, collectively called "hadrons":

- $q\bar{q}$ combination of quark and anti-quark known as "mesons", are integral spin particles following Bose-Einstein statistics.

- *qqq* combination of three quarks known as "baryons", are half-integral spin particles following Fermi-Dirac statistics.

There are six different flavours of quarks which means different kinds: up (u), down (d), strange (s), charm (c), bottom (b) and top (t). The anti-particles of quarks *i.e.* Antiquarks have opposite signs of electric charge, baryon number, strangeness, charm, bottomness and topness. Quarks are fermions with spin-$\frac{1}{2}$ and therefore should obey the Pauli's exclusion principle, *i.e.* no two identical fermions can exist in same quantum state. However, in three particular baryons (Δ^{++} = uuu, Δ^{-} =ddd and Ω^{-}= sss), all three quarks have the same quantum numbers with at least two quarks having their spin in the same direction because there are only two choices: spin up ($\uparrow$) and spin down ($\downarrow$). This would seem to violate the Pauli's exclusion principle. Thus, it was suggested that quarks possess another quantum number which enables them to interact strongly with one another. This quantum number has three-fold degree of freedom known as color.

Quarks have three primary color charges: red (R), green (G) and blue (B). Antiquarks have complementary colors: cyan ($\bar{R}$), magenta ($\bar{G}$) and yellow ($\bar{B}$). All particle states observed in nature are *"colorless"*; baryons have a color state "RGB" and mesons have color states of $R\bar{R}$, $G\bar{G}$ and $B\bar{B}$. Gluons, the quanta of the color field that bind the quark states are bicolored and come in eight states: $R\bar{B}$, $R\bar{G}$, $B\bar{G}$, $B\bar{R}$, $G\bar{R}$, $G\bar{B}$, $\frac{1}{\sqrt{2}}(R\bar{R}-B\bar{B})$, $(\frac{1}{\sqrt{6}}(R\bar{R}+B\bar{B}-2G\bar{G}))$. We would expect $3^2 = 9$ combinations from three colors and three anticolors, but one state $(\frac{1}{\sqrt{3}}(R\bar{R}+B\bar{B}+G\bar{G}))$ carries no net color and is excluded.

Leptons are fractionally spin-$\frac{1}{2}$ particles which do not strongly interact. Leptons can either carry one unit of electric charge or be neutral. The charged leptons are the electron (e), muon (μ)and tau (τ). Each of these types has a negative charge and a distinct mass. Each charged lepton has as associated neutral partner called neutrino: ν_e, ν_μ and ν_τ , that has no electric charge and no significant but a non-zero mass. The mass of the antileptons is identical to that of the leptons, but all of the other properties are reversed. Table 1.2 shows the three families of "fermion" constituents of matter. Particles in higher generations have heavier mass and are

Gen	Leptons(spin = $\frac{1}{2}$)			Quarks(spin = $\frac{1}{2}$)		
	Flavor	Charge	Mass (MeV/c^2)	Flavor	Charge	Mass (MeV/c^2)
1	e	-1	0.511	d	-$\frac{1}{3}$	3.0-7.0
	ν_e	0	$< 2\times10^{-6}$	u	+$\frac{2}{3}$	1.5 - 3.0
2	μ	-1	105.66	s	-$\frac{1}{3}$	95±25
	ν_μ	0	<0.19	c	+$\frac{2}{3}$	(1.25±0.09)×10^3
3	τ	-1	1776	b	-$\frac{1}{3}$	(4.70±0.07)×10^3
	ν_τ	0	<18.2	t	+$\frac{2}{3}$	(172.5±2.7)×10^3

Table 1.2: Three generations of elementary particles.

unstable. Therefore, particles in higher generations decay into particles in lower generations conserving quantum numbers (Charge, Lepton number, Baryon Number and Spin).

1.1.3 Quantum Chromodynamics (QCD)

Quantum Chromodynamics (QCD) [3], the gauge field theory that describes the strong interactions of colored quarks and gluons, is the SU(3) component of the $SU(3) \otimes SU(2) \otimes U(1)$ group describing Standard Model (SM) of particle physics.

QCD has specific features known as asymptotic freedom and confinement, which determines the behaviour of quarks and gluons in particle reactions at high and at low energy scales:

- **Confinement**: means color-charged particles *i.e.* quarks and gluons, cannot be found individually and are confined in groups with other quarks. All particles observed in nature are colorless like baryons (three quark with three different colors) and mesons (quark-antiquark with opposite color). Particles such as *ud* or *uddd* that cannot be combined into color-neutral states are never observed.

  The quarks in a given hadron exchange gluons. If one of the quarks in a given hadron is pulled away from its neighbors, the color-force field stretches between

that quark and its neighbours. In doing so, more and more energy is added to the color-force field as the quarks are pulled apart. At some point, it is energetically favorable for the color-force field to "snap" into a new quark-antiquark pair and the energy in this process is conserved because the energy of the color-force field is converted into the mass of the new quarks. Thus quarks cannot exist individually because the color force increases as they are pulled apart. The property is called *"quark confinement"*, which helps in understanding why we have not seen isolated quarks so far.

- **Asymptotic Freedom**: The term "Asymptotic Freedom" is used to describe the behaviour of quarks at high energy or momentum transfers, or - equivalently - at small distances. Also this feature is based on experimental observations. In high energy scattering processes between leptons (e.g. electrons or neutrinos) with protons or neutrons, the dynamics reveal that scattering occurs at pointlike and massless constituents, the "quarks", rather than at a homogeneous object. Apparently, at sufficiently high momentum transfers, quarks behave like free or weakly bound particles. Mathematically, in QCD the effective coupling constant is given by:

$$\alpha_s(Q^2) = \frac{12\pi}{33 - 2n_f ln(\frac{Q^2}{\Lambda^2})} \tag{1.1}$$

where n_f is the number of quarks flavors, is QCD scaling parameter and Q is momentum transfer during the interaction. As $Q^2 \to \infty$, $\alpha_s \to 0$, which means that at large Q^2, the interaction is quite weak. Thus the fact that the strong interaction becomes "weak" at high energy scales and vanishes to zero at asymptotically high energies, led to the term "Asymptotic Freedom".

1.1.4 Electro-Weak Theory

One of the greatest triumphs of the theoretical physics in the second half of the 20^{th} century was the discovery, made independently by Abdus Salam and by Steven Weinberg in 1967, to describe the weak interaction and the electromagnetic interaction in one mathematical formalism, as a single force - the electroweak interaction. The sim-

plest unification of parity violating weak force and parity conserving electromagnetic force is done using $SU(2)_L \otimes U(1)_Y$ gauge theory. This Electroweak theory [5] [6] [7], describes both the electromagnetic force and the weak force in one unified framework. Superficially, these forces appear quite different. The weak force acts only across distances smaller than the atomic nucleus, while the electromagnetic force can extend for great distances, weakening only with the square of the distance. Moreover, comparison of the strength of these two fundamental interactions between two protons, for instance, reveals that the weak force is some 10^{-4} times weaker than the electromagnetic force. Yet one of the major discoveries of the 20^{th} century has been that these two forces are different facets of a single, more-fundamental electroweak force. The electroweak theory arose principally out of attempts to produce a self-consistent gauge theory for the weak force, in analogy with quantum electrodynamics (QED), the successful modern theory of the electromagnetic force developed during the 1940s.

During the 1960s Sheldon Lee Glashow, Abdus Salam and Steven Weinberg independently discovered that they could construct a gauge-invariant theory of the weak force, provided that they also included the electromagnetic force. Their theory required the existence of four massless particles, two electrically charged and two neutral, to mediate the unified electroweak interaction. The short range of the weak force indicates, however, that it is carried by massive particles. This implies that the underlying symmetry of the theory is hidden, or "broken," by some mechanism that gives mass to the particles exchanged in weak interactions but not to the photons exchanged in electromagnetic interactions. The assumed mechanism involves an additional interaction with an otherwise unseen field, called "the Higgs field", that pervades all space. The quanta of this Higgs field is known as Higgs boson.

In the early 1970s Gerardus't Hooft and Martinus Veltman provided the mathematical foundation to renormalize the unified electroweak theory proposed earlier by Glashow, Salam and Weinberg. Renormalization removed the physical inconsistencies inherent in earlier calculations of the properties of the carrier particles, permitted precise calculations of their masses and led to more-general acceptance of the electroweak theory. Then later on in 1983, the experimental verification of the existence of force

carriers, the neutral Z particles and the charged W particles, at high-energy proton-antiproton collisions at the European Organization for Nuclear Research (CERN) established the Electro-Weak theory. The masses of the particles were found to be consistent with their predicted values.

1.2 Shortcomings of Standard Model

As we have discussed so far, all particle physics phenomena are extremely well described within the SM. It provides a very elegant theoretical framework and it's predictions are verified at the level of 0.1 % by various colliders like LEP, SLAC, KEK and TEVATRON. Inspite of being the most successful theory and surviving the experimental axes, SM has several shortcomings. These shortcomings prevent SM to become the ultimate theory of Nature (or precisely, ultimate theory of particle interactions). Few of them, which motivate Physicists to search for physics beyond SM, are:

- The fourth fundamental force in nature: the gravitational force is not included in SM [8].
- In the SM, Higgs boson mass is quadratically divergent when radiative corrections are applied. Some fine tunings are required to suppress this divergence.
- The coupling constants of the EM, weak and strong interactions varies with energy which is experimentally verified. These couplings are predicted to unify at single value, α_G at very high energy scale $\sim(10^{16}$ GeV/c) which is predicted by Grand Unified Theory (GUT) [9]. In SM, this type of unification is not possible as observed from extrapolation of experimentally measured couplings to very high energy region. On the other hand, unification is accessible in more general theories like supersymmetry(SUSY).
- In SM, neutrinos are assumed to be massless but recent experimental observations, like neutrino oscillations exhibit that the neutrinos should have finite mass [10].

- SM is not able to explain existence of dark matter and dark energy which are the dominant part of the universe.
- SM is not able to explain the asymmetry between the matter and antimatter.

So despite the SM's effectiveness at describing the phenomena within its domain, it is nevertheless incomplete. Perhaps it is only a part of a bigger picture that may includes new physics that has so far been hidden deep in the subatomic world or in the dark recesses of the Universe. This incomplete understanding of the particle physics led to the requirement of the Large Hadron Collider (LHC). LHC is the highest energy proton-proton collider with 14 TeV designed center-of-mass energy at CERN (detail in Chapter 2)

In the early phase of the LHC data taking, it is essential to study the theoretically well understood SM processes like Drell-Yan. This study is important to calibrate the detector, establishing the SM in this new energy regime and for the tuning of Monte-Carlo models, which are required to be done before any new physics searches.

1.3 Motivation to study Drell-Yan

1.3.1 Historic perspective of Drell-Yan process

The initial studies on muon pair production in hadron-hadron collisions was first done at BNL (Brookhaven National Laboratory) by Christenson *et al.* [11] and the results obtained by them are shown in Figure 1.2. Two important interesting features were observed in these results: (i) the shoulder like structure near the muon pair mass of 3 GeV/c^2, which was later discovered to be the J/ψ particle by a muon pair production experiment at BNL [13] and (ii) the rapid fall-off the cross-section with increasing muon pair mass was not consistent with the point like cross-sections observed in deep inelastic electron scattering. Calculations of Sidney Drell and Tung-Mow Yan (1970, 1971) explained most features of the process [14] by extending the parton model [15] [16] developed to explain deep inelastic lepton scattering and this process came to be known, after their names, as the "Drell-Yan process" (DY). The

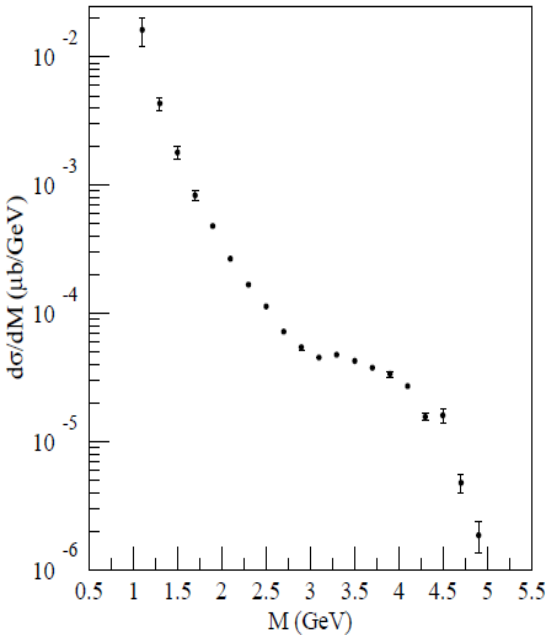

Figure 1.2: The dilepton cross-section as measured by Christenson *et al.* at Brookhaven National Laboratory [12].

DY process describes the annihilation of a quark-antiquark pair and the production of a dilepton pair via intermediate Z boson or virtual photon. Figure 1.3 shows the Feynman diagram for the production of lepton pair through DY process. DY production of lepton pair is one of the most basic measurements at hadron colliders to understand the SM. Predictions of the DY model explain most features of the dilepton continuum produced in hadron-hadron collisions however, it fails to predict the overall magnitude of the cross-section by a factor of approximately 1.5 to 2. This factor, traditionally known as the K-factor, results from neglecting terms of higher order in the cross-section formula, which was later predicted by the QCD calculations, taking into account the effect of gluon emission and absorption. Higher order electromagnetic radiative corrections to the leading order cross-section have also been calculated [17]. Also, QCD provides the explanation of large average transverse momenta of dileptons (initially not well understood) by including the effects of gluon emission and scattering. For the DY process:

$$A(P_1) + B(P_2) \rightarrow l^+ + l^- + X \tag{1.2}$$

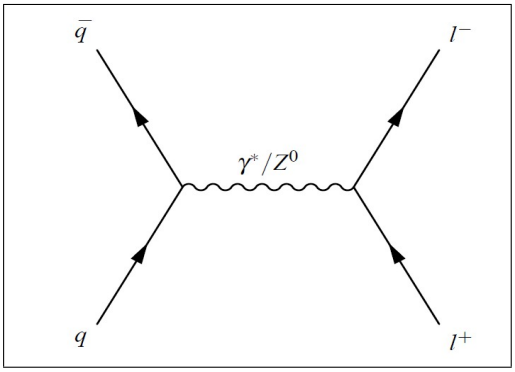

Figure 1.3: Feynman diagram of the Drell-Yan lepton pair production.

where A and B are the incoming hadrons with momenta P_1 and P_2 respectively and X denotes any additional final state particle. The total cross-section for the above process of the production of massive dileptons through quark-antiquark annihilation can be expressed in terms of the hard partonic cross-section with the parton densities of the hadrons A and B and summing over all the quark-antiquark combinations as:

$$\sigma = \sum_{flavour} \int dx_1 dx_2 f_q(x_1) f_{\bar{q}}(x_2) \hat{\sigma}_{q\bar{q}\to l^+l^-} \tag{1.3}$$

where $\hat{\sigma}_{q\bar{q}\to l^+l^-}$ is the partonic cross-section for the DY process, $f_q(x_1)dx_1$ is the probability of finding a quark with $p_1 = x_1P_1$ and $f_{\bar{q}}(x_2)$ is the probability of finding an antiquark with $p_2 = x_2P_2$. The cross-section for proton-antiproton scattering is the sum over all the flavours, which requires knowledge of the incoming hadron types as well as the longitudinal momentum distributions $f_q(x_q)$ and $f_{\bar{q}}(x_{\bar{q}})$ of the interacting partons where x_q and $x_{\bar{q}}$ are the usual longitudinal momentum fractions of the interacting partons relative to the momenta of their parent hadrons. Let us consider first the partonic cross-section [12] given as:

$$\sigma_{q\bar{q}\to\gamma^*\to l^+l^-} = \frac{4\pi\alpha^2}{3M^2}\frac{1}{3}e_i^2 \tag{1.4}$$

where $\alpha = \dfrac{e^2}{4\pi}$ is the fine structure constant, here the cross-section is reduced by the final factor of $\dfrac{1}{3}$ since the color-charge of the quark and antiquark must match, e_i is the fractional charge on the quark and M is the dilepton mass. This is the hard scattering cross-section for a specific quark flavour in the center-of-mass frame of

the interacting partons, where $\hat{s}$ is the center-of-mass energy squared of the partons. Putting everything together, the double differential cross-section for the lowest order DY process becomes [14];

$$\frac{d^2\sigma}{dM^2dy} = \frac{4\pi\alpha^2}{9M^4}[\sum_{flavour} M_q^2 x_1 f_q(x_1) x_2 f_{\bar{q}}(x_2))] \quad (1.5)$$

This is the cross-section for the lowest order DY process shown in Figure 1.3. Thus, the rapid fall in the cross-section observed in the Figure 1.2 with the invariant mass of dimuon system is attributed to the appearance of the M^{-4} factor in the cross-section and also due to the the appearance of parton distribution function $f_q(x)$ which also falls off rapidly as x$\rightarrow$ 1, shown in Figure 1.4.

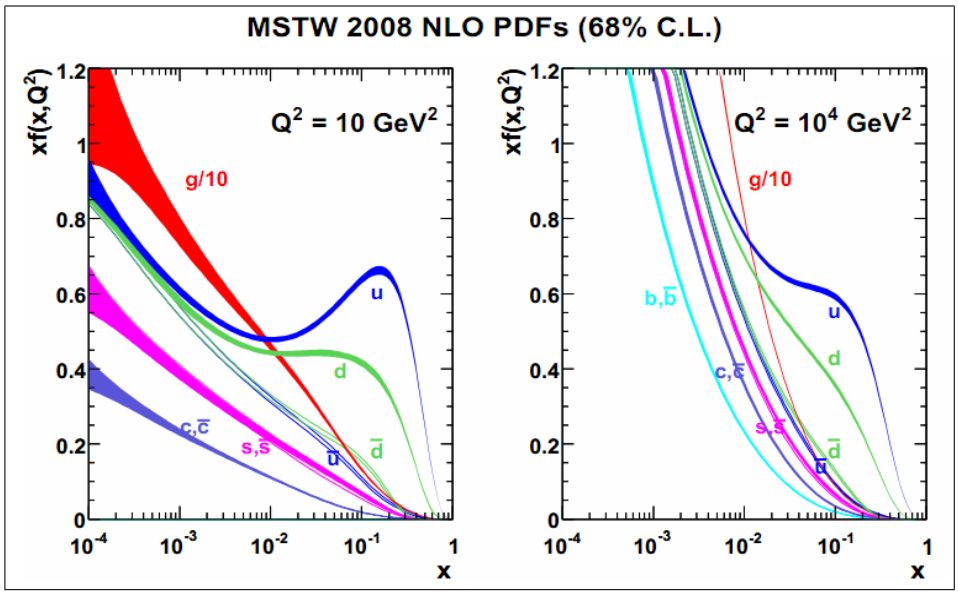

Figure 1.4: Parton Distribution Functions as a function of x for up and down valence, and charm and strange sea quarks and gluons for a Q^2=10 GeV^2 (left) and $Q^2 = 10^4$ GeV^2 (right). The PDFs shown are MSTW2008 NLO PDF set [18]

1.3.2 Importance of Drell-Yan process

The Drell-Yan (DY) process offers many interesting and important characteristics for the study at hadron colliders. In DY process, the QCD effects enter only in the initial

state, therefore the theoretical prediction for the DY production rate is quite precise and hence can be used as confirmation of the Standard Model (SM) at high energies.

In the SM , the production of high mass lepton pairs above the Z mass in hadron-hadron collisions is dominated by the DY process. The DY process also forms an irreducible background to the search for physics beyond the SM in high mass lepton pairs. This means that in searching for new particles such as Z' for the indications of extra dimensions, the contribution of the DY process needs to be measured with high precision.

The DY events can be used to study the ISR effect, which can be used in measurement of top-quark mass M_t by $t\bar{t}$ production, in which it is difficult to disentangle the ISR jets from the FSR jets. Thus, DY data provides a unique opportunity to study ISR effect since in DY, QCD effects enters only in initial state [19].

The di-lepton pair production can be used to constrain the proton structure function at $Q^2 \sim M_{ll}$ using the relation $x_{1,2} = \frac{Q^2}{s} e^{\pm y}$. The angular forward-backward asymmetry of the charged leptons potentially provide information on the parton density function of the proton. Also these measurements will eventually lead to a better determination of effective weak mixing angle, $sin^2\theta_w$, than currently achieved [20]. Since measurement of W-mass, a crucial SM parameter, is affected by the uncertainty in the knowledge of W transverse momentum, eventually the DY events around the Z-mass can be used for accurate extrapolation of the boson transverse momentum from the Z-mass scale to the W-mass scale.

At LHC, the DY rate is reasonably large and hence the process will also be used for the physics tools commissioning phase of the experiments. The DY process will be used for the momentum and energy scale calibration through the measurements of mass of the Z boson ($M_Z = 91$ GeV/c^2) in muon and electron final states.

Interestingly, the nature of the Underlying Event (UE) in hadron collisions, consisting of multiparton interaction as well as the beam-beam remnants, can be studied using DY events. The simplistic nature of the DY final state provides an easy separation of the hard-scattered part from the soft component in hadron-hadron collision. Thus, the DY events form an important component in model-tuning exercise to de-

scribe phenomenologically the softer interactions or the so-called UE.

1.3.3 Underlying Event Study using Drell-Yan

An event in hadron-hadron inelastic collision as shown in the Figure 1.5, all happening inside the radius of a proton [21], consists of various components:

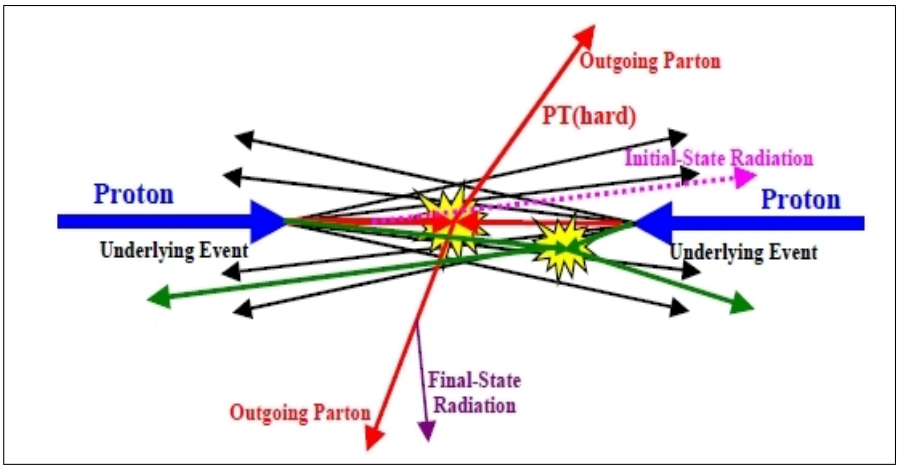

Figure 1.5: The various components of the proton-proton collision at hadron collider.

- Hard scattering, is characterized by the presence of a particle or cluster of particles with a large transverse momentum or mass.

- Beam-Beam remnants (BBR), which are what is left over after a parton is knocked from each of the two initial beam hadrons. These are one of the reasons why hadron-hadron collisions are more messy than electron-positron annihilations.

- Initial state (ISR) and Final state radiation (FSR) which results from the gluon emission and photon bremsstrahlung.

- In addition to the hard 2-to-2 parton-parton scattering and the beam-beam remnants' sometimes there is a second semi-hard 2-to-2 parton-parton scattering known as Multi Parton Interaction (MPI).

The Underlying Event consists of both BBR and MPI. However, on an event-by-event basis it is difficult to separate out these two components from the particles which comes from ISR and FSR. Hence, a study of the Underlying Event inevitably involves a study of the BBR plus MPI plus initial and final-state radiation.

In order to search physics beyond the SM at a hadron-hadron collider, it is essential to have Monte-Carlo models that accurately simulate collision events. To do this one must not only have a good model of the hard-scattering part of the process, but good understanding of the BBR, MPI and radiations is also required. Understanding of the UE activity is very crucial at hadron colliders for lepton and photon isolation, vertex reconstruction, missing energy and jet energy correction, etc.

To measure the UE activity, it is important to identify and separate out the hard scattering components. For this purpose one can use the topological structure of the hard scattering process to define the regions that are sensitive to the soft components of the interaction. By using the different topologies, such as leading track, leading jet, back-to-back dijet production or Drell-Yan (DY) process, one can partially isolate the UE component from the hard component.

The DY process provides a complementary approach for the UE measurement, where a clean separation of the hard interaction from the soft QCD component is possible. Moreover, it is one of the experimentally clean and theoretically well-understood processes. The absence of QCD FSR and low probability of photon bremsstrahlung from the muons can be exploited to study different kinematic regions with varying Z boson recoil, due to harder or softer ISR. The previous UE measurement using DY process with proton-antiproton collision data collected at 1.96 TeV centre-of-mass energy at Tevatron has been reported in [22].

In this thesis, the differential cross-section measurement for the Drell-Yan process is pp collision at $\sqrt{s}$ =7 TeV has been presented. The cross-section measurement normalized to the measurement of the cross-section in the Z-mass peak region is reported, in the dimuon invariant mass range 15-600 GeV/c^2. The normalized cross-section values are quoted in the full phase space. We have also presented the first measurement of the Underlying Event activity using the Dell-Yan process at the LHC.

The goal of this analysis is to provide data that can be used to test and improve the QCD Monte-Carlo models of the Underlying Event. These measurements uses the proton-proton collision data at $\sqrt{s} = 7$ TeV corresponding to an integrated luminosity of 36 pb^{-1} collected with CMS experiment at the LHC during year 2010.

1.4 Thesis Organization

In the present thesis, we have performed two analysis using CMS data: (I) Measurement of the Drell-Yan differential cross-section using dimuon final state, (II) Underlying Event (UE) Study using Drell-Yan All these studies have been performed using data collected with CMS at $\sqrt{s}$= 7 TeV, during the Year 2010 at the LHC. In this chapter, a brief overview of the Standard Model (SM), ElectroWeak theory, shortcomings of SM and the need of Large Hadron Collider are given. The subsequent chapters of the thesis are organized as follows:

Chapter 2 covers the brief overview of the Large Hadron Collider and its various parameters. In this chapter the main emphasis is given on the Compact Muon Solenoid (CMS) detector, as present work utilizes the CMS detector features. The brief overview of various sub-detectors of CMS experiment, their construction and interaction of particles with the active material of different detector components has also been discussed.

Chapter 3 gives a brief description of the event generation methodology with different Monte-Carlo event generators, simulation of the detector geometry and reconstruction of the particles in the detector. This chapter gives an overview of the reconstruction of the beam spot, Vertex, tracks and muons. Details of all the QCD models used for the tuning of the Underlying Event parameters has also been discussed. The Monte Carlo data samples which are used in both: the study of Drell-Yan process and the study of Underlying Event (UE) using DY, are also discussed in detail.

Chapter 4 covers the details of the analysis workflow used in the Measurement of the Drell-Yan differential cross-section using dimuon final state. In this chapter, the DY signal and possible background processes have been discussed and also

the Monte-Carlo cut-based estimation of the level of all the background processes is given. The details of the Muon identification, isolation and Drell-Yan event selection are also discussed. Section giving an overview of the estimation of the single muon trigger, identification and isolation efficiencies based on Data-Driven TagAndProbe method has also been included. The details about the Detector Acceptance, Final-State-Radiation (FSR) correction and the correction of the experimental results for the detector effects has been given in this chapter. In the end, the final cross-section measurement of the DY process in experimental data and comparison with the theoretical predictions, have been discussed.

Chapter 5 covers the details of the analysis workflow used in the study of the Underlying Event (UE) using Drell-Yan process. In this chapter, the details of the vertex selection, muon selection, Drell-Yan event selection and track selection are given. This chapter covers the measurement of the UE observables and details of the correction of the experimental results to the particle level. In the end, the final corrected experimental UE results and comparison with the various MC QCD models have been discussed.

Chapter 6 summarizes the experimental results and observations of the analysis presented in this thesis.

2

Large Hadron Collider and CMS Experiment

Between the border of France and Switzerland in a tunnel at 100 meters underground, the largest experiment in human history is currently active. Two decades of planning, developing and building came to an end in Year 2009, when the Large Hadron Collider(LHC) [23] finally started the collision operation. Roughly 10,000 physicists from more than thirty Nations all over the world have been working jointly to achieve this project, unified by the wish to understand the universe we live in. The core of the project is the Large Hadron Collider (LHC) and its four independent particle detectors ATLAS, CMS, ALICE and LHCb.

The Large Hadron Collider (LHC) is a superconducting magnet accelerator, hosted at the *European Organization for Nuclear Research* (CERN, French: Organization Europenne pour la Recherche Nuclaire), Geneva (Switzerland). It is a proton-proton collider aiming for the discovery of the Higgs boson and physics beyond the Standard Model with a centre-of-mass (CM) energy of up to 14 TeV. It was built during the Years 2000 to 2008 into the existing tunnel complex of the Large Electron Positron (LEP) collider. After eight years of construction, the LHC had the first beams injected in the Summer of Year 2008, had a major technical accident in September 2008. Again it was made operational and on 23rd November 2009, the first LHC collision became

available at 900 GeV center-of-mass. Then few months later, on 30th March 2010, protons were accelerated up to energies of 3.5 TeV, resulting in a centre-of-mass energy of $\sqrt{s} = 7$ TeV. The LHC is currently the worlds most high-energetic proton accelerator, with a designed luminosity L = 10^{34} $cm^2 s^{-1}$ and designed 7 TeV energy of the protons. In the Year 2010, a peak luminosity of $\mathcal{L} = 2{\times}10^{32} cm^{-2} s^{-1}$ was

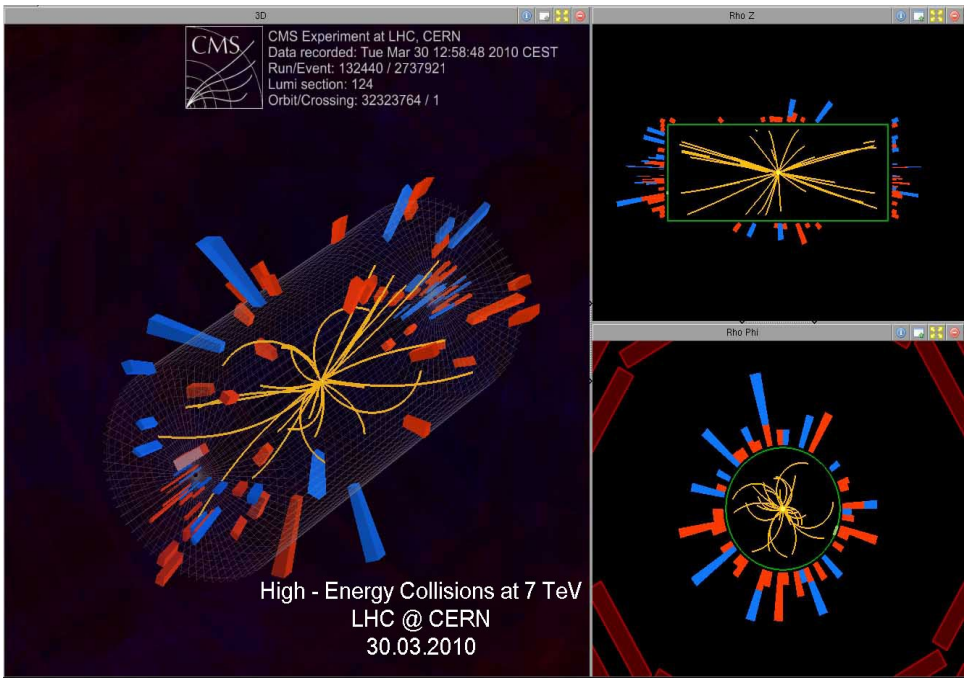

Figure 2.1: A beautiful 7 TeV E_{cm} pp collision event seen in CMS, from the very first minutes this regime was established.

achieved. On 22 April 2011, CERN's Large Hadron Collider set a new world record for the beam intensity at a hadron collider, when it collided beams with a luminosity of $4.67{\times}10^{32} cm^{-2} s^{-1}$. This exceeds the previous world record of $4.024{\times}10^{32} cm^{-2} s^{-1}$, which was set by the US Fermi National Accelerator Laboratorys Tevatron collider in the Year 2010, and marks an important milestone in LHC commissioning.

The current LHC run is scheduled to continue to the end of 2012. That will give the LHC experiments time to collect enough data to fully explore the energy range accessible with 7 TeV CM energy for new physics before preparing the LHC for higher energy running.

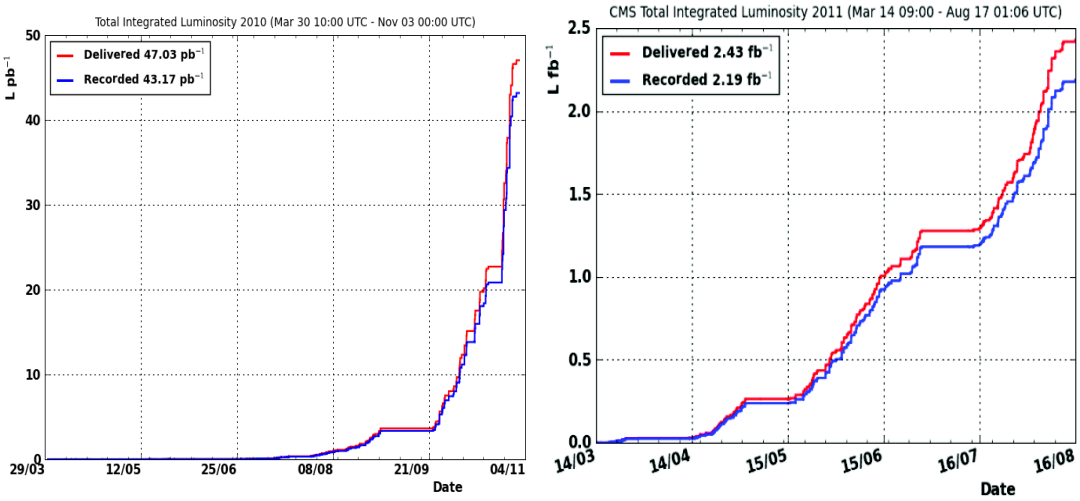

Figure 2.2: Graph of total integrated luminosity collected at CMS during (left) 2010 and (right) 2011 run.

2.1 Layout of Large Hadron Collider

The basic layout of LHC follows the LEP tunnel geometry is shown in Figure 2.3. The LHC tunnel has eight arcs and eight straight sections. Each straight section is approximately 528m long and can serve as an experimental or utility insertion. The two high luminosity experimental insertions are located at diametrically opposite straight sections: the ATLAS experiment is located at Point 1 and the CMS experiment at Point 5. Two more experimental insertions are located at Point 2 and Point 8, which also include the injection systems for Beam 1 and Beam 2, respectively. The injection kick occurs in the vertical plane with the two beams arriving at the LHC from below the LHC reference plane. The beams cross from one magnet bore to the other at four different locations. The remaining four straight sections do not have beam crossings. Insertions at Points 3 and 7 each contain two collimation systems. The insertion at Point 4 contains two RF systems: one independent system for each LHC beam. The straight section at Point 6 contains the beam-dump insertion, where the two beams are vertically extracted from the machine using a combination of horizontally deflecting fast-pulsed ("kicker") magnets and vertically-deflecting double steel septum

magnets. Each beam features an independent abort system. The LHC accelerator lattice has evolved over several versions. The LHC machine comprises 1232 dipole

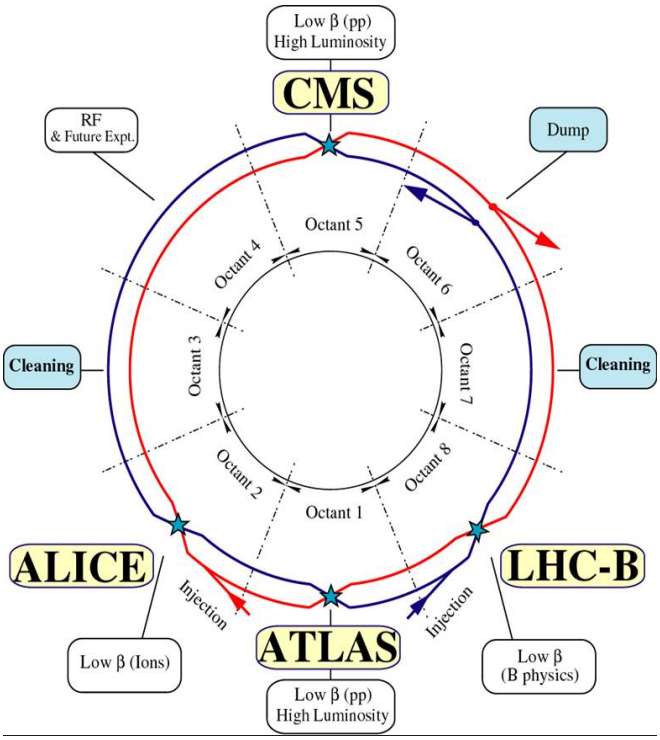

(a)

Figure 2.3: Schematic layout of the LHC

magnets, which provide a magnetic dipole field of 8.33T at an energy of 7 TeV per proton beam. The superconducting dipole magnets are cooled with super-fluid helium down to temperatures of 1.9 K. Each proton beam is separated into bunches of Np = 1.15×10^{11} protons per bunch, which have a spacing of 25ns. This corresponds to a collision frequency of 40 MHz. The design value for the number of bunches per beam is nb = 2808.

2.1.1 Accelerator systems and Injector complex

Figure 2.4 gives an overview over the LHC accelerator complex. The LHC is supplied with protons via the following injector chain:

Linac2 → Proton Synchrotron Booster(PSB) → Proton Synchrotron (PS) → Su-

per Proton Synchrotron (SPS) → LHC. Prior to being injected into the main accel-

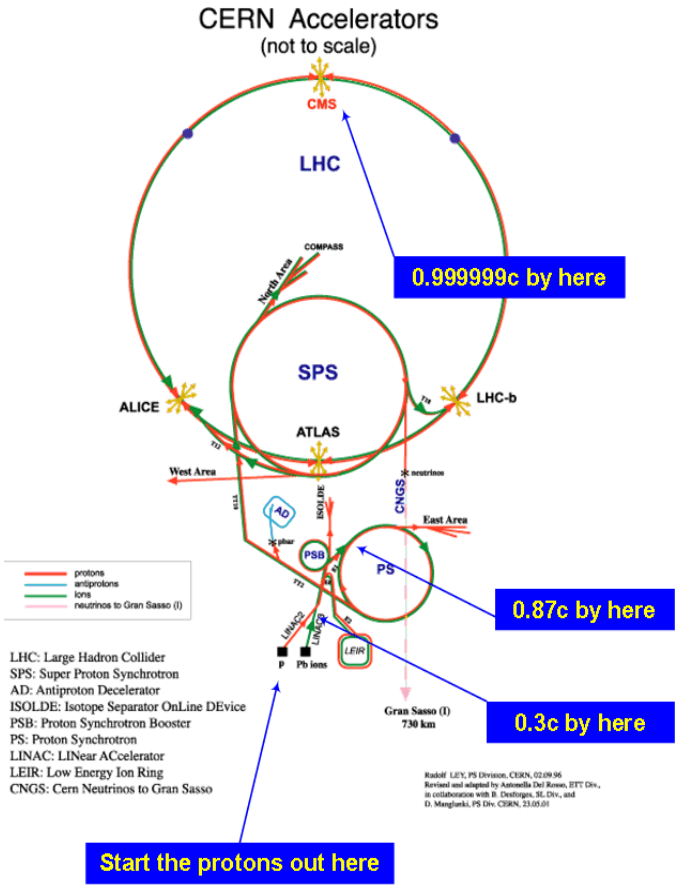

Figure 2.4: The Large Hadron Collider's (LHC) accelerator complex, in Geneva (Switzerland).

erator, the particles are prepared by a series of systems that successively increases their energy. The first system is the linear particle accelerator LINAC-2 accelerating protons to 50-MeV, which feeds the Proton Synchrotron Booster (PSB). By PSB the protons are accelerated to 1.4 GeV and injected into the Proton Synchrotron (PS), where they are accelerated to 26 GeV. Finally the Super Proton Synchrotron (SPS) is used to further increase their energy to 450 GeV before they are at last injected (over a period of 20 minutes) into the main LHC ring. Here the proton bunches are accumulated, accelerated (over a period of) to their peak energy 7 TeV and finally circulated for 10 to 24 hours while collisions occur at the four intersection points.

2.1.2 Luminosity and Center-of-mass energy

The luminosity is a measurement of the number of the collisions that can be produced in a detector per square centimeter and per second. The luminosity $\mathcal{L}$ of a collider experiment is defined as:

$$\mathcal{L} = \frac{N_1 N_2 n_b f_{rev}}{A_t^{eff}}, \tag{2.1}$$

where

- n_b is the number of bunches in one beam.
- N_i is the number of particles in each bunch (i = 1,2)
- f_{rev} is the revolution frequency and
- $A_t^{eff} = 4\pi\sigma_x \times \sigma_y$ is the effective transverse area of the beam, where $\sigma_{x,y}$ is the standard deviation of the particle distribution in the beam

The center-of-mass energy for a given beam energy E_{beam} at collider experiment is given as:

$$E_{CM}^{collider} = 2E_{beam}, \tag{2.2}$$

2.1.3 Experiments at the LHC

There are four main experiments at the Large Hadron Collider: ATLAS, CMS, ALICE and LHCb. The CMS [24] and ATLAS [25] experiments are multi-purpose detectors. They are designed to cover the full spectrum of measurements at the energy frontier and precision measurements of Standard Model processes. Important areas of new physics searches are the potential discovery of the Higgs boson, as well as supersymmetric particles and exotic signatures. ATLAS and CMS are complemented by two special purpose experiments: LHCb [26] is particularly designed for the study of b-physics at a peak luminosity of $10^{32} cm^{-2} s^{-1}$ and TOTEM [27] for the measurement of the elastic proton-proton cross-section. The LHCb will also allow for performing precise measurements of CP-violation, which allow for indirect searches of new physics in the rare decays. In addition to the proton beams, the LHC was also operated

with heavy-ion beams at the end of 2010. The ALICE [28] experiment is a dedicated heavy-ion experiment for the studies of lead-lead collisions and subsequently for the search of Quark-Gluon Plasma. The design energy per nucleon in Pb-Pb collisions is 2.76 TeV, which results in a total energy of 1148 TeV of two colliding lead nuclei.

The total proton-proton cross-section at the LHC at $\sqrt{s}$=14 TeV is expected to be roughly 100 mb. At design luminosity the general-purpose detectors will therefore, observe an event rate of approximately 10^9 inelastic events/sec. This leads to a number of formidable experimental challenges viz number crunching. The online event selection process (trigger) must reduce the huge rate to about 100 events/s for storage and subsequent data analysis. The short time between bunch crossings, 25 ns, has major implications for the design of the read-out and trigger systems.

At the design luminosity, a mean of about 20 inelastic collisions will be superimposed on the event of interest. This implies that around 1000 charged particles will emerge from the interaction region every 25 ns. The products of an interaction under study may be confused with those from other interactions in the same bunch crossing. This problem clearly becomes more severe when the response time of the detector element and its electronic signal is longer than 25 ns. This is called pile-up and effect of this pile-up can be reduced by using high-granularity detectors with good time resolution, resulting in low occupancy. However this requires a large number of detector channels and resulting millions of detector electronic channels require very good synchronization. The large flux of particles coming from the interaction region leads to high radiation levels, requiring radiation-hard detectors and front-end electronics. The detector requirements to meet the goal of the physics programme at the LHC are mentioned as follows:

- Good muon identification and momentum resolution over a wide range of momenta and angles, good dimuon mass resolution (1% at 100 GeV) and the ability to determine unambiguously the charge of muons with $p < 1$ TeV.

- Good charged-particle momentum resolution and reconstruction efficiency in the inner tracker. Efficient triggering and ofine tagging of t's and b-jets, requiring

pixel detectors close to the interaction region;

- Good electromagnetic energy resolution, good di-photon and di-electron mass resolution (1% at 100 GeV), wide geometric coverage, π^0 rejection and efficient photon and lepton isolation at high luminosities;

- Good missing-transverse-energy and dijet-mass resolution, requiring hadron calorimeters with a large hermetic geometric coverage and with ne lateral segmentation.

The Compact Muon Solenoid (CMS), one of the two general purpose detectors at the LHC, meets the above goals of the LHC physics programme. The detail about the CMS detector is discussed in net section.

2.2 Compact Muon Solenoid

The CMS detector is one of the two general purpose detectors at the LHC. A comprehensive description of the CMS detector is given in [24]. The CMS detector is a hermetic, 4π multi-purpose detector, shown in Figure 2.5. All sub-detectors are arranged concentrically around the cylindrical beam pipe and interaction point (IP). The CMS detector is divided into a central region, called barrel and two endcap regions. The main feature of the CMS detector is the 3.8T magnetic field, created by a superconducting solenoid, which allows an excellent momentum resolution of reconstructed charged particles(objects). Furthermore, it has three different subdetectors for the detection of muons, which are located outside the solenoid. In the barrel region, aluminium drift tubes (DT) are used and cathode strip chambers (CSC) in the endcaps. Both muon systems are complemented by Resistive Plate Chambers (RPC) for improved trigger timing. The sandwich-like arrangement of the muon detectors and the iron return yoke give rise to the characteristics appearance of the CMS detector. The weight of the solenoid including the iron return yoke is 10,000 tons, the total weight of the whole detector is 12,500 tons. Its dimensions are a length of 22 m and a diameter of 15 m. Therefore the detector is denoted as “compact”.

The fully silicon-based inner tracking system comprises a 3-layer silicon-pixel and a 10 layers silicon-strip detector, which allow for an excellent spatial resolution close to the IP, as well as a high momentum resolution. The electromagnetic calorimeter (ECAL) is composed of lead-tungstate crystals, which provide an excellent electromagnetic energy resolution for the measurement of electrons and photons. It is optimized for a potential discovery of a light, neutral Higgs boson, decaying into a pair of photons ($H^o \rightarrow \gamma\gamma$). A sampling hadronic calorimeter (HCAL) composed of brass absorbers and plastic scintillators completes the calorimetric system, which is hosted inside the solenoid. One feature of the CMS detector is, that the inner tracking system, as well as the complete calorimetry (ECAL and HCAL) are hosted inside the solenoid coil. The calorimetric system is supplemented by an additional hadronic outer (HO) calorimeter, which detects possible tails of hadronic showers, referred to as "tail-catcher".

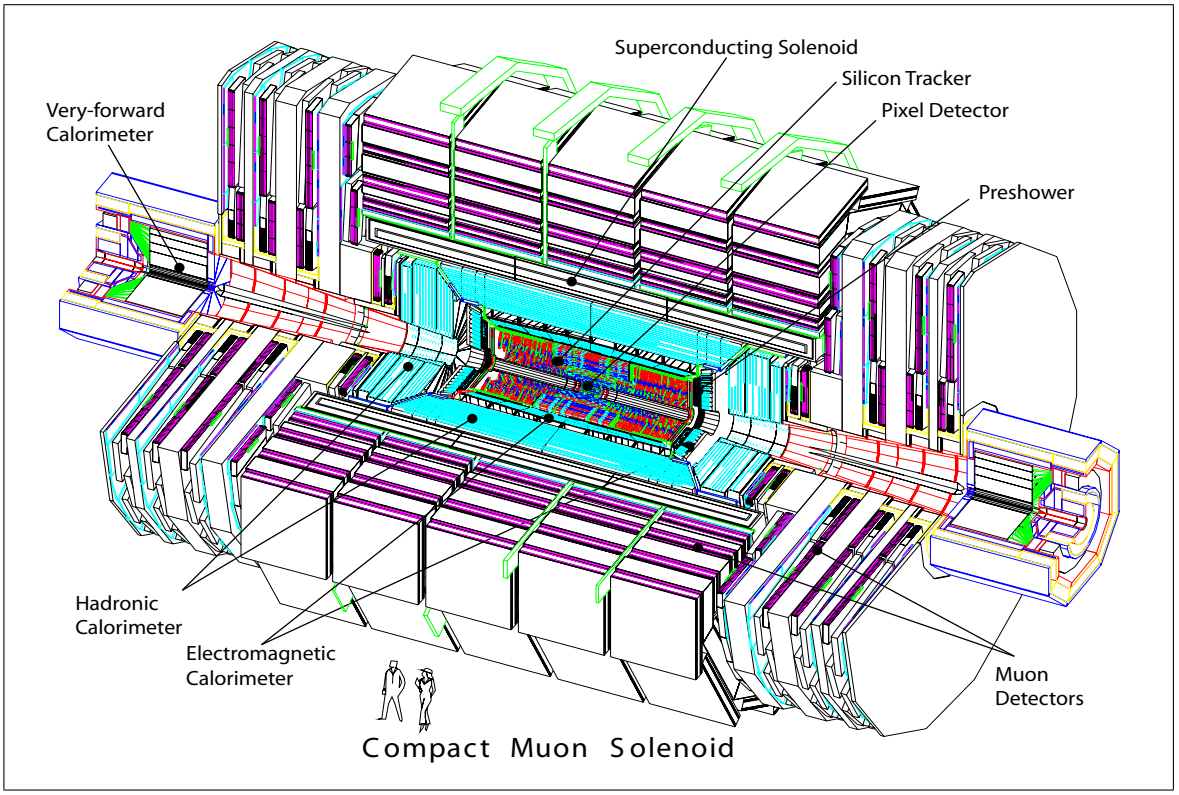

Figure 2.5: The Compact Muon Solenoid at the LHC.

2.2.1 CMS Co-ordinate system

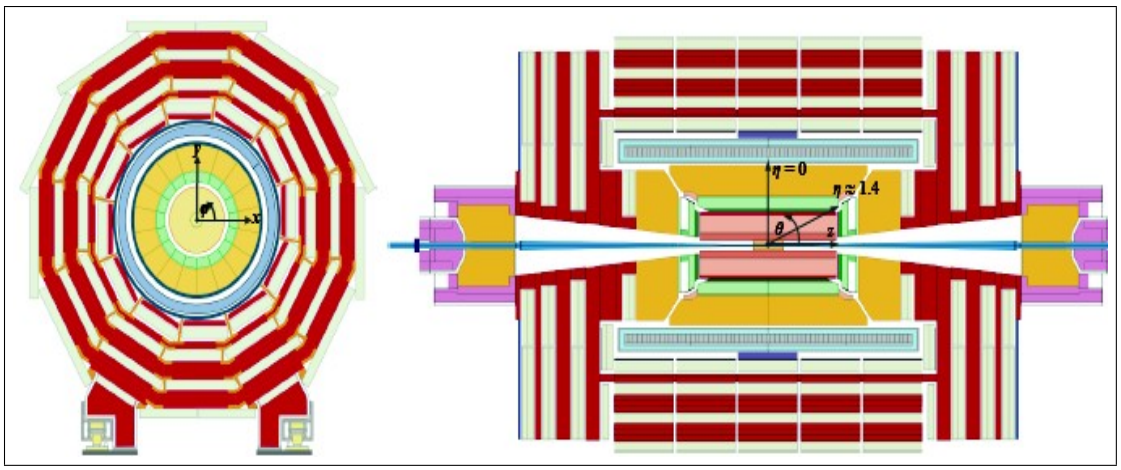

Figure 2.6: (Left) Transverse or cross-sectional view and (right) longitudinal view of the CMS detector .

Figure 2.6 (left) represents the cross-sectional and (right) represents the longitudinal view of CMS. The coordinate system adopted by CMS has the origin centered at the nominal collision point inside the experiment:

- the y-axis points vertically upward.
- the x-axis points radially inward toward the center of the LHC.
- the z-axis points along the beam direction toward the Jura mountains.
- the azimuthal angle ϕ is measured from the x-axis in the x-y plane.
- the radial coordinate in this plane is denoted by r.
- the polar angle θ is measured from the z-axis.

2.2.2 SuperConducting Magnet

The CMS detector requires a very strong magnetic field in order to induce enough bending of the charged particles so that the momentum of the charged particles can

be measured up to the highest momentum particle expected at the LHC energy. The superconducting magnet for CMS detector has been designed to reach a 4T eld in a free bore of 6-m diameter and 12.5-m length with a stored energy of 2.6 GJ at full current. The ux is returned through a 10,000 ton yoke comprising of 5 wheels and 2 endcaps, composed of three disks. Figure 2.7 shows artistic view of the CMS magnet.

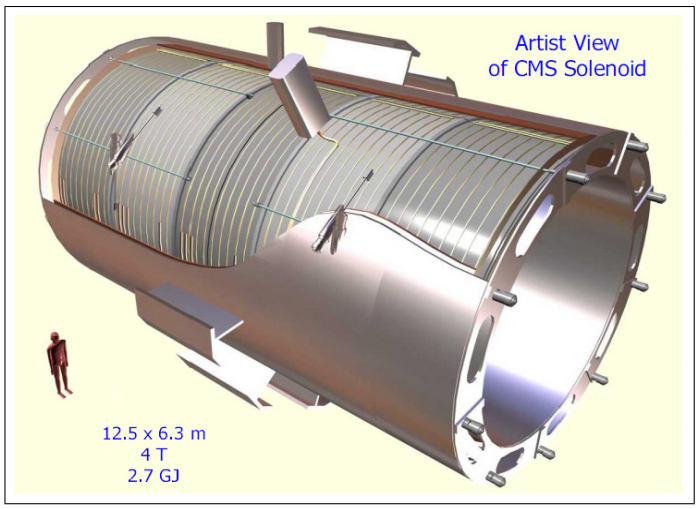

Figure 2.7: Artistic view of CMS solenoidal magnet.

2.2.3 Inner Tracking System

The expected LHC physics program requires a robust, efficient and precise reconstruction of the trajectories of charged particles with transverse momentum above 1 GeV in the pseudorapidity range $|\eta| < 2.5$. A precise measurement of the secondary vertices and the impact parameters is necessary for the efficient identification of heavy flavours which are produced in many of the interesting physics channels. Together with the electromagnetic calorimeter and the muon system, the tracker has to identify electrons and muons, respectively. In order to reduce the event rate from the LHC bunch crossing rate of 40 MHz to about 100 Hz, which can be stored permanently, tracking information is heavily used in the high level trigger of CMS.

The inner tracking system of CMS is designed to provide a precise and efficient

measurement of the trajectories of the charged particles emerging from the LHC collisions, as well as a precise reconstruction of secondary vertices. It surrounds the interaction point and has a length of 5.8m and a diameter of 2.5 m. The CMS solenoid provides a homogeneous magnetic field of 4T over the full volume of the tracker. At the LHC design luminosity of $10^{34} cm^{-2-1}$ there will be on an average about 1000 particles from more than 20 overlapping proton-proton interactions, traversing the tracker for each bunch crossing, *i.e.* every 25 ns. Therefore a detector technology featuring high granularity and fast response is required, such that the trajectories can be identified reliably and attributed to the correct bunch crossing. However, these features imply a high power density of the detector electronics which in turn requires efficient cooling. However this is in direct conflict with the aim of keeping the minimum amount of material in order to limit multiple scattering, bremsstrahlung, photon conversion and nuclear interactions. A compromise had to be found in this respect. The intense particle flux will also cause severe radiation damage to the tracking system. The main challenge in the design of the tracking system was to develop detector components able to operate in this harsh environment for an expected lifetime of 10 years. These requirements on granularity, speed and radiation hardness lead to a tracker design entirely based on silicon detector technology.

The inner tracking system is divided into two sub-detectors: pixel tracker, which is also referred to as vertex detector and the strip tracker. Both subsystems are fully based on silicon sensors. The inner tracking system consists of 66 million silicon pixels and 9.6 million silicon strips. Figure 2.8 shows a schematic view of the CMS inner tracking system.

- **Silicon Pixel detector**

  In the barrel region, close to the interaction point, three layers of pixel detectors are placed in parallel to the beam pipe at radii of r = 4.4, 7.3 and 10.2 cm with a size of a pixel of $100 \times 150 cm^2$. Additionally, there are two pixel endcap disks in the forward direction transverse to the beam line, which both have two pixel layers at distances of $|z| = 34.5$ and 46.5 cm. The pixel tracker is also referred

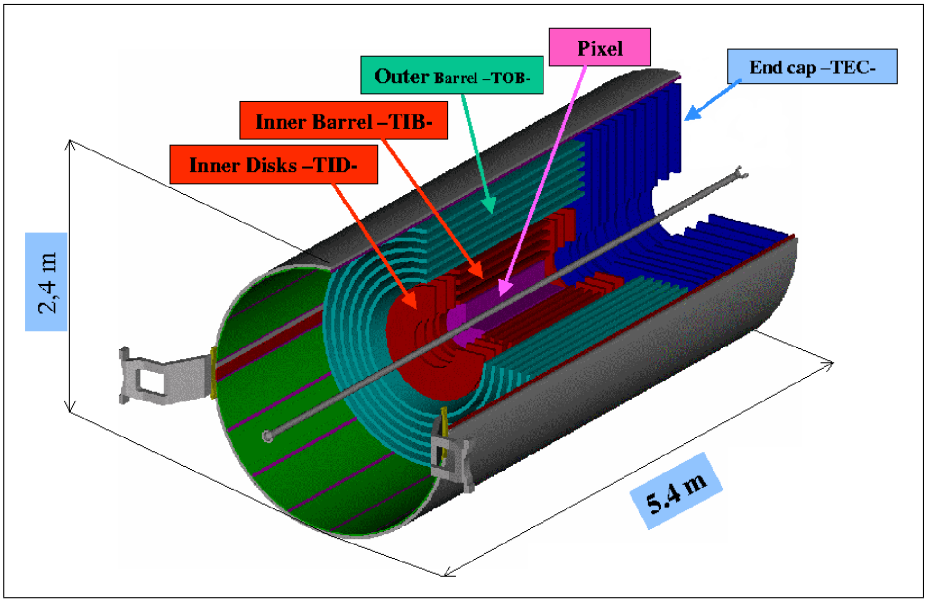

Figure 2.8: Schematic view of the CMS inner tracking system.

to as vertex detector, because the main task of the inner tracking system is to provide information about the primary interaction point (primary vertex) and displaced interaction points (secondary vertices) from the decay of long-lived unstable particles, like bottom or charm quarks. Due to the strength of high magnetic field, charged particles traversing the silicon sensors are detected by the Lorentz force. In the endcap disks, the blades carrying the pixel modules are rotated by 20^0 to compensate for the detection, which leads to a turbine-like geometry of the endcaps, which is shown in Figure 2.9.

- **Silicon strip detector**

  The silicon strip tracker system provides a coverage of $|\eta| < 2.4$ and consists of almost 15400 modules, which are mounted on a carbon-fiber structure and are operated at a temperature of around -20 ^0C. The strip tracker covers a region between $20 < r < 110$ cm, where the particle flux decreases with respect to the innermost region of the pixel tracker. Therefore silicon micro-strip detectors are used. The tracker inner barrel (TIB) consists of four layers of strip detectors. In the first two layers of the TIB, the modules are mounted as stereo modules

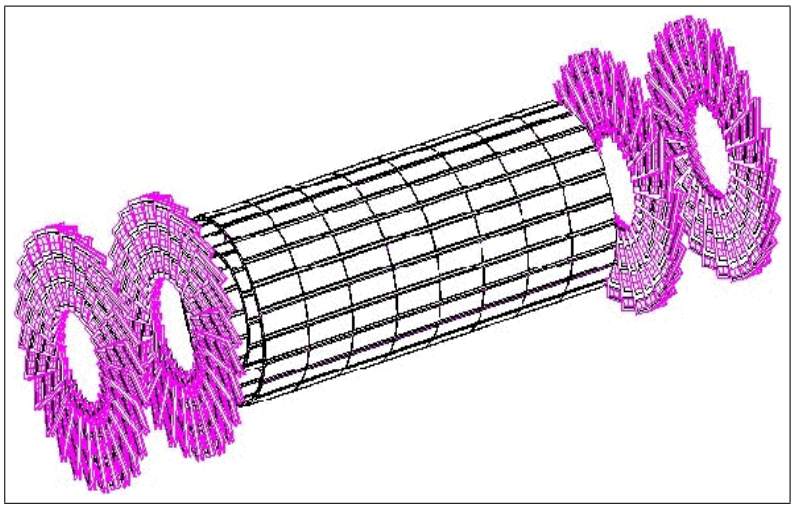

Figure 2.9: Pixel detector of CMS inner tracking system.

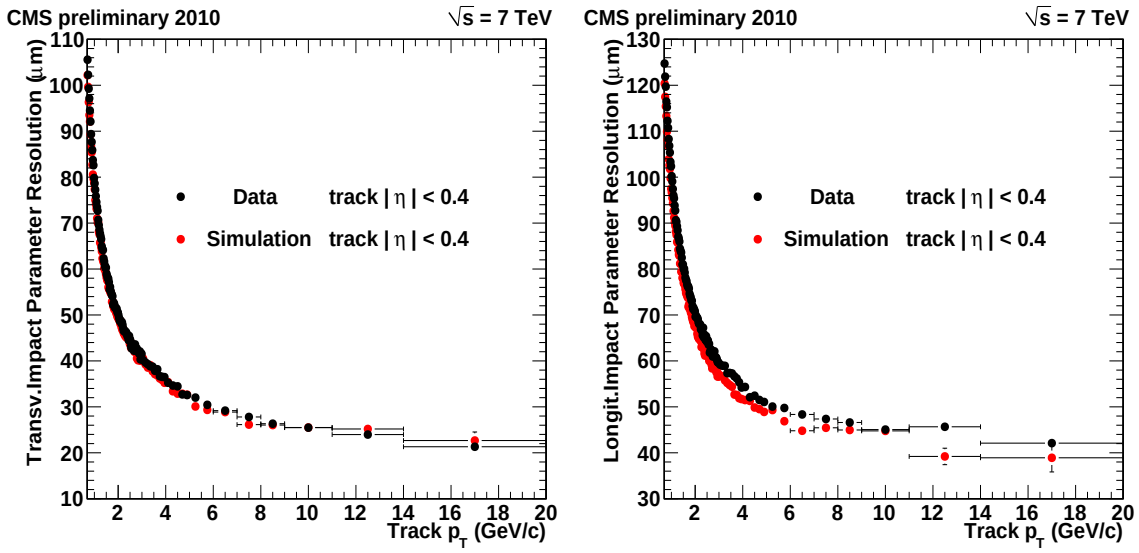

Figure 2.10: Measured resolution of the track transverse (left) and longitudinal impact parameter as a function of the track transverse momentum. Only central tracks with $|\eta| < 0.4$ are considered. Black and red points are data and MC simulation respectively.

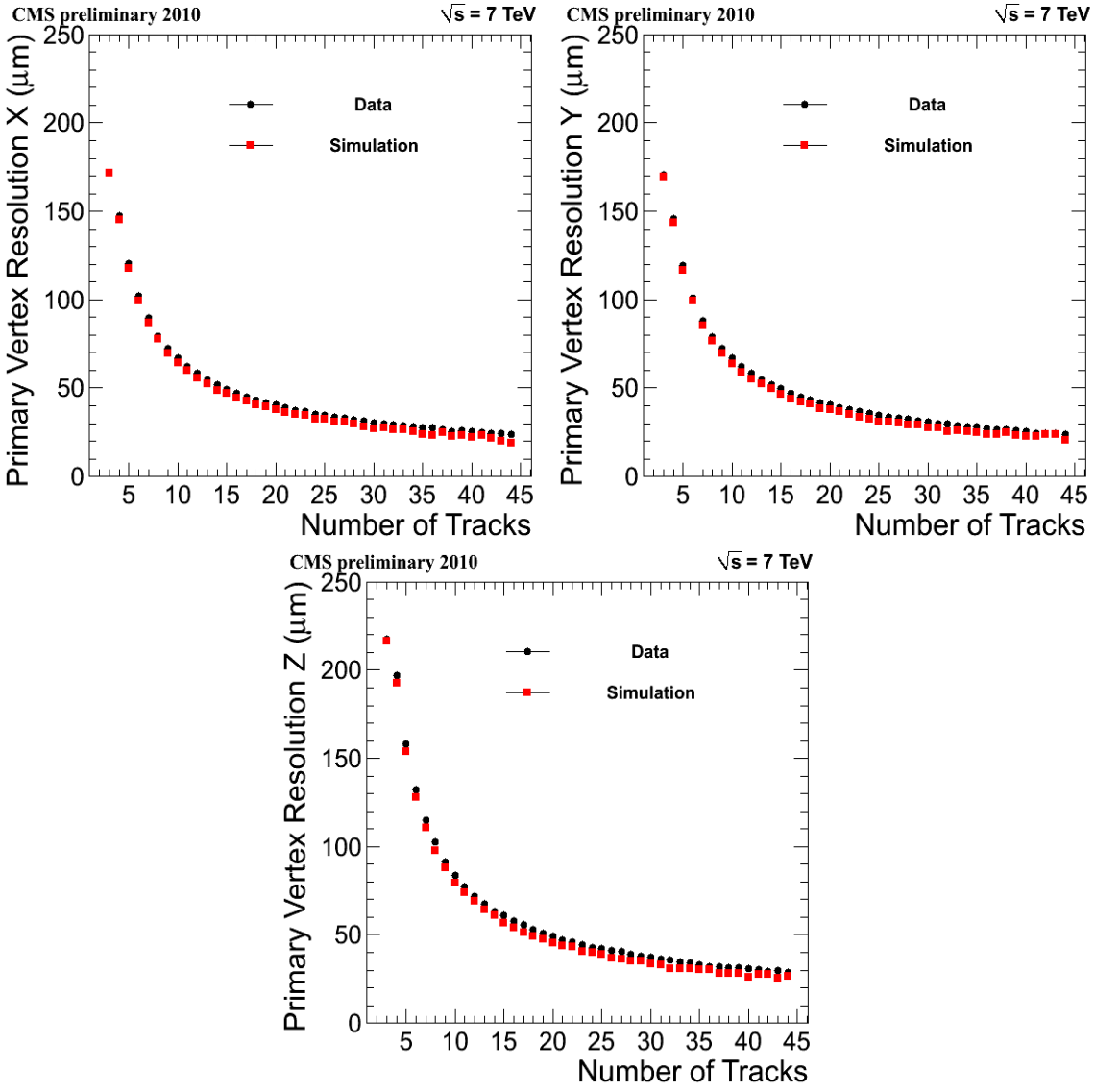

Figure 2.11: Primary vertex resolution in x (top left), y (top right) and z (bottom) as function of the number of tracks used in the fitted vertex.

with an angle of 100 mrad in order to provide a measurement in (r-ϕ) and (r-z) direction. The outermost region of the inner tracking system is referred to as the tracker outer barrel (TOB), which covers a radius between $55 < r < 110$ cm. The significantly lower particle flux allows for the use of larger-pitch silicon microstrip detectors with a good signal-to-noise ratio. The TOB comprises six layers of strip detectors, where the first two layers are also mounted as stereo modules. In the forward region, there are nine layers of micro-strips in each of the two tracker endcaps (TEC). Additionally,there are three layers of tracker inner disks (TID) on each side, in order to fill the gap in the transition region between TIB and TEC.

Figure 2.10 shows the transverse and longitudinal impact parameter resolution as a function of track transverse momentum. The transverse resolution is better than the longitudinal, since the transverse beam size is measured more precisely than the longitudinal one. The study of the resolution of the primary vertex reconstruction as a function of the number of tracks used in fitting the vertex is reported in [29] and the performance is shown in Figure 2.11. The results shown in Figures 2.10 and 2.11 are using pp collisions data collected at 7 TeV CM energy corresponding to an integrated luminosity of 10.9 nb^{-1}.

2.2.4 Electromagnetic Calorimeter

The calorimetry provides an inclusive energy measurement of the particles. Energy of electromagnetically interacting particles, like the electron and the photon, are measured in the electromagnetic calorimeter (ECAL). The electromagnetic calorimeter of CMS detector is a hermetic homogeneous calorimeter made up of 61,200 lead tungstate ($PbWO_4$) crystals [30] mounted in the central barrel part, closed by 7324 crystals in each of the two endcaps. To have better showering, a preshower detector is placed in front of the endcap crystals. Avalanche photo-diodes (APDs) are used as photodetectors in the barrel and vacuum photo triodes (VPTs) in the endcaps. With the use of high density crystals, the calorimeter has fine granularity and is ra-

diation resistant, which all are important characteristics in the LHC environment. One of the driving criteria in the design was the capability to detect the decay to two photons of the postulated Higgs boson. This capability is enhanced by the good energy resolution provided by a homogeneous crystal calorimeter. The characteristics

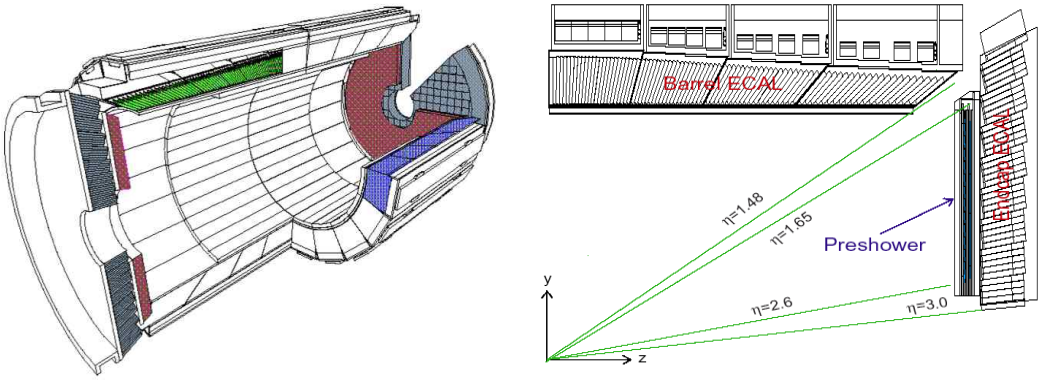

Figure 2.12: Electromagnetic calorimeter of the CMS detector.

of the PbWO4 crystals make them an appropriate choice for operation at the LHC. The crystals are characterized by high density (8.28 g/cm^3) and a short radiation length (X_0=0.89 cm), so the calorimeter is very compact and can be placed inside the magnetic coil. Furthermore, it has a small Molière radius (R_M=2.2 cm), which results in a fine granularity, needed because of high particle density produced at the LHC. Molière radius is the radius of a cylinder containing 90% of the shower's energy deposition. In recent years, $PbWO_4$ scintillation properties and other qualities have been progressively improved, leading to the mass production of optically clear, fast and radiation-hard crystals. The scintillation decay time of these production crystals is of the same order of magnitude as the LHC bunch crossing time: about 80% of the light is emitted in 25 ns. The ECAL barrel (EB) covers a region in pseudorapidity of $0 < |\eta| < 1.479$, shown in Figure 2.12. The inner radius of the EB is 129 cm. The crystals of the ECAL have a front face cross-section of 22×22 mm^2 and a length of 230 mm, which corresponds to nearly 26 radiation lengths. The crystals in the EB are grouped into 36 identical supermodules. The ECAL endcaps (EE) cover a region in pseudorapidity of $1.479 < |\eta| < 3.0$. Each endcap consists of two semi-circular

aluminium plates (dees), where 25 crystals are arranged into an array of 5×5 supercrystals. They have a front face cross-section of 28.6×28.6mm^2 and a length of 220mm, which corresponds to nearly 25X$_0$.

In front of each EE, a preshower (ES) device is mounted between $1.653 < |\eta| < 2.6$, which is shown in Figure 2.12. The aim of the preshower detector is to identify the signal of photons coming from the neutral pions (π^0), by making use of its high granularity. The preshower is a sampling calorimeter made of 2 layers of lead radiators and silicon strip sensors situated immediately after the lead radiators. The total thickness of the preshower is 20 cm (= 3X$_0$) long.

The energy resolution of a calorimeter can be parametrized as:

$$(\frac{\sigma}{E})^2 = (\frac{S}{\sqrt{E(GeV)}})^2 + (\frac{N}{E(GeV)})^2 + C^2 \quad (2.3)$$

where S is the stochastic term which includes the effects of fluctuations in the number of the photo-electrons, as well as in the shower containment, N the noise term includes contribution from the electronics and pile-up and C the constant term related to the calibration of the calorimeter. The ECAL energy resolution in test beams using electrons of 20 to 250 GeV has been measured [31] to be:

$$(\frac{\sigma}{E})^2 = (\frac{2.8\%}{\sqrt{E}(GeV)})^2 + (\frac{12\%}{E(GeV)})^2 + (0.3\%)^2 \quad (2.4)$$

The result is in good agreement with the design-goal performance expected for a perfectly calibrated Calorimeter.

2.2.5 Hadron Calorimeter

The hadronic calorimeter allows the energy and position measurement of the hadrons. This calorimeter plays an essential role in the identification of the quarks and gluons, by measuring the energy and direction of the jets. Moreover, it can indirectly detect particles that do not interact with the detector material such as the neutrino (by conservation of the momentum in transverse plane *i.e.* missing transverse energy). The measurement of the missing transverse energy is really important in the search of supersymmetric particles. For good missing energy resolution, a calorimeter covering

a large range of pseudorapidity is required. In addition, the HCAL will also aid in the identification of electrons, photons and muons in conjunction with the tracker, electromagnetic calorimeter and muon systems.

The design of the hadron calorimeter (HCAL) is strongly influenced by the choice of magnet parameters since most of the CMS calorimeter is located inside the CMS superconducting magnet coil and surrounds the ECAL system. An important requirement of the HCAL is to minimize the non-Gaussian tails in the energy resolution and to provide good containment of hadronic shower and hermeticity for missing energy measurements. The HCAL design maximizes the material inside the magnet coil in terms of interaction lengths. The brass has been chosen as absorber material as it has reasonable short interaction length and it is non-magnetic material . The requirement of maximizing the amount of absorber before the magnet, results into minimum space for the active medium. The scintillator tile technology makes an ideal choice. It consists of plastic scintillator tiles having wavelength-shifting (WLS) fibres to transport the light. The WLS fibres are spliced to high attenuation-length clear fibres outside the scintillator that carry the light to the readout system-photodetectors. The photodetection readout is based on multi-channel hybrid photodiodes (HPDs). The gap between the barrel and the endcap HCAL, through which the cable services of the ECAL and inner tracker pass, is inclined at 53^0 and points away from the center of the detector.

The CMS HCAL is thus subdivided into four regions, 2 barrels-HB (HCAL Barrel) and the HO (HCAL Outer) and 2 endcaps- HE (HCAL Endcap) and the HF (HCAL Forward), which provide a good segmentation, a moderate energy resolution and a full angular coverage upto $|\eta| = 5$.

The barrel (HB) part of HCAL consists of 32 towers covering the pseudorapidity region -1.4< $|\eta|$ <1.4, resulting in 2304 towers with a segmentation $\Delta\eta \times \Delta\phi = 0.087$ $\times$ 0.087. There are 15 brass plates, each with a thickness of about 5 cm, plus 2 external stainless steel plates for the mechanical strength. The particles leaving the ECAL volume first sees a scintillator plate with a thickness of 9 mm rather than 3.7 mm for other plates. There are two endcaps (HE), each one consists of 14 η towers

with 5^0 segmentation, covering the pseudorapidity region $1.3 < |\eta| < 3.0$. For the outermost towers (at smaller η), the ϕ segmentation is 5^0 and the η segmentation is 0.087. For the 8 innermost towers, the ϕ segmentation is 10^0, while η segmentation varies from 0.09 to 0.35 at the highest η. The total number of HE towers is 2304. The region with $3.0 < |\eta| < 5.0$ is covered with the help of hadron forward detectors (HF). These are made up of steel and quartz fibres. The signal originates from the Cerenkov light emitted in the quartz fibres, which is then channeled by the fibres to photomultipliers. There are 13 towers in η, all with a size given by $\Delta\eta = 0.175$, except for the lowest η towers with $\Delta\eta = 0.1$ and highest η towers with $\Delta\eta = 0.3$. The ϕ segmentation of all towers is 10^0, except for the highest η one, which has $\Delta\phi = 20^o$. This leads to 900 towers and 1800 channels in the 2 HF modulus. The HCAL acceptance region and layout is shown in Figure 2.13.

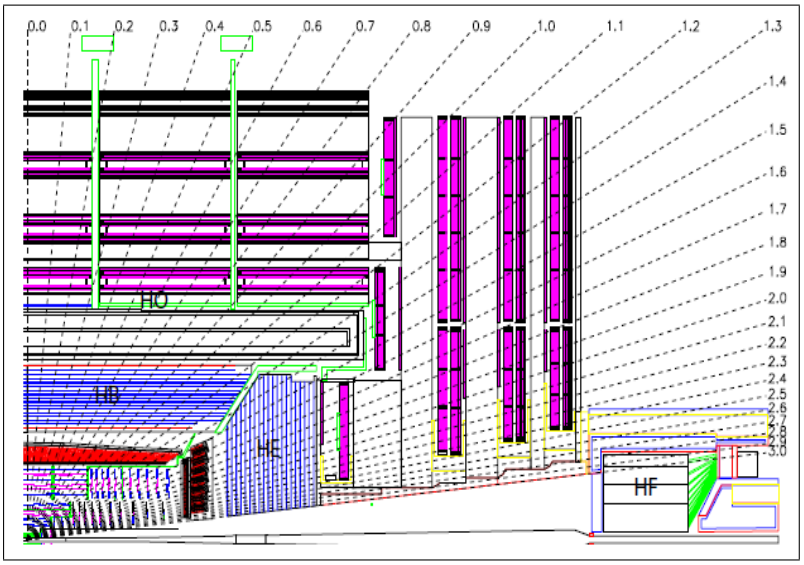

Figure 2.13: Longitudinal cross-section of the quarter of the CMS detector showing the positions of the hadronic calorimeter barrel (HB), hadronic calorimeter endcap (HE), forward hadronic calorimeter (HF) and outer hadronic calorimeter (HO).

2.2.6 Outer Hadron Calorimeter

The HCAL plays an important role in CMS experiment for the measurement of jets and missing energy. The HCAL is inside the solenoid and not thick enough to contain complete hadronic shower. So HCAL is extended outside the solenoid coil. This extended part of HCAL is called Outer Hadronic Calorimeter (HO) [32]. The HO utilizes the coil as an additional absorber material equal to 1.4=sinθ interaction lengths (λ). It will be used to measure energy for late shower development and to measure the shower energy beyond the geometrical reach of HB. Close to the interaction point at $\eta = 0$,where HB provides minimum interaction length to the hadrons. Therefore, the central ring (Ring 0) has two layers of HO plastic scintillators. All other rings($\pm$1,$\pm$2) have single HO layer. The total depth of the hadron calorimeter is thus extended to a minimum of 11.8λ as shown in Figure 2.14, except the barrel-endcap boundary region. The HO layers are physically located inside the barrel muon system.

The design of HO is constrained by the geometry of the muon system. The sizes and positions of the tiles in HO are supposed to roughly map the layers of HB to make towers of granularity 0.087 $\times$ 0.087 in η and ϕ. The HO is physically divided into five rings in η direction. The rings are numbered -2, -1, 0, 1, 2 with increasing η. Each ring of the HO is divided into 12 identical ϕ sectors and each sector has 6 slices or trays in ϕ direction. The ϕ slices of a layer are identical in all the sectors. The scintillation light from the tiles is collected using wave length shifting (WLS) fibers of diameter 0.94 mm and transported to the photo detectors located on the structure of the return yoke by splicing a clear fiber (high attenuation length).

2.2.7 Muon System

Muon detection is a powerful tool for recognizing signatures of interesting processes over the very high background rate expected at the LHC with full luminosity. For example, the predicted decay of the Standard Model Higgs boson into ZZ or ZZ*, which in turn decay into 4 leptons, has been called “gold plated” for the case in which all the leptons are muons. Besides the relative ease in detecting muons, the

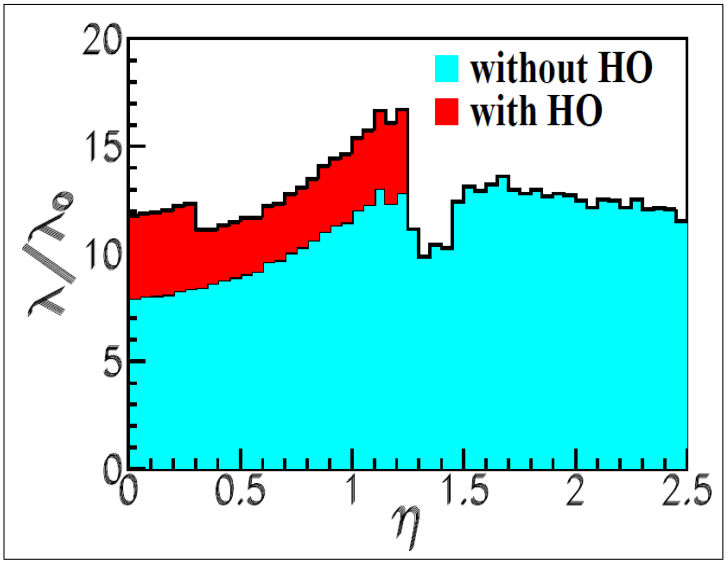

Figure 2.14: Number of interaction lengths till the last sampling layer of the hadron calorimeter as a function of η. The two shaded regions correspond to the setups with or without the outer hadron calorimeter.

best 4-particle mass resolution can be achieved if all the leptons are muons because they are less affected than electrons by radiative losses in the tracker material. This example and other particles from SUSY models, emphasize the discovery potential of muon final states and the necessity for wide angular coverage for muon detection.

Therefore, as is implied by the experiment's middle name, the detection of muons is of central importance to CMS: precise and robust muon measurement was a central theme from its earliest design stages. The muon system has 3 functions: muon identification, momentum measurement and triggering. Good muon momentum resolution and trigger capability are enabled by the high field solenoidal magnet and its flux-return yoke. The latter also serves as a hadron absorber for the identification of muons. The material thickness crossed by muons, as a function of pseudorapidity, is shown in Figure 2.15

The CMS muon system is designed to have the capability of reconstructing the momentum and the charge of the muons over the the entire kinematic range of the LHC. The CMS detector uses 3 types of gaseous particle detectors for muon identifi-

cation namely- Resistive Plate Chambers, Cathode Strip Chambers and Drift Tubes. The detail of all these detectors can be found in ref [33]. Due to the shape of the solenoid magnet, the muon system was naturally driven to have a cylindrical barrel section and 2 planar endcap regions. Because the muon system consists of about 25,000 m^2 of detection planes, the muon chambers had to be inexpensive, reliable and robust. A schematic view of the one quadrant of the CMS muon system is shown in Figure 2.16.

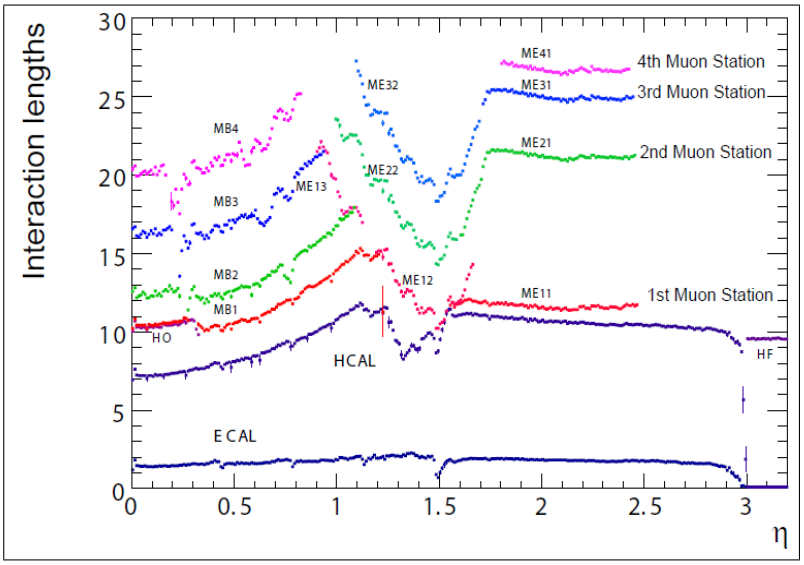

Figure 2.15: Material thickness in interaction lengths at various depths, as a function of pseuodorapidity.

Drift Tube Chambers

The Drift Tube Chambers (DT) [34] muon subsystem, covers pseudo-rapidity range, $|\eta| < 1.2$. It consist of five wheels, each wheel divided into 12 sectors, each covering an azimuthal region of 30 degrees. Sectors are numbered anticlockwise, starting from the right-most vertical sector shown in Figure 2.17, in the direction of increasing azimuthal angle, ϕ. Each sector consisting of four chambers, one on inside of the magnet return yoke, one on the outside and two sandwiched in between the magnet return yoke. The support for the magnet return yoke is placed in between the chambers, so

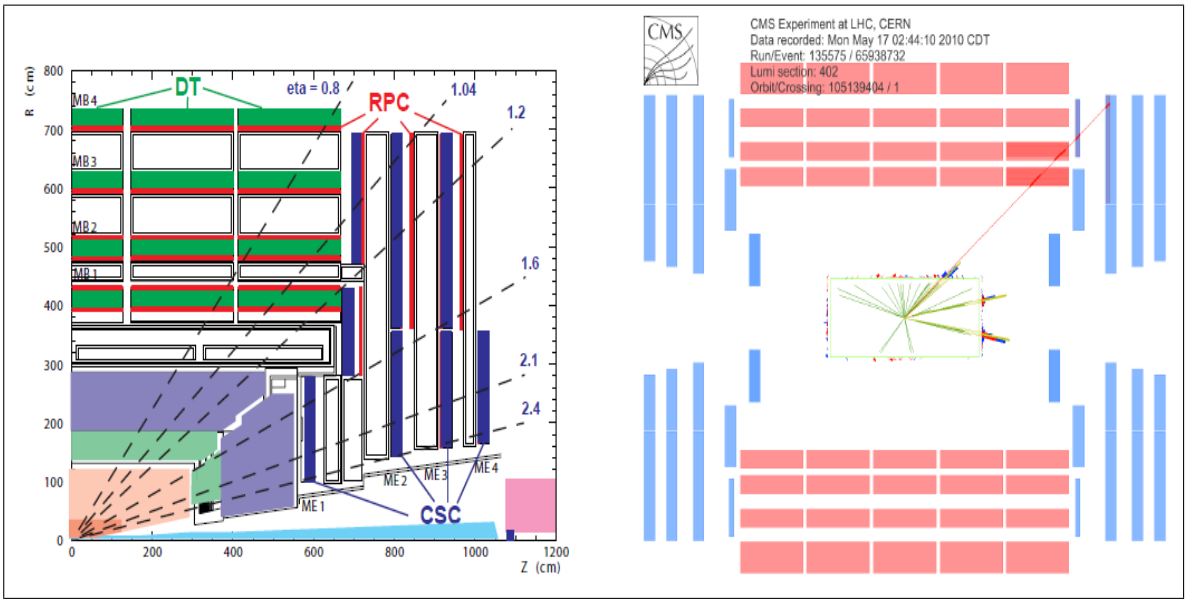

Figure 2.16: Layout of the one quadrant of the CMS (left) and a display of the collision event with a muon crossing the DT and CSC chambers in the overlap region between barrel and endcap (right).

they do not overlap in azimuthal angle ϕ, thus insuring complete ϕ coverage by the DT chambers.

Each drift-tube chamber is made of either two or three superlayers (SL), each superlayer, in its turn, is made of four layers of long rectangular drift cells staggered by half a cell. The drift cell is 2.4m long with the cross-section 13 $\times$ 42 mm^2. A thin anode wire is stretched in the middle of the tube along the long side of it. The characteristic transverse dimension of the drift cell is 21 mm, thus the maximum drift time is 380 ns in the gas mixture of 85% Ar and 15% CO_2. The two superlayers on outside of the chamber have wires inside the cell parallel to the beam line, thus accurate measurement of the azimuthal angle. The superlayer inside the chamber has wires perpendicular to the beam line, thus measuring the z-position. The z-measuring superlayer is not present in the last muon station. The superlayer is a basic measuring unit of the DT station.

One SL, that is, a group of 4 consecutive layers of thin tubes staggered by half a tube, gives excellent time-tagging capability, with a time resolution of a few nanosec-

onds. This capability provides local, stand-alone and efficient bunch crossing identification. The time tagging is delayed by a constant amount of time equal to the maximum possible drift-time, which is determined by the size of the tube, the electrical field and the gas mixture. The design and the precise mechanical construction of the DT chamber allowed them to achieve 100 μm precision in global $r-\phi$ position measurement.

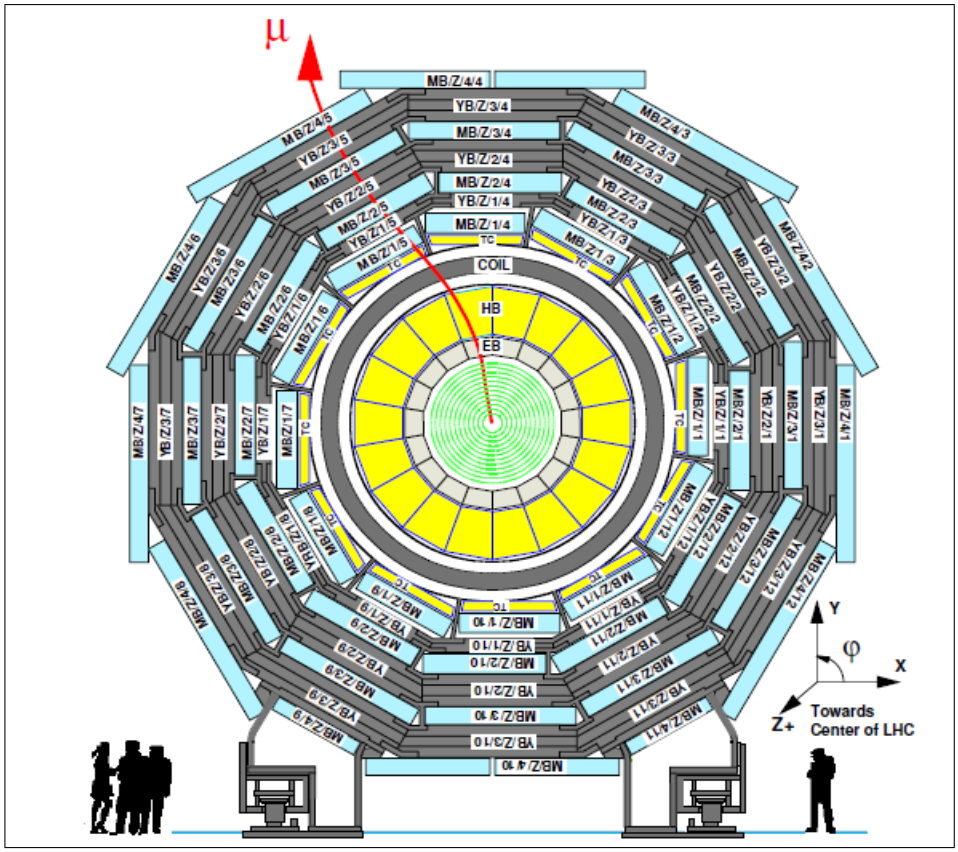

Figure 2.17: Layout of the CMS barrel muon DT chambers in one of the 5 wheels. The chambers in each wheel are identical with the exception of wheels -1 and +1 where the presence of cryogenic chimneys for the magnet shortens the chamber in 2 sectors. Note that in sectors 4 (top) and 10 (bottom) the MB4 chambers are cut in half to simplify the mechanism assembly and the global chamber layout.

Cathode Strip Chambers

The Cathode Strip Chambers (CSCs) [35] constitute an essential component of the CMS muon detector, providing precise tracking and triggering of muons in the endcaps. Their performance is critical to many physics analyses based on muons. The region between 0.9< $|\eta|$ <1.2 is covered by both the DT chambers and CSC. There are 468 CSCs in the 2 Muon Endcaps. Each Endcap consists of 4 "stations" of chambers, labeled ME1 to ME4 in order of increasing distance from the collision point, which are mounted on the disks enclosing the CMS magnet, perpendicular to the beam direction. In each disk the chambers are divided into 2 concentric rings around the beam axis (3 for ME1 chambers). Each CSC 2.18 (right) is trapezoidal in shape

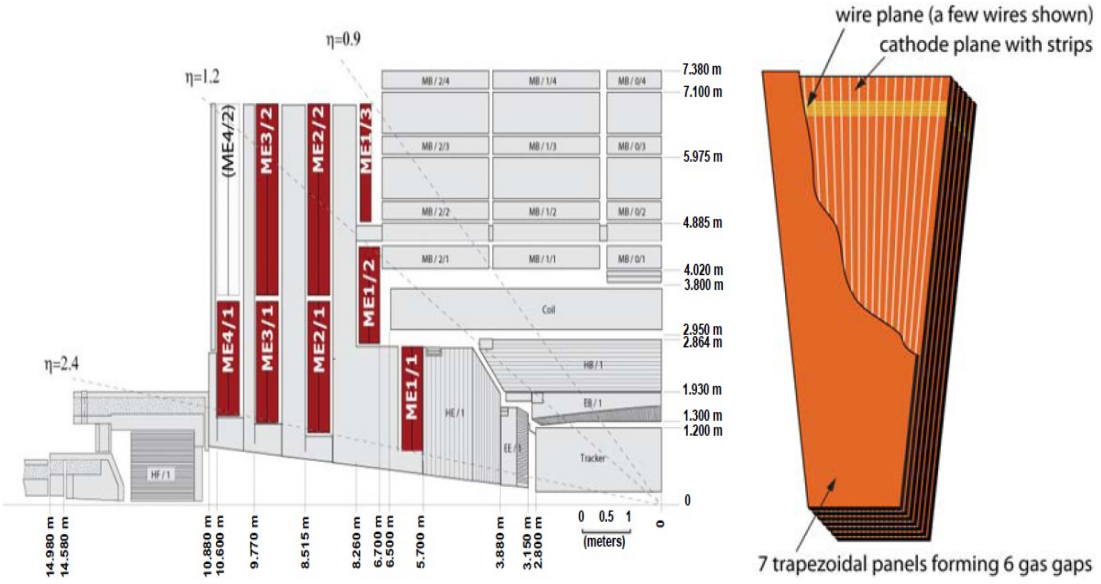

Figure 2.18: The layout of muon cathode strip chambers (CSC) in one quarter of the CMS. Most of the cathode strip chambers are highlighted in dark-red, the ME4/2 chamber is not highlighted, because it was thought that it would not be installed at the start-up of the LHC, but delays in the LHC start-up allowed for it to be installed for the first data.

and consists of 6 gas gaps, each gap having a plane of radial cathode strips and a plane of anode wires running almost perpendicularly to the strips. All CSCs, except

those in ME1/3, are overlapped in ϕ to avoid gaps in the muon acceptance. There are 36 chambers in each ring of a muon station, except for the innermost (highest η) rings of ME2-ME4 which have 18 chambers. The gas ionization and subsequent electron avalanche caused by a charged particle traversing each plane of a chamber produces a charge on the anode wire and an image charge on a group of cathode strips. Thus, each CSC measures the space coordinates (r, ϕ, z) in each of the 6 layers. Figure 2.18 (left) shows drawing of quadrant of CMS detector highlighting the CSC subdetector.

Resistive Plate Chamber System

Resistive Plate Chambers (RPC) [36] are gaseous parallel-plate detectors that combine adequate spatial resolution with a time resolution comparable to that of scintillators [37,38]. An RPC is capable of tagging the time of an ionizing particle in a much shorter time compare to the 25ns between LHC bunch crossings (BX). Therefore, a fast dedicated muon trigger device based on RPCs can identify unambiguously the relevant BX to which a muon track is associated with, even in the presence of the high particle rate and background expected at the LHC. Signals from such a device directly provide the time and position of a muon hit with the required accuracy. A trigger based on RPCs has to provide the BX assignment to candidate tracks and estimate the transverse momenta with high efficiency in an environment where rates may reach 10^3 Hz/cm^2.

The RPC detectors are employed in CMS as a dedicated trigger system in both the barrel as well as in the endcap regions. They complement the muon tracking system: drift tubes (DT) in the barrel and cathode strip chambers (CSC) in the endcaps. From the geometrical point of view, the muon system is divided into five wheels in the barrel and three disks in each endcap. Each barrel wheel is divided into 12 sectors, covering the full azimuthal dimension Figure 2.19. Each sector consists of four layers of DTs and six layers of RPCs, with a total of 480 RPC stations covering average area of 12 m^2. The two innermost DT layers are sandwiched between RPC layers (RB1$_{in}$ and RB1$_{out}$ for the innermost DT layer, RB2$_{in}$ and RB2$_{out}$ for the second one). The third and fourth DT layers are complemented with a single RPC

layer, placed on their inner side (RB3 and RB4).For the initial data-taking period, until the next long shutdown of the LHC accelerator, the RPC coverage extends only to the pseudo-rapidity region $|\eta| < 1.6$, which would be increased later on.

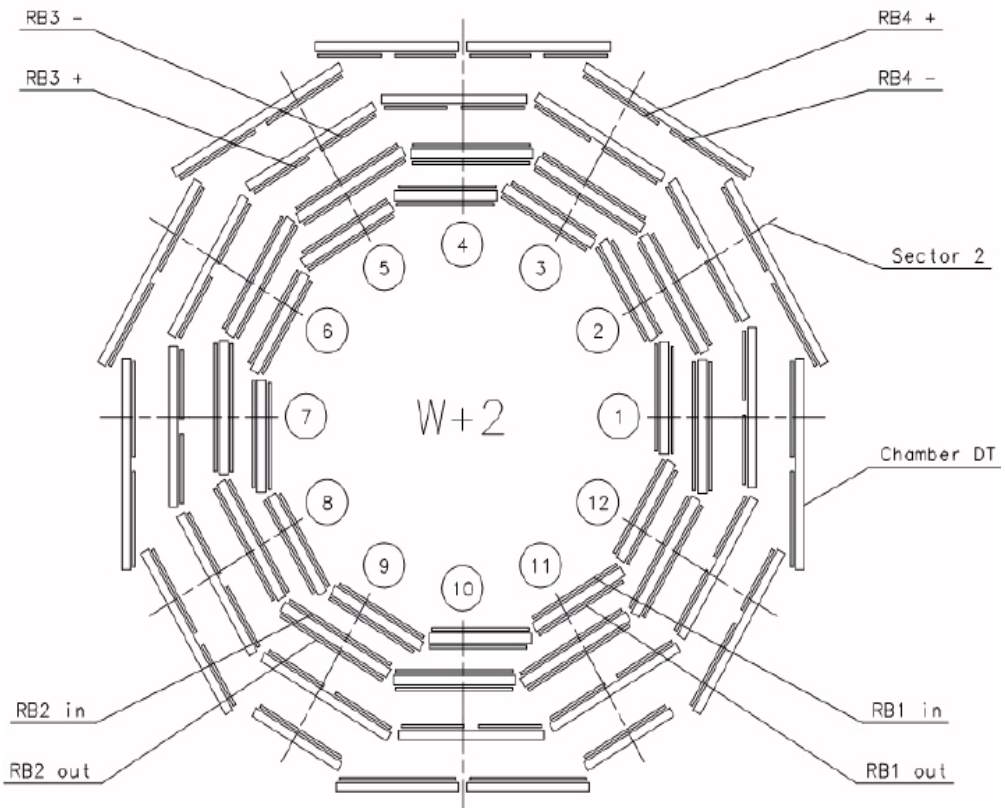

Figure 2.19: Transverse view of the muon system layout in the barrel region, showing the positions of the DT and RPC stations.

The measurement of the momentum of the charged particles is affected by systematic uncertainties due to the limited knowledge and modeling of the detector material, the magnetic field, the alignment and the reconstruction algorithms used to fit the track trajectory. By studying the mass of resonances like Z, improvements in the modeling of the detector material and eventually the final calibration of the tracks and muons can be achieved. The study of the resolution of the transverse momentum as a function of muon pseudorapidity [39], measured with 40 nb^{-1} of integrated luminosity with CMS is shown in Figure 2.20

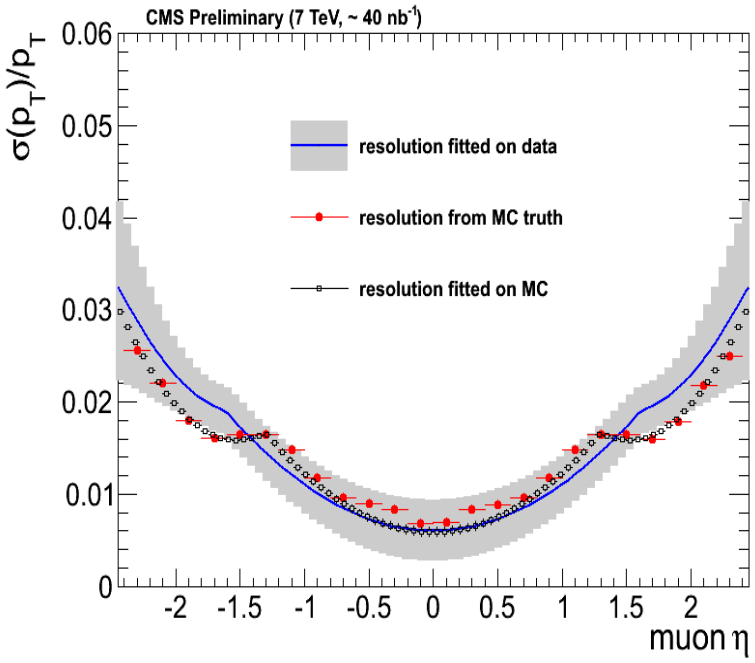

Figure 2.20: Resolution on transverse momentum as measured with$\sim$ 40 nb^{-1} of integrated luminosity (black line) compared to the Monte Carlo resolution computed from Monte Carlo truth (red points) and from the fit as described in Section 4.2 (black squares). The gray band in data represents the error on the fitted function for data computed from the errors on the parameters.

2.2.8 Trigger system

Level-1 Trigger

The LHC provides proton-proton with a very high interaction rate. For protons the beam crossing interval is 25ns, corresponding to a crossing frequency of 40 MHz. Depending on luminosity, several collisions occur at each crossing of the proton bunches (approximately 20 simultaneous proton-proton collisions at the nominal design luminosity of $10^{34} cm^{-2} s^{-1}$). Since it is impossible to store and process the large amount of data associated with such a high number of events with LHC bunch crossing, a drastic rate reduction has to be achieved. This task is performed by the trigger system, which is the start of the physics event selection process. The rate is reduced in two steps called Level-1 (L1) Trigger [40] and High-Level Trigger (HLT) [41], respectively.

The Level-1 Trigger consists of custom-designed, largely hardware based programmable electronics, whereas the HLT is a software based system implemented in a filter farm of about one thousand commercial computer processors. The rate reduction capability is designed to be at least a factor of 10^6 for the combined L1-Trigger and HLT. The design output rate limit of the L1 Trigger is 100 kHz. The L1 Trigger uses coarsely segmented data from the calorimeters and the muon system, while holding the high-resolution data in pipelined memories in the front-end electronics. The High Level Triggers, implemented as a computer processing farm that is designed to achieve a rejection factor of 10^3, write up to 100 events/second to mass computer storage. The last stage of High Level Trigger processing does reconstruction and event filtering with the primary goal of making data sets of different signatures on easily accessed media.

The L1 Trigger System is organized into three major subsystems: the L1 Global Calorimeter trigger (GCT), the L1 Global Muon trigger (GMT) and the L1 Global trigger (GT). The muon trigger is further organized into subsystems representing the 3 different muon detector systems, the Drift Tube Trigger in the barrel, the Cathode Strip Chamber (CSC) trigger in the endcap and the Resistive Plate Chamber (RPC) trigger covering both barrel and endcap. The L1 muon trigger also has a global muon

trigger that combines the trigger information from the DT, CSC and RPC trigger systems and sends this information to the L1 Global trigger. The Global trigger takes the decision to reject an event or to accept it for further evaluation by the HLT. The decision is based on algorithm calculations and on the readiness of the sub-detectors and the Data Acquisition System(DAQ), which is determined by the Trigger Control System (TCS). The Level-1 Accept (L1A) decision is communicated to the sub-detectors through the Timing, Trigger and Control (TTC) system. The architecture of the L1 Trigger is depicted in Figure 2.21. The L1 Trigger has to analyze event information for every bunch crossing. The allowed L1 Trigger latency, between a given bunch crossing and the distribution of the trigger decision to the detector front-end electronics, is 3.2 μs. The processing must therefore be pipelined in order to enable a quasi-deadtime-free operation. The L1 Trigger electronics is housed partly on the detectors, partly in the underground control room located at a distance of approximately 90m from the experimental cavern.

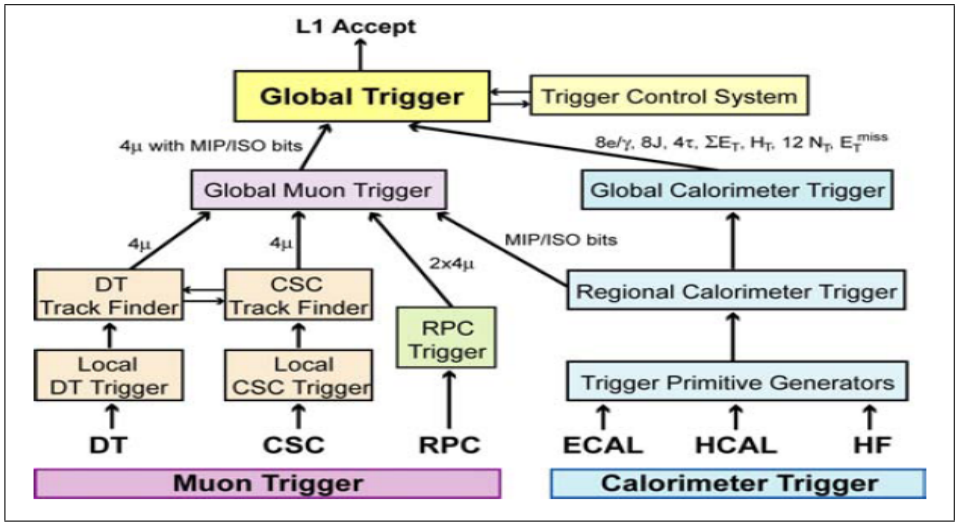

Figure 2.21: Architecture of Level-1 trigger

Data Acquisition and High Level Trigger

The architecture of the CMS detector Data Acquisition system(DAQ) is shown schematically in Figure 2.22. The CMS Trigger and DAQ System is designed to collect and

analyze the detector information at the LHC bunch crossing frequency of 40 MHz. The DAQ System must sustain a maximum input rate of 100 kHz and must provide enough computing power for a software filter system, the High Level Trigger (HLT), to reduce the rate of stored events by a factor of 1000. Thus the main purpose of the Data Acquisition (DAQ) and High-Level Trigger (HLT) system is to read the CMS detector event information for those events that are selected by the Level-1 Trigger and to select, from amongst those events, the most interesting ones for output to mass storage. The proper functioning of the DAQ at the desired performance will be a key element in reaching the physics potential of the CMS experiment. In addition,

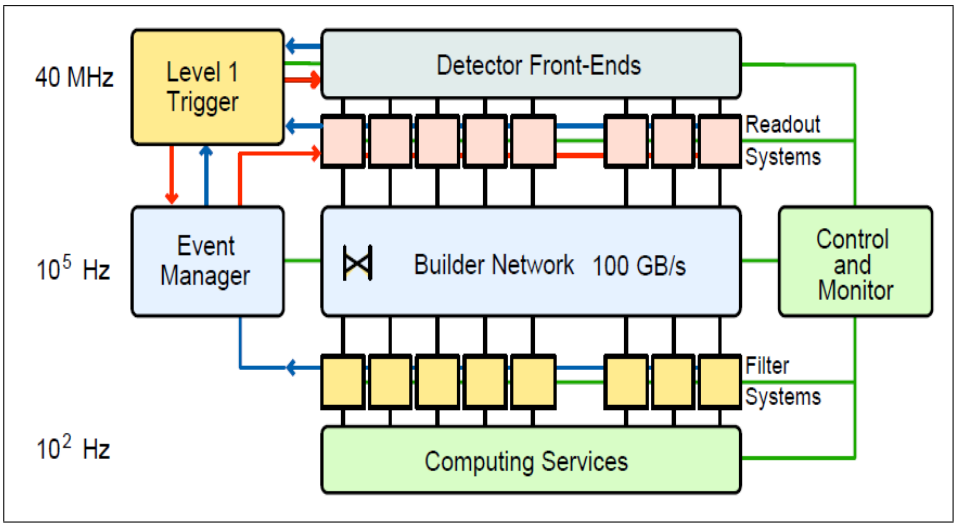

Figure 2.22: Architecture of Data Acquisition system

to maximize this physics potential, the selection of events by the HLT must be kept as broad and as inclusive as possible, not to loose signal too. In summary, the online event filtering process in the CMS experiment will be carried out in two steps:

- The Level-1 Trigger, with a total processing time of 3 μs, including the latencies for the transport of the data and control signals. During this time interval, the data are stored in the pipeline memories in the front-end electronics. The Level-1 Trigger is designed to accept a maximum rate of 100 kHz.

- The High-Level Trigger, with a total processing time of up to $\sim$ 1s. During this

time interval, the data are stored in random-access memories. The High-Level Trigger is designed to output a maximum mean event rate of $\sim$ 100 Hz.

2.3 Particle Detection through interaction with detector Material

Collider detectors which are designed to discover new particles, must be designed to observe all possible decay products, identify them and should be capable of measuring their position and energy very accurately. Particle identification is the most important aspect while designing a detector. The basic layout of the modern collider detector is remarkably uniform.

- During bunch crossing of beams, interaction would take place and particles would be produced in the interaction. These produced particles are required to be detected by the various detector components. The particle produced at the interaction point (IP) has to pass first through the tracking device made up of silicon detector. Tracking device is the innermost part of the CMS detector close to the IP. When charged particle passes through it, it creates electron-hole pairs which get collected by electrodes to give signal. To remove the thermally generated electron-hole pairs, the silicon detector is setup in reverse bias. Signals from different silicon-pixels and strips are combined to form track of charged particles.

- After the detector tracking layers, the particles enters into Electromagnetic calorimeters(ECAL). In ECAL, the electromagnetic particles, electrons and photons deposit most of their energy by EM interactions (*i.e.* ionization, bremsstrahlung, pair production, Compton scattering, etc.). An energetic electron passing into the ECAL, will radiate photons, through Bremsstrahlung. If the energy of the Bremsstrahlung photon is sufficiently high ($> 2M_e$ $\sim$1.02 MEV) it will, in turn, produces an electron-position pair, through pair-production. The pair production partners will then each radiate photons. The processes of

Bremsstrahlung and pair-production will then results into an "electromagnetic shower", shown in Figure 2.23. The growth of this shower will continue until the secondary particles are no longer capable of multiplying. At that point, the maximum number of shower particles, N_{max}, exits. Beyond the depth of the shower maximum, the number of electrons dies away due to ionization and photons by Compton scattering. The energy loss by an electron is characterized in terms of radiation length (X_0), defined by the relation:

$$-\frac{dE}{dx} = \frac{E}{X_0} \tag{2.5}$$

Thus radiation length, is defined as the distance over which the electron losses (1/e) fraction of its energy by radiation loss only. The other quantity, which

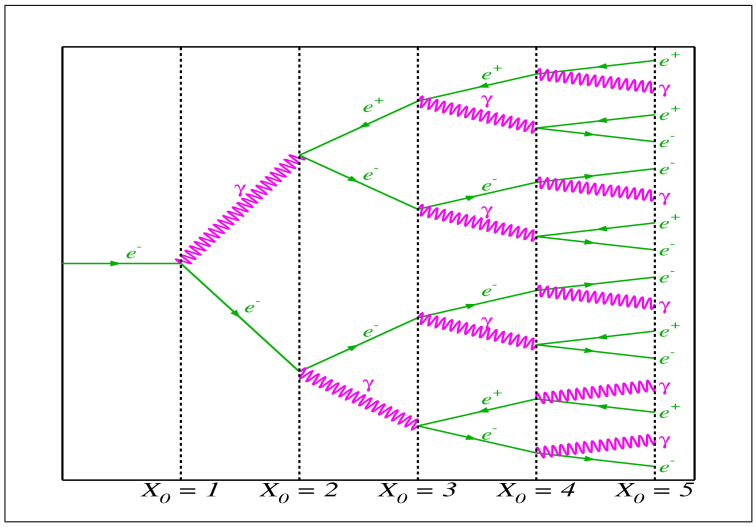

Figure 2.23: Schematic view of an electromagnetic shower.

is vitally important for describing the electron energy loss mechanism, is the critical energy, E_c. The critical energy is that energy above which radiative processes dominates. For an electron with energy less than 8 MeV (E_c of electron in lead), the electron loss mainly occurs through ionization, whereas for high energies radiative process dominates. Figure 2.24 shows the various mechanisms by which electron losses energy while passing through lead. For photons with energy less than 500 KeV, photoelectric effect dominates. In case energy is higher than 500 KeV and less than few MeV energy lose by Compton

scattering dominates. When the energy of photons increases above 100 MeV, pair-production cross-section dominates. Muons do not show EM showering usually because its critical energy is ∼300 GeV, so it deposits energy because of ionization only. The charged hadrons also deposit energy by ionization process only. The material of EM calorimeter is chosen in such a way that full EM shower for electron and photon remains confined within this detector. For example, in CMS we use $PbWO_4$ crystals which have radiation length (X_0) of 0.9 cm and total thickness of the calorimeter is $25X_0$ to contain full EM shower. So all electrons and photons produced in the interaction are absorbed in the ECAL and energy, direction of these particles is measured.

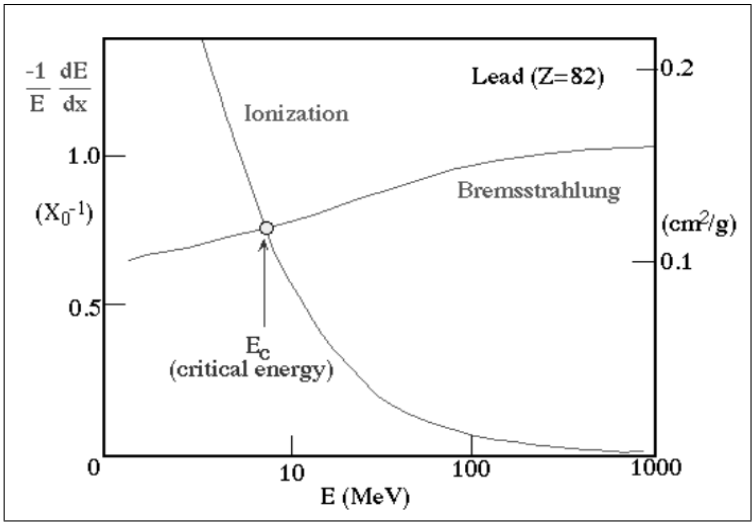

Figure 2.24: Fractional energy loss of electron per radiation length in lead as function of electron energy.

- The next detector layer which the particle has to travel is the hadronic calorimeter (HCAL), where the charged and neutral hadrons deposit their energy. The detection of hadron energies is more complex than electromagnetic processes. In passing through matter, a hadron can therefore build up a shower through multiple strong interactions, resulting in the production of a large number of particles in each secondary interaction. This process results into hadron shower

development. The hadron shower can be parametrized by a "nuclear interaction length (λ_0)", similar to the radiation length for electromagnetic showers. For heavy materials, the interaction length is much larger than the radiation length, so the hadronic showers start later than the electromagnetic shower and last long too. This forms the basis of setting ECAL before the HCAL while designing a detector. However, unlike the case of electromagnetic shower, it should be noted that there are many different processes are possible in the development of high energy hadronic showers, due to which in general not all the hadron energy will be "visible":

- Electromagnetic component: Some of the hadronic particles like η and π_0 decay in two energetic photons which initiate the EM shower. On an average one third of the mesons produced in the first interaction are π_0. If kinematically allowed, charged hadrons produce more π_0 in next interaction. Thus good fraction of hadronic shower consists of EM shower also. Depending on the numbers of π_0-mesons produced in the early stages of the hadronic cascade, the shower may develop in either a predominantly electromagnetic or a hadronic mode contributing substantially to the variation in energy deposit, which will limit the energy resolution in a hadronic calorimeter.

- Up to 30% of hadron energy may be lost due to nuclear excitation and nuclear break-up, spallation or "evaporation" of slow neutrons and protons and by the escape of neutrinos and also muons which produce by the decay of heavy mesons, from the calorimeter. In case of hadrons, the medium itself is excited unlike the electromagnetic calorimeter in which the medium does not participate in cascade processes such as Bremsstrahlung and pair-production. In hadronic cascade, due to the interaction themselves with the nucleons of the nucleus, a substantial amount of hadronic energy will go into "binding energy losses" where the nucleus is excited. However, the binding energy ultimately appears in the calorimeter when the nu-

cleus de-excites emitting a slow neutron, photon or other fragment, but the calorimeter response time is short as compared to this de-excitation process, thus this energy deposit in not detected.

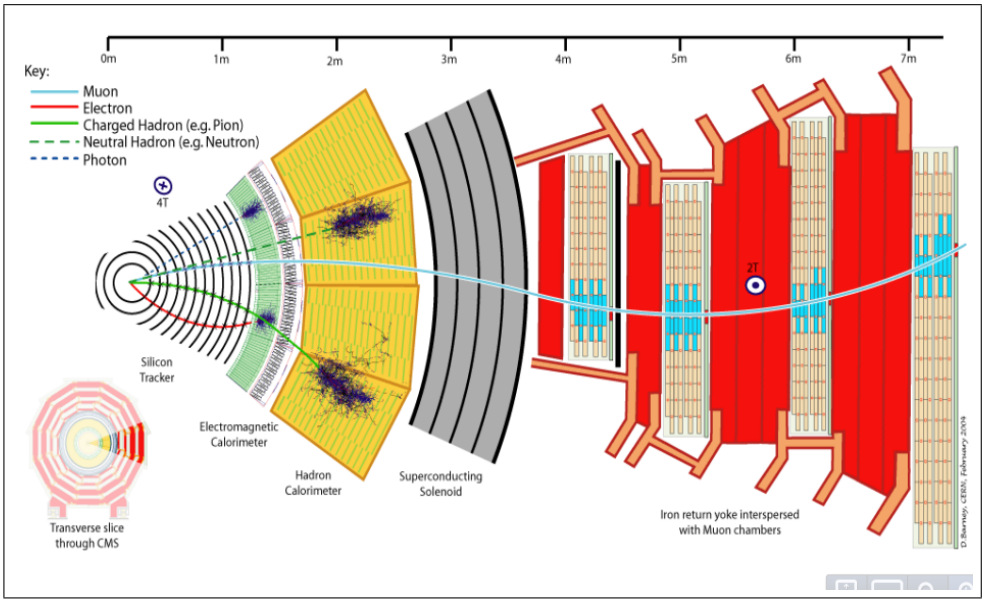

Figure 2.25: Slice of CMS detector showing interactions of various particles in sub-detectors of CMS.

The next layer and the final sub-detector which the particles has to enter are the muon chambers. At the end of HCAL, only muons and neutrinos survive. Neutrinos passes the detector without any interaction. Therefore, the only particles being in the muon chambers are the muons, which are weakly interacting, having high mass and critical energy. So in ECAL and HCAL it deposits energy equal to minimum ionizing particle. Thus Muon will the only particle passing through chamber and being detected by this system. The various types of interactions of particles in different parts of CMS detector are shown in Figure 2.25.

In this Chapter, we have discussed in brief the LHC proton-proton collider and its general purpose CMS detector and its various components. In the end, we have also discussed about the mechanisms by which various particles produced in the pp interaction deposit their energy in various sub-detectors of CMS and get detected.

3

Event Reconstruction and Monte Carlo Samples

In high energy physics, the method to simulate the Experimental data is done in two stages, event generation and detector simulation. Event generators describe the particle reactions among primary interacting particles and produce the momentum vectors of the generated particles in the interactions. The output of an event generator is used as input for a detector simulation program.

The simulation is an intrinsic part of any high-energy experiment as much as the particles detectors themselves. It is the art of mimicking nature and man-made particle detectors. It is a mandatory component of any high energy physics experiment from the design stage to the final results. The simulation study of a detector and the physics processes is quite important before the start of experiment and even after starting of real data taking in an experiment. It helps in checking the performance of various components of the detector when different types of particles pass through it. Using simulation study, it is possible to decide analysis strategy and nature of backgrounds for a physics process. Once data taking starts, it becomes important to compare results from simulated studies with the real data. This helps in tuning event generators and checking modeling of detector in simulation. No data analysis or physics interpretation can be performed without the help of simulated data acting

as a reference to the experimental output. All the results from real data rely on the efficiency and the acceptance correction factor estimated from the simulated events. Even the associated systematic errors include the simulation uncertainties, thus the quality of physics results strongly depends on the quality of its simulation.

The general structure of a simulation package consists of two main parts, namely: the physics process modeling which leads to the event generation and the particles detector simulation with designed layout. The reconstruction part is same for both the simulation and real data flow. The general structure of the physics process modeling and event generation procedure is shown in Figure 3.1 and are discussed briefly in next Sections.

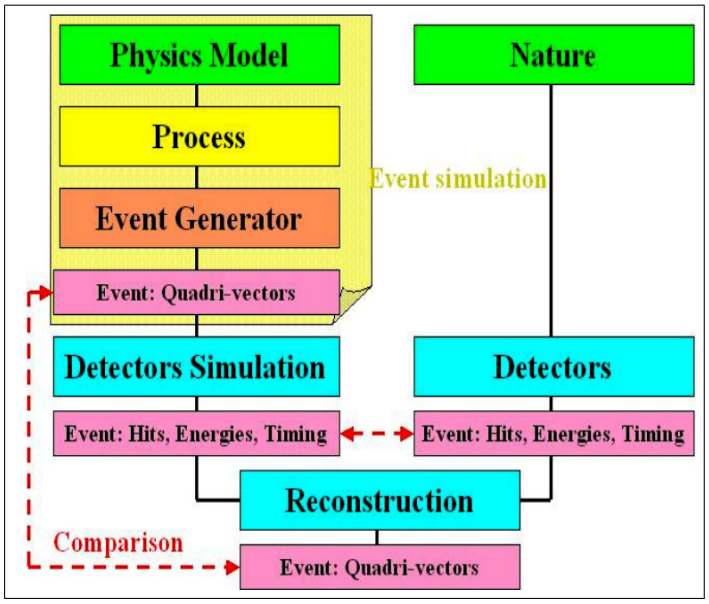

Figure 3.1: Basic steps in event generation, simulation and data analysis.

3.1 Event Generators

The main objective of the event generators is to generate events as realistic as could be from a real experiment. Event generators are intended to generate complete events by subdividing the task into simpler steps. For generating a given hard process, the basic steps are as follows: generation of the Feynman diagrams involved in the process,

construction of the matrix elements which after being integrated over whole phase space provides the total and differential cross-section. Finally, events are randomly generated according to the full differential cross-section and provides a set of four momentum vectors each associated with one of the final state particle. The hard scattering final states often contain partons-(quarks and gluons), which cannot exist in the bare state. These partons get hadronized to produce hadrons as they move apart. Thus a general scheme of the event generation assumes the evaluation of the hard process, then evolve the event through a parton showering and hadronization step and the decay of the unstable particles. The event information contains the four momenta of all the final state particles (hadrons, leptons and photons) and the position of their decay vertices.

There are specific generator packages such as Pythia-6 [42, 43] and Pythia-8 [45, 46] which simulate the transformation of partons into hadrons through the parton showering and hadronization algorithms. At hadron colliders like LHC, the hadronic processes are even more complex due to non-elementary structure of proton. There will be large number of possible initial hard scattering states. Moreover, the multiple interaction between the partons, not involved in the hard scattering, must be taken into account. During the collision of two proton bunches in LHC, more than 20 inelastic events are superimposed on the single possible interesting event. These events must also be simulated in order to come as close as possible to the real situation in the CMS detector. The details of the implementation of various physics aspects are different in each of these generators, however the underlying principle is same for all the generators.

3.1.1 Pythia-6

The Pythia-6 program is frequently used for event generation in high-energy physics. The emphasis is on multiparticle production in collisions between elementary particles. This in particular means hard interactions in e^+e^-, pp and ep colliders, although other applications are also envisaged. The program is intended to generate complete events, in as much detail as experimentally observable ones, within the bounds of our

current understanding of the underlying physics.

Pythia contains a much richer selection, with around 300 different hard processes. These may be classified in many different ways. One is according to the number of final-state objects: we speak of 2→1 processes, 2→2 ones, 2→3 ones, etc. This aspect is very relevant from a programming point of view: the more particles in the final state, the more complicated the phase space and therefore the whole generation procedure. In fact, Pythia is optimized for 2→1 and 2→ 2 processes only.

Parton distributions functions are most familiar for hadrons, such as the proton, which are inherently composite objects, made up of quarks and gluons. Since we do not understand QCD, a derivation from first principles of hadron parton distribution functions does not yet exist. Also for fundamental particles, such as the electron, is it convenient to introduce parton distributions. The function $f_e^e(x)$ thus parameterizes the probability that the electron that takes part in the hard process retains a fraction x of the original energy, the rest being radiated (into photons) in the initial state. Of course, such radiation could equally well be made part of the hard interaction, but the parton-distribution approach usually is much more convenient. There is a kind of possible generalization. The two processes, $qq \to \gamma^*/Z^0$ studied in hadron colliders and $ee \to \gamma^*/Z^0$, studied in e^+e^- colliders, are really special cases of a common process, $ff \to \gamma^*/Z^0$, where f denotes a fundamental fermion, *i.e.* a quark, lepton or neutrino. The whole structure is therefore only coded once and then slightly different couplings and color prefactors are used, depending on the initial state considered. Usually the interesting cross-section is a sum over several different initial states, e.g. $uu \to \gamma^*/Z^0$ and $dd \to \gamma^*/Z^0$ in a hadron collider. This kind of summation is always implicitly done, even when not explicitly mentioned in the text.

In every process that contains colored and/or charged objects in the initial or final state, gluon and/or photon radiation may give large corrections to the overall topology of events. Starting from a basic 2→2 process, this kind of corrections will generate 2→3, 2→4, and so on, final-state topologies. As the available energies are increased, hard emission of this kind is increasingly important, relative to fragmentation, in determining the event structure. Two traditional approaches exist for the modeling of

perturbative corrections. One is the matrix-element method, in which Feynman diagrams are calculated, order by order. In principle, this is the correct approach, which takes into account exact kinematics and the full interference. The second possible approach is the parton-shower one. Here an arbitrary number of branchings of one parton into two (or more) may be combined, to yield a description of multijet events, with no explicit upper limit on the number of partons involved. This is possible since the full matrix-element expressions are not used, but only approximations derived by simplifying the kinematics and the interference.

Let us now turn to the fragmentation process. As the q and $\bar{q}$ move apart, the potential energy stored in the string increases and the string may break by the production of a new $q\bar{q}$ pair, so that the system splits into two colour-singlet systems $q\bar{q}$ and $\bar{q}q$. If the invariant mass of either of these string pieces is large enough, further breaks may occur. In the "Lund string fragmentation model" [47], the string break-up process is assumed to proceed until only on-mass-shell hadrons remain, each hadron corresponding to a small piece of string with a quark in one end and an antiquark in the other

3.1.2 Pythia-6 Tunes

In a hadronic collision, the colliding parton only takes some fraction of the total beam energy, leaving behind a residual which takes the rest. This hadron residual is known as "Beam-remnant". For a proton beam, a u-quark colliding would leave behind a ud-diquark beam remnant, with an anti-triplet color charge. The remnant is therefore color-connected to the hard interaction, and forms part of the same fragmenting system. The understanding of this hadron residual is very important at hadron colliders. Similarly, each of the beam particles contains a number of partons and so the probability for several interactions in one and the same event is not be negligible. In principle these additional interactions could arise because one single parton from one beam scatters against several different partons from the other beam, or because several partons from each beam take place in separate 2-to-2 scatterings. These semi-hard 2-to-2 scattering process is known as MultiParton Interaction (MPI). The

understanding of MPI is also very primitive. The "Beam-Beam remnants" (BBR) and "MultiParton Interaction" (MPI) are collectively known as "Underlying Event" (UE). Pythia contains several parameters which can be adjusted to control the behaviour of the processes defined above. A specified set of these parameters that has been adjusted to better fit some aspects of the data is referred to as a *"tune"*. The list of the Pythia parameters relevant for describing the Underlying Event are mentioned in Table 3.1. In the study of "Underlying Event activity", we have used the Monte-Carlo samples generated using various Pythia-6 Tunes.

In all the above mentioned parameters in the table, one parameter which is of great importance is the PARP(90) also designated as ϵ. The perturbative 2-to-2 parton-parton differential cross-section diverges like $1/\hat{p}_T^4$, where $\hat{p}_T^4$ is the transverse momentum of the outgoing parton in the parton-parton center-of-mass frame. Pythia regulates this cross-section by including a smooth cut-off p_{T0} as follows: $1/\hat{p}_T^4 \rightarrow 1/(\hat{p}_T^2 + \hat{p}_{T0}^2)^2$. This approaches the perturbative result for large scales and is finite as $\hat{p}_T \rightarrow 0$. The primary hard scattering processes and the MPI are regulated in the same way with the one parameter p_{T0}. This parameter governs the amount of MPI in the event. Smaller values of p_{T0} results in more MPI due to a larger MPI cross-section. CDF studies indicate that p_{T0} is around 2 GeV/c [48]. However, this cut-off is expected to have a dependence on the overall center-of-mass hadron-hadron collision, E_{cm}. Pythia parameterizes this energy dependence as follows:

$$p_{T0}(E_{cm}) = (E_{cm}/E_0)^{\epsilon} \qquad (3.1)$$

where E_0 is some reference energy and the parameter ϵ determines the energy dependence. A brief description of each tune on the basis of these parameters and their performance is given below:

- **Pythia-6 Tune DW**: Tune DW [49] is a Pythia 6.2 [43] tune with (Q^2-ordered parton showers and old MPI model) designed to fit the CDF Underlying Event data at 1.96 TeV. Tune DW uses ϵ = PARP(90)= 0.25, which is different than the default Pythia 6.2 value of ϵ=0.16. The value of ϵ=0.25 has been determined by comparing the UE activity in the CDF data at 1.8 TeV and 630 GeV [51].

Parameters	Description
MSTP(81)	MultiParton Interaction ON
MSTP(82)	3 or 4; multiple interactions assuming a varying impact parameter and a hadronic matter overlap consistent with a double Gaussian matter distribution
PARP(82)	Multiparton Interaction p_T cut-off
PARP(83)	Fraction of matter containing within a core of radius PARP(84)
PARP(84)	Core Radius
PARP(85)	probability that an additional interaction in the old Multipleinteraction formalism gives two gluons, with colour connections to nearest neighbours in momentum space
PARP(86)	probability that an additional interaction in the old Multipleinteraction formalism gives two gluons, either as described in PARP(85) or as a closed gluon loop. Remaining fraction is supposed to consist of quarkantiquark pairs.
PARP(89)	Reference Energy Scale
PARP(90)	MPI energy dependence
PARP(62)	Initial state cut-off radiation
PARP(64)	Soft Initial state radiation scale
PARP(67)	Hard initial state radiation scale
MSTP(91)	Gaussian Intrinsic k_T
PARP(91)	Width of Gaussian Intrinsic k_T
PARP(93)	Intrinsic k_T upper cut-off

Table 3.1: Description of the parameters of Pythia-6 Tunes which control the Underlying Event activity. The first 9 parameters tune the Multiple parton interactions. PARP(62), PARP(64) and PARP(67) tune the initial-state radiation and the last three parameters set the intrinsic k_T of the partons within the incoming proton-proton

Pythia Tune DW does a very nice job in describing the CDF Run 2 Underlying Event data [22] and has been used as a Pre-LHC reference tune. It has done well at predicting the behavior of the Underlying Event activity at 900 GeV and 7 TeV at the LHC [52]. Tune DW is based on CTEQ5L [53] Parton Distribution Function (PDF) set.

- **Pythia-6 Tune D6T**: Pythia 6.2 Tune D6T [49, 55] use the default value of PARP(90) *i.e.* ϵ=0.16. It is similar to Tune DW, except it uses the CTEQ6L1 [54] PDF set. Tune D6T has also been used as Pre-LHC tune and it describes the lower energy UA5 and Tevatron data. Tune D6T has been found to produce more activity in the Underlying Event at energies above the Tevatron than the Tune DW, but predict less activity than Tune DW in the Underlying Event at energies below the Tevatron.

- **Pythia-6 Tune Z1**: Tune Z1 is a Pythia 6.4 [44] tune based on CTEQ5L PDF set. The main changes in Pythia 6.4 with respect to Pythia 6.2 are: parton showers are p_T ordered rather than mass ordered, MPI is also a part of the parton showering. ISR and FSR also using p_T ordering algorithms. It implements the results of the Professor tunes [56] considering the fragmentation and the color reconnection parameters of the AMBT1 tune [57]; preliminary CMS UE results at 7 TeV have been used to tune the parameters governing the value and the $\sqrt{s}$ dependence of the transverse momentum cutoff that in Pythia regularizes the divergence of the leading order scattering amplitude as the final state parton transverse momentum $\hat{p}_T$ approaches 0.

- **Pythia-6 Tune Z2**: Tune Z2 is similar to Tune Z1, except for the transverse momentum cutoff at the nominal energy of $\sqrt{s_0}$= 1.8 TeV which is decreased by 0.1 GeV/c *i.e.* the PARP(82) parameter has been changed from 1.932 in Z1 to 1.832 in Tune Z2. This tune is based on CTEQ6L PDF set.

3.1.3 Pythia-8

Pythia-8 [45] is a clean new start, to provide a successor to Pythia-6. While previous Pythia versions were written in Fortran, Pythia-8 represents a complete rewrite in C++. The current release is the first main one after this transition and does not yet in every respect replace the old code. Pythia-8 also uses the new Pythia MPI model [58], which is interleaved with parton showering. In Pythia-6 version, initial-state radiation (ISR) and MPIs are interleaved, while Final-state radiation (FSR) is only considered afterwards. The argument is that it is primarily MPI and ISR that compete for beam momentum, while in Pythia-8 the main change is the additional interleaving of FSR along with ISR and MPI. The initial and the final-state algorithms are based on the new p_T-ordered evolution while the older mass or (Q^2) ordered algorithms have not been implemented. In the present work, only Tune 4C of Pythia-8 has been used. The new Pythia-8 version 4C [58] has also been tuned to the early LHC data and is based on CTEQ6L1 PDF set.

3.1.4 POWHEG

The Leading order (LO) calculations, implemented in the context of general purpose Shower Monte Carlo (SMC) programs *i.e.* Pythia or HERWIG [59], have been the main tools used in the various analysis. The SMC programs generally include dominant QCD effects at the leading logarithmic level, but do not enforce NLO accuracy. These programs were routinely used to simulate background processes and signals in physics searches. When a precision measurement was needed, to be compared with an NLO calculation, one could not directly compare the experimental results with the output of SMC program, since the SMC does not have the required accuracy.

In view of the positive experience with the QCD calculations at the NLO level in the phenomenological study at electron and hadron colliders, it has become clear that SMC programs should be improved, when possible, with NLO results. The problem of merging NLO calculations with parton shower simulations is basically that of avoiding overcounting, since the SMC programs do implement approximate

Parameters	Tune DW	Tune D6T	Tune Z1	Tune Z2
PDF Set	CTEQ5L	CTEQ6L1	CTEQ5L	CTEQ6L1
MSTP(81)	1	1	21	21
MSTP(82)	4	4	4	4
PARP(82)	1.9	1.8387	1.932	1.832
PARP(83)	0.5	0.5	0.356	0.356
PARP(84)	0.4	0.4	0.651	0.651
PARP(85)	1.0	1.0	1.0	1.0
PARP(86)	1.0	1.0	1.0	1.0
PARP(89)	1.8 TeV	1.96 TeV	1.8 TeV	1.8 TeV
PARP(90)	0.25	0.16	0.275	0.275
PARP(62)	1.25	1.25	1.025	1.025
PARP(64)	0.2	0.2	1.0	1.0
PARP(67)	2.5	2.5	4.0	4.0
MSTP(91)	1.0	1.0	1.0	1.0
PARP(91)	2.1	2.1	2.1	2.1
PARP(93)	15.0	15.0	10.0	10.0

Table 3.2: Parameters of various Pythia-6 Tunes which control the Underlying Event activity.

NLO corrections already. Several proposals have appeared in the literature that can be applied to both e^+e^- and hadronic collisions. One of them is "Positive Weight Hardest Emission Generator" called as POWHEG [60]. In the POWHEG method, the hardest radiation is generated first, with a technique that yields only positive-weighted events using the exact NLO matrix elements. The POWHEG output can then be interfaced to any SMC program that is either p_T-ordered, or allows the implementation of a p_T veto [61]

3.1.5 TAUOLA

The TAUOLA MC package is an Universal interface for the processing of the decay of τ leptons, as described in [62]. The package incorporates a substantial amount of results from high precision τ lepton measurements. The universal interface of TAUOLA requires the general purpose MC generator, such as Pythia-6, to produce stable τ leptons. The event content, which is provided by the MC generator, is searched through for all stable τ leptons and neutrinos. It is required, that a flavored pair of particles ($\tau^+\tau^-$ or $\tau\nu_\tau$) originates from the same mother particles. Finally, the decay of the pair is performed by TAUOLA.

3.2 CMS Detector Simulation

Simulated events are of great importance in checking and/or correcting for non-trivial or unforeseen detector or physics effects, as well as comparing detector performance with expectations. With the possible exception of the effect being studied, simulated events should be as close as possible to real data events. Hence the primary goal of the simulation programme is to model closely the physical interactions involved, the detector performance and the event reconstruction The CMS full simulation is based on the Geant4 simulation toolkit [63] which includes a rich set of physics processes describing electromagnetic and hadronic interactions in detail.

Geant4 also provides tools for modeling the full geometry and the interfaces required for retrieving information from particle tracking through the subdetectors. It

also allows the description of the magnetic field. The Geant4 functionality is interfaced to the core of CMS software through one single module coming with a set of parameters which are configurable at run time. Among them, one of the most relevant is the physics list for the processes to be simulated. Many physics lists for both hadronic and electromagnetic interactions have been tested together with different particle production cuts. An interface for the possible tuning of the Geant4 objects at simulation time is also implemented. The detailed CMS detector simulation workflow is described as follows:

- A physics group configures an appropriate Monte Carlo event generator to produce the data samples of interest.
- The production team/system runs the generator software to produce generator event data files in High-Energy Physics Monte-Carlo (HepMC) [64] format.
- The physics group validates the generator data samples and selects a configuration for the GEANT4 simulation (detector configuration, physics cuts, etc.)
- The production team/system runs the GEANT4-based simulation of CMS, with generator events as input, to produce (using the standard CMS framework) persistent hits in the sensitive detectors
- The physics group validates this hit data which are then used as input to the subsequent digitization step, allowing for pile-up. This step converts hits into digitizations (also known as "digis") which correspond to the output of the CMS electronics.

The output of the simulation program is used as input for reconstructing the Physics objects.

3.3 Particle Object Reconstruction

Reconstruction is the operation of constructing physics quantities from the raw data collected in the experiment. In order to perform an analysis, the raw data has to be

converted into particle classes, which are referred to as physical objects, *e.g.* electrons, muons, jets or photons. The process of the reconstruction of these uses the information of one or more subdetectors of the CMS experiment to build different classes of particle candidates.

The reconstruction process can be divided into 3 steps, corresponding to local reconstruction within an individual detector module, global reconstruction within a whole detector and combination of these reconstructed objects to produce higher-level objects. The reconstruction units providing local reconstruction in a detector module use as input real data from the DAQ system or simulated data representing the real data. These data in either case are called "digis". The output from the reconstruction units are "RecHits", reconstructed hits which are typically position measurements (from times or clusters of strips or pixels) in tracking-type detectors (Muon and Tracker systems) and calorimetric clusters in Calorimeter systems. The RecHits are used as the input to the global reconstruction.

In the global reconstruction step information from the different modules of a subdetector are combined, although information from different subdetectors is not. For example, Tracker RecHits are used to produce reconstructed charged particle tracks and Muon RecHits are used to produce candidate muon tracks. The final reconstruction step combines reconstructed objects from individual subdetectors to produce higher-level reconstructed objects suitable for high-level triggering or for physics analysis. For example, tracks in the Tracker system and tracks in the Muon system are combined to provide final muon candidates and electron candidates from the Calorimeter system are matched to tracks in the Tracker system. The process of reconstruction and identification of all the objects used in this analysis: tracks, vertices, beam spot, electrons and muons has been described in next subsections.

3.3.1 Beam Spot reconstruction

When two proton bunches passing through the beam-pipe cross at the center of the detector, some of the protons in those bunches interact. Each hard collision of proton produces multiple particles originating from the point of collision. This

point is called the *primary interaction vertex*. Since the proton bunches have a finite size, the collisions of the individual protons do not always occur at exactly the same point. Instead, they are distributed over a finite volume. This locus of collision points is called the *beam spot*. The short-lived particles originating from the proton collision can decay some distance away from the primary interaction point with several secondary particles originating at the point of decay. This point is called the *secondary vertex*.

The beam spot position and the center of the CMS detector do not exactly coincide. In addition, due to changing LHC parameters and conditions the position of the beam spot may change with respect to the previous known position. A beam-constraint can be used to improve the momentum resolution for tracks coming from the primary vertex. The precise knowledge of the beam spot can also be used in the High-Level trigger (HLT) as a precise estimate of the primary interaction point to be used in many physics analysis. The precise knowledge of the beam spot position is also important for efficient track reconstruction. The detail on the beam spot reconstruction can be found in [65]. If the beam spot is displaced with respect to the center of CMS as indicated in Figure 3.2, there will be a correlation between the transverse distance of the point-of-closest-approach of the track to the CMS center (d_{xy}) and the azimuthal angle (ϕ) of the track. We can parametrize this correlation to first order as follows:

$$dxy(\phi, z_p) = x_{bs}sin\phi + \frac{dx}{dz}sin\phi z_p - y_{bs}cos\phi - \frac{dy}{dz}cos\phi z_p \qquad (3.2)$$

where x_{bs} and y_{bs} are the beam spot position at z = 0. $\frac{dx}{dz}$ and $\frac{dy}{dz}$ are the slopes of the beam spot and z_p is the longitudinal position of the track's point-of-closest approach to the center of the CMS.

Thus, to determine the beam spot parameters (x_{bs}, y_{bs},$\frac{dx}{dz}$ and $\frac{dy}{dz}$),we can use the above parameterization to fit the measured dependence between the track's ϕ and d_{xy}.

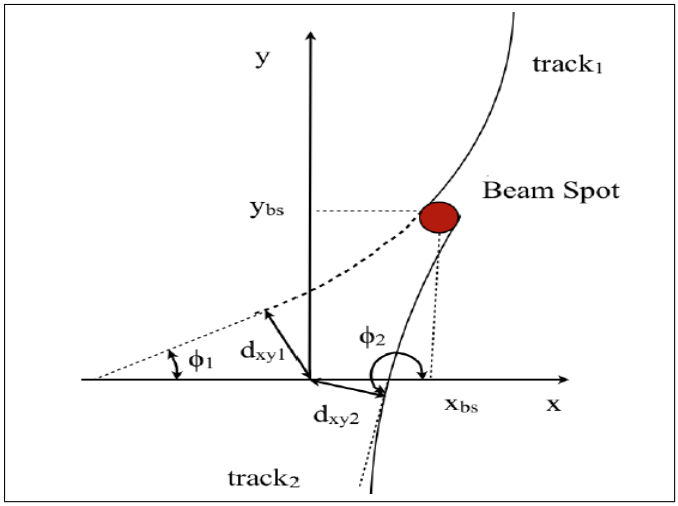

Figure 3.2: Shows two tracks originating from a displaced beam spot. The impact parameters d_{xy_i} and the azimuthal angles ϕ_i of each track are measured at the point-of-closest-approach of the track to the center of CMS.

3.4 Vertex Reconstruction

The main goal of primary vertex reconstruction is the precise determination of the collision points in proton-proton interactions. Because of the high track multiplicity in the final states expected in proton collisions at the LHC experiments, novel vertex reconstruction algorithms are required. The vertex reconstruction problem has been decomposed into two steps: vertex finding and vertex fitting.

The default algorithm for the vertex fit is the "Adaptive Vertex Fitter" [66, 67]. It is a robust fitter that efficiently downweights outlier tracks. It can be used with and without the beam spot constraint. As the adaptive fitter downweights tracks, the χ^2 of the vertex fit is no longer a measure of the quality of a vertex. The weights assigned to individual tracks by the adaptive fitter are stored with the vertex. The weighting function has a rather sharp turn on for the last iterations of the adaptive fitter and most weights are either close to 1 (good tracks) or close to 0 (outliers). The sum of weights roughly corresponds to the effective number of tracks accepted by the adaptive vertex fitter. This sum is directly related to the number of degrees

of freedom assigned to the vertex through $Ndof = 2\sum w_i - 2$ for an unconstrained fit and $Ndof = 2\sum w_i$ for a fit with beam constraint. A commonly used quality is $Ndof > 4$ which corresponds to at least 4 tracks assigned to the (unconstrained) vertex because the weight of every track is always (slightly) smaller than 1.

The default clustering algorithm sorted the tracks according to their z-coordinate and split the listed tracks into clusters whenever the distance between two tracks was larger than a configurable parameter z_{sep} (a value of 2 mm). This works well as long as the resolutions σ_z of the track z-coordinates are significantly better than z_{sep}. A small value of z_{sep} tends to split off low resolution tracks. This can lead to inefficiencies of the track assignment, the complete loss of low multiplicity vertices and spurious (fake) vertices from multiple split off tracks. A tight track selection can reduce these effects at the cost of efficiency, especially for soft events. Large values of σ_z can avoid splitting but increase the probability of merging two nearby vertices. The adaptive fitter in such a case usually downweights most tracks of one of the vertices, which is thus effectively lost. In cases when the signal vertex is merged with a relatively hard pile-up vertex, the distance to the nearest reconstructed vertex can be much larger than expected from the calculated resolution. Before vertices are stored in the vertex collection, they are sorted according to the sum of p_T^2 of all tracks in the cluster. To reduce the impact of possibly large errors for high momentum tracks the p_T is reduced by one $\sigma(p_T)$ before summing. The weights determined by the adaptive vertex fit are not used for this sum in order not to downweight tracks from decays. Whether or not the signal event is likely to correspond to the first vertex in the list depends on the Physics channel being studied.

3.5 Track Reconstruction

Track reconstruction [68] in a dense environment needs an efficient search for hits during the pattern recognition stage and a fast propagation of trajectory candidates. The trajectory of the charged particle traversing the tracker, is affected by the energy losses of the particle due to radiation and interaction with the material of the

detector, by small angle multiple scatterings [69] and by the non-uniformity of the magnetic field. Thus, by knowing the parameters of particle's trajectory at various points in the detector, we will know the location of the particle's origin, its momentum, the sign of its charge and how much energy it has lost while traversing the detector. As the charged particle traverses the detector, it leaves a trace of small energy deposits in each tracker sensor it crosses. Thus to find the parameters of the trajectory of the particle we need to determine the positions of these energy deposits and then reconstruct the trajectory from those positions. This task is performed by the track reconstruction software. The track reconstruction in CMS is performed in five iterations:

- **Local reconstruction** consists in clustering into hits the strip and pixel signals produced by charged particles on the silicon detectors of the tracking system. The positions of the hits are estimated along with the corresponding uncertainties.

- **Seed generation** provides initial track-candidates for the full track reconstruction, each obtained using only a few Tracker hits. A seed defines initial trajectory parameters and errors.

- **Track finding** is based on a global Kalman filter and is responsible of finding the track-candidates that correspond to charged particles of interests. Because trajectories are built in parallel and they are allowed to share hits, this module is also responsible for cleaning the resulting track-candidates collection by removing duplicates.

- **Final Track fit** module estimates the parameters of trajectories with ultimate precision by means of a Kalman filter and smoother.

- **Track selection** module rejects ghosts requiring that the final tracks match a minimum set of quality cuts.

The track reconstruction is almost fully efficient for muons within the acceptance. Muons are the charged particles that are best reconstructed in the tracker. They

mainly interact with the silicon detector through ionization and their energy loss by bremsstrahlung is generally negligible, except when muons are produced with an initial energy higher than about 100 GeV. Therefore these particles usually cross the whole volume of the tracking system, producing detectable hits on all the sensitive layers of the apparatus. Finally, muon trajectories are scattered exclusively by multiple-scattering, whose effects are straightforward to include inside the Kalman filter formalism.

For isolated muons with a transverse momentum between 1 GeV/c and 100 GeV/c, the global tracking efficiency is higher than 99% in the full η range of the Tracker acceptance and the efficiency does not depends on the ϕ direction of the particles. The average hit-finding efficiency is higher than 99% both in the barrel and in the endcaps, it is still above 97% in the barrel-transition region where the layer navigation is more complicated and the material budget of the Tracker is more significant. The trajectory contamination due to spurious hits produced by electrical noise or δ-rays is lower than per-mille.The reconstruction of pions suffers from the substantial amount of material present in the tracker. Requiring at least 8 reconstructed hits it varies typically between 80% and 90% depending on momentum and rapidity .

3.6 Muon Reconstruction

The nature of the CMS detector, identification of muons is more efficient and misidentification contamination is much less as compared to electrons. Muons are much heavier than electrons and therefore their energy loss in materials is much less. Thus they leave only a track in the central tracker system, a small energy deposit in the calorimeters. Then penetrate the calorimeters, the solenoid and the return yoke steel leaving a track in the muon system. The Muon reconstruction [70] is performed in 3 stages : local reconstruction, standalone reconstruction and global reconstruction. Standalone muon reconstruction uses only information from the muon system, while global muon reconstruction also uses silicon tracker hits.

3.6.1 Local Muon Reconstruction

In the local Muon reconstruction, raw data is unpacked to create digis, which are an organized arrangement of digital data at the per-channel level. These digis are then combined to form RecHits which give the information of local X and Y coordinates and other related information. These recHits are then associated into groups by pattern recognition algorithm to form "segments" which give the straight-line parameters of a candidate muon producing those hits. Detail about the local muon reconstruction can be found in [71].

- **Segment reconstruction in Drift tubes (DT)**: The segment reconstruction works on the r-ϕ and r-z projections independently and is performed in 3 steps: The first step begins by selecting 2 hits in different layers, starting from the most separated. Both hypotheses, left and right, are considered. The pair is kept if the angle of this proto-segmental is compatible with a track pointing to the nominal interaction point. For each pair, additional compatible hits are searched for in all layers. It is possible that the left and right hypotheses are both compatible with the segment. In this case, the ambiguity is solved later. At this stage, a linear fit is performed using the hit positions and errors for each collection of hits. The segment with the maximum number of hits and the minimum χ^2 is retained; all the others are rejected. Finally, a muon quality criterion is applied, requiring the number of hits ≥ 3 and the $\chi^2/ndof < 20$. The same algorithm is applied for a single superlayer r-z or, in the case of the r-ϕ projection for 2 SLs, considering all 8 layers together. In all cases, a protection against the detector being too noisy is applied, so the reconstruction is not attempted if the number of hits is greater than a predefined number. The pattern recognition described above, produces a set of segment candidates. A consistency check is performed in order to test whether 2 segments share the same hit. Conflicts are solved on the basis of the number of hits and the χ^2 of the segment.

- **Segment Reconstruction in Cathode Strip Chambers (CSC)**: The inputs to the local reconstruction are the detected signals from the cathode strips and anode wires. The information about these signals are contained in the strip and wire digis, respectively. The basic procedures for local reconstruction in the endcap muon CSCs is to obtain the pulse height in each strip and then to cluster neighbouring strips to determine the probable position of incidence of the incident muon. Each of the 6 layers of a chamber is considered independently. A two-dimensional RecHit is created at each intersection of a 3-strip cluster and a wire group. At a later stage of local reconstruction, the RecHits in the 6 layers of a chamber are fit to form a "track segment" for use in the first stage of the muon track reconstruction.

- **Segment Reconstruction in Resistive Plate Chambers (RPC)**: In the RPCs, the results of the local reconstruction are points in the plane of the detector. A clustering procedure is first performed, using all the strips that have a signal. The procedure combines all adjacent fired strips into a cluster. Once all the clusters are formed, the reconstructed point for each is defined as the "center of gravity" of the area covered by that cluster of strips. In the barrel, where the strips are rectangular, this point is simply the center of a rectangle. In the endcap, the computation is more complicated since the area covered by the clusters are trapezoids of variable shape. The assumption is that each group of strips is fired as the result of a single particle crossing the chamber plane and that this crossing can have taken place anywhere with flat probability over the area covered by the strips of that cluster. Errors are computed under the same assumption of flat probability. Therefore, they are simply $\sigma_i = L_i/\sqrt{12}$ (i = 1, 2), where Li is the length of the ith side of the rectangle.

3.6.2 Standalone Muon Reconstruction

The standalone muon reconstruction uses only data from muon detectors, the silicon tracker is not used. Both the muon tracking detectors (DT and CSC) and RPCs

are used for the reconstruction of muon. Despite the coarser spatial resolution, the RPCs complement the tracking chambers, especially where the geometrical coverage is problematic, mostly in the barrel-endcap overlap region. The reconstruction starts with the track segments from muon chambers obtained by the local reconstruction. The state vectors (track positions, momentum and direction) associated with the segments found in the innermost chambers are used to seed the muon trajectories, working from inside out, using Kalman track fitting technique [72]. The individual hits, from DT chambers in barrel and from CSC in endcaps, are used as measurement in the Kalman-filter procedure. A suitable χ^2 cut is applied to reject bad hits, mostly due to showering, delta rays and pair production. In case no matching hits (or segments) found due to detector inefficiency, geometrical cracks, etc. Then the track search is continued in next muon station. The state is propagated from one station to next using GEANE package [73] which takes into account the muon energy loss in the material. The track parameters and the errors are updated at each step. The procedure is iterated until the outermost measurement surface of the muon system is reached. Finally Kalman filter is applied, working from outside in and the track parameters are defined at the innermost muon station.

3.6.3 Global Muon Reconstruction

The global/Level-3 muon reconstruction is performed by extending the muon trajectories to include hits in the silicon tracker system (silicon strip and silicon pixel detectors). Starting from a standalone reconstructed muon, the muon trajectory is extrapolated from the innermost muon station to the outer tracker surface, taking into account the muon energy loss in the material and the effect of multiple scattering. The GEANE package is currently used for the propagation through the steel, the coil and the calorimeters. Silicon layers compatible with the muon trajectory are then determined and a region of interest within them is defined in which to perform regional track reconstruction. The determination of the region of interest is based on the track parameters and their corresponding uncertainties of the extrapolated muon trajectory, obtained with the assumption that the muon originates from the

interaction point. The definition of the region of interest has a strong impact on the reconstruction efficiency, fake rate and CPU reconstruction time: well measured muons are reconstructed faster and with higher efficiency than poorly measured ones.

Inside the region of interest, initial candidates for the muon trajectory (regional seeds) are built from pairs of reconstructed hits. The 2 hits forming a seed must come from 2 different tracker layers and all combinations of compatible pixel and double-sided silicon strip layers are used in order to achieve high efficiency. In addition, a relaxed beam spot constraint is applied to track candidates above a given transverse momentum threshold to obtain initial trajectory parameters. Starting from the regional seeds, a track-reconstruction algorithm, based on the Kalman-filter technique, is used to reconstruct tracks inside the selected region of interest. The track-reconstruction algorithm consists of the following steps: trajectory building (seeded pattern recognition), trajectory cleaning (resolution of ambiguities) and trajectory smoothing (final fit).

In the first step, the trajectory builder transforms each seed into a set of trajectories. Starting from the innermost layer, the trajectory is propagated to the next tracker reachable layer and updated with compatible measurements found on that layer. In the second step, the trajectory cleaner resolves ambiguities between multiple trajectories that may result from a single seed on the basis of the number of hits and the χ^2 of the track fit. In the final step, all reconstructed tracks are fitted once again, without a beam spot constraint, using the hits in the muon chambers from the original standalone reconstruction together with the hits in the silicon tracker. To resolve possible ambiguities a second cleaning step is performed which selects the final muon candidates on the basis of a χ^2 cut. The selected trajectories are then refitted excluding measurements (hits or segments) with high χ^2 values in muon stations with high hit occupancy. In addition the trajectories are refitted using silicon tracker hits plus hits in the innermost muon station (excluding RPC hits). Then the χ^2 probability of the fit is compared with the χ^2 probability of the tracker only trajectory in order to detect muon bremsstrahlung or any kind of significant energy loss of the muon before the first muon station. This procedure is important for the accurate

momentum reconstruction of very high p_T (TeV) muons. The precise reconstruction of these objects is very challenging because of catastrophic energy loss and severe electromagnetic showers in the muon system.

3.7 Monte-Carlo Samples Analyzed

In the present work, we have analyzed the proton-proton collision data collected at CMS experiment during 2010 run at 7 TeV center-of-mass energy, which corresponds to an integrated luminosity of 36 pb^{-1}. On the basis of the online trigger selection, data is stored into different blocks e.g muon triggered data is stored separately from electron triggered data. In this analysis, we have used the Single-Muon triggered data, in which at online trigger selection, atleast one muon is required in an event above a given p_T threshold. In particular, the following two single muon triggered primary data stream have been used, which corresponds to two distinct periods of LHC machine setup:

- $/Mu/Run2010A - Nov4ReReco\_v1/RECO$
- $/Mu/Run2010B - Nov4ReReco\_v1/RECO$

For comparing the experimental results with predictions of theory, the signal and the background samples generated by various Monte-Carlo generators have been used. The description of all the Monte-Carlo(MC) samples used in the study of Drell-Yan process and the Underlying Event (UE) analysis is described as follows:

3.7.1 Monte-Carlo Samples for the Study of Drell-Yan process

- **Signal Monte-Carlo**: We have used the Drell-Yan process generated using NLO Monte Carlo (MC) generator POWHEG interfaced with the Pythia parton-shower event generator, using the CT10 [74] parametrization of the PDFs. The sample have been generated in two different mass bins of final state muons, by

Description of the Monte-Carlo samples used in Drell-Yan Study			
Dataset	Generator	x-section (pb)	Events
DYToMuMu_M-10To20	Powheg+Pythia	3320	1993383
DYToMuMu_M-20	Powheg+Pythia	1666	1998931
QCD_Pt-15to20_MuPt5Enriched	Pythia	579200000	2884915
QCD_Pt-20to30_MuPt5Enriched	Pythia	236300000	236300000
QCD_Pt-30to50_MuPt5Enriched	Pythia	53070000	11431864
QCD_Pt-50to80_MuPt5Enriched	Pythia	6351000	10748755
QCD_Pt-80to120_MuPt5Enriched	Pythia	785100	3191979
QCD_Pt-120to150_MuPt5Enriched	Pythia	92950	998503
QCD_Pt-150_MuPt5Enriched	Pythia	47580	1022541
TT_TuneZ2_7TeV-pythia6-tauola	Tauola+Pythia	94.3	1099550
DYToTauTau_M-20	Tauola+Pythia	1300	2057446
WToMuNu_TuneZ2	Pythia	7899	5330940
Upsilon1SToMuMu_2MuEtaFilter	evtGen+Pythia	99900	2323818
Upsilon2SToMuMu_2MuEtaFilter	evtGen+Pythia	75400	1148581
Upsilon3SToMuMu_2MuEtaFilter	Pythia	2850	936405
WWtoAnything_TuneZ2	Tauola+Pythia	28	2061760
WZtoAnything_TuneZ2	Tauola+Pythia	10.5	2194752
ZZtoAnything_TuneZ2	Tauola+Pythia	4.3	2113368

Table 3.3: Summary of the Generators, cross-section and number of events of various Monte-Carlo samples used in the study of Drell-Yan process.

putting a cut on the mass of the final state muons. Low mass sample is generated by requiring the invariant mass of two muons at the generator level to be lie in the mass window, $10 < M_{\mu\mu} < 20$ GeV/c^2 and the high mass sample is generated, by requiring the invariant mass $M_{\mu\mu} > 20$ GeV/c^2.

- **Monte-Carlo samples for background processes**:

  - **QCD multijet events**: MC sample for QCD multijet process is generated using Pythia-6 having Tune-Z2 for the Underlying Event modeling. A lower and an upper cut off on the $\hat{p}_T$ of hard interaction *i.e.* (CKIN(3) and CKIN (4) parameter in Pythia), has been applied at the generation level to produce the QCD sample in different $\hat{p}_T$ bins. A generator level filter has also been applied to select atleast one muon with $p_T \geq 5$ and $|\eta| < 2.5$, coming from the decays of heavy mesons *i.e.* kaons or pions. Six QCD samples generated with the generator level transverse momentum $\hat{p}_T$ lie in the range: 15-20, 20-30, 30-50, 50-80, 80-120, 120-150 and 150-∞ GeV/c (*i.e* no upper cut), have been used in this analysis.

  - **DY** $\rightarrow \tau^+\tau^- +$ **X** : has been generated using TAOULA package interfaced with parton shower generator Pythia-6 having Tune-Z2. A lower cut on the invariant mass of the final state particles has been set to 20 GeV/c^2, *i.e.*) CKIN(1) parameter in Pythia-6.

  - **W + jets**: process with W decaying into muon and neutrino generated with Tune-Z2 of Pythia-6 generator.

  - $t\bar{t}$ **+ jets and Dibosons (WW,WZ and ZZ)**: processes generated using TAOULA and parton showered with Pythia-6 Tune-Z2 have been used.

  - $\Upsilon(1S, 2S, 3S) \rightarrow \mu^+\mu^-$: process generated using evtGen [75] and parton-showered with Pythia-6-Tune Z2 have been used.

MC samples used in the Study of Underlying Event using DY			
Dataset	Generator	QCD Model	x-section (pb)
DYToMuMu_M-20	Pythia-6	Tune-DW	1300
DYToMuMu_M-20	Pythia-6	Tune-D6T	1300
DYToMuMu_M-20	Pythia-6	Tune-Z2	1300
DYToMuMu_M-20	Pythia-8	Tune-Z1	1300
DYToMuMu_M-20	Pythia-8	Tune-4C	1300

Table 3.4: Summary of the Generators, cross-section and QCD models of Drell-Yan signal Monte-Carlo samples used in the study of Underlying Event using Drell-Yan process.

3.7.2 Monte-Carlo samples for the Study of Underlying Event using Drell-Yan process

For the study of Underlying Event (UE) using DY process, various QCD models of Pythia-6 and Pythia-8 Monte-Carlo event generators have been analyzed. The detail about all the Pythia-6 and Pythia-8 tunes have been explained earlier. For this study, the official $DY \rightarrow \mu^+\mu^-$ sample with $M_{\mu\mu} > 20$ GeV/c^2 generated with tune DW, D6T and Z2 of Pythia-6 Event generator have been used to understand the UE activity. The official samples for Tune Z1 and Tune 4C were not available, so they have been generated privately without any detector simulation to compare the corrected experimental results with the theory predictions.

In this Chapter, a brief description about the various steps involved in any Physics analysis has been discussed. We have discussed about the steps involved in the generation of the Monte-Carlo samples. Then the description of the detector simulation has been given. The reconstruction of the beam spot, tracks, vertex and muons, *i.e.* of all the Physics objects used in the present work, have been discussed in detail. We have discussed in brief about the various Monte-Carlo event generators *i.e.* Pythia-6, Pythia-8, POWHEG and TAUOLA, used for the study of both the Drell-Yan process

and Underlying Event using Drell-Yan. The details about the various QCD models and their parameter which are used to control the Underlying Event activity have also been discussed.

4

Study of Drell-Yan Process with CMS

Drell-Yan (DY) [76] is a Standard Model (SM) process having large production cross-sections for leptonic final states. The differential cross-section of DY process depends on the Parton Distribution Functions (PDF) of the proton. The SM prediction for the DY process is highly developed [77] allowing for the tests of perturbative QCD. The measurements of the DY process provides useful constraints and information to be able to tune parameters in various theoretical tools like "Fully Exclusive W and Z production (FEWZ)" simulation code [78] and more precise tests of Standard Model can also be performed with DY.

In this study, we present the measurement of the differential cross-section ($d\sigma/dM$), in the dimuon channel for the dimuon mass range 15 GeV/c^2 < $M_{\mu\mu}$ <600 GeV/c^2. We have concentrated on the analysis of DY process with two muons in the final state in pp collisions at 7 TeV using the CMS detector and the study is based on 36.0±1.4 pb^{-1} of CMC data taken during the year 2010. The CMS detector is optimized for triggering on and measuring muons, over the full detector acceptance in p_T and $|\eta|$ using single muon triggers. There has been extensive analysis of the detection and the reconstruction of muons in CMS detector for the purpose of various studies and this has been documented in numerous CMS publications [70] [79]. Since muons are well reconstructed and identified in the muon chambers of the CMS detector, so the muon final state has been chosen to study the DY process in the present study.

The goal of this analysis is the measurement of the inclusive DY differential cross-section ($d\sigma/dM$) over as wide a range of dimuon mass as possible using two oppositely charged muons detected with the CMS detector. In order to reduce the systematic errors and to achieve the best precision, the cross-section in each mass bin is normalized to the cross-section of the mass region defined by 60 GeV/c^2 < $M_{\mu\mu}$ <120 GeV/c^2 around the Z-resonance peak , for which the cross-section has also been measured precisely by the Electroweak group at CMS Experiment [85]. Thus in present analysis measurement is performed for the DY production cross-section in each mass bin of the muon pair with respect to the cross-section of DY events around Z-peak region *i.e.* the results are presented as: $((1/\sigma_Z)(d\sigma/dM))$. The advantage of taking this ratio is that the effect of many systematic uncertainties get minimized or canceled when above division is performed.

The mass range 15-600 GeV/c^2 considered in this study, corresponds to the Feynman x-range 0.0003-0.633, of the partons initiating the interactions. The DY differential cross-section has been calculated using the formula given as follows:

$$\sigma = \frac{N_U}{A * FSR * \mathcal{L}}. \tag{4.1}$$

where N_U is the background subtracted yield corrected for DY selection and the detector resolution. It is further corrected for the detector acceptance 'A' and Final State Radiation (FSR) effect. Using these numbers the DY cross-section is estimated in each mass bin and then the ratio (R) of the cross-section is estimated as $R = \sigma/\sigma_Z$. Hence the ratio of the cross-section measurements does not depend on the knowledge of the integrated luminosity ($\mathcal{L}$).

4.1 Drell-Yan Signal and Potential Backgrounds

4.1.1 Drell-Yan Signal

The Drell-Yan (DY) process is a quark-antiquark annihilation through the intermediate Z/γ^* state, into an oppositely charged lepton pair. In the muon channel, signal is manifested by the presence of two oppositely charged muons, sharing a common

primary vertex with relatively high p_T as well as isolated in all the components of the detector. For the DY signal process, the POWHEG MC sample with CT10 PDF set has been used.

4.1.2 Background Processes

All the background samples used have been generated with Pythia Monte-Carlo event generator. There are various physical processes and instrumental phenomena that can mimic the DY signal signature and are considered as backgrounds:

- **QCD hadronic interaction process**: has very high production rate at the LHC energy, contributes maximally in the low-mass region of DY events. The heavy mesons, due to bottom and charm quarks, produced copiously in these events, decay semi-leptonically into muons with large branching ratios, eventually providing two muons in a large number of events. However, the muons from the decay of charged pions and kaons in flight are relatively soft *i.e.* having low p_T and mostly cannot survive the DY selection thresholds.

- **DY$\rightarrow \tau^+\tau^- + \mathbf{X}$** : process has the potential of mimicking the signal events, specially when there is no constraint on the missing energy during the event selection. The branching ratios for Z decays to charged lepton pairs *i.e.* $\mu^+\mu^-$, e^+e^- and $\tau^+\tau^-$ each, is 3.3% and the branching ratio for $\tau \rightarrow \nu_\tau\mu\nu_\mu$ is about 17%. Thus the muons coming from DY$\rightarrow \tau^+\tau^-$ would have invariant mass typically giving a value lower than M_Z, as opposed to the direct decay of the Z boson into two muons, ($Z \rightarrow \mu^+\mu^-$). Thus DY$\rightarrow \tau^+\tau^-$ + X will be dominating in the low and the intermediate invariant mass regions, $\sim$ (15 GeV/c^2 $< M_{\mu\mu} <$ 70 GeV/c^2).

- **W + jets**: process with $W \rightarrow \mu\nu$ having branching ratio of about 11%, can pose as a background, when one of the associated jets, mostly the leading one, fakes as a muon. Though the corresponding probability for the jet faking as a muon is small $\sim 10^{-5}$, however the production rate of W + jets events is large

at the LHC energy. Thus, W+jets is also one of the important background to be considered in the DY study.

- $t\bar{t}$ **+ jets**: process can be another source of dimuons where the muons are mainly due to the leptonic decays of W-bosons produced in top and anti-top decays. This background process would dominant in the high-mass region of DY mass spectrum as the muons from a top cascade decay is highly boosted.

- **Dibosons (WW, WZ and ZZ)**: Among these processes, following decay modes lead to two muons in the final state: $Z \to \mu\mu$, $W \to \mu\nu$. A fraction of dimuons coming from the processes ZZ and WZ pair decays may form same-sign muon pairs also and these pairs can be easily removed by the opposite-sign muon selection criteria. The remaining fraction of the background from these process would be relatively small.

- $\Upsilon(1S, 2S, 3S) \to \mu^+\mu^-$: The invariant mass of the dimuons coming from the Υ gives a resonance at Υ mass *i.e.* ~ 9.5 GeV/c^2. Thus this background is important only in the lower dimuon invariant mass bins. We have considered the 15-600 GeV/c^2 mass region in this study, which is much higher than Upsilon mass peak.

- **Cosmic muons**: Energetic Cosmic muon traversing through the CMS detector would appear as two well-reconstructed muons of opposite charge sign. The majority of muons coming from cosmic rays are characterized by a large impact parameter and an opening angle very close to π radians. So this background can be minimized by putting a tight threshold on the impact parameter and by requiring the selection cut on the opening angle between the two muons coming from Z, not to be close to π radians.

4.2 Drell-Yan Event Selection

Before discussing the details of the Drell-Yan (DY) event selection, here the methodology used for the selection and the optimization of the muon isolation variable has

been discussed.

4.2.1 Muon Isolation Optimization

Isolation is one of the few tools available in the pp environment to distinguish between the leptons which are produced in high p_T process and the leptons produced copiously in the background QCD and other jet rich processes. Isolation in this sense is a check of how much activity accompanies a lepton, while it traverses through the detector. We can measure this activity in three different sub-detectors of the CMS: the tracker, the electromagnetic calorimeter (ECAL) and the hadronic calorimeter (HCAL). Isolation in high p_T environments gives a handle for reducing background type events (usually non-isolated) and selecting signal type events (usually isolated). As most of the new physics discoveries using CMS will couple to electrons, photons and muons, so it is important to study and optimize the isolation performance for these particles.

For $DY \rightarrow \mu\mu$ signal events, there is less additional activity around muons except for bremsstrahlung photons. On the contrary, the muons in the background events, in particular those from the heavy meson decays (in QCD process), are produced in jets and thus accompanied by nearby particles in the cone. Thus, to select signal events, an isolation criteria is defined to be satisfied strictly by both the muons. The isolation algorithms that have been developed rely on the comparison of the total energy deposited in a cone around the muon with a pre-defined threshold. The deposit can be the transverse energy in a calorimeter or the sum of transverse momenta of reconstructed charged-particle tracks. The cone axis is chosen according to the muon direction with a procedure that is tailored to the specific properties of each algorithm. The geometrical definition of the cone is given by the condition $\Delta R < \Delta R_{MAX}$, where $\Delta R = \sqrt{(\Delta\eta)^2 + (\Delta\phi)^2}$ with $\Delta\eta$ and $\Delta\phi$ being the distances in pseudorapidity and azimuthal angle between the deposit and the cone axis, respectively. The muon itself contributes to the energy measurement inside the cone. This contribution (called the veto value) can be subtracted to improve the discriminating power of the isolation algorithm. A schematic illustration of the isolation cone is shown in Figure 4.1. In

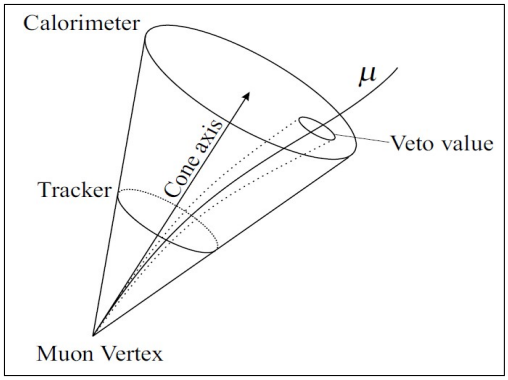

Figure 4.1: Schematic illustration of the isolation cone. The muon direction at the vertex defines the cone axis. The energy deposit ($\sum p_T$ or $\sum E_T$) in the cone is computed and the muon contribution is removed by excluding the small area around the muon (the "veto" value) from the cone. Comparison of the deposit in the cone with a pre-defined threshold determines the muon isolation.

this analysis, all the possible isolation conditions have been studied and optimized using MC sample in order to achieve maximum signal significance. The different definitions of the isolation variable studied in this analysis, are summarized as given below:

- **Tracker isolation (I_{Tr})**: variable is defined as the sum of the transverse momentum of all the tracks with $p_T > 1.0$ GeV/c in an isolation cone of $\Delta R = 0.3$ around the muon track with a veto cone of radius 0.01 to exclude the muon track. $I_{Tr} = \sum p_T$.

- **Relative tracker isolation ($\frac{\sum p_T}{p_T^\mu}$)**: variable is the tracker isolation variable normalized with the p_T of the candidate muon.

- **Combined isolation variable (I_{TEH})**: is the sum of the isolation variables defined for the tracker and calorimeter sub-systems of the detector. Tracker isolation variable is already defined. Calorimeter isolation variable is defined as the scaler sum of the energy of the calorimeter clusters in a cone of radius $\Delta R = 0.3$.

  $I_{TEH} = \sum(p_T(tracks) + E_T(ECAL) + E_T(HCAL))$

- **Relative Combined Isolation ($\frac{I_{TEH}}{p_T^\mu}$)** : is the combined isolation variable I_{TEH} normalized with the p_T of the muon candidate.

  $\frac{I_{TEH}}{p_T^\mu} = \frac{\sum(p_T(tracks)+E_T(ECAL)+E_T(HCAL))}{p_T^\mu}$

- **Combined tracker and HCAL based isolation variable (I_{TH})**: is the sum of the isolation variables defined for tracker and hadron calorimeter excluding the ECAL deposit in a cone of radius $\Delta R = 0.3$.

  $I_{TH} = \sum(p_T(tracks) + E_T(HCAL))$

- **Relative Combined tracker and HCAL based Isolation ($\frac{I_{TH}}{p_T^\mu}$)** : is the tracker and HCAL based isolation variable I_{TH} normalized with the p_T of the candidate muon.

  $\frac{I_{TH}}{p_T^\mu} = \frac{\sum(p_T(tracks)+E_T(HCAL))}{p_T^\mu}$

For simplicity, a convention has been adopted *i.e.*, all the variables which are normalized to the p_T of the candidate muon are referred to as "Relative" and others as "Absolute" isolation variables. Figure 4.2 (a) shows the comparison of the signal (ϵ_{signal}) vs background ($\epsilon_{background}$) efficiency for tracker based [I_{Tr},($\frac{\sum p_T}{p_T^\mu}$)], (b) for tracker, ECAL and HCAL based [I_{TEH},$\frac{I_{TEH}}{p_T^\mu}$] and (c) for the only tracker and HCAL based [I_{TH},$\frac{I_{TH}}{p_T^\mu}$] isolation variables. It is clear from the figures that in all the cases, the "Relative" isolation variables has better performance as compared to "Absolute" isolation variables. In each case, for a given background rejection efficiency "Relative" variables have more signal selection efficiency as compared to "Absolute" one.

Next step is the choice of the best relative isolation variable among all three defined: $\frac{\sum p_T}{p_T^\mu}$, $\frac{I_{TEH}}{p_T^\mu}$ and $\frac{I_{TH}}{p_T^\mu}$. In our DY event selection (described in next Section), we are requiring both the muons to be isolated. Thus choice of the best relative isolation variable has been done on the basis of the comparison of the efficiency of the two muons in an event to be isolated as a function of the invariant mass of the dimuon system for the three defined variables. Figure 4.3 shows the dependence of the DY isolation efficiency (*i.e.*, the efficiency of the two muons to be isolated), on the reconstructed dimuon mass for 3 different criteria of relative isolation. One can see

that the relative combined I_{TEH} variable has a dip in the DY efficiency which is due to the presence of photons due to Final State Radiation(FSR). However, the tracker and HCAL based relative isolation variable $\frac{I_{TH}}{p_T^{\mu}}$ used in this study has a better signal efficiency and has no dip in the region of intermediate masses 40-90 GeV/c^2. Thus we have opted for the relative combined tracker and HCAL based isolation variable in the present study.

The optimization of the cut value for this variable has been done on the basis of the statistical significance S=$N_{sig}/\sqrt{N_{sig}+N_{bkd}}$, where N$_{sig}$ and N$_{bkd}$ are the number of signal and background events. The cut value for this isolation variable has been optimized to be 0.15.

4.3 Event Selection

The selection of the experimental data sample for the Drell-Yan (DY) cross-section measurement is performed in two steps: the online event selection and the offline event selection, using a cut based approach. The cuts have been optimized to get the maximum signal yield, by keeping a low level of the background.

- **Online Event Selection**

  Below the Z-mass peak and especially at low masses, the muon transverse momenta are quite low. Thus to achieve the maximum signal yield, triggers having lowest p_T thresholds have been used. During data taking, various triggers has to be prescaled with increasing instantaneous luminosity to accommodate with the total bandwidth for the event recording. For experimental data, events are required to pass the un-prescaled trigger with the minimum threshold on the transverse momentum of the muon candidate. The combination of various single muon triggers *i.e.* HLT_Mu9, HLT_Mu11 and HLT_Mu15 have been used depending on run range as summarized in Table 4.1. These trigger paths do not require any isolation condition on muon.

- **Offline Event Selection**

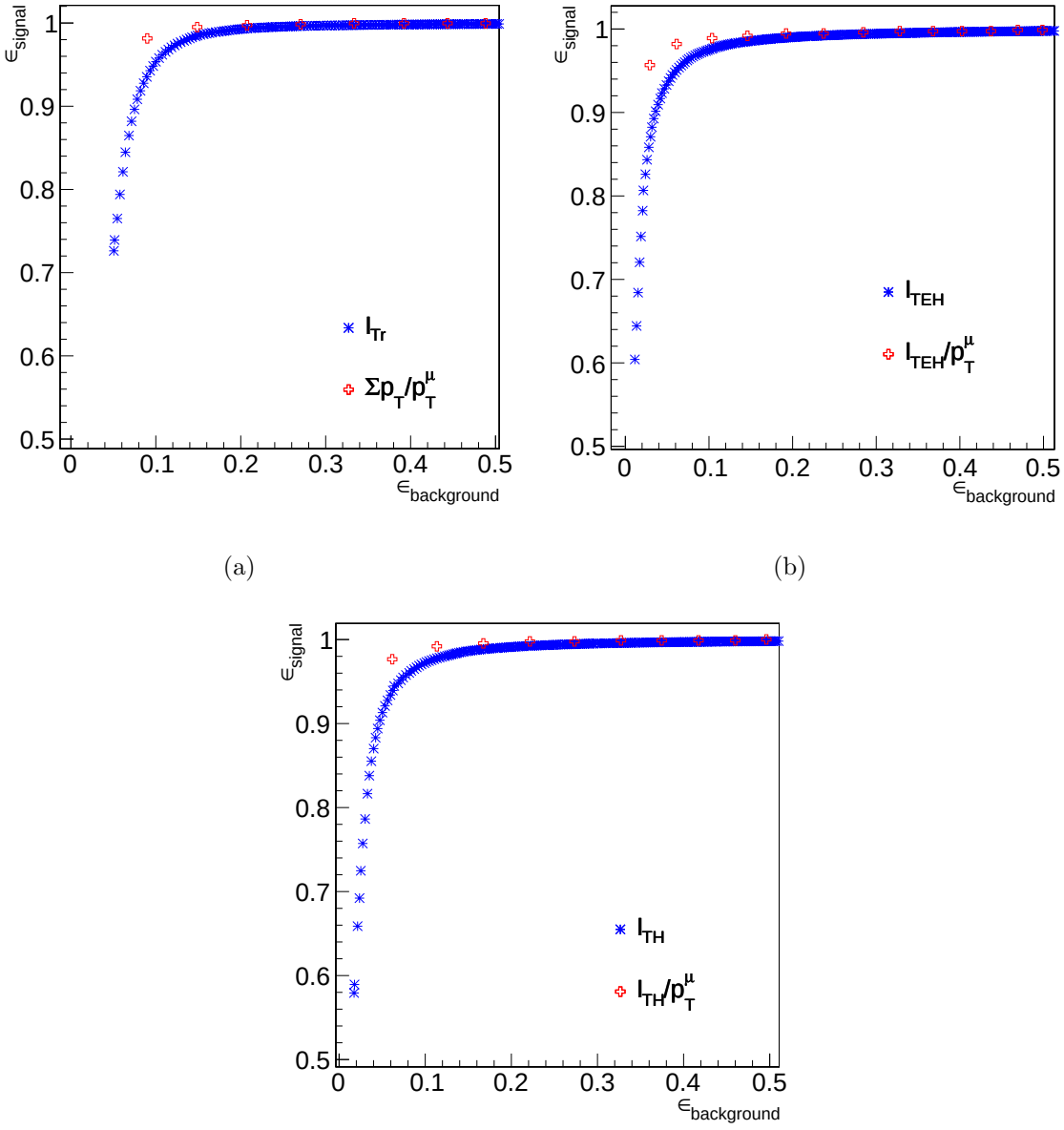

(a) (b)

(c)

Figure 4.2: Comparison of the signal (ϵ_{signal}) vs background ($\epsilon_{background}$) efficiencies (a) for $[I_{Tr},(\frac{\sum p_T}{p_T^\mu})]$, (b) for the $[I_{TEH},\frac{I_{TEH}}{p_T^\mu}]$ and (c) for the $[I_{TH},\frac{I_{TH}}{p_T^\mu}]$ isolation variables.

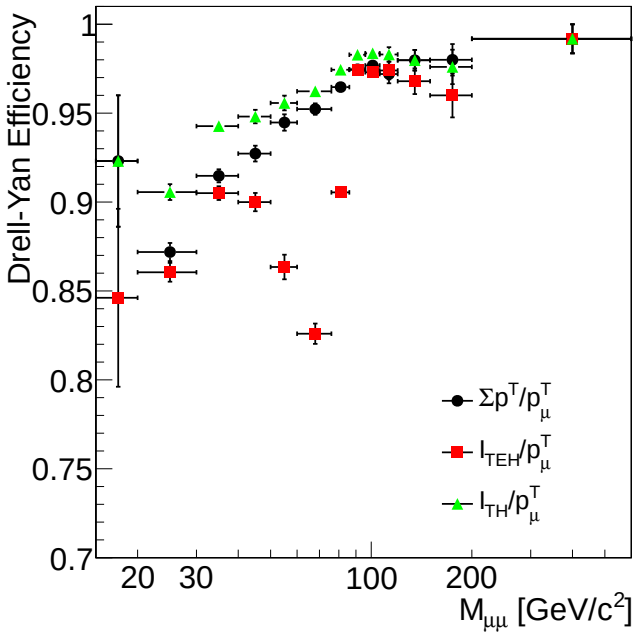

Figure 4.3: Drell-Yan isolation efficiency in various bins of reconstructed dimuon mass for three different criteria of relative isolation: I_{TH} using tracker and HCAL only, I_{TEH} using tracker, ECAL and HCAL and I_{Tr} using tracker only.

Details of HLT Trigger Paths			
Trigger path	HLT Thresholds	Run range	Data ($\int \mathcal{L}$dt pb^{-1})
HLT_Mu9	$p_T > 9$ GeV/c, $\|\eta\| < 2.4$	132440-147116	8.1
HLT_Mu11	$p_T > 11$ GeV/c, $\|\eta\| < 2.4$	147196-148058	9.5
HLT_Mu15	$p_T > 15$ GeV/c, $\|\eta\| < 2.4$	148882-149294	18.4

Table 4.1: Summary of the trigger paths according to the run range applied on data.

In this analysis, muons which are reconstructed as global and tracker muon are considered. Requiring the muon to be both global and tracker muon is effective against muons from decays-in-flight, punch-through and accidental wrong matches with the tracker tracks (in the case of global muons) or with noisy segments (in the case of tracker muons). However it is a rather loose requirement for high p_T prompt muons. To obtain a muon sample with minimum backgrounds, offline kinematic, muon identification and isolation cuts are applied on each muon in an event.

– **Kinematics**

For the single muon trigger scenario, the leading muon is required to have $p_T > 16$ GeV/c within $|\eta| < 2.1$ and a sub-leading muon with $p_T > 7$ GeV/c within $|\eta| < 2.4$. The p_T and η cuts (the kinematic and the geometric detector acceptance cuts) are applied in order to ensure that a muon falls within the detector fiducial volume and can reach the muon system of the CMS detector. The offline p_T cut is an important cut against the QCD background, which is a dominant source of background muons in the region below the Z-mass peak.

The offline p_T cuts have been optimized to achieve the maximum statistical significance in as wide a mass range as possible, paying particular attention to the region below the Z-mass peak, since QCD background is a major contamination in this mass region. The optimum combination is $p_T > 16$ GeV/c for the leading muon and $p_T > 7$ GeV/c for the second leading muon. Figure 4.4 (left) and (right) show the Data and MC comparison for the transverse momentum (p_T) distribution of the first leading muon and the second leading muon, respectively after all the cuts except the cut on the variable itself. All the background and signal MC predictions are stacked and compared with data. As can be seen from the figure, SM predictions are reproducing the data quite well in all the distributions. A sharp edge around 10 GeV/c of leading muon p_T is due to the requirement

of the online HLT trigger. There is also a bump around 45 GeV/c which is due to the muons coming from the Z boson. Since in the hadron-hadron collisions in CM system, most of the time the Z boson is expected to be produced at rest, so the muons coming from the decay of Z boson would have transverse momentum $\sim M_Z/2$.

Figure 4.5 (left) and (right) show the Data and MC comparison for the pseuodorapidity distribution of the first leading muon and the second leading muon respectively, after all the cuts except the cut on the variable itself. All the background and signal MC predictions are stacked and compared with data. As can be observed from these figures, SM predictions are reproducing the data quite well in all the distributions.

– Muon Identification

The following set of requirements optimized by the "Muon Physics Object" group at CMS are imposed on a global muon track:

* The global track fit is required to have $\chi^2/ndof < 10$.
* A muon is required to have at least 11 valid hits inside the tracker. This cut is motivated by a very poor transverse momentum measurement with a low number of hits on the track (which is η dependent).
* A muon must have at least 1 valid pixel hit on a silicon tracker track. This cut is effective against remaining decays-in-flight.
* A muon must have at least 1 valid muon hit in the muon chambers used in a global track fit. This is a loose (yet potentially powerful) cut to reject the muons from the decays-in-flight of hadrons and punch-through at high p_T.
* A muon must use hits from segments located in at least two muon stations. This cut, particularly effective against punch-through and accidental matches, is also consistent with the logic of the CMS muon trigger system, which also requires at least two muon stations in order to give a meaningful estimate of the transverse momentum.

* The transverse impact parameter (d_{xy}) of the muon in the $r-\phi$ plane with respect to the beam spot is required to be less than 2 mm. This is a powerful cut to reject muons coming from cosmic rays and other backgrounds. The muons coming from the signal vertex are expected to have very small d_{xy}, however the muons coming from cosmic muons as well as those from the decays-in-flight of heavy mesons would have large large value of d_{xy}.

Figure 4.6 (a), (b), (c) and (d) show the Data and MC comparison for the number of tracker hits, number of pixel hits, normalized χ^2 and number of muon hits, respectively. Figure 4.7 (a), (b) and (d) show the Data and MC comparison for the transverse impact parameter d_{xy} w.r.t the beam spot for the leading muon, for the second leading muon and the number of matches per muon in the muon chambers, respectively. All the background and signal MC predictions are stacked and compared with data. As can be seen from the figure, SM predictions are reproducing the data quite well in all the distributions.

– **Muon Isolation**

We require a muon to be isolated in the tracker and the HCAL. The following isolation condition has been required:

$$I_{TH}/p_T^{\mu} = \frac{\sum(p_T(tracks) + E_T(HCAL))}{p_T^{\mu}} < 0.15 \qquad (4.2)$$

Figure 4.7 (c) shows the Data and MC comparison of the isolation variable after all the cuts except the cut on the variable itself *i.e.* (N-1) cut. As is clear from the figure, there is a large deposit around the muon in case of QCD background, however the deposit around signal muon is very small. Thus this cut is very effective in reducing a large fraction of QCD background, which dominates in the low mass region.

– **Trigger matching**

Each muon must be matched within a cone of radius 0.2 to a trigger object that fired the muon trigger path. The trigger matching is performed to

make sure that the event was actually triggered by a signal muon, which is especially important when estimating the efficiency with the data driven technique known as TagAndProbe.

- **Drell-Yan Muon pair selection**

  After the good muon selection, we form the opposite sign charged pairs considering all the possible permutations of the muons available in an event. The highest mass muon pair is kept for further analysis. The selected dimuon pair is required to pass the following offline selection cuts:

  – Muons should be of opposite charge.

  – The dimuon vertex probability should be at least 2%. This requirement significantly reduces the remaining QCD background. Figure 4.8 (right) shows the distribution of the vertex probability for the dimuon candidate after all the muon identification, kinematic and isolation cuts except the cut on the variable itself.

  – The muons should not have a pronounced back-to-back geometry which is peculiar to the traversing cosmic muons *i.e.* the opening angle between the two muons has to be different from π by more than 5 mrad. The following condition is required to be fulfilled:

  $$\alpha_{3D} = \alpha cos((\vec{p}_1^{\,track}, \vec{p}_2^{\,track})/p_1^{track}/p_2^{track}) < 5mrad \qquad (4.3)$$

  Figure 4.8 (left) shows the distribution for the 3-D angle or the opening angle between the dimuon candidate after all the muon identification, kinematic and isolation cuts except cut on the variable itself (N-1) cut.

4.4 Drell-Yan Event Selection Efficiencies estimated using Monte-Carlo Cut-based Method

In this section, we are reporting the event selection efficiencies measured for various selection cuts based on Monte-Carlo (MC) simulation. In an event, we are requiring

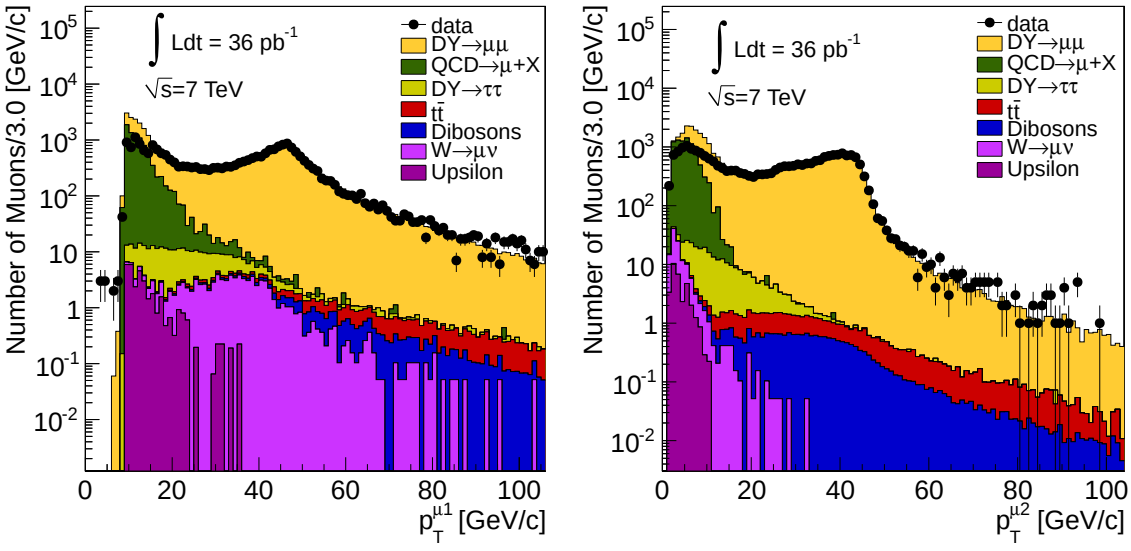

Figure 4.4: Data and MC comparison after offline selection with a cut on the variable plotted excluded *i.e.* (N-1) cut: (left) leading muon p_T, (right) second leading muon p_T.

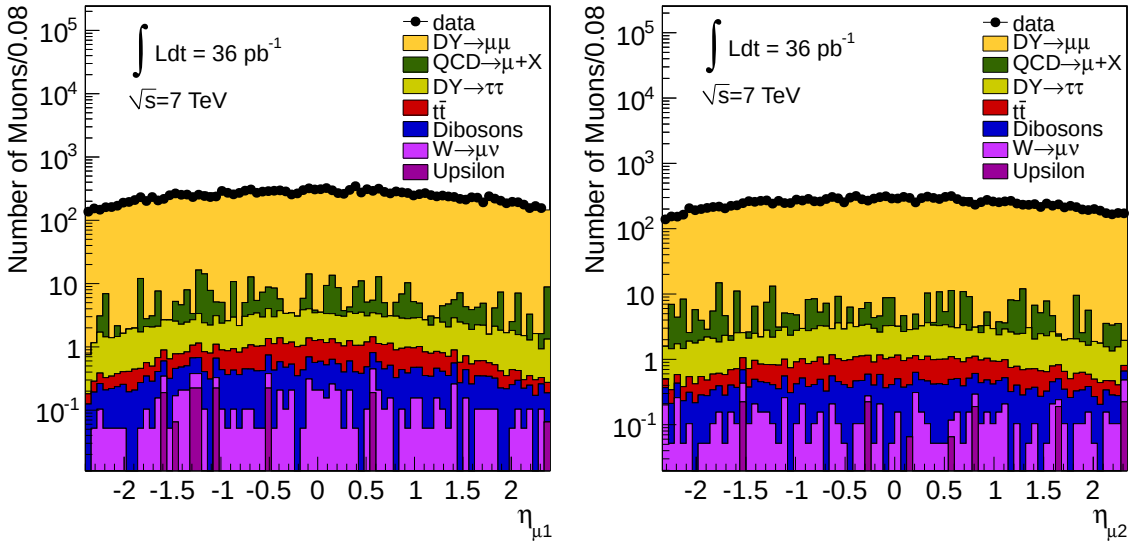

Figure 4.5: Data and MC comparison after offline selection with a cut on the variable plotted excluded *i.e.* (N-1) cut: (left) leading muon η, (right) second leading muon η.

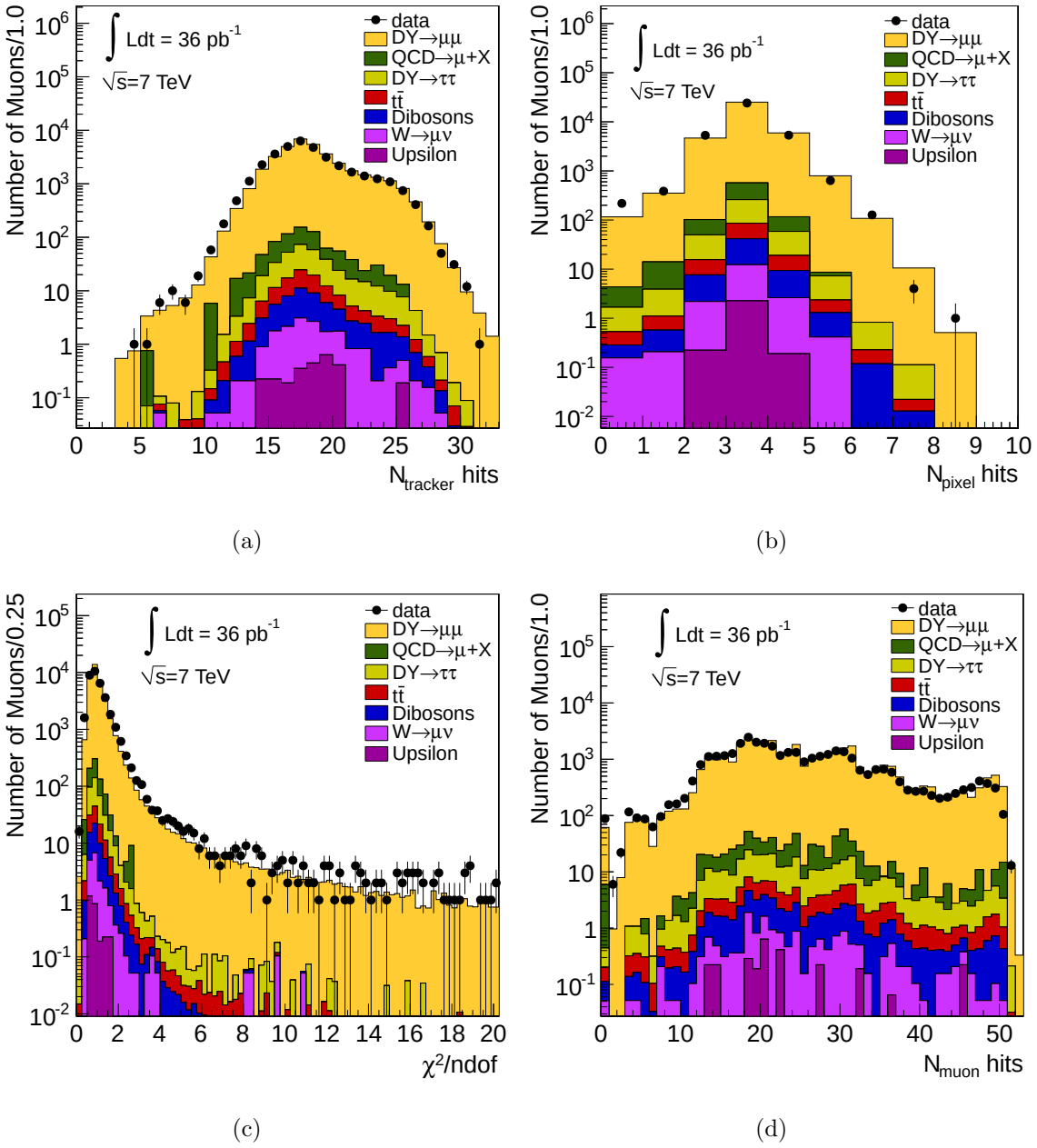

Figure 4.6: Data and MC comparison after offline selection with a cut on the variable excluded *i.e.* (N-1) cut: (a) number of hits in tracker, (b) pixel hits (c) show the normalized χ^2 and (d) number of hits in the muon chamber.

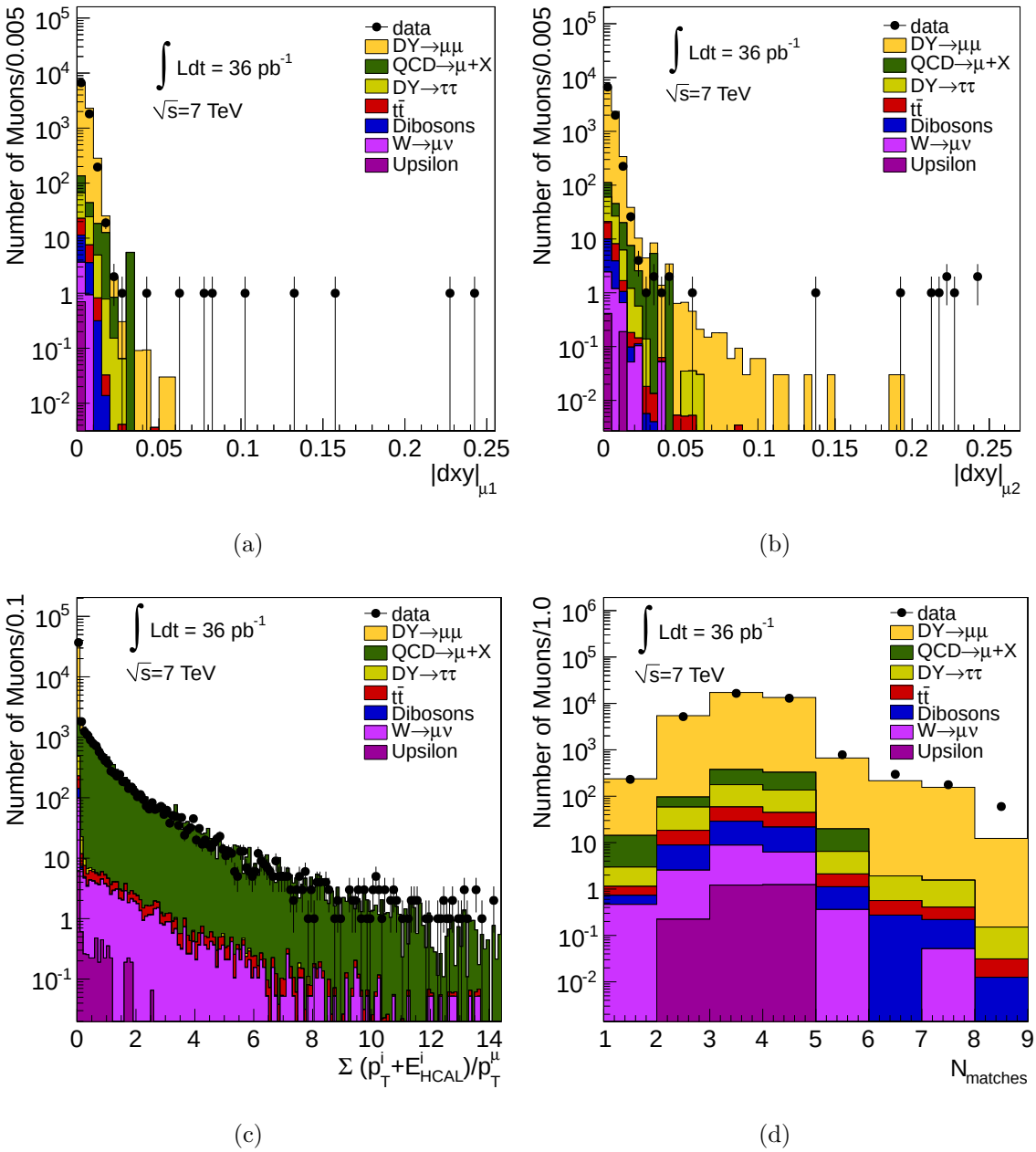

Figure 4.7: Data and MC comparison after offline selection with a cut on the variable plotted excluded *i.e.* (N-1) cut: (a) d_{xy} of the leading muon, (b) d_{xy} of the second leading muon w.r.t the beam spot (c) $\sum \frac{(p_T(tracks)+E_T(HCAL))}{p_T^{\mu}}$ and (d) number of matches in muon segment per muon.

the two leading muons to pass each selection cut. Thus the efficiencies reported here are basically, the dimuon selection efficiency in an event. The efficiencies shown in Table 4.2, 4.3 and 4.4 are the relative efficiencies *i.e.* the efficiency of a given cut relative to the previous one. In Table 4.2, we present the comparison of the cut-wise efficiencies of Drell-Yan (DY) MC POWHEG sample generated in low invariant mass range 10< $M_{\mu\mu}$ <20 GeV/c^2, high invariant mass range $M_{\mu\mu}$ >20 GeV/c^2 and the efficiency of the experimental data. The numbers shown in this table, gives an estimate about the strength of each selection cut to select the dimuon event and to reject the background. The large discrepancy in data and signal MC is because in data there is huge amount of backgrounds. The numbers in Table 4.3 shows the efficiencies for all the Electroweak (dibosons, $t\bar{t}$, DY$\rightarrow$ $\tau\tau$) backgrounds and the numbers in Table 4.4 shows the relative efficiencies for the QCD background.

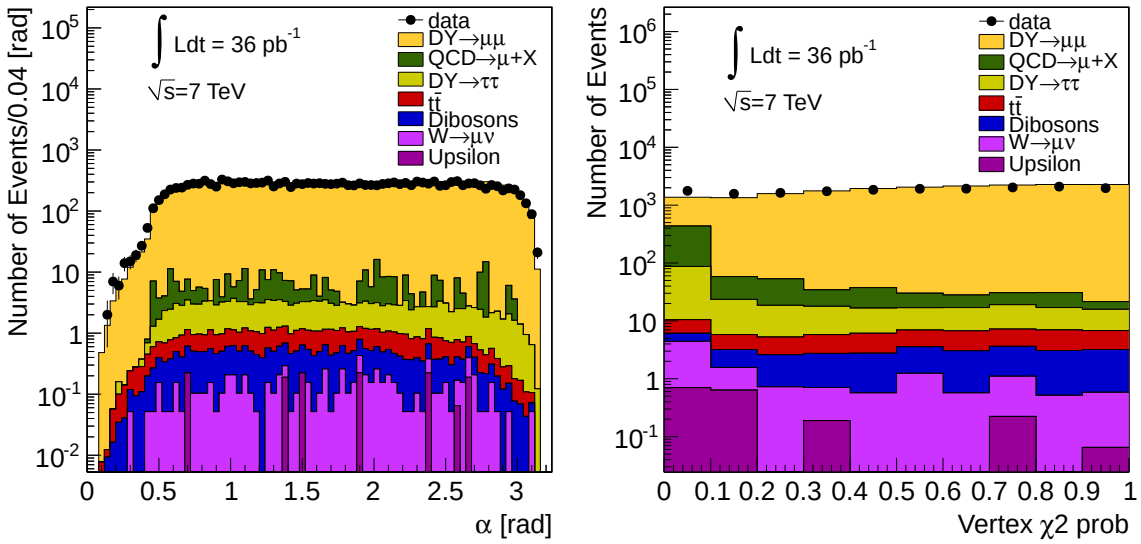

Figure 4.8: Data and MC comparison after offline selection with a cut on the variable itself excluded: (left) shows the 3D angle between the two muons and (right) shows the vertex probability distribution.

Cut-Wise Event Selection Efficiency			
Event selection	DY→ $\mu\mu$ ($10 < M_{\mu\mu} < 20$) GeV/c^2	DY→ $\mu\mu$ ($M_{\mu\mu} > 20$) GeV/c^2	Experimental data
Trigger	0.11±0.000	0.67±0.000	0.20±0.000
Muon pair=1	0.60±0.001	0.65±0.000	0.04±0.000
Muon ID	0.91±0.001	0.96±0.000	0.78±0.001
Isolation	0.84±0.001	0.96±0.000	0.19±0.001
pt cut	0.06±0.001	0.82±0.000	0.37±0.002
eta cut	0.94±0.003	0.91±0.000	0.92±0.002
α >0.005	0.49±0.007	1.00±0.000	0.92±0.002
vtx prob	0.98±0.002	0.54±0.000	0.56±0.003

Table 4.2: The efficiencies of Drell-Yan event selection cuts for the signal MC and Data. The efficiencies reported here are relative w.r.t the previous cut.

4.5 Data-Driven estimation of the single muon efficiencies using TagAndProbe Method

In this analysis, the muon identification, isolation and trigger efficiencies have been estimated using the data driven approach so called TagAndProbe method. Using this technique it is possible to obtain almost unbiased estimate of the efficiencies of the different stages of muon trigger and offline reconstruction.

The TagAndProbe [80] is a data-driven approach for measuring the particle efficiencies. It utilizes a known mass resonance (*e.g.* J/Ψ, Υ, Z) to select particles of the desired type and probe the efficiency of a particular selection criterion on those particles. In general the "tag" is an object that passes a set of very tight selection criteria designed to isolate the required particle type (usually an electron or muon, though in principle the method is not strictly limited to these). Tags are often referred to as a selected "golden" electrons or muons and the fake rate for passing tag

Cut-Wise Event Selection Efficiency estimated from Monte-Carlo						
Event selection	WW	ZZ	WZ	$t\bar{t}$	W$\mu\nu$	DY$\rightarrow \tau\tau$
Trigger	0.18±0.000	0.11±0.000	0.14±0.000	0.31±0.000	0.61±0.000	0.08±0.000
Muon pair=1	0.08±0.0005	0.53±0.001	0.20±0.001	0.19±0.001	0.01±0.000	0.09±0.001
Muon ID	0.89±0.002	0.95±0.001	0.93±0.001	0.85±0.001	0.64±0.003	0.92±0.002
Isolation	0.73±0.003	0.88±0.001	0.84±0.002	0.23±0.002	0.22±0.004	0.87±0.003
pt cut	0.93±0.002	0.94±0.001	0.97±0.001	0.91±0.003	0.09±0.005	0.57±0.005
eta cut	0.93±0.002	0.93±0.001	0.93±0.001	0.97±0.002	0.94±0.015	0.93±0.003
α >0.005	0.98±0.001	0.99±0.000	1.00±0.000	0.98±0.001	0.92±0.018	1.00±0.001
vtx prob	0.68±0.003	0.53±0.001	0.52±0.002	0.67±0.004	0.62±0.030	0.64±0.006

Table 4.3: The efficiencies of Drell-Yan event selection cuts for the Electroweak backgrounds. The efficiencies reported here are relative w.r.t. the previous cut.

Cut-Wise Event Selection Efficiency estimated from Monte-Carlo							
Event selection	QCD15-20	QCD20-30	QCD30-50	QCD50-80	QCD80-120	QCD120-150	QCD150-Inf
Trigger	0.10±0.000	0.16±0.000	0.24±0.000	0.32±0.000	0.37±0.000	0.40±0.001	0.43±0.001
Muon pair=1	0.02±0.000	0.03±0.000	0.04±0.000	0.06±0.000	0.07±0.000	0.07±0.000	0.08±0.000
Muon ID	0.76±0.005	0.78±0.002	0.79±0.001	0.78±0.001	0.75±0.002	0.72±0.003	0.65±0.003
Isolation	0.23±0.006	0.12±0.002	0.04±0.001	0.01±0.000	0.00±0.000	0.00±0.000	0.00±0.000
pt cut	0.00±0.001	0.01±0.002	0.04±0.003	0.10±0.009	0.18±0.025	0.12±0.048	0.26±0.068
eta cut	1.00±0.000	0.88±0.046	0.93±0.021	0.91±0.025	0.93±0.037	1.00±0.000	0.82±0.116
α >0.005	1.00±0.000	0.89±0.048	0.81±0.033	0.50±0.047	0.36±0.074	0.50±0.204	0.33±0.157
vtx prob	0.00±0.000	0.53±0.074	0.48±0.042	0.46±0.047	0.48±0.077	0.67±0.192	0.57±0.187

Table 4.4: The efficiencies of Drell-Yan event selection cuts for QCD sample binned according to the cut on the p_T at the generator level. The efficiencies reported here are relative w.r.t the previous cut.

selection criteria should be very small ($\ll$1%). A generic set of the desired particle type (*i.e.* with potentially very loose selection criteria) known as "probes" is selected by pairing these objects with tags such that the invariant mass of the combination is consistent with the mass of the resonance. Combinatoric backgrounds may be eliminated through any of a variety of background subtraction methods such as fitting, or sideband subtraction. The definition of the probe object depends on the specifics of the selection criterion being examined. The efficiency itself is measured by counting the number of "probe" particles that pass the desired selection criteria:

$$\epsilon = \frac{P_{pass}}{P_{all}} \tag{4.4}$$

where P_{pass} is the number of probes passing the selection criteria and P_{all} is the total number of probes counted using the resonance. It is worthwhile to note that in some cases a probe object will also pass the tag selection criteria. In this case it will appear in both the tag and probe lists and produce a double pairing in the same event. The efficiency formula as written above accounts for these double pairings.

For this analysis, Z$\rightarrow \mu^+\mu^-$ events with $70 < M_{\mu\mu} < 130$ GeV/c^2 mass window, has been selected to measure the individual single muon efficiency factors in both the experimental data and MC. In a given Z peak event, one muon candidate, called the "tag", passes the trigger criteria, muon identification and muon isolation requirements. The other muon candidate in the same event, called the "probe", is required to pass specific criteria for which the efficiency is being measured in each step. The efficiency is calculated as the fraction of probe muons which pass the specific selection criteria to the total number of probe muons.

4.5.1 Single Muon Efficiency Factorization

In our study, the "tag" has been defined as a muon reconstructed as both tracker and global muon with $p_T > 20$ GeV/c and $|\eta| > 2.1$. "Tag" is also required to pass all the muon quality cuts and isolation cut. We have factorized the total single muon

selection efficiency into the following conditional terms:

$$\epsilon(\mu, sel) = \epsilon(track|standAlone).\epsilon(global|track).\epsilon(id|(track + global) \\ \epsilon(iso|(id + track + global)).\epsilon(trig|sel) \quad (4.5)$$

All these conditional efficiency terms are explained as follows:

- $\epsilon(track|standAlone)$ - is the offline track reconstruction efficiency. Our probe in this case is the muon track found in the muon chambers only, so the requirement on the passing probe is to be reconstructed as a tracker track as well.

- $\epsilon(global|track)$ - is the efficiency for a muon to be identified as "global" muon. We have required the probe to be tracker track, so the requirement of the passing probe to be global muon gives the efficiency for a muon to be reconstructed in the muon chambers of the detector.

- $\epsilon(id|(track + global))$ - is the muon identification efficiency. We have required the probe to be muon reconstructed as both tracker and global muon and the passing probe must be identified as a "good muon" satisfying all the offline muon quality cuts explained in Section 4.3.

- $\epsilon(iso|(id + track + global))$ - is the muon isolation efficiency. For this term, probe is defined both as tracker and global muon passing all the muon quality cuts. For the isolation efficiency - Passing probe must pass the muon isolation requirement.

- $\epsilon(trig|sel)$ - is the muon trigger efficiency. For this term, our probe is the muon reconstructed as both tracker and global muon passing muon isolation and quality cuts. For the trigger efficiency passing probe should pass the High-Level trigger path required in an event.

The single muon efficiencies are determined as a function of probe p_T and η. Table 4.5 reports the trigger efficiencies of HLT_Mu9, HLT_Mu11 and HLT_Mu15 trigger paths for single muons in the experimental data. Figure 4.9 (a) and (b) show the HLT_Mu9

trigger efficiency as function of probe p_T and η for the run 2010A corresponding to 3.2 pb^{-1} of integrated luminosity. As can be observed from the Figure (b), there is a dip in the efficiency as a function of probe η in the transition region 1.0< $|\eta|$ <1.02 of DT and CSC muon chambers, which leads to an overall lesser efficiency. This is mainly related to time synchronization of the muon detector at start-up phase of the detector which was improved in the new runs.

Figure 4.9 (c) and (d) show the HLT_Mu9 trigger efficiency as function of probe p_T and η for the run 2010B corresponding to 5.0 pb^{-1} of integrated luminosity. As can be observed from the Figures 4.9 (c) and (d) the efficiency in the transition region $1.0 < |\eta| < 1.02$ is improved as compared to previous runs resulting into the overall increase in HLT_Mu9 efficiency by ∼4%. The HLT_Mu9 trigger efficiency estimated in MC simulation is 0.952±0.0003. As HLT_Mu9 was the only trigger path available in the MC sample during this analysis, so the trigger efficiency numbers for HLT_Mu11 and HLT_Mu15 are not available from simulation. Figure 4.10 shows the HLT_Mu11 and HLT_Mu15 trigger efficiencies of the CMS data for the run-range corresponding to integrated luminosity of 9.2 pb^{-1} and 18.4 pb^{-1} respectively.

The muon tracking, global, Identification and isolation efficiencies have been reported only for the run-range corresponding to 18.4 pb^{-1} of integrated luminosity. Figure 4.11, 4.12, 4.13 and 4.14 (left) and (right) show the comparison of data and simulation for global, tracker, muon-id and isolation efficiencies as function of probe p_T and η respectively. Both the data and MC are in good agreement as is clear from all the figures. It is also clear by looking at the numbers for all the efficiencies reported in Table 4.6.

Trigger Efficiencies using TagAndProbe				
	HLT_Mu9 (Run 2010A)	HLT_Mu9 (Run 2010B)	HLT_Mu11	HLT_Mu15
Data	0.877±0.009	0.917±0.006	0.924±0.004	0.928±0.003

Table 4.5: Estimation of the High-Level Trigger efficiencies for single muon trigger paths in different run ranges of 2010 data.

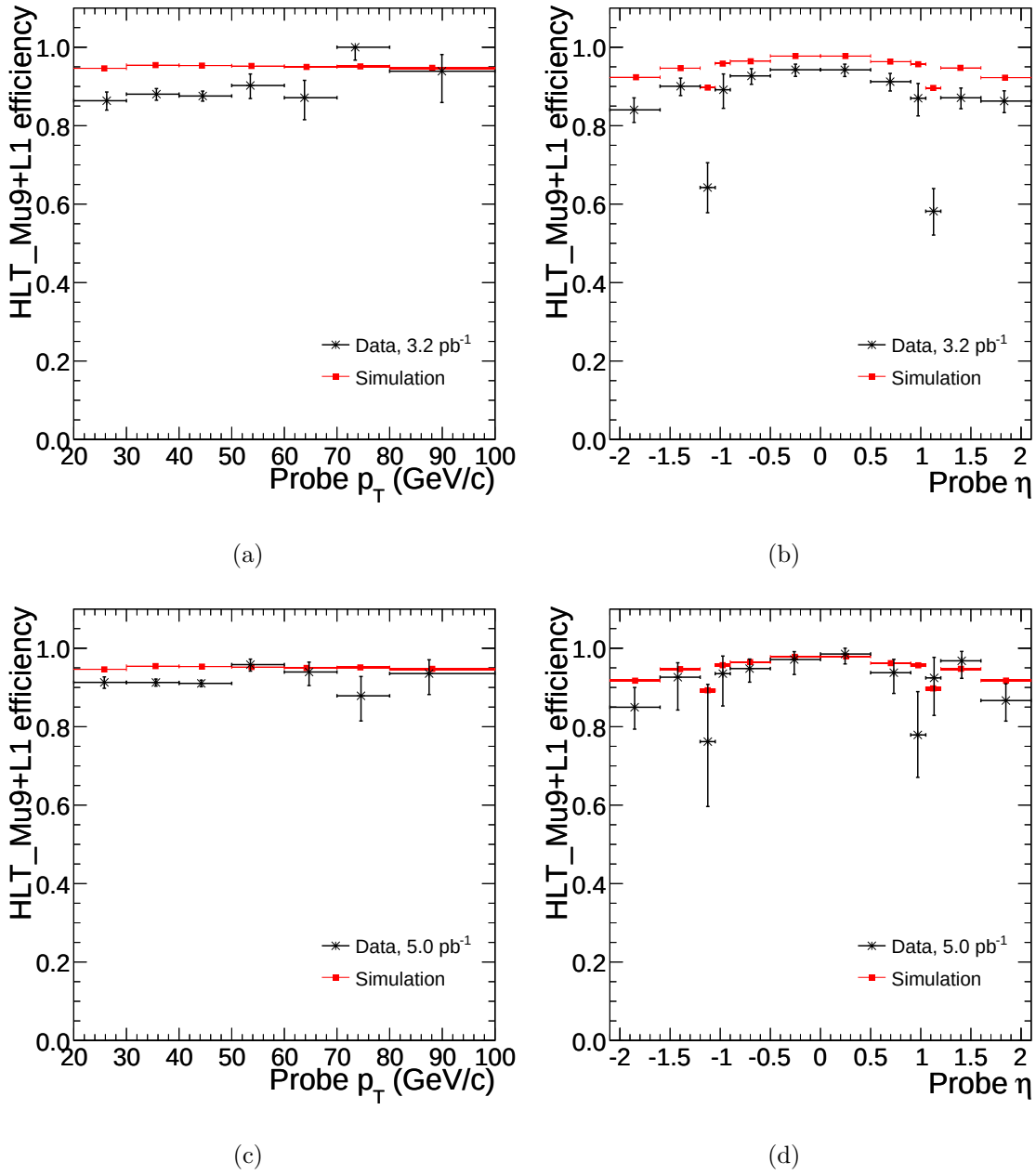

(a) (b)

(c) (d)

Figure 4.9: Data and MC comparison of the HLT_Mu9 trigger efficiency. (a) and (b) show the trigger efficiency for HLT_Mu9 using CMS data of run 2010A as a function of probe p_T and η. Figure (b) and (c) show the HLT_Mu9 trigger efficiency using CMS data of run 2010B as a function of probe p_T and η.

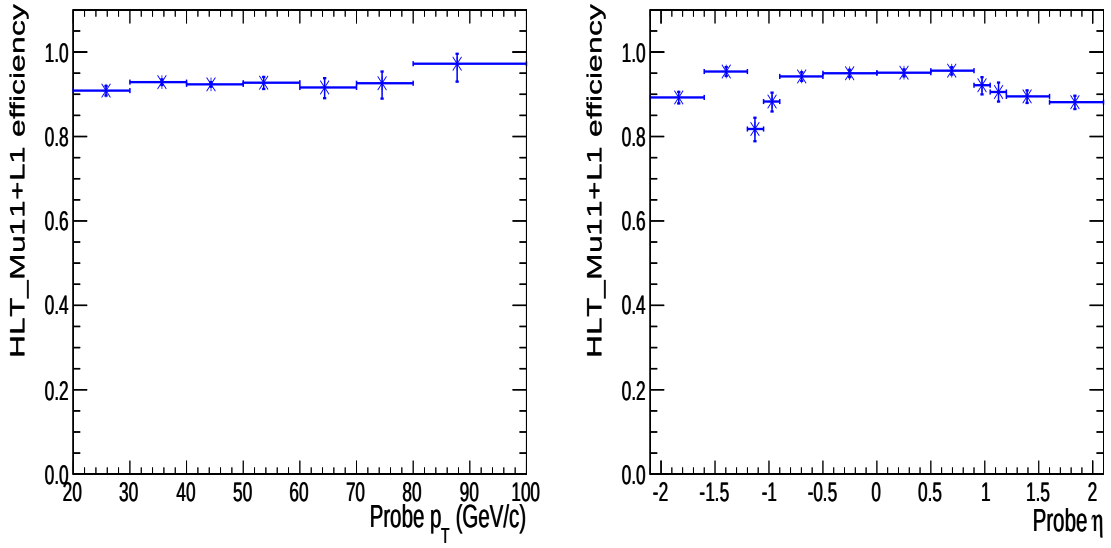

(a)

(b)

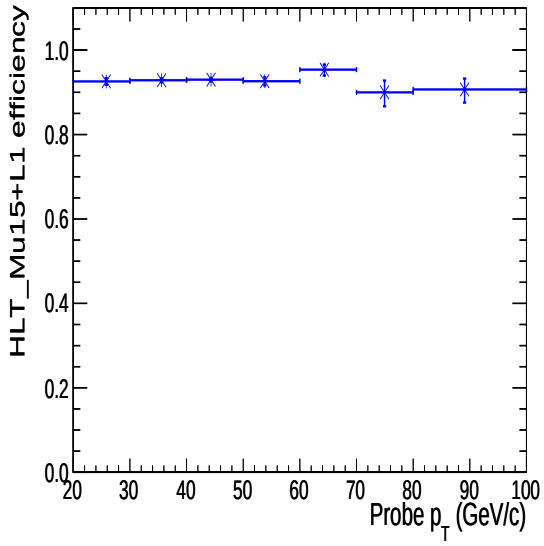

(c)

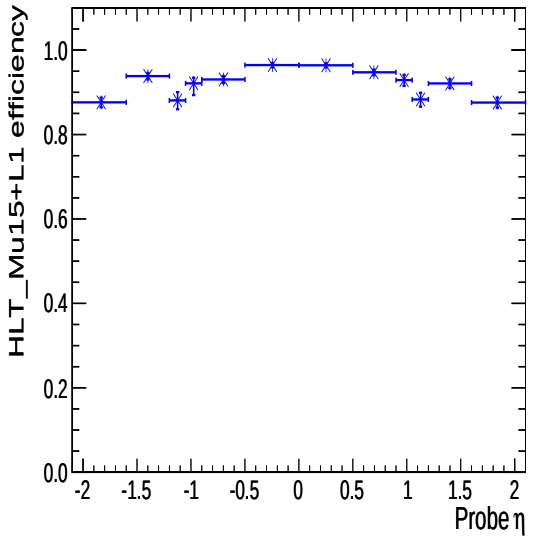

(d)

Figure 4.10: Trigger efficiency of HLT_Mu11 trigger path for the experimental corresponding to an integrated luminosity of 9.2 pb^{-1} (a) as a function of probe p_T, (b) as a function of η. Similarly figures (b) and (c) show the HLT_Mu15 trigger efficiency as function of probe p_T and η for experimental data corresponding to an integrated luminosity of 18.4 pb^{-1} respectively.

Muon Identification and Isolation Efficiencies using TagAndProbe			
	Data	MC	$\frac{Data}{MC}$
Global Muon	0.999±0.006	0.992±0.0001	1.007±0.006
Tracker Muon	1.00±0.001	0.995±0.009E^{-2}	1.005±0.001
Muon Id	0.971±0.010	0.979±0.0002	0.992±0.010
Isolation	0.985±0.006	0.993±0.0001	0.992±0.006

Table 4.6: Estimation of the muon identification and isolation efficiencies for data and simulation. The total data used here corresponds to 18.4 pb^{-1} of integrated luminosity.

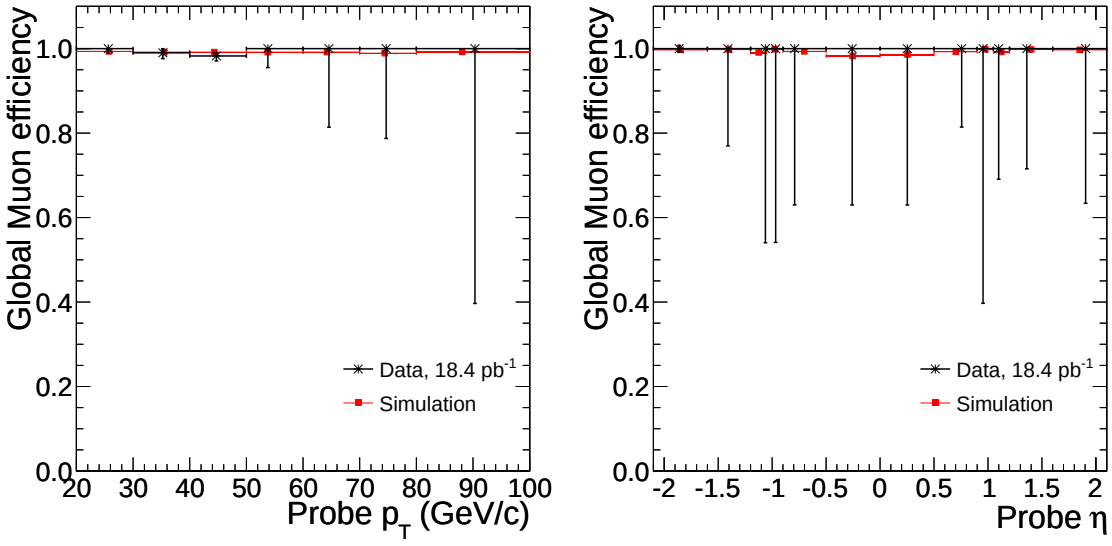

Figure 4.11: Data and MC comparison of the efficiency for a muon to be reconstructed as "global" muon as function of probe p_T (left) and probe η (right). The CMS data used here corresponds to an integrated luminosity of 18.4 pb^{-1}.

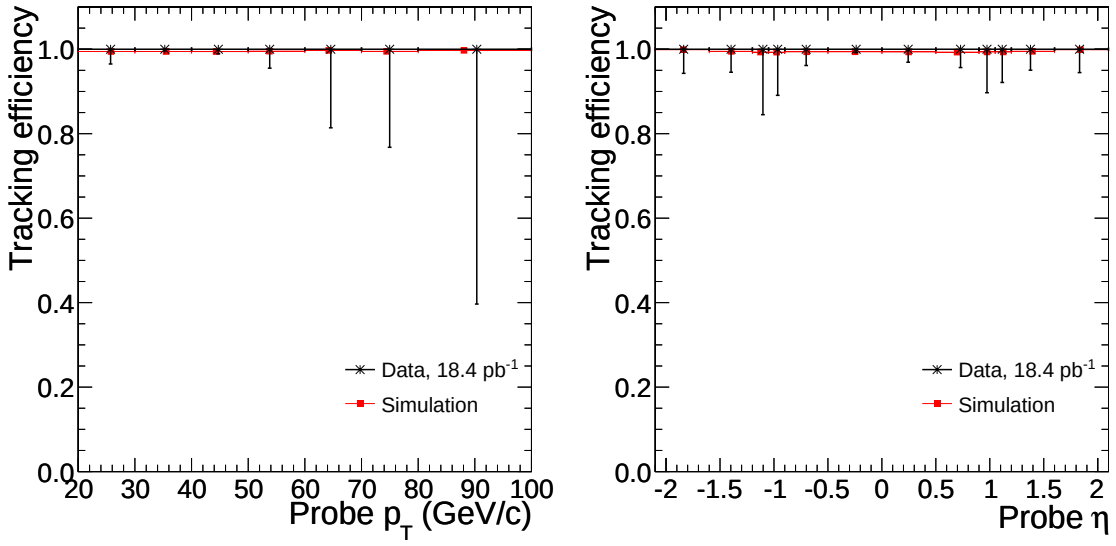

Figure 4.12: Data and MC comparison of the efficiency for a muon to be reconstructed as "tracker" muon as function of probe p_T (left) and probe η (right). The CMS data used here corresponds to an integrated luminosity of 18.4 pb^{-1}.

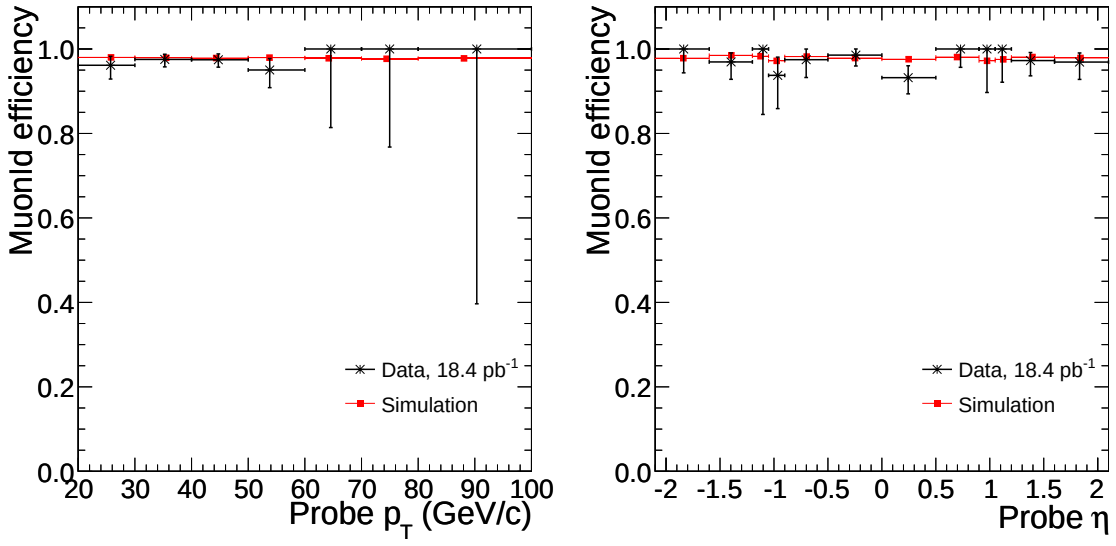

Figure 4.13: Data and MC comparison of the efficiency for a muon to be identified as a "good" muon which is passing all the muon quality cuts, as function of probe p_T (left) and probe η (right). The CMS data used here corresponds to an integrated luminosity of 18.4 pb^{-1}.

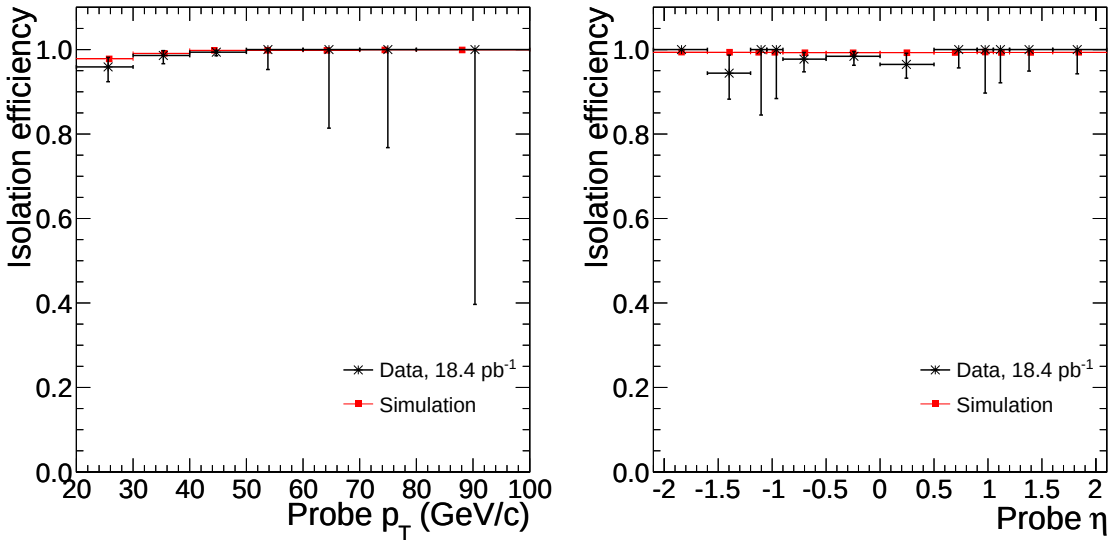

Figure 4.14: Data and MC comparison of the efficiency for a muon to be isolated as a function of probe p_T (left) and probe η (right). The CMS data used here corresponds to an integrated luminosity of 18.4 pb^{-1}.

4.6 Drell-Yan Signal and Background Yields

Several physical and instrumental backgrounds contribute to the Drell-Yan (DY) analysis. The potential sources of backgrounds are already discussed in Section 4.1.1. There are two categories of dimuon backgrounds: the first category of backgrounds composed of two genuine muons and the second contributes where at least one daughter is a misidentified muon. Most of the genuine dimuon background contribution comes from $t\bar{t}$, WW, WZ and ZZ production, as well as from the DY$\rightarrow \tau^+\tau^-$ pairs. The $DY \rightarrow \tau^+\tau^-$ background is sizable and dominant in the middle mass ranges whereas $t\bar{t}$ background dominates in the high mass regions. The diboson contributes to the background level only mildly. The misidentified muon backgrounds originating from the QCD multijet and W+jet events dominates in the low mass region. We have relied on the MC cut-based analysis to predict the proper amount of background, expected from each of the sources.

Figure 4.15 shows the expected shapes and relative yields of these several dimuon sources after passing the DY selection. The yield of signal and various backgrounds es-

timated from Monte-Carlo (MC) samples are stacked and compared with the dimuon yield in data. As can be seen from the figure, the MC estimation is reproducing the data quite well. Table 4.7 shows the number of dimuon events in all dimuon backgrounds and the observed dimuon yield in experimental data in each invariant mass bin after passing the DY selection criteria. The second and third column of this table, reports the QCD and all other Electroweak backgrounds estimated using MC cut-based analysis, the fourth column reports the number of observed dimuon events in experimental data before correction. The last column reports the background subtracted dimuon event yield in experimental data analyzed. As we can see, after all the selections, QCD background mainly dominates in only the lower mass bins and as moving to higher dimuon mass region, the contribution from QCD background vanishes, however there is small contribution from other background processes in the higher mass region.

4.6.1 Estimation of dimuon background using data driven $e\mu$ method

Methodology

In this study, to cross-check the level of the background from the MC based analysis, a data-driven $e\mu$ method which is based on the reconstruction of $e\mu$ pairs, for the estimation of the genuine muon background sources *i.e.* $DY \rightarrow \tau^+\tau^-$, $t\bar{t}$, WW and WZ processes have been used.

The dominant electroweak background from low invariant mass and towards the Z peak is $DY \rightarrow \tau^+\tau^-$. Beyond the Z mass peak, background contributions from $t\bar{t}$ and WW production becomes significant. In this region, backgrounds from other diboson channels *e.g.* (WZ and ZZ) are small. All these processes are flavour-symmetric, having a branching ratio to a pair of leptons of different flavour, $e\mu$, twice as large as the branching ratio to $\mu^+\mu^-$. Consequently, the $\mu^+\mu^-$ backgrounds from the modes $DY \rightarrow \tau^+\tau^-$, $t\bar{t}$ and WW can be measured from a relatively clean sample of their decays to $e\mu$ pair. In this study, this measurement technique is referred to as the "$e\mu$

Observed dimuon yield in Data and Backgrounds estimated from MC				
Invariant Mass	Backgrounds		N_{obs}	N_{obs}-N_{bg}
bin (GeV/c^2)	QCD	Others	(Data)	(Data)
15-20	16±5	2±2	257±16	240±17
20-30	91±10	18±5	820±27	711±32
30-40	57±8	42±7	1010±32	912±35
40-50	26±6	39±7	668±26	603±28
50-60	17±5	28±6	445±21	399±23
60-76	0.2±0.8	23±5	766±28	743±29
76-86	0.3±1	7±3	1621±40	1614±40
86-96	5±3	13±4	11100±105	11082±106
96-106	2±2	3±2	779±28	774±28
106-120	-	3±2	172±13	169±13
120-150	-	4±3	144±12	140±12
150-200	-	4±2	51±7	47±8
200-600	-	3±2	30±5	27±6

Table 4.7: Dimuon yield observed in experimental data after all selection cuts, estimated backgrounds (MC based) and background subtracted yields in data.

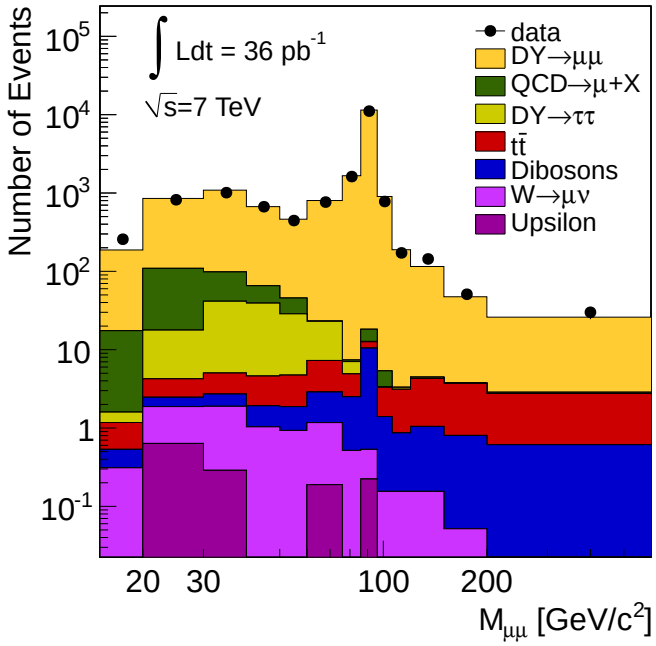

Figure 4.15: The observed dimuon invariant mass spectra. No corrections are applied to the distributions. The points with error bars represent the data, while the various contributions from simulated events are shown as stacked histograms. The "QCD" contribution results from processes associated with QCD and could be a genuine or mis-reconstructed muons.

method". In this method, the events from the genuine muon background sources are treated as "$e\mu$ events" and the backgrounds like QCD and W+jets which contains only one real muon or electron and another is misidentified will serve as "backgrounds" to the $e\mu$ events. The relationship between the number of $\mu^+\mu^-$ and $e\mu$ events can be expressed as follows:

$$N^{Est}_{\mu^+\mu^-} = \frac{A}{2}\frac{1}{1+R}N^{Obs}_{e\mu} \tag{4.6}$$

where A = $2N_{\mu\mu}/N_{e\mu}$, $N_{\mu\mu}$ and $N_{e\mu}$ are the numbers of $\mu^+\mu^-$ and $e\mu$ events reconstructed in MC. Therefore A is a ratio of the detector acceptance times selection and reconstruction efficiencies for $\mu^+\mu^-$ events to the $e\mu$ the events. $N^{Obs}_{e\mu}$ is the number of $e\mu$ events observed in experimental data and R is the ratio of $e\mu$ backgrounds *i.e.* QCD and W+jets to the $e\mu$ events. Thus R becomes $(N_{W+jets} + N_{QCD})/(N_{DY\to\tau\tau+N_{t\bar{t}}+N_{WW})}$. When there is no $e\mu$ background in that case R=0. The $N^{Est}_{\mu^+\mu^-}$ are the estimated number of the $\mu^+\mu^-$ background events. The $N^{Est}_{\mu^+\mu^-}$, has been estimated on a bin by bin basis, because A and R are not constant as a function of invariant mass.

4.6.2 $e\mu$ event selection

In this method of background estimation, the first important step is to select a pure $e\mu$ sample from data, which is not contaminated by any signal event *i.e.* $\mu^+\mu^-$ events. The following selection criteria is chosen for the muon and electron to select a pure $e\mu$ sample:

- **Muon selection**

  The selection of muon candidate is same as described in Section 4.3, except for the cut on the transverse impact parameter calculated w.r.t beam spot, d_{xy}. For the $e\mu$ method, we require a muon to have $d_{xy} < 0.2$ mm. This cut has been tightened to reduce the backgrounds with misidentified muons *i.e.* QCD and W+jets. The matching of the muon with the trigger object has not been required.

- **Electron selection**

  The electron selection is same as adopted by the DY di-electron channel [81]. The selection cuts are described as follows:

  - **Kinematics**: Electron candidate is required to be within the good ECAL detector acceptance defined as: $|\eta_{SC}| < 1.4442$ for barrel and $1.566 < |\eta_{SC}| < 2.5$ for endcap, with η_{SC} being the η of the electrons supercluster (SC).
  - **Isolation**: A relative combined isolation criteria has been required for the electron to be isolated. Since the electron is required to lie in the ECAL detector acceptance region, therefore two isolation conditions are defined for both the barrel and the endcap regions separately in a cone of radius $\Delta R = 0.3$:
    - Isolation for Barrel $= \frac{\sum p_T(Tracker)+max(0,E_T(ECAL)-1.0)+E_T(HCAL)}{p_T^e} < 0.01$
      In the barrel region, 1 GeV/c of ECAL energy deposition has been subtracted to account for noise (pedestal).
    - Isolation for end-caps $= \frac{\sum p_T(Tracker)+E_T(ECAL)+E_T(HCAL)}{p_T^e} < 0.10$
  - **Photon Conversion Rejection**: To minimize the electrons coming from the photon conversions, it is required that the electron track has no missing hits in the tracker before the first hit in the reconstructed track assigned to the electron. Electrons are rejected when a partner track consistent with a photon conversion is found. The consistency of electron and partner track with a photon conversion is established, which is based on the opening angle (Dcot) and on the separation in the transverse plane (Dist) at the point at which the electron and partner tracks are parallel.
  - **Identification**: Electron identification involves selection based on cluster shape variable $\sigma_{i\eta i\eta}$, track-cluster matching variables $|\Delta\phi_{i\eta}|$ and $|\Delta\eta_{i\eta}|$ and hadronic activity in HCAL, *i.e.* H/E. Here $\Delta\phi_{i\eta} = |\eta_{SC} - \eta_{track}^{extrap.}|$, where η_{sc} is the η position of supercluster and $\eta_{track}^{extrap.}$ is the track pseudorapidity at the closest position to the supercluster position; and $\Delta\phi_{i\eta} = |\phi_{SC} - \phi_{track}^{extrap.}|$,

where ϕ_{sc} is the ϕ position of the supercluster and $\phi_{track}^{extrap.}$ is the track ϕ position at the closest position to the supercluster position; The exact values of all these cuts are summarized in Table 4.8.

- $e\mu$ **Candidate Selection**

  After the good muon and good electron selection, next step is to select an event containing an $e\mu$ pair. For this purpose, an opposite charged $e\mu$ pair has been required in an event, with an electron having supercluster $E_T > 7.0$ GeV/c and $|\eta_{SC}| < 2.5$, and muon with $p_T > 16$ GeV/c and $|\eta| < 2.1$. In order to estimate the $\mu^+\mu^-$ background accurately from the $e\mu$ sample from data, it is necessary to keep the same kinematic cuts on $e\mu$ pair as the adopted for $\mu^+\mu^-$ pair. Thus we require electron with $E_T > 7.0$ GeV/c and muon with $p_T > 16$ GeV/c.

  We could have done the reverse as well *i.e.* $E_T > 16.0$ GeV/c and muon with $p_T > 7$ GeV/c, but this choice was not possible because of the triggers available in the experimental data samples analyzed. We are using the single muon triggered samples which requires at least one muon above a certain p_T threshold during the online selection. The lowest unprescaled trigger thresholds available in the present data are 9, 11 and 15 GeV/c, so if we put a 7 GeV/c cut on muon, then we can loose the events in which a trigger with 15 GeV/c threshold has been fired.

  Thus to keep enough statistics for this study, a choice of 16 GeV/c cut on leading muon p_T and 7 GeV/c threshold on the E_T of electron in $e\mu$ pair has been adopted. We have not required trigger matching for both electron and muon because the lowest unprescaled trigger threshold for the electron in the analyzed data, available was 17 GeV/c, which is higher than the kinematic p_T cut requirement of 16 and 7 GeV/c.

4.6.3 Results of $e\mu$ method

- **Validation test**

Electron Identification Cuts		
Variable	barrel	end-cap
I_{rel}^{comb}	0.10	0.10
Missing hits	0	0
Dcot	0.02	0.02
Dist	0.02	0.02
$\sigma_{i\eta i\eta}$	0.02	0.03
$\lvert\Delta\phi_{i\eta}\rvert$	0.06	0.03
$\lvert\Delta\eta_{i\eta}\rvert$	0.004	0.007
H/E	0.04	0.025

Table 4.8: The values of the isolation, conversion rejection and identification cuts for the electron in the barrel and endcap detector regions.

This method is first checked with the "validation test" using MC sample. Validation test is applied using the formula given as follows:

$$N_{\mu^+\mu^-}^{Est} = \frac{A}{2} N_{e\mu}^{Obs} \tag{4.7}$$

Figure 4.16 shows the histogram for the validation test. In the validation test, first of all, the factor A has been calculated by taking the ratios of the reconstructed dimuon events to the $e\mu$ events. Then using this factor A, number of dimuon background events has been estimated in MC. Figure 4.16 shows the comparison of the number of $\mu^+\mu^-$ events (red bullets) estimated using data-driven $e\mu$ method in MC with the number of $\mu^+\mu^-$ events predicted by cut-based method(blue-line) in MC. Since the factor A is known exactly bin-by-bin, so we can observe an exact agreement as expected, between the observed $\mu^+\mu^-$ events and estimated $\mu^+\mu^-$ events in MC sample. The results of the validation test are reported in Table 4.10. The second column of this table corresponds to the $\mu^+\mu^-$ events estimated from the cut-based analysis and the third column shows the $\mu^+\mu^-$ events estimated in MC using $e\mu$ method. As can be observed, the

entries in both the columns are exactly same. Therefore this method has been completely validated using the Monte-Carlo (MC) samples and can be used for the estimation of $\mu^+\mu^-$ background events in experimental data.

- **Estimation of $\mu^+\mu^-$ background events in data**

  In order to estimate $\mu^+\mu^-$ background events in experimental data, first step is to compare the shape of $e\mu$ spectrum both in data and MC. Figure 4.17 (left) shows the shape comparison of $e\mu$ spectrum for data and various MC samples. As can be observed from the figure, the MC simulations are describing the data quite well, both in terms of shape and in terms of the number of $e\mu$ events. This distribution of $e\mu$ events in data and MC, corresponds to an integrated luminosity of 36.0 pb^{-1}.

  The 2^{nd} column of Table 4.9 reports the number of $e\mu$ events observed in data and MC. As can be seen from the table, the numbers of $e\mu$ events in data amounts to 197 $\pm$ 14 (stat) and in MC the number is 214 $\pm$ 15 (stat). Both the numbers are in good agreement within the statistical uncertainty. However, there is a difference of 8.0% between data and MC which has been taken as systematic uncertainty on the $e\mu$ method. After the shape comparison of $e\mu$ spectrum in data and MC, the $e\mu$ method to estimate the $\mu^+\mu^-$ background events in data has been applied. The contribution of the genuine $\mu^+\mu^-$ background sources $DY \rightarrow \tau^+\tau^-$, $t\bar{t}$ and WW has been estimated from $e\mu$ data using Equation 4.6. Figure 4.17(right) shows the comparison of $\mu^+\mu^-$ background distribution estimated in data using $e\mu$ method with the background distributions obtained from MC using cut-based method. As can be observed from the figure, the number of $\mu^+\mu^-$ background events estimated in data is in quite-well agreement with the predictions of MC. The number of $\mu^+\mu^-$ background events estimated in data using $e\mu$ method corresponds to 153 $\pm$ 23 (stat) $\pm$ 8 (syst) events which is in good agreement with 163 $\pm$ 13, the number of the $\mu^+\mu^-$ background events predicted by MC using cut-based analysis. Table 4.10 shows the comparison of the number of $\mu^+\mu^-$ background events estimated in data in

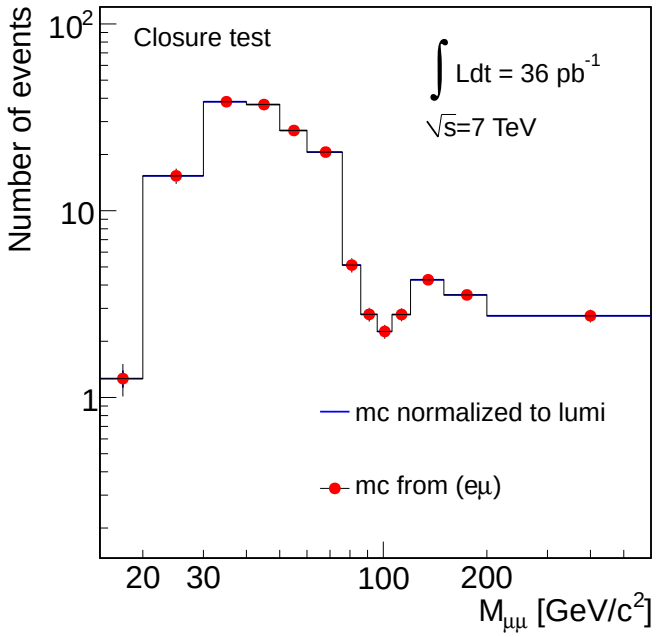

Figure 4.16: Histogram showing the "Validation test" of $e\mu$ method using MC. The line corresponds to the $\mu^+\mu^-$ distribution predicted by MC and the "red" bullets are the $\mu^+\mu^-$ events estimated from $e\mu$ method using MC . As the $e\mu$ events are MC and the detector acceptances are known exactly on a bin-by-bin and mode-by-mode basis, exact agreement is expected between the predicted $\mu^+\mu^-$ distribution and MC.

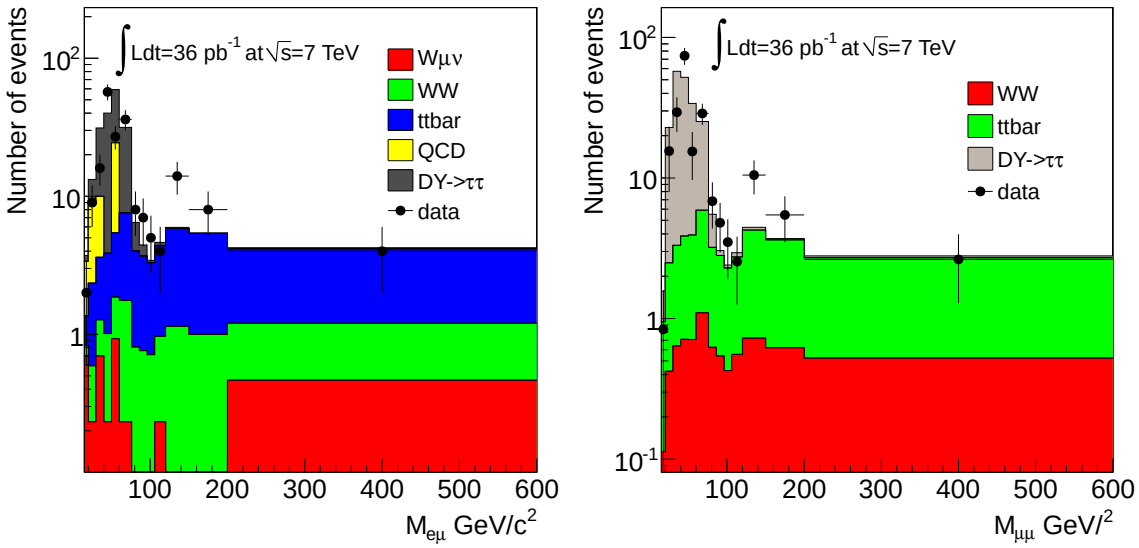

Figure 4.17: (Left) shows the comparison of the $e\mu$ event yield observed in experimental data with the yield of $e\mu$ events predicted in various genuine sources of $\mu^+\mu^-$ backgrounds and (right) shows the $\mu^+\mu^-$ events estimated in experimental data using $e\mu$ data. The background samples $DY \rightarrow \tau\tau$, $t\bar{t}$ and WW are stacked and compared with data. Good agreement is observed between the MC cut based predictions and the $\mu^+\mu^-$ numbers estimated using $e\mu$ in experimental data.

Summary of $e\mu$ and $\mu^+\mu^-$ events		
	$e\mu$ events	$\mu^+\mu^-$ events
Data	197 ± 14	153 ± 23 (from $e\mu$)
MC	214 ± 25	163 ± 13 (prediction in MC)

Table 4.9: Total $e\mu$ and $\mu^+\mu^-$ events observed in data and predictions in MC.

each invariant mass bin using $e\mu$ method with the predictions of MC. The numbers in the second column are the MC prediction for $\mu^+\mu^-$ background events using cut-based method and the numbers in the fourth column corresponds to $\mu^+\mu^-$ background events estimated in data using $e\mu$ method. The numbers in both the columns are in good agreement within statistical uncertainty. The numbers in the third column are the results of Validation test. Thus the results of data driven $e\mu$ method are matching quite-well with the predictions of cut-based analysis. However, for our final cross-section measurements the numbers estimated using the cut-based analysis method have been used.

4.7 Detector Acceptance and FSR correction

The reconstructed dilepton invariant mass distributions cannot be directly compared to the spectra provided by the theoretical models. It is not only because of the limited detector acceptance coverage of the detector, but also because the observed spectra are affected by the Final State Radiation (FSR), a process usually not included in the Monte-Carlo (MC) calculations. We define "post-FSR" and "pre-FSR" to be attached to any quantity referred to before and after the FSR effects (eventually) occur. Therefore, the measurement of $d\sigma/dM$ requires a two-step correction procedure. First, the measured, post-FSR spectra are corrected for the detector acceptance efficiency. Then, as a second step, the detector acceptance corrected spectra are themselves altered by a bin-by-bin FSR correction factor which relates the yields before and after the FSR has taken place. Then this corrected spectra can be compared

Bin-by-Bin estimation of $\mu^+\mu^-$ background events using $e\mu$ method			
mass bin GeV/c^2	MC total bkd prediction (Cut-based analysis)	MC $\mu^+\mu^-$ bkd (Validation test)	$\mu^+\mu^-$ bkd events in data (estimated from $e\mu$)
15-20	1.3±1.1	1.2±1.2	0.7±1.3
20-30	15.4±4.0	15.4±4.2	10.4±8.4
30-40	38.3±6.3	38.3±6.5	19.6±10.1
40-50	37.0±6.2	37.0±6.3	52.7±17.1
50-60	26.9±5.3	26.9±5.3	12.2±6.8
60-76	20.6±4.6	20.6±4.7	23.5±9.7
76-86	5.1±2.3	5.1±2.3	6.3±5.4
86-96	2.8±1.7	2.8±1.7	4.4±4.4
96-106	2.3±1.5	2.3±1.5	3.3±3.8
106-120	2.8±1.7	2.8±1.7	2.4±2.9
120-150	4.3±2.1	4.3±2.1	10.0±7.8
150-200	3.5±1.9	3.5±1.9	5.2±4.8
200-600	2.7±1.7	2.7±1.7	2.6±3.1

Table 4.10: Bin-by-Bin estimation of $\mu^+\mu^-$ events in MC and data (from $e\mu$) method.

with the theoretical calculations.

4.7.1 Detector Acceptance

Due to the geometry of the detector, not all the particles coming from the interaction point can be registered in the detector. In this study, the geometrical and the kinematic detector acceptance 'A', has been defined by using the muons from which the Final State Radiation (FSR) process has been taken place. Detector acceptance has been defined as the ratio of the events having two muons passing the DY kinematic p_T and η cuts to the total number of DY events generated. The Acceptance is calculated using the following equation:

$$A = \frac{N^A}{N^{GEN}} \tag{4.8}$$

where N^{GEN} is the total number of DY events generated and N^A are the events inside the geometrical and kinematic acceptance in a given invariant mass bin. The acceptance as a function of the invariant mass is shown in Figure 4.18. The acceptance

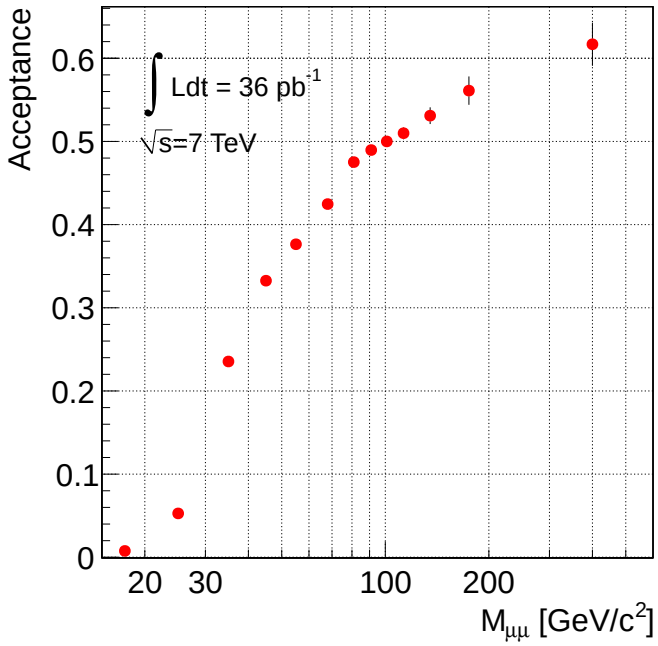

Figure 4.18: Detector acceptance of $DY \rightarrow \mu^+\mu^-$candidates as a function of the post-FSR generator level invariant mass of the DY system.

could also be defined by using the muons with pre-FSR quantities, but it would not resolve the FSR dependence on it. By defining the acceptance using pre-FSR muons, one would also need to introduce additional systematics uncertainty. Thus the acceptance has been defined using the post-FSR muons. The accuracy of the acceptance calculations depends on the quality of the MC generation and simulation. In particular it is sensitive to FSR modeling. It is also sensitive to the potential deviations of MC from experimental data in various kinematic distributions, which are partially governed by uncertainties in theoretical models and PDFs of the partons in the proton. It is important that the MC reproduces well the relevant distributions in data for muons and FSR photons or an appropriate correction in acceptance need to be introduced to reproduce the data.

4.7.2 FSR correction

Final state radiation (FSR) changes the observed invariant dimuon mass, computed from the 4-momenta of the two muons. If the final state (FSR) photons with sizable energy are emitted, the observed mass can be substantially lower than the "physical" mass of the propagator in the hard interaction. At masses above the Z-mass peak, this tends to shift towards lower masses, though with a relatively small number of events. Thus reducing the observed number of events for a given bin. Below the Z-mass peak, the effect is dramatic: as the Z peak cross-section is orders of magnitude higher. Thus even a modest amount of radiation can heavily contaminate the region below the Z peak, resulting in an enhanced number of observed events. The bin-by-bin factors to correct from the "post-FSR" to the "pre-FSR" spectrum, has been calculated by taking the ratio of "post-FSR" invariant mass with the "pre-FSR" mass using POWHEG MC sample.

$$FSR - correction = \frac{N^{GEN}_{post-FSR}}{N^{GEN}_{pre-FSR}} \tag{4.9}$$

Figure 4.19 shows the effect of FSR on the invariant mass of dimuon system in the full phase space *i.e.* no acceptance cuts are applied. As can be seen, the effects are especially pronounced below the Z peak. After applying the FSR correction, the

Detector acceptance and FSR correction factors.		
Invariant Mass bin (GeV/c^2)	Detector acceptance (%)	FSR correction in acceptance (%)
15-20	0.77±0.01	97.1±0.02
20-30	5.3±0.03	98.2±0.03
30-40	23.6±0.13	98.8±0.13
40-50	33.9±0.25	105.9±0.26
50-60	39.4±0.37	125.6±0.39
60-76	44.8±0.32	173.3±0.39
76-86	48.0±0.25	168.8±0.32
86-96	49.0±0.09	91.6±0.08
96-106	50.0±0.37	88.1±0.36
106-120	51.0±0.77	91.5±0.73
120-150	53.0±1.03	93.3±1.00
150-200	55.5±1.73	94.8±1.71
200-600	59.5±2.58	93.1±2.59

Table 4.11: Drell-Yan acceptance for "post-FSR" muons per invariant mass bin and the FSR correction factor calculated bin-by-bin after the acceptance cuts.

invariant mass of the dimuon system is in perfect agreement with the propagator mass. This transition to pre-FSR quantities (generator level Z/γ^* mass) is also important as some available theoretical tools do not include FSR. This transition is done by relying on the MC information. Thus the correction of the $d\sigma/dM$ to the pre-FSR level is an important step to compare the experimental measurements with the theory. Table 4.11 reports the acceptance and FSR correction factor calculated bin-by-bin, which are further used to correct the experimental results.

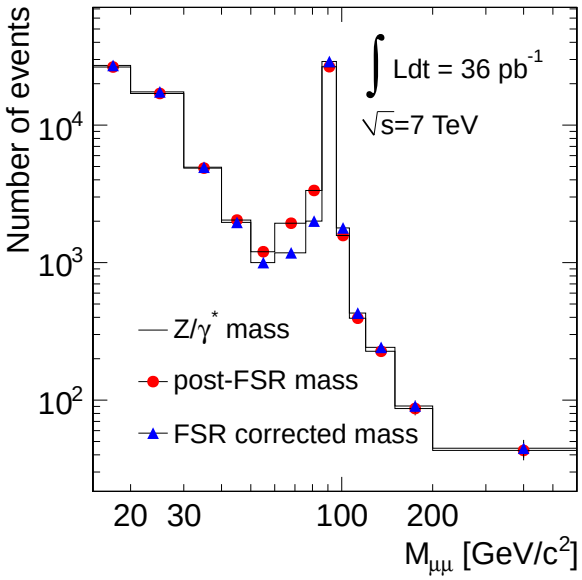

Figure 4.19: Effects of FSR on the Drell-Yan mass spectrum, computed with POWHEG MC in full phase-space for the dimuon channel.

4.8 Experimental Results

4.8.1 Unfolding of Experimental Distributions

The experimental distributions are often distorted or migrated to adjacent bins due to Final State Radiation, the detector resolutions, systematic biases and detection efficiencies. Our goal is to measure the Drell-Yan (DY) differential cross-section and

compare it with the Standard Model (SM) theoretical expectations. With such distortions or migrations, the measurement of the differential cross-section distribution can be affected and it is difficult to compare the experimental results with the theory as well as with the other experiments.

Thus for a better comparison with theory, using the invariant mass resolution found in MC, we have unfolded dimuon invariant mass distribution measured in experimental data to remove the above mentioned effects. However using this unfolding, we correct only the detector resolution and selection efficiencies. The unfolded distribution is then corrected for the acceptance and the FSR effect by using the numbers given in Table 4.11. The response matrix for the unfolding is produced with the post-FSR muons after passing the acceptance cuts, which is described in the next Section. For unfolding technique, the RooUnfold software package [82] has been used.

4.8.2 Response Matrix

The detector effects on experimental measurements are parametrized by using a response matrix that maps the (binned) true distribution onto the measured one. For 1-dimensional true and measured distribution bins T_j and M_i, the response matrix element R_{ij} gives the fraction of the events from bin T_j that end up measured in bin M_i. The response matrix is usually determined using Monte Carlo simulation. The unfolding procedure is able to reconstruct the true T_j distribution from the measured M_i distribution, taking into account the measurement uncertainties due to statistical fluctuations in the finite measured sample. The "True" invariant mass spectrum T_j is related to the observed one M_i (in the limit of no background) by the relation:

$$M_{obs,i} = \sum R_{ij} T_{true,j} \tag{4.10}$$

The original invariant mass spectrum is obtained by inverting the response matrix as:

$$N_U \equiv T_{true,j} = \sum (R_{ij})^{-1} M_{obs,i} \tag{4.11}$$

RooUnfold package provides several algorithms for solving this problem. We have used the "Bayesian" method of the RooUnfold package to unfold the experimental

results. "Bayesian" method of RooUnfold works for 2-D and 3-D distributions as well, it is able to take into account the bin migration and can be used for the unfolding of the distributions which have different binning.

In this analysis, the response matrix is calculated using the simulated sample of DY events, defining the "true mass" as the "generator level" dimuon invariant mass by using the muons passing the acceptance cuts and after FSR has taken place. The reconstructed events passing the full DY selection in the sample is used to calculate the response matrix. The loss of events caused by reconstruction and selection inefficiencies is factored out from the unfolding procedure and the unfolded results are then corrected for the acceptance factors as a subsequent step. Then an FSR correction factor has also been applied on the corrected cross-section to take into account FSR effect.

Figure 4.20 shows the correlation plot between the generator level and reconstructed dimuon mass. As can be observed from the figure, the response matrix is close to diagonal. The few significant off-diagonal elements present are found immediately next to the diagonal elements. Thus there is very small dispersion or, equivalently, a very small migration in $M_{\mu\mu}$ as one moves from generator level to the reconstruction level.

- **Validation test of Unfolding Method**

  The unfolding technique using RooUnfold package has been first tested using MC sample only. First the response matrix is calculated using the "generator" level or "truth" invariant mass and "reconstructed" mass from MC sample. Then the reconstructed invariant mass distribution of the simulated sample is unfolded using the Equation 4.11. Figure 4.21 (left) shows the comparison of the unfolded, truth and measured mass distributions in the validation test and (right) gives a qualitative estimate of the deviation of the unfolded mass from the truth mass. As is clear from the figure, the unfolded distribution reproduces the truth mass very well, so this method is fully validated to unfold the measured invariant mass distribution in experimental data.

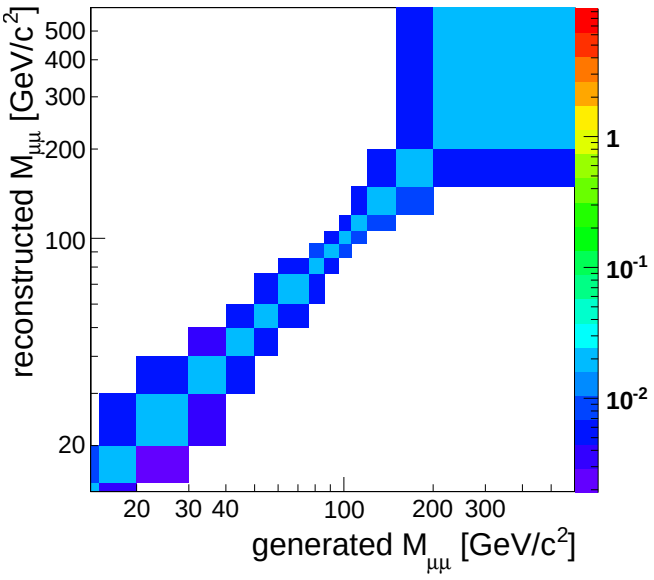

Figure 4.20: The response matrix computed with POWHEG MC within the detector acceptance. The distribution is normalized column-wise.

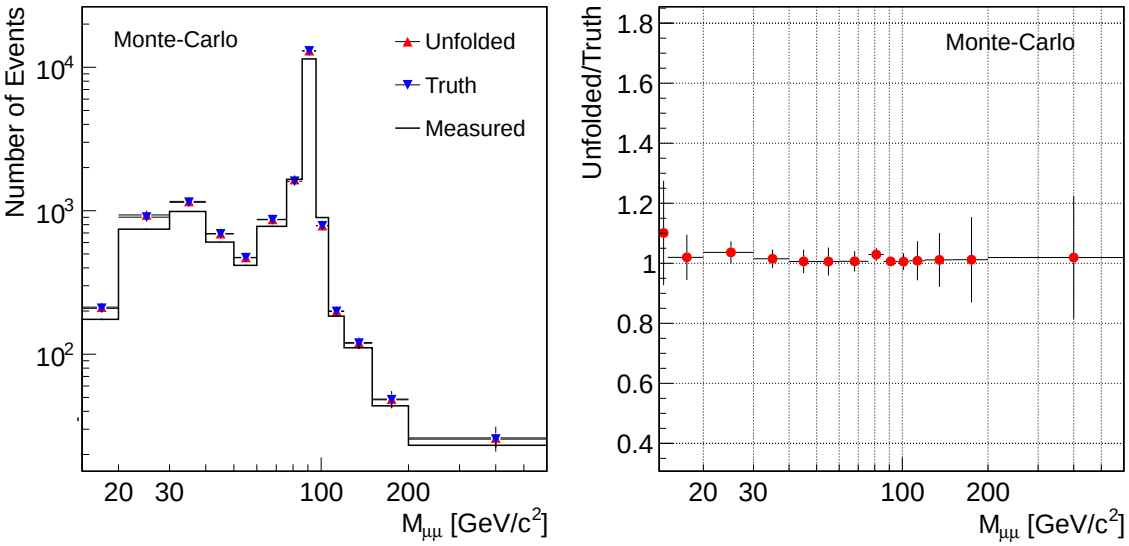

Figure 4.21: (Left) plot shows the comparison of the "unfolded", "truth" and "measured" mass distribution from MC and (right) shows the qualitative estimate of the deviation of the "unfolded" distribution from the "truth" mass.

- **Unfolding of Mass-distribution**

  After the validation of the unfolding procedure with MC sample, the background corrected *i.e.* (N_{obs}-N_{bkd}) yield in data for the detector effects has been unfolded. For the unfolding of experimental distribution, the measured mass distribution is first corrected for the backgrounds and then the resulting distribution is unfolded using the response matrix, calculated using the MC. Figure 4.22 shows the comparison of "unfolded", "measured" distributions in experimental data with the "truth" mass obtained from MC. As can be observed from the figure, the unfolded data distribution is in good agreement with the "truth" mass. Table 4.12 reports the observed and unfolded yield obtained from experimental data in each dimuon invariant mass bin. Then using this background corrected and unfolded yield in data, the DY cross-section in each invariant mass bin has been calculated using the formula:

$$\sigma = \frac{N_U}{\mathcal{L}} \tag{4.12}$$

  Figure 4.23 shows the comparison of "unfolded", "measured" cross-section in data with the "truth" cross-section obtained from MC.

The correction with the selection efficiencies ϵ, is already taken care by the unfolding procedure. Thus in the next step, the cross-section is corrected bin-by-bin in each invariant mass bin for the Acceptance and FSR correction factors using the numbers reported in Table 4.11. The corrected cross-section is given as:

$$\sigma_{corr} = \frac{\sigma}{A * FSR} \tag{4.13}$$

Figure 4.24 shows the comparison of "unfolded" experimental data and the "truth" distributions of the detector acceptance and FSR corrected cross-section (σ_{corr}). Table 4.13 reports the bin-by-bin measured, unfolded cross-section from data and truth cross-section from MC . As can be observed from the Figure and Table, there is a large discrepancy between the unfolded data results and truth distribution in the lowest invariant mass bin. This can be explained as follows: In this study, for the signal DY

Observed and Unfolded yield in data		
Invariant Mass bin (GeV/c^2)	N_{obs}	N_U
15-20	257±16	298±17
20-30	820±27	892±30
30-40	1010±32	1070±33
40-50	668±26	693±26
50-60	445±21	453±21
60-76	766±28	830±29
76-86	1621±40	1613±40
86-96	11100±105	12664±112
96-106	779±28	652±26
106-120	172±13	182±13
120-150	144±12	155±12
150-200	51±7	52±7
200-600	30±5	31±6

Table 4.12: Number of the observed and unfolded dimuon events in data. The unfolded yield is obtained after subtracting the background contribution in data.

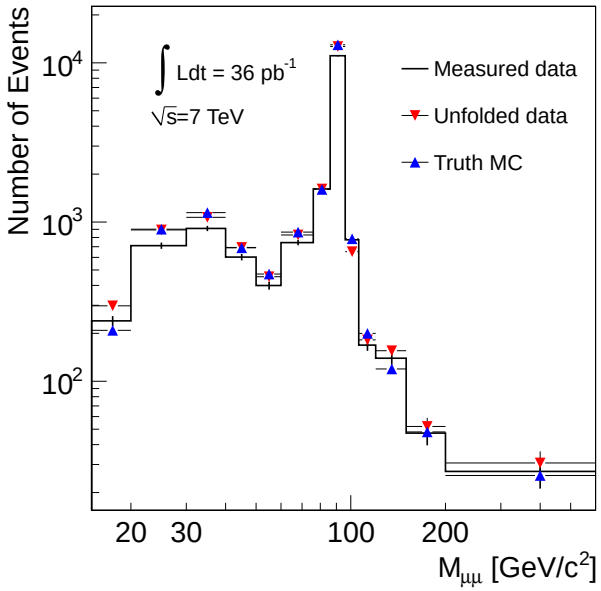

Figure 4.22: Comparison of dimuon yield for the "unfolded", "measured" distributions from data with the "truth" distribution. The "Truth" distribution has been obtained from MC.

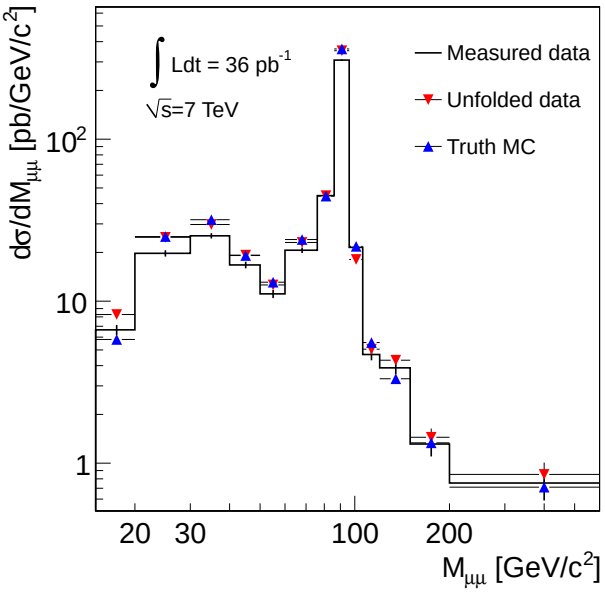

Figure 4.23: Comparison of the "unfolded", "measured" cross-section in data with the "truth" cross-section obtained from MC. The cross-section reported here is not corrected for the detector acceptance and Final State Radiation correction factors.

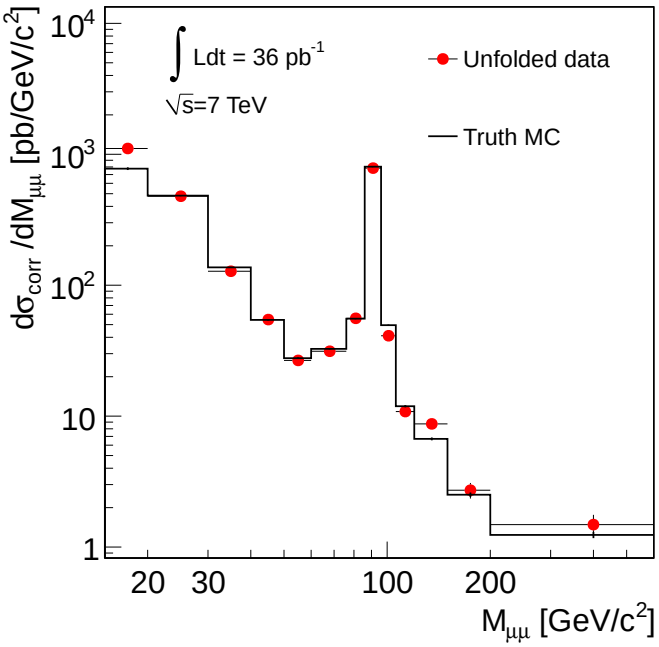

Figure 4.24: Comparison of the "unfolded" cross-section with the "truth" cross-section in each invariant-mass bin. The cross-section reported here is corrected for the acceptance and the Final State Radiation correction factors. The unfolded distribution is matching well with the truth distribution.

process, the POWHEG MC sample has been used. The POWHEG simulation combines the next-to-leading order (NLO) calculations with a parton showering which is not enough to properly describe the low invariant mass region of the dimuon mass spectra. The two high p_T leptons required in the analysis must form a small angle at low mass and therefore the dilepton system gets significantly boosted, something to be compensated by hard radiation in the transverse plane. This means that these low-mass events are of the type "γ^* + hard jet" at first order and therefore the next-to-next leading order correction (NNLO) becomes essential for a reliable estimate of the detector acceptance corrections.

4.8.3 Systematic Uncertainties

Systematic uncertainties have been evaluated for each step in the determination of the dimuon invariant mass spectrum. The acceptance-related uncertainties are a special case as they only apply to the acceptance corrected results, *i.e.* results in the full phase space and are approximately the same for the dimuon and dielectron channels (the FSR uncertainties are treated separately). The acceptance uncertainty resulting from the knowledge of the PDFs is estimated using Pythia with CTEQ6.1 PDF set by a reweighting technique [83], with a negligible statistical uncertainty given the very large simulated sample. Since we are making a shape measurement, normalized the Drell-Yan (DY) cross-section to the dimuon cross-section in the Z-mass peak region, the analysis only depends on the uncertainty of the ratio of acceptances, A_i/A_{norm}, where A_i is the acceptance for the invariant mass bin i and A_{norm} is the acceptance for the invariant mass of the Z-mass peak region. The dominant systematic uncertainty on the cross-section measurement in the dimuon channel is the uncertainty on the background estimation, which is, however, relatively small, given the low background levels. This uncertainty is evaluated from data using two independent background subtraction methods. The next most important uncertainties are related to the muon efficiency and to the muon momentum scale and resolution. The former is determined using the large sample of Z events decaying to dimuons. Uncertainties in the latter are mostly caused by residual mis-alignments between the muon chambers and the silicon

Invariant Mass in (GeV/c^2)	Cross section (pb)		
	Measured (data)	Unfolded (data)	Truth (MC)
15-20	6.7±0.1	1107.2±72.2	776.0±18.5
20-30	19.7±0.7	478.1±17.4	483.3±4.0
30-40	25.3±0.8	127.8±4.1	136.8±1.0
40-50	16.7±0.7	54.6±2.1	54.3±0.5
50-60	11.1±0.6	26.6±1.3	27.7±0.3
60-76	20.6±0.8	31.3±1.1	32.6±0.3
76-86	44.8±1.1	55.9±1.2	55.5±0.4
86-96	308.0±3.0	784.0±5.0	804.0±2.0
96-106	21.5±0.8	41.1±1.2	50.0±0.5
106-120	4.7±0.4	10.8±0.7	12.0±0.2
120-150	3.9±0.3	8.7±0.7	6.7±0.2
150-200	1.3±0.2	2.7±0.4	2.5±0.1
200-600	0.8±0.1	1.5±0.3	1.2±0.1

Table 4.13: Bin-by-Bin comparison of the unfolded and (acceptance*FSR) corrected cross-section (σ_{corr}) from the experimental data with the "truth" cross-section. The "truth" cross-section is obtained from the POWHEG MC sample having CT10 PDF set. The "measured" experimental cross-section *i.e.*, the cross-section before the unfolding procedure is also shown.

Summary of Systematic Uncertainties in (%)							
Mass-bin (GeV/c^2)	Efficiency correction	Background	Unfolding	FSR	Other sources	Total	Detector acceptance
15-20	1.1	3.6	0.4	1.5	1.0	4.2	$^{+2.2}_{-3.0}$
20-30	1.1	3.1	0.2	1.1	1.0	3.6	$^{+1.9}_{-3.2}$
30-40	1.2	1.9	0.1	0.7	1.0	2.6	$^{+1.7}_{-3.0}$
40-50	1.2	1.7	0.2	0.7	1.0	2.4	$^{+1.7}_{-2.9}$
50-60	0.8	2.1	0.2	0.5	0.5	2.4	$^{+1.7}_{-2.8}$
60-76	0.6	1.0	0.2	1.4	0.5	1.9	$^{+1.6}_{-2.6}$
76-86	0.4	0.2	1.7	2.0	0.5	2.7	$^{+1.5}_{-2.5}$
86-96	0.3	0.05	0.2	0.5	0.5	0.8	$^{+1.5}_{-2.4}$
96-106	0.3	0.4	3.8	0.5	0.5	3.9	$^{+1.5}_{-2.4}$
106-120	0.3	1.4	0.7	0.5	3.0	3.4	$^{+1.5}_{-2.3}$
120-150	1.1	2.0	0.4	0.5	1.0	2.6	$^{+1.5}_{-2.1}$
150-200	2.1	6.0	0.9	0.5	1.0	6.5	$^{+1.4}_{-1.8}$
200-600	2.1	10.0	0.1	0.5	1.0	10.3	$^{+1.2}_{-1.4}$

Table 4.14: Summary of systematic uncertainties in the muon channel (in %). The "Total" is a quadratic sum of all sources without "Detector acceptance". With the exception of "Detector acceptance", the numbers correspond to the individual measurements per bin and not the ratio to the Z peak region.

tracker, potentially not reproduced in the simulation. The momentum resolution and the momentum scale uncertainties are included in the unfolding procedure, hence the resulting shape is affected by these systematic effects. The level of the momentum scale uncertainty has been evaluated introducing a bias in the MC reconstruction and unfolding the resulting dimuon mass distribution with the unfolding matrix determined from the nominal (unbiased) MC sample. The bias is on the reconstructed invariant mass and is based on the maximal difference between MC and the data Z peak positions as obtained with variations in the p_T and η requirements.

Next source of uncertainty arise due to the FSR effect. Studies of photons [84] reconstructed near a muon track in a DY event indicate that the FSR simulation is remarkably accurate. A corresponding systematic uncertainty is evaluated by examining how the results changes by modifying the fraction of FSR events and the energy and angle distributions of the radiated photon within proper statistical variations.

Other systematic effects that could affect the dimuon yield in the experiment data have been considered, such as the impact of additional soft pp collisions that happen in coincidence with the studied interaction and the effects of the dimuon vertex probability requirement and of residual data-simulation discrepancies. A combined uncertainty is reported for these "other" sources in Table 4.14, where all systematic uncertainties in the dimuon channel are listed.

4.9 Results and Discussions

The Drell-Yan (DY) cross-section (σ_i) per invariant mass bin i, is calculated according to Equation 4.1. In order to provide a measurement independent of the luminosity uncertainty and to reduce any other systematic uncertainties, σ_i the cross-section in each invariant mass bin, is normalized to the cross-section of the Z-mass peak region. It is defined as the DY cross-section in the invariant mass region $60 < M_{\mu\mu} < 120$ GeV/c^2. The cross-section of the Z-mass peak region measured in this analysis is 923 $\pm$ 5 (stat) $\pm$ 6 (syst) $\pm$4% (lumi) pb, is consistent with the CMS measurement of the Z-mass peak cross-section [79] which is 974 $\pm$0.7 (stat) $\pm$0.7 (syst) $\pm$ 4% (lumi)

pb. Thus the final result of this analysis is presented in the form of the ratio of two cross-sections, the R-factor which is described as follows:

$$R^{i}_{post-FSR} = \frac{N^{i}_{U}}{A_i * FSR_i} / \frac{N^{norm}_{U}}{A_{norm} * FSR_{norm}} \tag{4.14}$$

where N^{i}_{U} is the number of events after the unfolding procedure, while the acceptances A_i and FSR_i have been defined earlier; N^{norm}_{U}, A_{norm} and FSR_{norm} refer to the quantities in the Z peak region. Table 4.15 shows the bin-by-bin comparison of

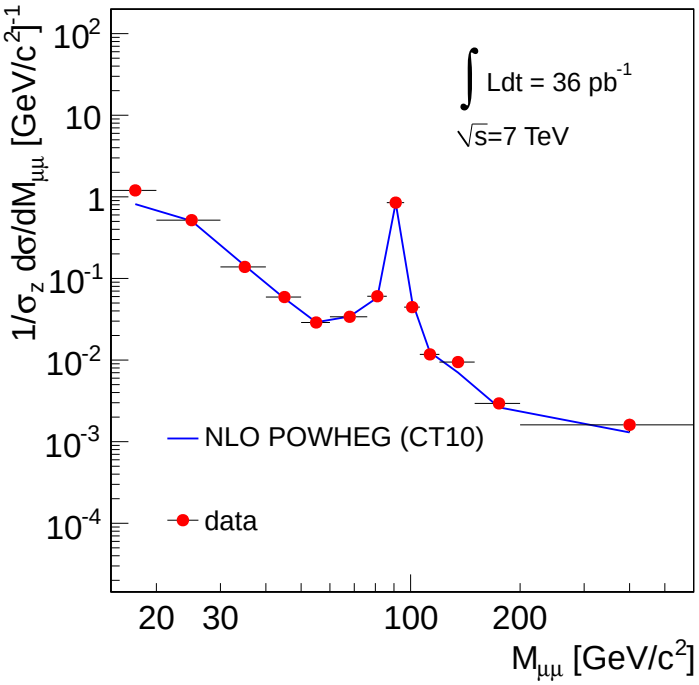

Figure 4.25: Shape of the Drell-Yan mass spectrum normalized to Z-peak compared with theory predictions at NLO with CT10 PDF set.

the R-factor calculated from the experimental results with the theory predictions. Theory predictions are obtained from the POWHEG MC sample having CT10 PDF set. The R-shape measurements between theory and experimental results are in good agreement within the statistical errors in all the mass-bins, except in the lowest mass bin. Figure 6.1 shows the shape comparison of the experimental results with the theoretical predictions. As can be observed from the figure, the experimental measurements are very well reproduced by the next-to-leading theoretical predictions.

Invariant Mass bin (GeV/c^2)	R-shape (data)	R-shape (theory)
15-20	1.199±0.0785	0.814±0.0194
20-30	0.518±0.0191	0.507±0.0043
30-40	0.138±0.0044	0.144±0.0011
40-50	0.059±0.0023	0.057±0.0006
50-60	0.029±0.0013	0.029±0.0004
60-76	0.034±0.0012	0.034±0.0003
76-86	0.061±0.0014	0.058±0.0004
86-96	0.849±0.0073	0.843±0.0027
96-106	0.045±0.0013	0.052±0.0005
106-120	0.012±0.0008	0.012±0.0002
120-150	0.009±0.0007	0.007±0.0002
150-200	0.003±0.0004	0.003±0.0001
200-600	0.002±0.0003	0.001±7.14e-05

Table 4.15: Result of the Drell-Yan spectrum normalized to Z-peak presented bin-by-bin. The errors mentioned here are only statistical.

In this chapter, we report the analysis for the measurement of differential cross-section of DY production with muonic final state. This measurement is based on the event sample of pp collisions at $\sqrt{s}$ = 7 TeV collected with the CMS experiment, corresponding to an integrated luminosity of 36.0±1.4 pb^{-1}. Event selection criteria have been optimized for the selection of good statistics of DY events with low contribution from background processes. Selection efficiencies are measured using data driven method (Tag and Probe) and found to be in good agreement with MC predictions. Data driven method for the estimation of background contribution is also reported which gives results consistent with estimation using MC samples. The measured cross-section is corrected for the detector effects, selection efficiencies, the detector acceptance and effect of Final State Radiation. The measured cross-section, over the wide range of invariant mass ($15 < M(\mu\mu) < 600$ GeV/c^2), is normalized to the cross-section in Z-resonance region and compared with the theory predictions. The measured cross-section from data shows good agreement with the next-to-leading order theoretical predictions.

5

Underlying Event Study using Drell-Yan

5.1 Introduction

For the Underlying Event (UE) measurement at hadron-hadron colliders, the topological structure of the hard scattering process can be used to define phase space that is sensitive to the UE components of the proton-proton interactions. The Drell-Yan (DY) process ($q\bar{q} \rightarrow Z/\gamma^* \rightarrow \mu^+\mu^-$), where a clean separation of the hard interaction from the soft QCD component is possible, provides an excellent place to study the UE. It is one of the experimentally clean and theoretically well-understood processes at the LHC with moderate event rate. The absence of QCD Final State Radiation (FSR) and low probability of photon bremsstrahlung from the muons can be exploited to study different kinematic regions with varying Z boson recoil, due to harder or softer Initial State Radiation (ISR).

The UE measurement using the DY process is complementary to the leading track jet topology [52] measurements performed at CMS at 7 TeV. In the case of leading track jet topology, energy scale (defined by transverse momentum of leading jet) can be explored from very low $\sim$ 1 GeV/c) to high value 100 GeV/c. However, in the case of DY topology, energy scale (defined by invariant mass of muon pair) can not be explored to same lower value due to large contamination from the background processes. In this measurement with DY process, dependence of the UE activity on

the invariant mass ($M_{\mu\mu} = \sqrt{((E_1^\mu + E_2^\mu)^2 - (\vec{p}_1^{\,\mu} + \vec{p}_2^{\,\mu})^2)}$) and resultant transverse momentum ($p_T^{\mu\mu} = |\vec{p}_{T,1}^{\,\mu} + \vec{p}_{T,2}^{\,\mu}|$) of the muon pair has been be studied.

DY events with dimuon invariant mass around the Z-resonance mass, 60 GeV/c^2 $< M_{\mu\mu} <$ 120 GeV/c^2, are least contaminated from the background processes and hence, most suited for the measurement of the UE activity. In the leading jet based measurements, the lowest energy scale of the event is set by the transverse momentum of the leading track jet and the UE activity from MultiParton Interactions (MPI) is observed to saturate for energy scales higher than 10 GeV/c. In the present analysis, instead, the lowest scale is set by $M_{\mu\mu}$ (60 GeV/c^2), well inside the region where the MPI contribution is expected to be saturated. Thus the study of UE activity as a function of $p_T^{\mu\mu}$, gives the important measure of the contribution from radiation. In this analysis it is also possible to minimize the radiation contribution by applying an upper cut on the $p_T^{\mu\mu}$ and study the dependence on the energy scale (invariant mass of muon pair). Thus the DY process for the UE measurements provides the handle to separate the radiations from MPI.

The present analysis aims to provide the measurement for the testing and tuning of the QCD models for the description of the UE in the proton-proton collisions. This analysis is based on the experimental data collected at CMS experiment at the LHC during the year 2010, which corresponds to an 36 pb^{-1} of integrated luminosity.

5.2 Methodology

The Underlying Event (UE) activity in the present analysis, is measured with reference to the resultant direction of the dimuon system, whereby three distinct topological regions are defined in the plane transverse to the beam direction, as shown in Figure 5.1. All the charged particles,excluding the pair of muons coming from Z/γ^*, with transverse momentum (p_T) above 0.5 GeV in the central region of the detector ($\eta < 2.0$) are considered for calculating the UE observables. The charged particles are categorized according to the azimuthal distance $\Delta\phi$ between the resultant direction of the dimuon system and that of the charged particles, as depicted in Figure 5.1.

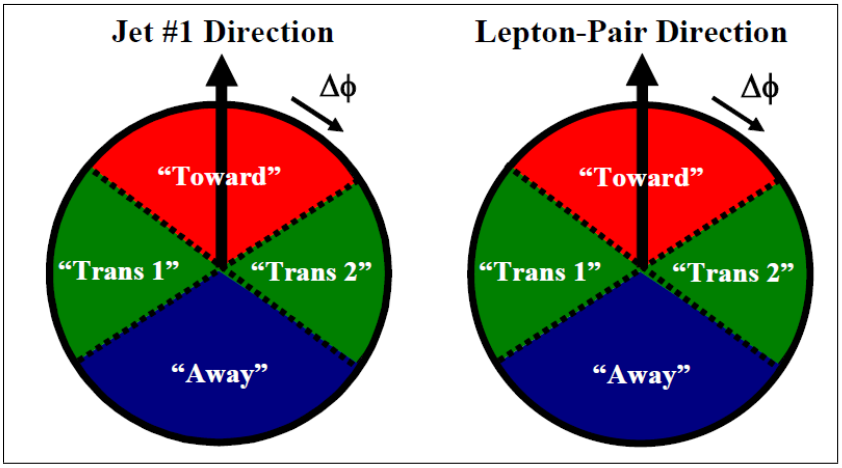

Figure 5.1: Illustration of correlations in azimuthal angle $\Delta\phi$ relative to: (left) the direction of the leading jet (highest p_T jet) in the event, in high-p_T jet production and (right) the direction of the lepton-pair in Drell-Yan (DY) production. The angle $\Delta\phi = \phi - \phi_{jet}(\Delta\phi = \phi - \phi_{pair})$ is the relative azimuthal angle between charged particles and the direction of jet (lepton-pair).

- Towards region, $|\Delta\phi| < 60^o$
- Transverse region, $60^o < |\Delta\phi| < 120^o$
- Away region, $|\Delta\phi| > 120^o$

The particle production in the *away* ($|\Delta\phi| > 120^o$) region is expected to be dominated by the component of the hard parton-parton interaction which balances the dimuon system. The *transverse* region ($60^o < |\Delta\phi| < 120^o$) get small spill-over contribution from the recoiling activity in *away* side whereas the *towards* region ($|\Delta\phi| < 60^o$) gets the least contamination from the hard interaction. As the required information about the hard and soft processes are extracted with good precision from the tracking and the muon systems of the detector, hence the derived observables are least affected by the uncertainties of the calorimetric measurements. The strength of the UE activity is measured in terms of the average charged particle multiplicity ($1/\mathrm{N}_{ev}$ $\Delta^2 N_{ch}/\Delta\eta\ \Delta(\Delta\phi)$) and the average scalar sum of p_T of the charged particles ($1/\mathrm{N}_{ev}$ $\Delta^2\Sigma p_T/\Delta\eta\ \Delta(\Delta\phi)$), which are expressed as density obtained dividing by the area of

the considered phase ($\eta - \phi$) space *et al.* ($8\pi/3$). The UE activity is studied as a function of kinematic variables such as $p_T^{\mu\mu}$ and $M^{\mu\mu}$. While performing the study of UE measurement as a function of $M^{\mu\mu}$, the $p_T^{\mu\mu}$ is required to be less than 10 GeV/c to reduce the radiation contribution. The UE variables are corrected for the detector effects using the various QCD models implemented in Monte Carlo (MC) simulations. The predictions for soft inelastic events are provided here by several tunes e.g DW, Z2, Z1 and D6T of the PYTHIA-6 event generator, version 6.420 [42, 44] and tune 4C of the PYTHIA-8 event generator, version 8.145 [45, 46].

5.3 Event Selection

For the UE measurement, it is essential to select events with DY candidate and minimum contribution from background processes. This section reports the various event selections used in this analysis for collection of pure DY events.

5.3.1 Event Trigger selection

Details of High-Level Trigger Paths		
Trigger path	HLT Thresholds	Run range
HLT_Mu9	$p_T > 9$ GeV/c, $\|\eta\| < 2.4$	132440-147116
HLT_Mu11	$p_T > 11$ GeV/c, $\|\eta\| < 2.4$	147196-148058
HLT_Mu15	$p_T > 15$ GeV/c, $\|\eta\| < 2.4$	148882-149294

Table 5.1: Summary of the trigger paths according to the run range applied on experimental data.

During experimental data taking, various triggers has to be pre-scaled with increasing instantaneous luminosity to accommodate with the total bandwidth for event storage. Thus, the events are required to pass through the single muon triggers which requires the event to contain, inclusively, atleast one muon with minimum transverse momentum $p_T > 9$, 11 or 15 GeV/c depending upon the run ranges as mentioned

below. There is no isolation condition required at the trigger level. Events in MC samples are required to satisfy HLT_Mu9 trigger condition.

5.3.2 Event Vertex Selection

Events from good run and good lumi-section are required to have the presence of atleast one reconstructed vertex. The vertices are required to have at least 5 degrees of freedom and being well centered with respect to the z-position of the beam spot. To accommodate the inevitable variations in the position of beam spot on an event-by-event basis within a fill, a window of 18 cm which is equivalent to 3σ of Gaussian fit of the separation between the z-position of vertex and the beam spot, has been applied. Figure 5.2(a) and 5.2(b) show the Gaussian fitted separation of z-position of vertex w.r.t. the beam spot for MC (with pile-up) and experimental data respectively. The transverse position (ρ) of the vertex with respect to the beam line is required to be less than 2 cm. Figure 5.3(a) shows the z-separation of the vertex from the beam spot for experimental data compared with MC (with and without pile-up scenario). From this plot it can be observed that MC simulation reproduces the vertex position quite well. Figure 5.3(b) shows the number of good vertices satisfying these quality criteria for experimental data and both types of MCs. The number of vertices are different in experimental data and MC (with pile-up), because amount of pile-up is different in MC as compared to that in experimental data. The vertex passing all the vertex selection cuts and with the highest scalar sum of the squared transverse momenta of the associated tracks is considered as the *signal vertex*.

5.3.3 Drell-Yan Event Reconstruction

Events passing the trigger and vertex selections are then searched for the Drell-Yan (DY) candidate by requiring to have atleast two muons in an event. The selection criteria for the muons is kept same as used by CMS ElectroWeak group, details of which can be found in ref [85]. Essentially the requirements pertain to good reconstruction, identification and isolation of two muons followed by kinematic cuts,

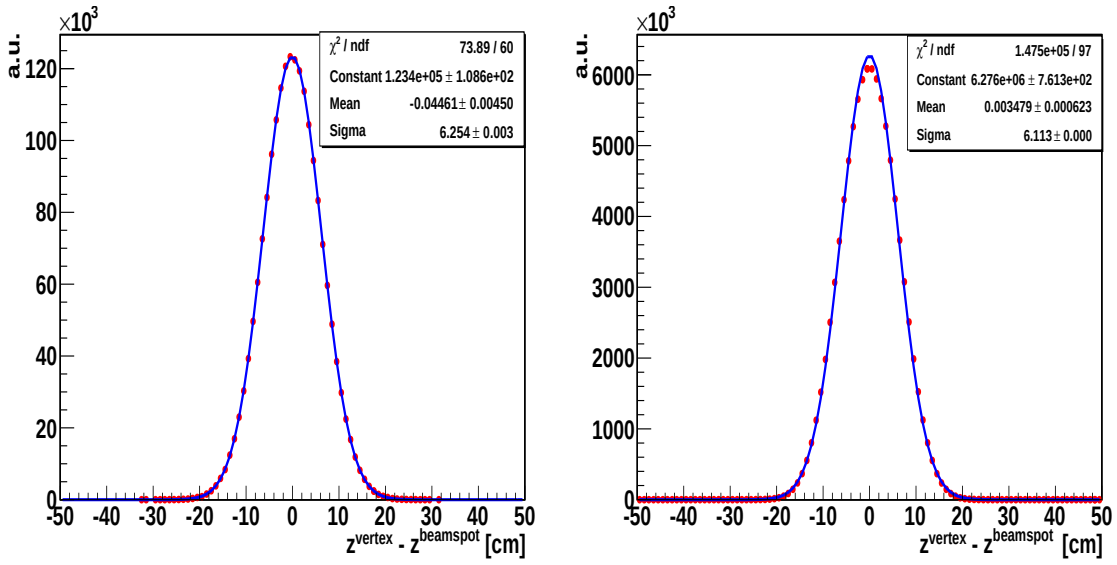

(a) (b)

Figure 5.2: The z separation of the vertex from the beam spot fitted with Gaussian (a) MC and (b) Data.

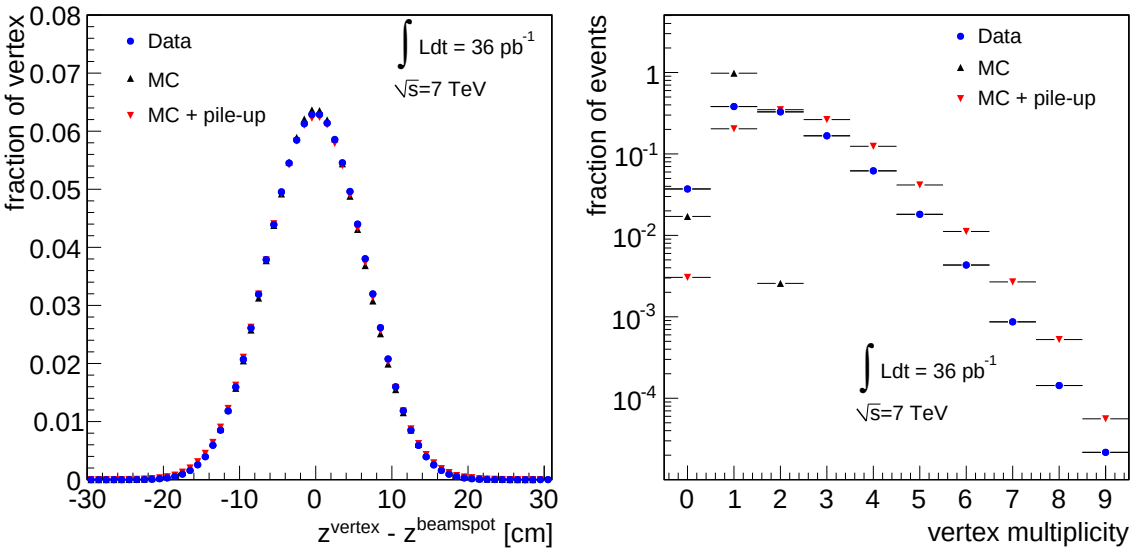

(a) (b)

Figure 5.3: Reconstructed vertex properties: (a) separation of the z-position of the vertex from the beam spot and (b) the number of good vertices reconstructed in an event.

to ensure that they are the constituents of a DY (Z/γ^*) candidate. The selection criteria for the muons, which are devised to reduce the background contamination and to select a pure inclusive DY event sample from experimental data, have been discussed briefly as follows:

Muon Selection

In this analysis, global muons have been used which are reconstructed by matching the muon track found in both the tracker and the muon chambers sub-system of the detector. Muons are further required to pass a set of offline kinematic, muon identification and isolation cuts to suppress the fake and the background muons.

- **Muon Identification cuts**: Muons are required to pass the muon identification cuts and the quality criteria, which are optimized by the "Muon Physics Object Group" of CMS, details can be found in [86] and described briefly as follows:

    1. In order to ensure well-reconstructed tracks, the muon candidates are required to have atleast 11 hits in the tracker subsystem of the detector.
    2. The transverse impact parameter, calculated with respect to the beam spot position, should be less than 2 mm.
    3. A global muon track fit is required to have normalized $\chi^2 < 10$.
    4. The muon track reconstructed within the tracker volume, should have atleast one valid pixel hit.
    5. There should be hits registered in atleast two muon stations by each of the muon tracks. This cut is particularly effective against hadron punch-through and accidental matchings. It is also consistent with the logic of the CMS muon trigger system, which requires at least two stations in order to give a good estimate of the transverse momentum.
    6. The number of valid hits in the muon chambers used in the global muon fit should be atleast 1. This is quite effective in rejecting muons coming from decay-in-flight and hadron punch-through at high transverse momentum.

7. Both the muons are required to be isolated. The isolation variable for a muon is defined as:

$$I = \Sigma(p_T(tracks) + E_T(electromagnetic) + E_T(hadronic))/p_T^{\mu} \quad (5.1)$$

where the sums are defined, excluding the muon track in a cone of radius = $\sqrt{(\Delta\eta)^2 + (\Delta\phi)^2} < 0.3$ around the muon direction, measured in the tracker and calorimetric subsystems of the detector. The muon is considered to be isolated if the variable $I < 0.15$.

- **Kinematic cuts**: The two leading muons satisfying the above identification criteria are then required to have transverse momentum greater than 20 GeV/c each and the first leading muon must have $|\eta| < 2.1$ and second leading muon should be in the detector fiducial volume with $|\eta| < 2.4$.

An event is considered to have DY candidate, if the invariant mass of the two selected good muons with opposite charge, lies in the mass window of 60-120 GeV/c^2. To ensure that the muons originate from the selected *signal vertex*, the transverse and longitudinal impact parameters of the muons, measured with respect to the *signal vertex*, are required to be less than 3 times of their respective uncertainty. Figure 5.4 (left) and (right) show the observed experimental data events and the various backgrounds estimated using simulation in [60-120] GeV/c^2 mass region as a function of $M_{\mu\mu}$ and $p_T^{\mu\mu}$ respectively. It is found that the estimated background contamination is negligible, less than 0.5%, with the above mentioned selection criteria.

5.4 Track Selection for Underlying Event

Only the tracks, which are well reconstructed in the pixel and silicon strip tracker and originates from the *signal vertex* are considered in the UE measurements. The Drell-Yan (DY) muons originating from the *signal vertex* are part of the hard interaction, so these muons are need to be excluded from the tracks considered for the UE measurement. The track is excluded if the both the spacing ΔR and the relative p_T difference $\Delta p_T/p_T$ between the tracks and the muon are less than 0.01. Figure 5.5(a)

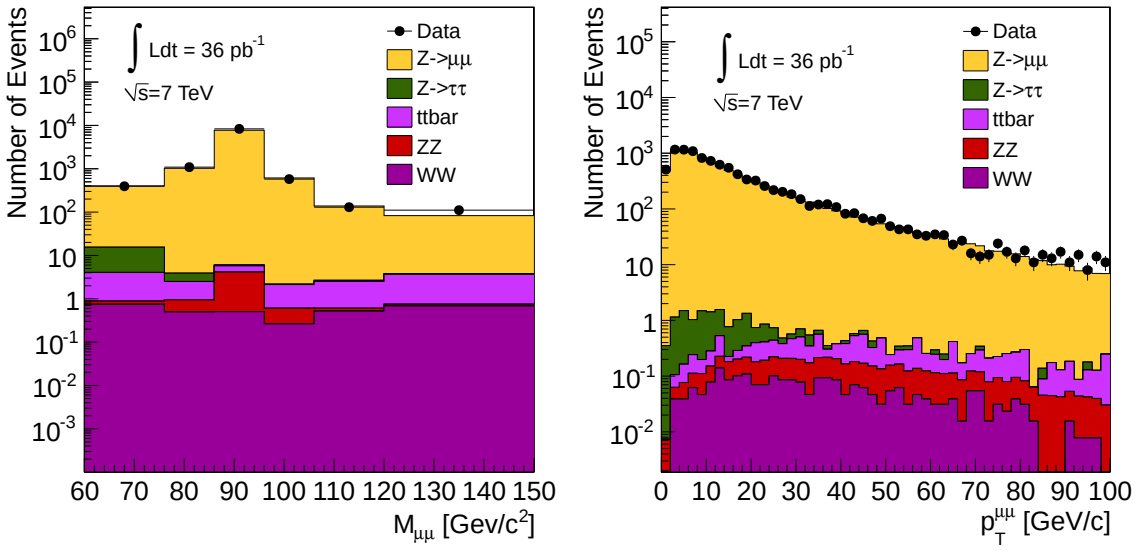

(a) (b)

Figure 5.4: (a) Observed invariant mass and (b) transverse momentum distribution in experimental data in [60-120] GeV/c^2 mass region after all the selection cuts. All the Monte-Carlo samples are stacked and compared with experimental data.

and (b) shows the ΔR and relative p_T difference between track and the selected muon for experimental data and Pythia-6 Z2 tune (with and without pile-up). The tracks are required to have $p_T > 0.5$ GeV/c and pseudorapidity $|\eta| < 2$. To keep low level of the fakes and the poorly reconstructed tracks, a *high purity* reconstruction algorithm, as defined by Tracking Physics Object Group of CMS [87], has been used. To reduce the contamination of the secondary tracks from decays of long-lived particles and photon conversions, the distance of the closest approach between the track and the *signal vertex* in the transverse (d_0) and the longitudinal plane (d_z), is required to be less than 3 times their respective uncertainties. The tracks with poorly measured momenta are removed by requiring $\sigma(p_T)/p_T < 5\%$, where $\sigma(p_T)$ is the uncertainty of the p_T measurement.

This track selection criteria adopted in this analysis has already been optimized in the UE measurements done with leading jet topology [52] at CMS. The distributions $d_0/\sigma(d_0)$ and $\sigma(p_T)/p_T$ are shown in Figure 5.6(a) and (b). These variables are plotted after applying selections on all the variables except itself *i.e.* (N-1) selections.

As can be seen from the distributions, experimental data and MCs shows a nice agreement for both the variables. Figure 5.6(c) shows the comparison of $d_z/\sigma(dz)$ for experimental data and Pythia-6 Z2 tune with and w/o pile-up. There is a large discrepancy between experimental data and MC w/o pile-up in $d_z/\sigma(d_z)$ distribution, experimental data has a long tail as compared to MC w/o pile-up, however the MC with pile-up does reproduces the trend of the $d_z/\sigma(d_z)$ distribution in experimental data quite well. This shows that the long tail in relative d_z distribution of tracks for experimental data is due to the effect of pile-up, which increases with the increase in the instantaneous luminosity.

To understand this discrepancy in detail, we have studied the tracks coming from the vertices other than the signal vertex. After a cut on relative d_0, the tracks coming from the other vertices, are further analyzed on the basis of the z-separation from the corresponding vertex. The tracks are divided into different sets depending on the closest vertex *i.e.* the tracks closest to 1^{st} vertex are classified separately from the tracks closest to the 2^{nd} vertex and so on. Figure 5.7(a) shows the relative d_z of the tracks calculated with respect to the closest vertex. Relative d_z of the tracks coming from different vertices are in good agreement with each other. For MC sample with pile-up, it has been found that 57% of the tracks, after the relative d_0 selection, are closest to the 1^{st} vertex than any other vertex. Remaining 43% of the tracks lie in the tail of relative d_z distribution with respect to the 1^{st} vertex. This fact is clear from the Fig. 5.7(b) which shows the relative d_z with respect to the 1^{st} vertex vs the relative d_z with respect to the 2^{nd} vertex for the tracks which are closest to 2^{nd} vertex.

It is evident that tracks which are closest to 2^{nd} vertex fall in the tail of relative d_z with respect to 1^{st} vertex. Similar distribution for 3^{rd} and 4^{th} vertices are also reported in Figure 5.7(c) and (d) respectively. This makes it clear that the tracks which lie in the tail of $d_z/\sigma(d_z)$ distribution in experimental data are associated with the other vertices rather than the signal vertex. The selection on the, $d_z/\sigma(d_z)$ variable, used in this analysis is very effective in removing the tracks coming from the other vertices and not from the Drell-Yan signal vertex. For example, in Pythia-6 Z2 tune with pile-up after the relative d_z criteria, 99.6% of the selected tracks are closest

to the 1st vertex and only 0.4% of the tracks are from other reconstructed vertices. This contribution can be further reduced by requiring the event to have exactly one vertex, but we can't afford to implement this selection in this analysis, because it will reject about 72% of the signal events. There are other aspects also by which pile-up can affect the UE measurement *i.e.* the vertex merging or splitting, causing inefficiency in vertex reconstruction. In the vertex reconstruction, if the tracks are closer than 2 mm, they are considered to be coming from the same vertex. Thus if the vertex arising from pile-up is closer than 2 mm to the signal vertex, these two will be reconstructed as one. This effect can be decreased by putting more stringent condition (*i.e.* the separation between the tracks while reconstructing vertex less than 2 mm), but that will affect adversely, by increasing the probability of vertex splitting, which eventually, will lead to the under-estimation of the UE activity.

Table 5.2 reports the relative efficiencies of different track selection criteria for experimental data, Pythia-6 Z2 tune with and without (w/o) pile-up events. The track selection efficiency differs for experimental data and MC events w/o pile-up, specially for the requirement on the longitudinal impact parameter, which is attributed to the increase in the pile-up events in experimental data which in turn leads to increase in the number of the background tracks. The track selection efficiencies in experimental data are not in perfect agreement with MC (with pile-up events) because the amount of pile-up overlayed in MC is not the same as in case of experimental data.

The selected tracks can get fake contributions from the secondaries and combinatorial backgrounds. These fake tracks do not have corresponding primary particles generated. So the reconstructed track is classified as *fake* if there is no generator level primary particle within a distance $\Delta R < 0.04$. Figure 5.8 (top left) and (right) shows the fake rate as a function of track η and p_T, respectively after all the track selections. The fake contribution is less than 3% in the region of interest *i.e.* $p_T > 0.5$ GeV/c and $|\eta|$ <2. Figure 5.8 center (left to right) and bottom (left to right) shows the shape comparison of track η, ϕ, p_T and multiplicity of the tracks for experimental data and Pythia-6 tune Z2 (with and w/o pile-up events), respectively.

Table 5.2: Track selection efficiency (%) for experimental data and PYTHIA-6 tune Z2 (with and without pile-up). For each cut, the quoted efficiency is relative to the previous cut.

Track Selection Efficiency			
Selection Variable	Data(%)	MC w/o pile-up(%)	MC with pile-up(%)
No muon in track collection	98.1	96.6	98.2
high purity	87.0	90.2	88.2
p_T >0.5 GeV/c	54.8	56.7	54.8
$\|\eta\|$ <2.0	82.8	82.9	82.5
$d_0/\sigma(d_{xy}) < 3.0$	80.9	81.9	82.1
$d_z/\sigma(d_z) < 3.0$	59.2	97.2	54.1
$\sigma(p_T)/p_T < 0.05$	97.8	97.0	97.5

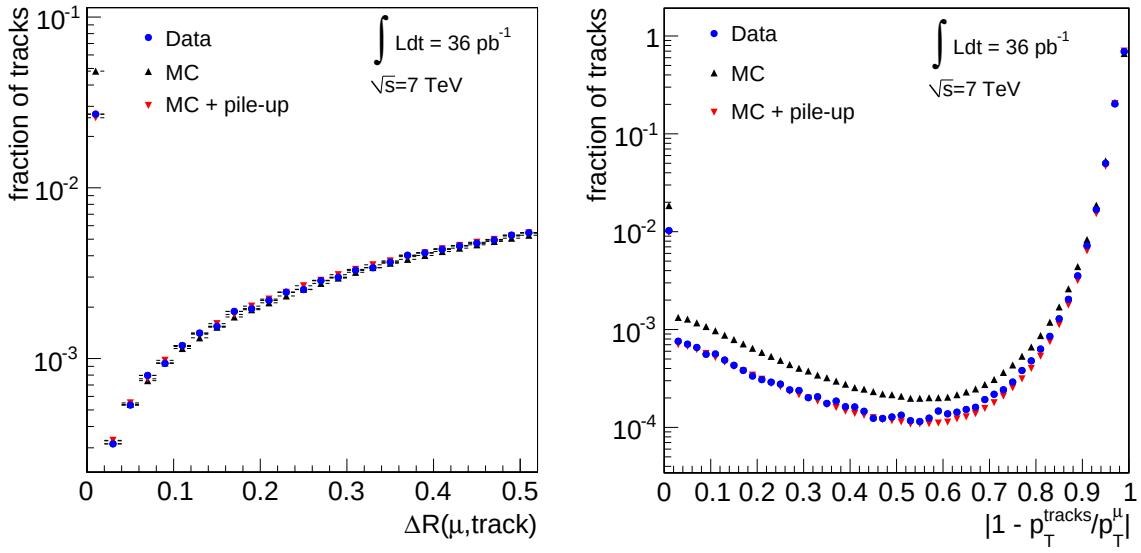

(a) (b)

Figure 5.5: (a) shows the ΔR matching and (b) shows the relative p_T difference between track and muon for experimental data and MCs.

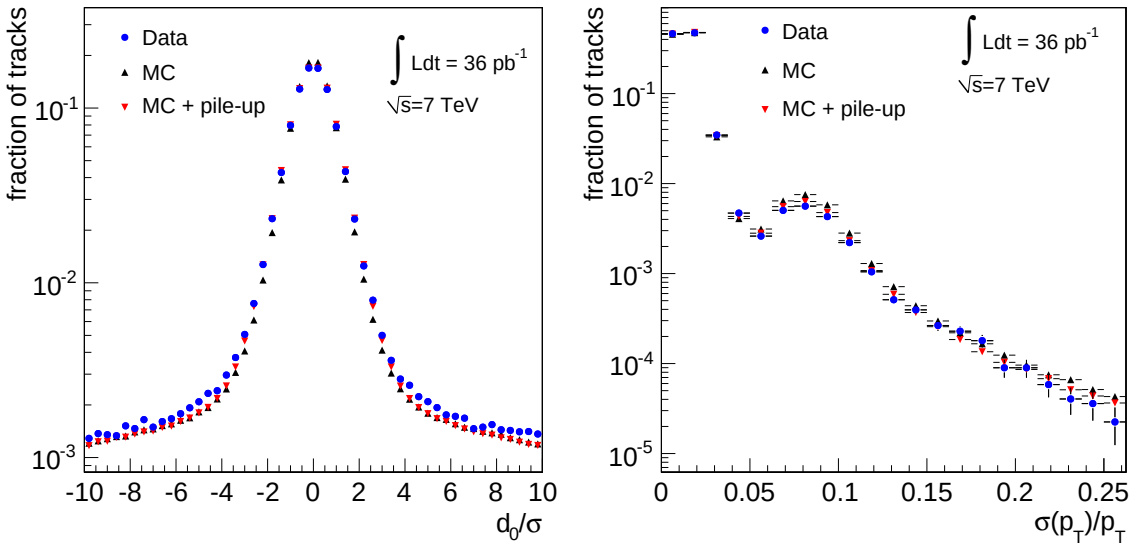

(a) (b)

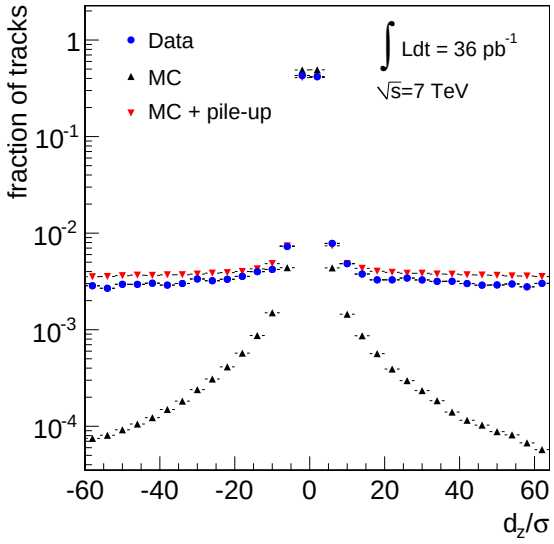

(c)

Figure 5.6: Comparison of (a) relative transverse impact parameter d_0/σ, (b) relative uncertainty in the p_T of tracks and (c) relative longitudinal impact parameter d_z/σ for Data and MC with and w/o pile-up.

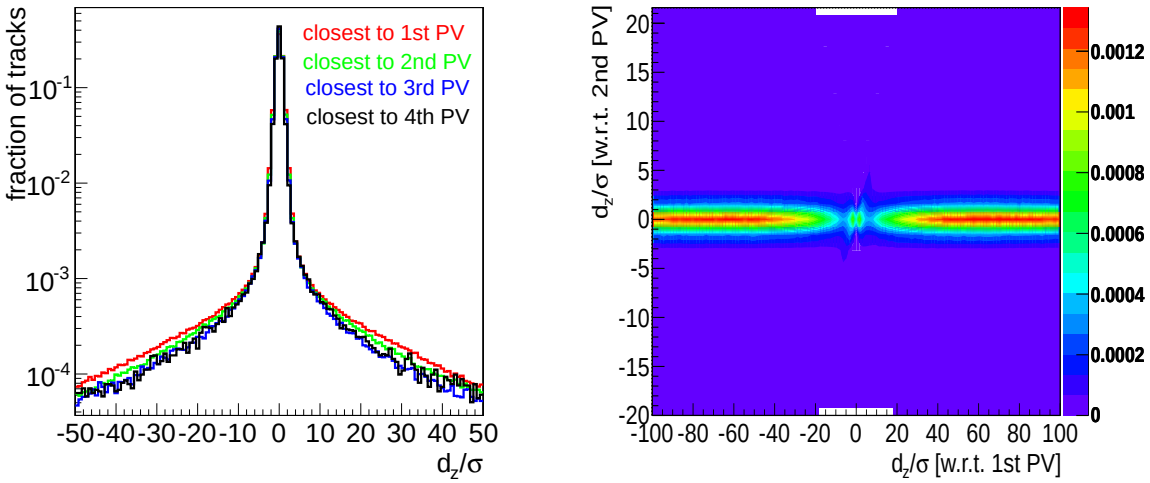

(a)

(b)

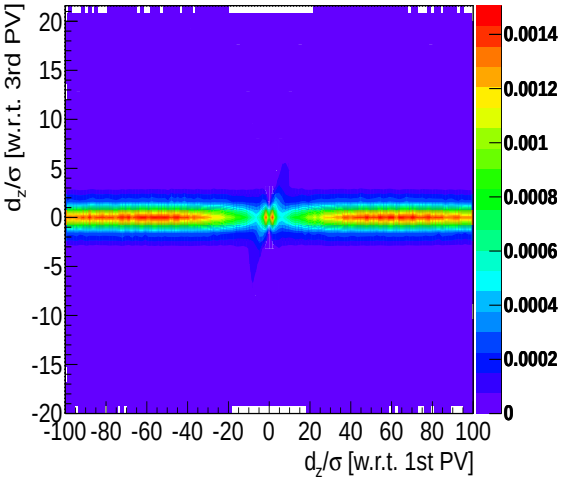

(c)

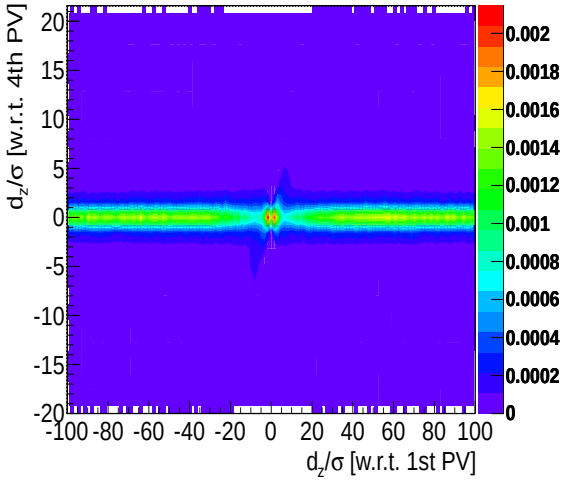

(d)

Figure 5.7: Comparison of (a) relative d_z of the tracks with respect to the closest vertex (b) relative d_z with respect to the 1^{st} vertex vs relative d_z with respect to the 2^{nd} vertex for the tracks which are closest to the 2^{nd} vertex (c) relative d_z with respect to 1^{st} vertex vs relative d_z with respect to the 3^{rd} vertex for the tracks which are closest to 3^{rd} vertex and (d) relative d_z with respect to 1^{st} vs relative d_z with respect to 4^{th} vertex for the tracks which are the closest to the 4^{th} vertex for Pythia-6 Z2 tune with pile-up events.

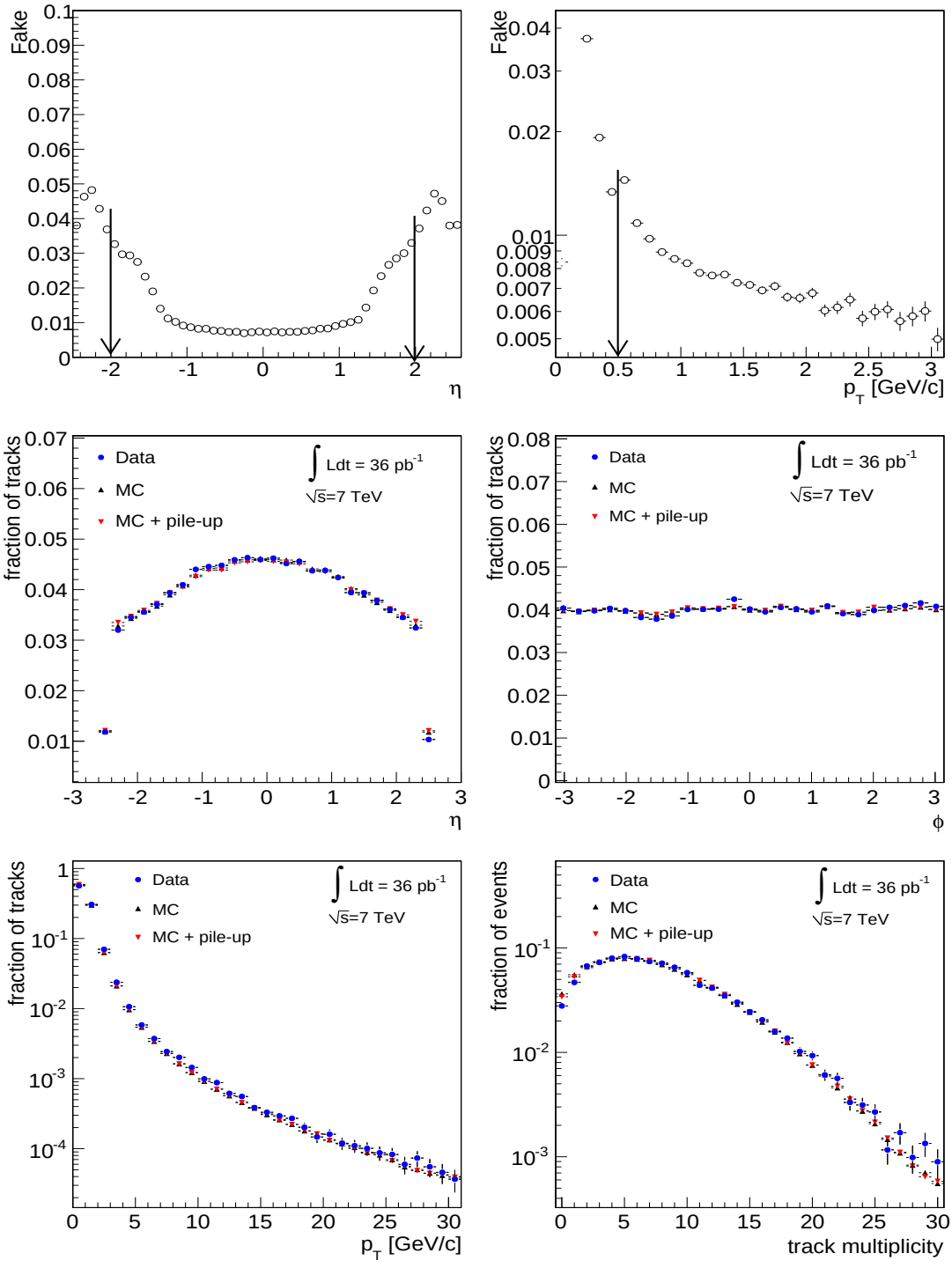

Figure 5.8: (Top left) and (top right) plots shows the fake rate as a function of track η and track p_T respectively. (Center left) and (center right) shows the shape comparison of track η and ϕ and, (bottom left) and (bottom right) shows the shape comparison of p_T and multiplicity of the tracks for experimental data and Pythia-6 Z2 tune with and w/o pile-up.

5.5 Underlying Event Measurements

To make the comparison of the Underlying Event (UE) observable measurements in experimental data with the theoretical predictions, we have used three Pythia-6 tunes Z2, D6T and DW as a reference. The UE activity is quantified in terms of the two variables, the average scalar sum of transverse momenta p_T of all the charged particles ($1/\mathrm{N}_{ev}\ \Delta^2\Sigma p_T/\Delta\eta\ \Delta(\Delta\phi)$) per unit pseudorapidity and per unit $\Delta\phi$ and the average number of charged particles ($1/\mathrm{N}_{ev}\ \Delta^2 N_{ch}/\Delta\eta\ \Delta(\Delta\phi)$) per unit pseudorapidity and per unit $\Delta\phi$. The dependence of these two observables on the resultant transverse momentum ($p_T^{\mu\mu}$) and invariant mass ($M_{\mu\mu}$) of the dimuon system has been studied.

Figure 5.9(a) shows the comparison of the number of tracks per unit pseudorapidity $dN_{\mathrm{chg}}/d\eta$ for experimental data and various MC tunes. However, Pythia-6 D6T tune seems to be over-estimating and Pythia-6 Z2 Tune seems to be under-estimating the UE activity as compared to experimental data. Pythia-6 DW is in good agreement with experimental data within the statistical uncertainty.

Figure 5.9(b) shows comparison of the average charge particle density and 5.9(c) shows the average p_T sum density as a function of $\Delta\phi$ for experimental data and different Pythia-6 MC tunes. Here $\Delta\phi$ is the separation between direction of tracks and dimuon system in the transverse plane. From these figures, one can justify the classification of three regions in ϕ space as discussed earlier. It is clearly visible that the prediction of Pythia-6 D6T tune over-estimates while tune Z2 under-estimates the track activity as compared to experimental data in both the *transverse* and the *towards* regions. Tune DW gives a better description of the UE measurements in experimental data. The UE activity is minimum in the *transverse* and the *towards* regions. It increases as one moves to the *away* region which is dominated by fragmentation of the *away* side parton balancing the dimuon system. The UE activity in the *transverse* region is slightly higher as compared to the *towards* region because the *transverse* region also gets some contribution from the *away* region activity.

Figure 5.10 (left column), shows the comparison of the average charge particle density as a function of transverse momentum of dimuon system $p_T^{\mu\mu}$, (top to bottom)

in the *towards*, *transverse* and the *away* regions respectively for experimental data and different MC tunes. Pythia-6 Z2 and Pythia-6 DW shows nice agreement with experimental data, in the *transverse* as well as in the *towards* regions, as $p_T^{\mu\mu} \rightarrow 0$. In the low p_T region, Pythia-6 D6T over-estimates the UE activity. As $p_T^{\mu\mu}$ increases, Pythia-6 Z2 and DW tunes predicts the smaller value of average charge particle density.

Figure 5.10 (right column), shows the comparison of the average scalar p_T sum density as a function of $p_T^{\mu\mu}$,(top to bottom) in the *towards*, *transverse* and the *away* regions respectively for experimental data and different MC tunes. The experimental data and Pythia-6 Z2 shows nice agreement in the *transverse* region as $p_T^{\mu\mu} \rightarrow 0$. In low $p_T^{\mu\mu}$ region, Pythia-6 D6T and DW over-estimate the UE activity. As $p_T^{\mu\mu}$ increases, Pythia-Z2 tune starts to show less activity as compared to experimental data, whereas Pythia-6 D6T and DW tunes give better agreement with experimental data. Similar conclusion can be drawn for the activity in *towards* region.

Figure 5.11 (left column) shows the comparison of the average charge particle density and (right column) shows the comparison of average scalar p_T sum density as a function of invariant mass ($M_{\mu\mu}$) of dimuon system, (top to bottom) in the *towards*, *transverse* and the *away* regions respectively for experimental data and different MC tunes. In order to minimize the contribution of radiation, $p_T^{\mu\mu}$ is required to be less than 10 GeV/c. From the figure, it is clear that Pythia-6 Z2 provides the best description for the average charge particle density, whereas average p_T sum density is described well by the predictions of Pythia-6 Z2 and DW models.

5.6 Unfolding of Underlying Event Observables

Any experimental measurement of an observable must be corrected for the distortions arising due to the detector resolutions as well as reconstruction and selection procedures adopted. This correction is necessary to compare the experimental results with the theoretical predictions. In this study, the bin-by-bin correction approach has been adopted to correct the experimental measurements. Figure 5.12 (left) and

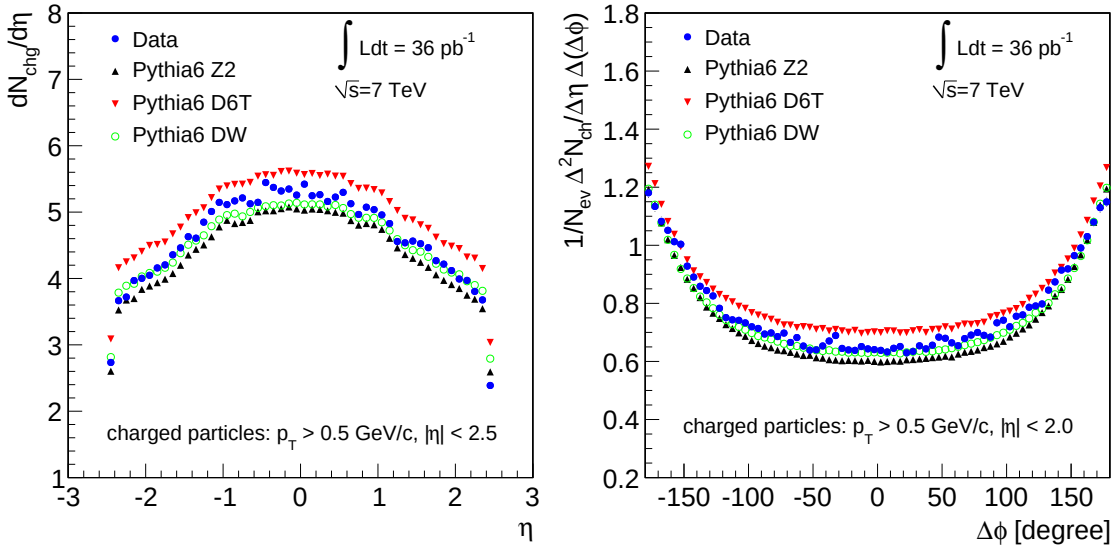

(a)

(b)

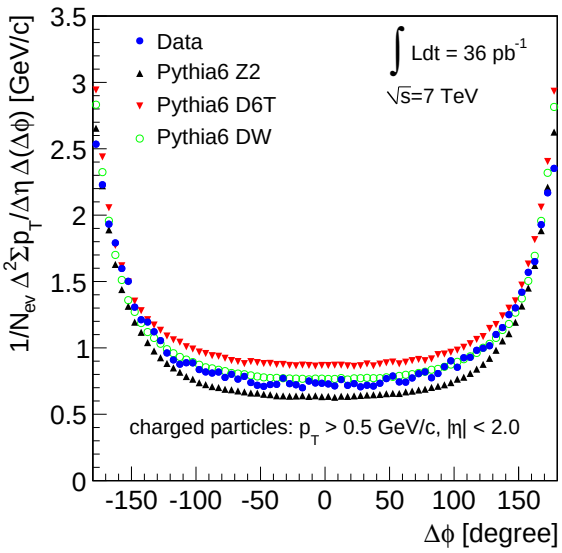

(c)

Figure 5.9: (a) shows the number of charged particles per unit pseudo-rapidity ($dN_{\rm chg}/d\eta$), (b) shows the average number of charged particles per unit pseudo-rapidity per unit $\Delta\phi$ for charged particle tracks with $p_T > 0.5$ GeV/c and $|\eta| < 2.0$. $\Delta\phi$ is the azimuthal angle between the resultant direction of the dimuon system and the charged tracks.(c) shows the average scalar sum of p_T of charged particles per unit pseudo-rapidity per unit $\Delta\phi$, for experimental data and different MC tunes as a function of $\Delta\phi$. Only tracks with $p_T > 0.5$ GeV/c and $|\eta|$ <2 are considered here.

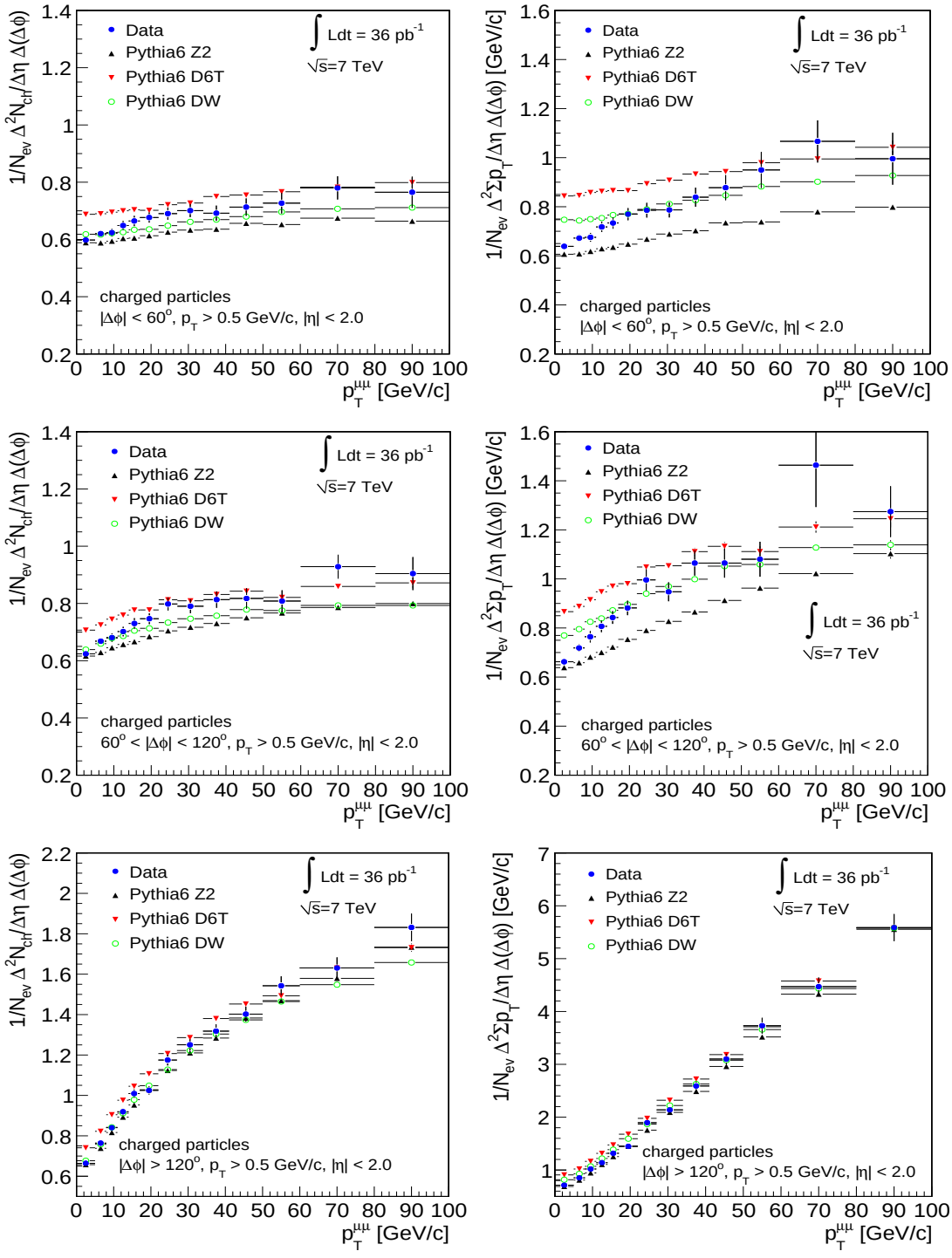

Figure 5.10: (Left column) shows average number of charged particles and (right column) shows the average scalar sum of the p_T of the charged particles, per unit pseudo-rapidity per unit $\Delta\phi$ from (top to bottom) in *towards*, *transverse* and *away* regions as a function of $p_T^{\mu\mu}$ for charged particle tracks with $p_T > 0.5$ GeV/c and $|\eta| < 2.0$.

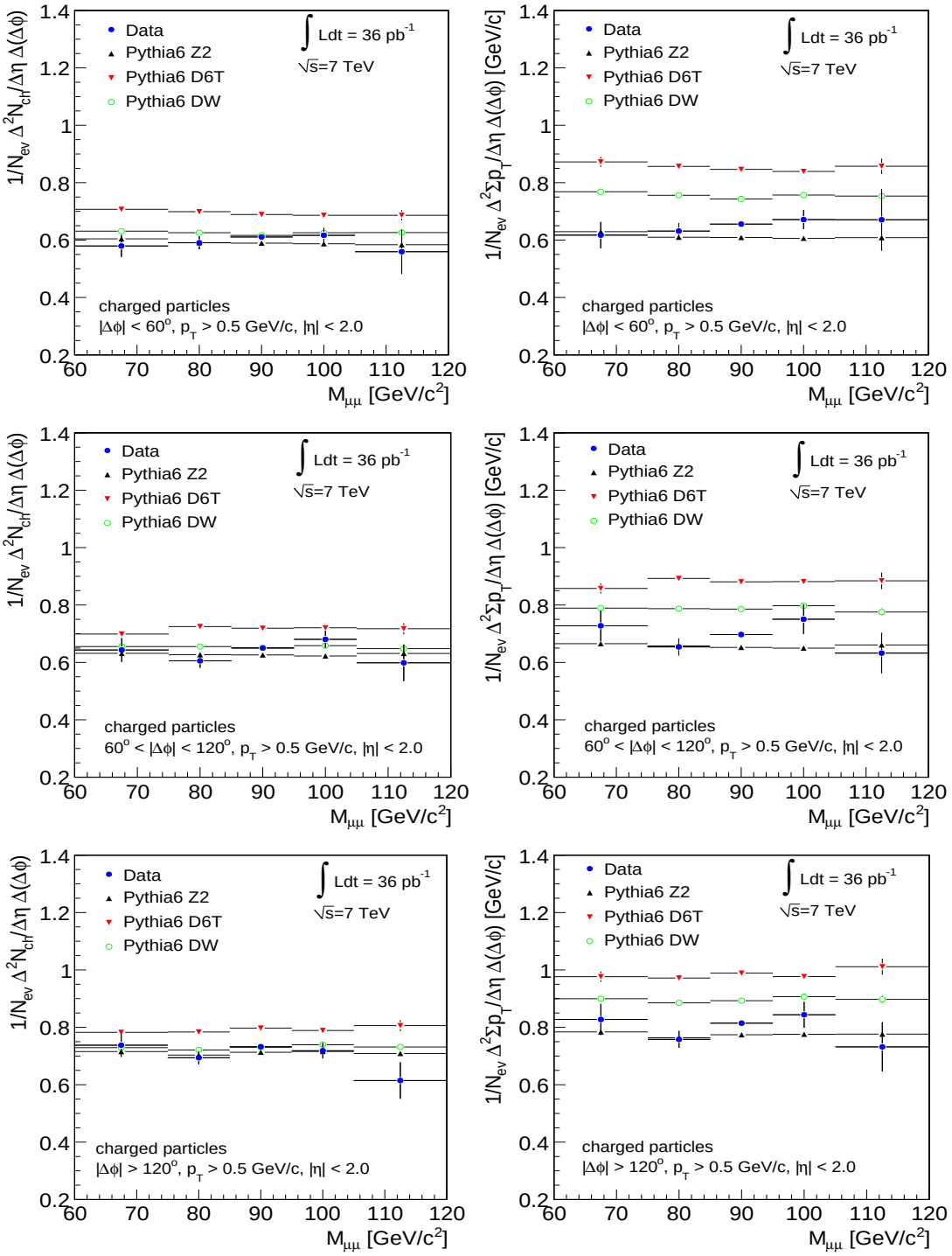

Figure 5.11: (Left column) shows average number of charged particles and (right column) shows the average scalar sum of the p_T of the charged particles, per unit pseudo-rapidity per unit $\Delta\phi$ from (top to bottom) in *towards*, *transverse* and *away* regions as a function of $M_{\mu\mu}$ for charged particle tracks with $p_T > 0.5$ GeV/c and $|\eta| < 2.0$

(right) shows the correlation plot between $p_T^{\mu\mu}$ at the generator and the reconstruction level. As can be seen from the correlation distribution, there is indeed a very small dispersion or equivalently, a very small migration in $p_T^{\mu\mu}$ as one moves from generator to reconstruction level. This supports the use of bin-by-bin correction method. At the generator level, DY-candidate is selected using two muons with p_T >20 GeV/c and having invariant mass in the window of [60-120] GeV/c^2. Only primary particles (*i.e.* stable particles, excluding muons) with $p_T > 0.5$ GeV/c and $|\eta|$ <2.0 are considered. Then the correction factor is calculated as ratio:$(\frac{Gen}{Rec})$. These correction factors, calculated using Pythia-6 Z2 tune MC, are then applied bin-by-bin on the uncorrected distributions.

Figure 5.13 shows the response factors $(\frac{Rec}{Gen})$ as a function of $p_T^{\mu\mu}$ for average charge particle density (left column) and the average scalar p_T sum density of charged particles (right column), (top to bottom) in the *towards*, *transverse* and *away* regions respectively. Similarly, Figure 5.14 (left column) and (right column) reports the response factors $(\frac{Rec}{Gen})$ as a function of $M_{\mu\mu}$ for average charge particle density and average scalar p_T sum density of charged particles respectively.

Fig. 5.15(left column) shows the comparison of uncorrected and corrected experimental data for average charge particle density and (right column) shows the comparison of uncorrected and corrected experimental data for average scalar p_T sum of charged particles as a function of $p_T^{\mu\mu}$, (top to bottom) in *towards*, *transverse* and *away* regions respectively. The generator level predictions from Pythia-6 Z2 tune are also overlayed for the comparison with the corrected experimental results. Pythia-6 Z2 describes the measurements quite well in the low $p_T^{\mu\mu}$ region and under-estimating the UE activity as compared to experimental data as we move to high $p_T^{\mu\mu}$ region. Similarly, Figure 5.16 (left column) and (right column) show the comparison of corrected and uncorrected experimental data overlayed with MC for average charge particle density and average scalar p_T sum density as a function of $M_{\mu\mu}$ respectively. From these plots it is clear that shape of corrected and uncorrected measurements are identical, thus the correction do not bias the measurements. Pythia-6 Z2 describes the measurements quite well as a function of $M_{\mu\mu}$.

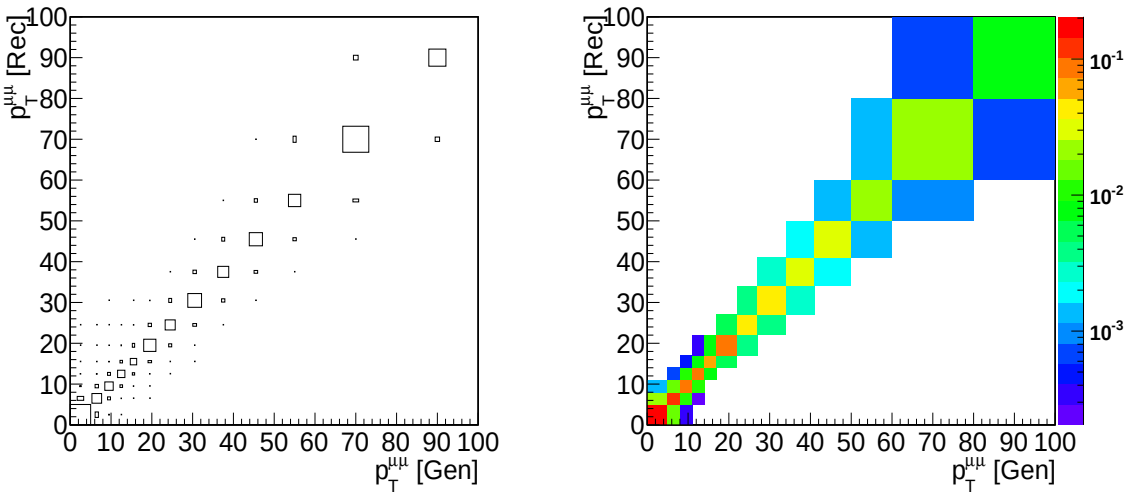

Figure 5.12: (a) The correlation between $p_T^{\mu\mu}$ at the generator and the reconstruction level and (b) shows the profile distribution of the average the $p_T^{\mu\mu}$ at reconstruction level as a function of $p_T^{\mu\mu}$ at generator level.

5.7 Study of Systematics in Experimental Results

Using corrected distribution from the experimental data, the systematic effects in the experimental results arising due to the different factors has been studied. These systematics include biases due to the different MC models considered for soft interaction, event trigger condition, track selection criteria, muon isolation criteria and due to the contribution from the fake tracks.

If the systematic effect is found to be very small, then a minimum of 0.2% is taken into account.

5.7.1 Systematics due to background processes

Total contribution of background processes has been found to be less than 0.5% after all the selection cuts, this contribution is however negligible, but the relative contribution may vary in different bins of $M_{\mu\mu}$ and $p_T^{\mu\mu}$. Figure 5.17 (left) shows the relative fraction of $t\bar{t}$ background as a function of $p_T^{\mu\mu}$ in mass window of 60-120

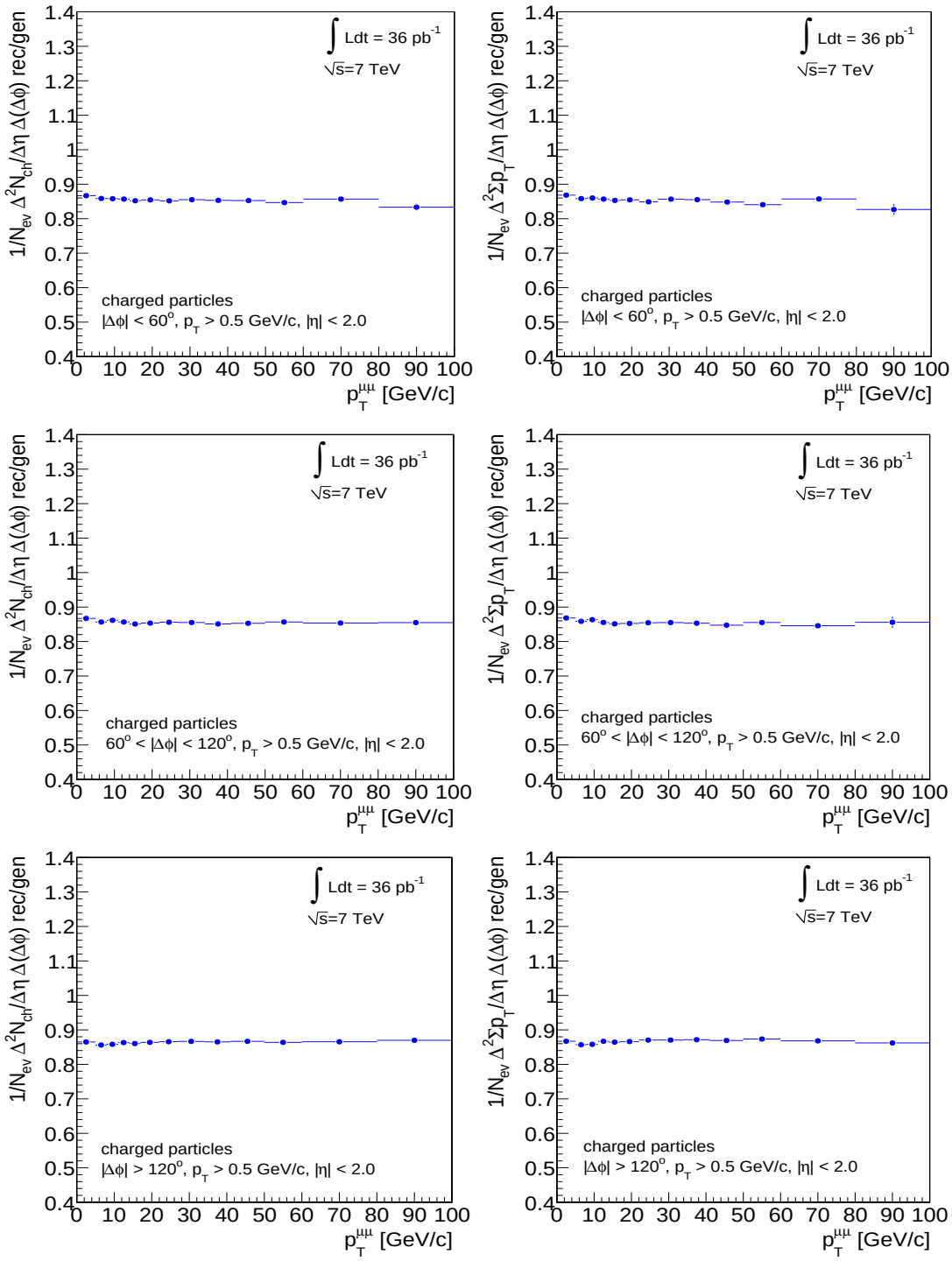

Figure 5.13: (Left column) shows the response factor ($\frac{Rec}{Gen}$) as a function of $p_T^{\mu\mu}$ for average number of charged particles and (right column) for the average scalar sum of the p_T of the charged particles, per unit pseudorapidity per unit $\Delta\phi$ from (top to bottom) in *towards*, *transverse* and *away* regions respectively.

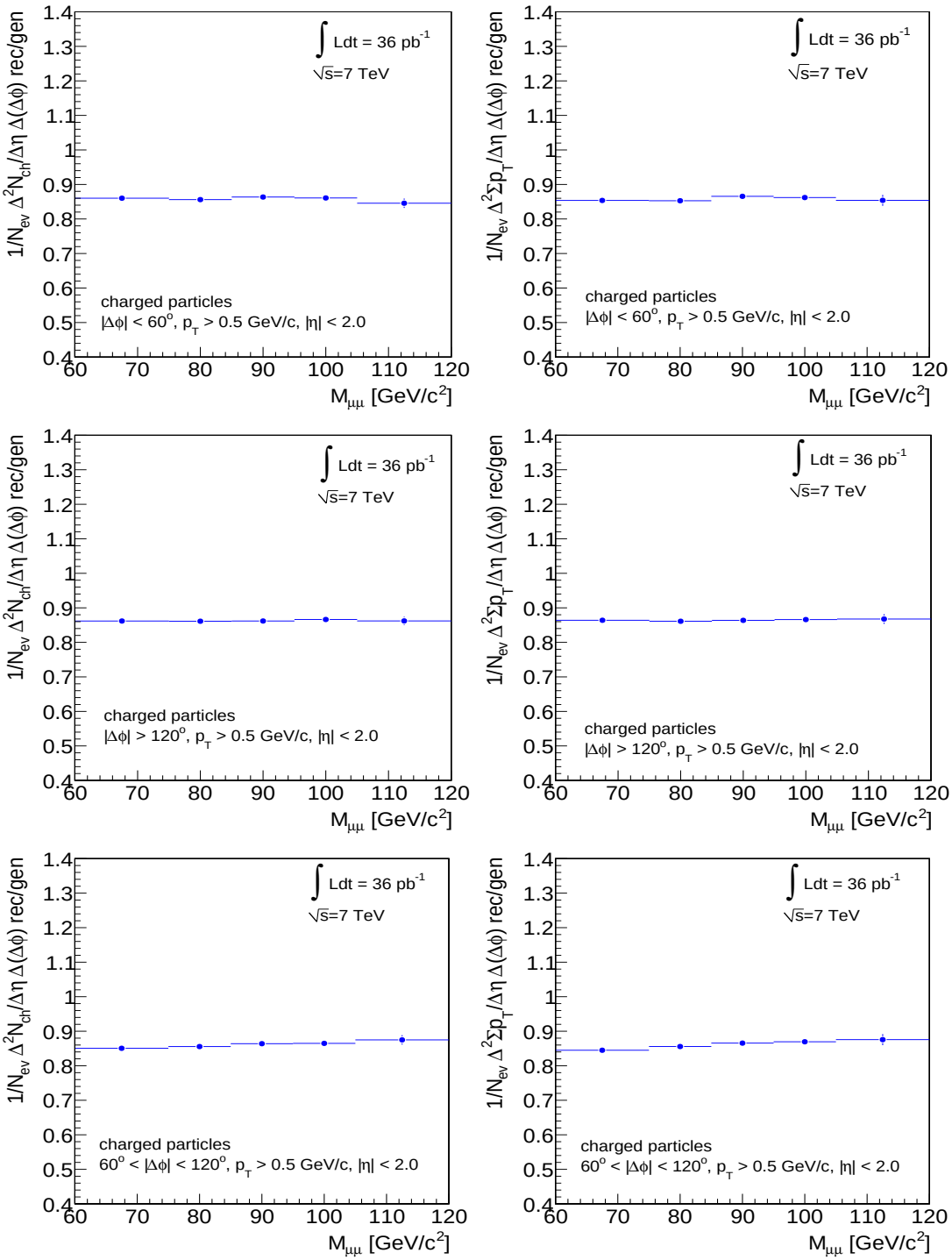

Figure 5.14: (Left column) shows the response factor ($\frac{Rec}{Gen}$) as a function of $M_{\mu\mu}$ for average number of charged particles and (right column) for the average scalar sum of the p_T of the charged particles, per unit pseudorapidity per unit $\Delta\phi$ from (top to bottom) in *towards*, *transverse* and *away* regions respectively.

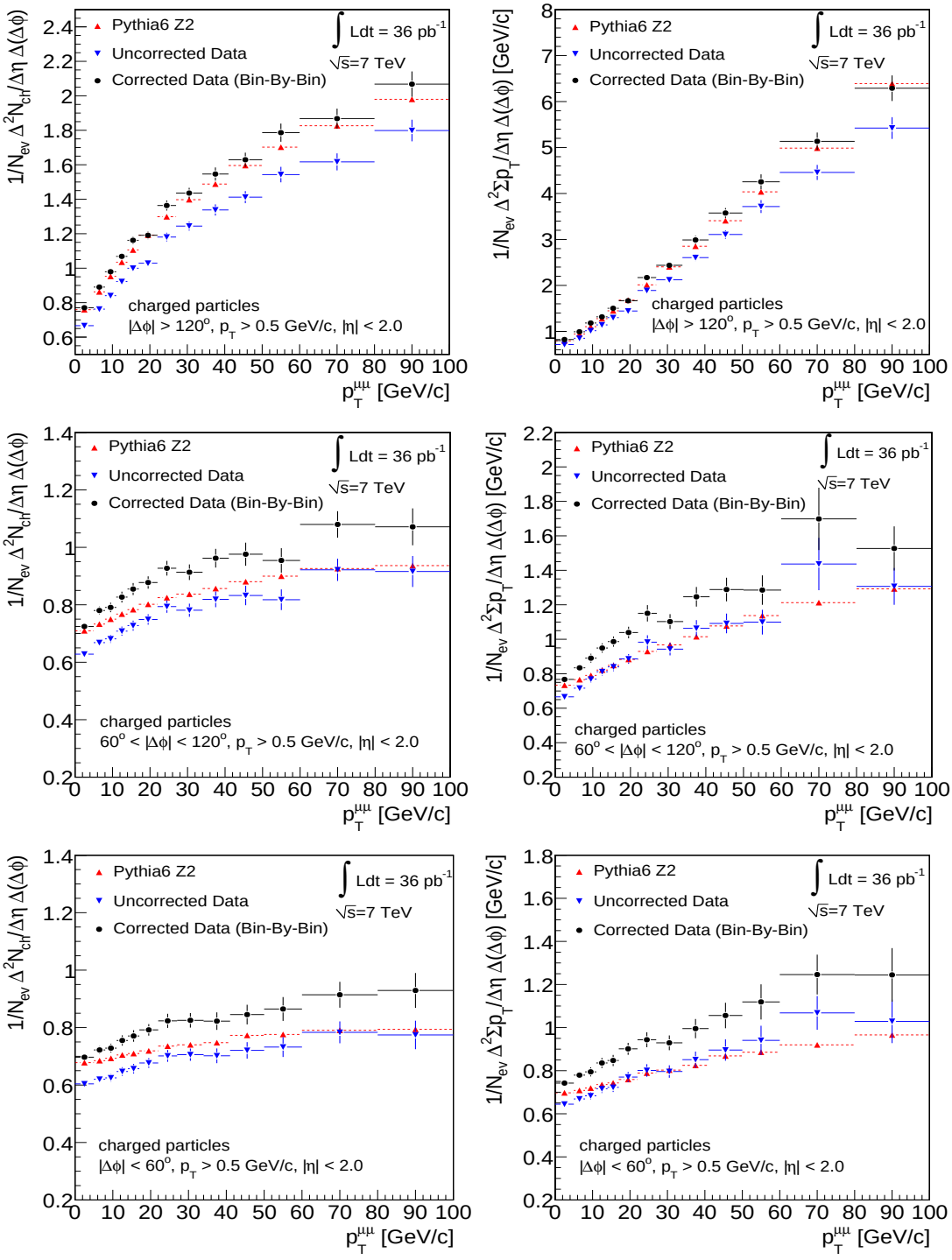

Figure 5.15: (Left column) shows the comparison of corrected and uncorrected experimental data as a function of $p_T^{\mu\mu}$ for the average charge particle density and (right column) for the average p_T sum density, per unit pseudorapidity per unit $\Delta\phi$ from (top to bottom) in *towards*, *transverse* and *away* regions respectively. Predictions from Pythia-6 Z2 tune MC are also overlayed for the comparison.

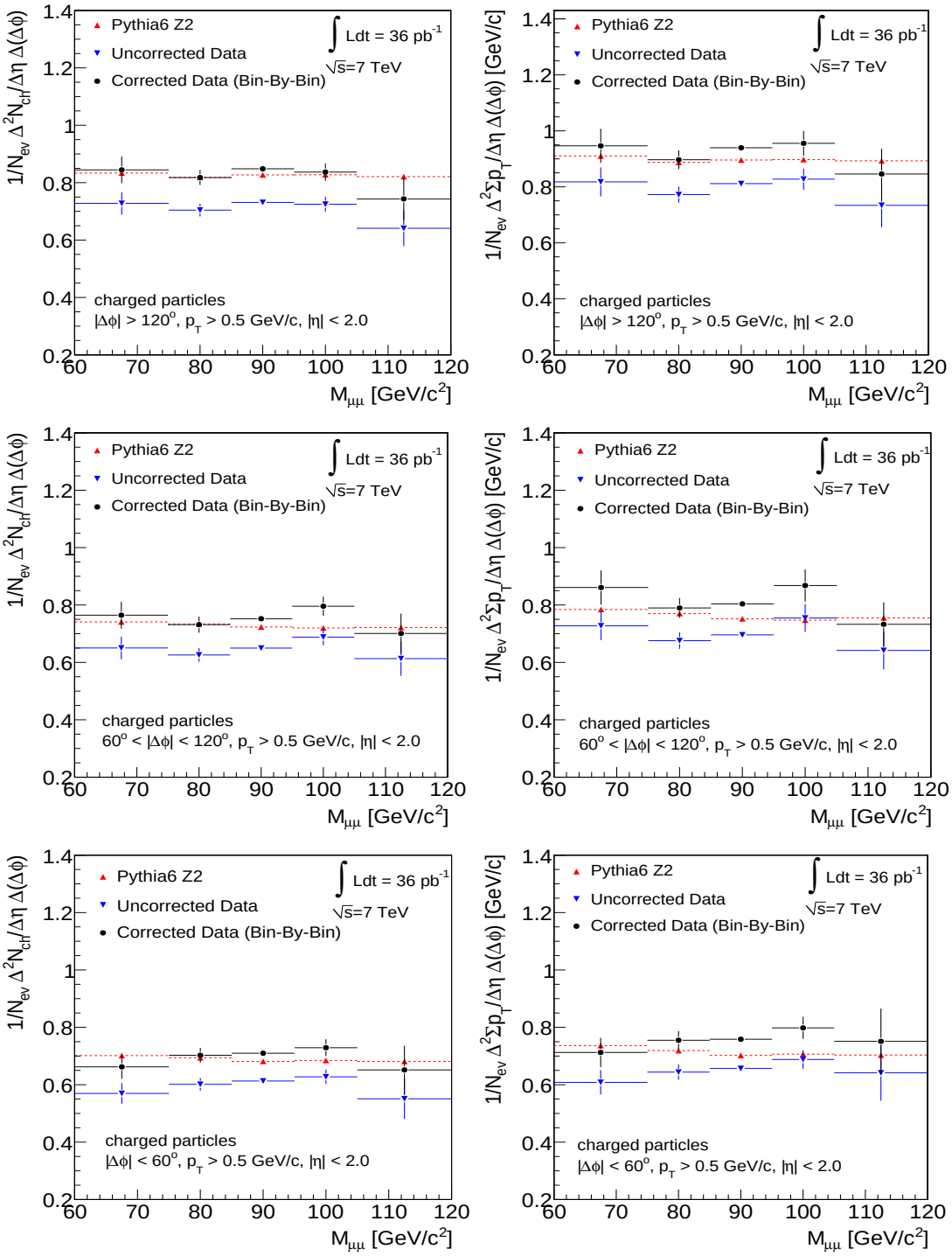

Figure 5.16: (Left column) shows the comparison of corrected and uncorrected experimental data respectively as a function of $M_{\mu\mu}$ for the average charge particle density and (right column) for the average p_T sum density, per unit pseudorapidity per unit $\Delta\phi$ from (top to bottom) in *towards*, *transverse* and *away* regions. Predictions from Pythia-6 Z2 tune MC are also overlayed for the comparison.

GeV/c^2 and Figure 5.17 (right) shows the relative fraction of $t\bar{t}$ background as a function of $M_{\mu\mu}$ with requirement of $p_T^{\mu\mu}$ less than 10 GeV/c. As can be seen from the figure, the relative contribution of the background is varying in each bin and is getting higher at large values of transverse momentum of dimuon system. To get the systematic bias, polynomial fit (p1) of the relative distributions is performed and the estimated bin-by-bin systematic bias is reported in Table 5.3.

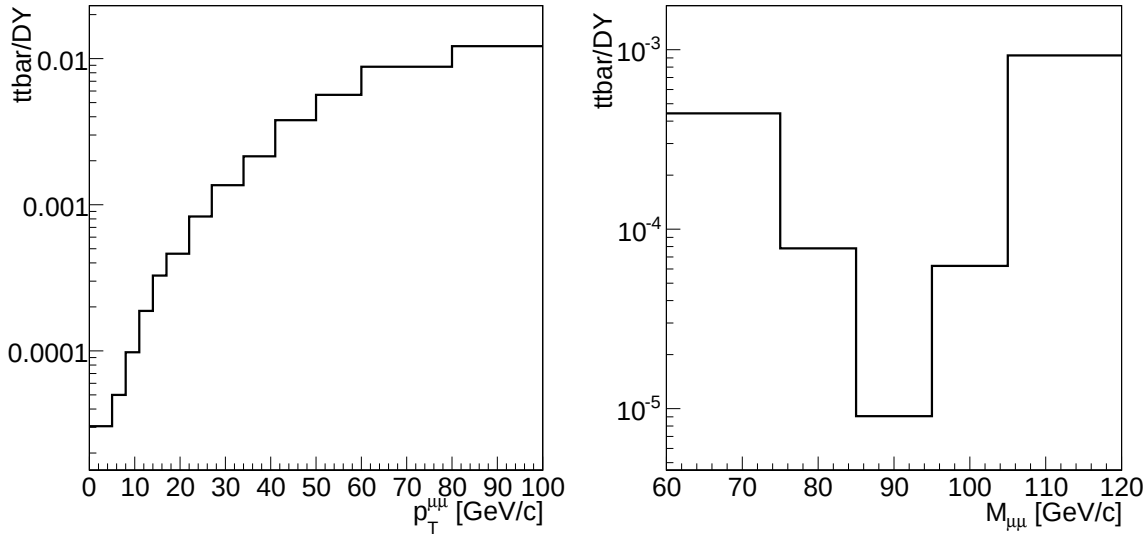

Figure 5.17: (Left) shows the relative fraction of $t\bar{t}$ as a function of $p_T^{\mu\mu}$ and (right) as a function of $M_{\mu\mu}$. The signal sample used for this estimation is Pythia-6 Z2 Tune.

5.7.2 Systematics due to different models of soft interactions

To estimate the effect of different QCD models, experimental data is corrected using the different Pythia tunes e.g Pythia-6 Z2 and Pythia-6 D6T. Ratio of the corrected distribution is then fitted with polynomial function. Systematics due to different QCD models is found to be 1-2%.

5.7.3 Systematics due to event trigger selection

In this analysis, experimental data is collected with high level trigger paths *i.e.* HLT_Mu9, HLT_Mu11 and HLT_Mu15. These triggers put a constraint on the trans-

Systematic bias (%) in UE observables due to $t\bar{t}$ background						
$p_T^{\mu\mu}$ GeV/c	$\frac{d^2N_{chg}}{d\eta d(\Delta\phi)}$ (away)	$\frac{d^2\Sigma p_T}{d\eta d(\Delta\phi)}$ (away)	$\frac{d^2N_{chg}}{d\eta d(\Delta\phi)}$ (trans)	$\frac{d^2\Sigma p_T}{d\eta d(\Delta\phi)}$ (trans)	$\frac{d^2N_{chg}}{d\eta d(\Delta\phi)}$ (towards)	$\frac{d^2\Sigma p_T}{d\eta d(\Delta\phi)}$ (towards)
0-5	0.2	0.2	0.2	0.2	0.2	0.2
5-8	0.2	0.2	0.2	0.2	0.2	0.2
8-11	0.2	0.2	0.2	0.2	0.2	0.2
11-14	0.2	0.2	0.2	0.2	0.2	0.2
14-17	0.2	0.2	0.2	0.2	0.2	0.2
17-22	0.2	0.2	0.2	0.2	0.2	0.2
22-27	0.2	0.2	0.2	0.3	0.2	0.3
27-34	0.2	0.2	0.2	0.4	0.2	0.4
34-41	0.2	0.2	0.2	0.6	0.2	0.6
41-50	0.2	0.2	0.3	0.8	0.3	0.8
50-60	0.2	0.2	0.4	1.1	0.4	1.0
60-80	0.2	0.2	0.5	1.5	0.5	1.4
80-100	0.2	0.2	0.7	2.0	0.7	1.9

Table 5.3: The bin-by-bin systematic bias (%) induced due to contamination from $t\bar{t}$ background process.

verse momentum of the leading muon only. These muons are then excluded from the charged track collection which is used to calculate the UE observables. Thus the UE observables are expected to be insensitive to the trigger condition. In order to evaluate the induced trigger bias, experimental data with no trigger condition is corrected using Pythia-6 Z2 Monte-Carlo having no trigger condition and are compared with corrected experimental data when trigger condition is applied on both experimental data and MC. The effect is also studied by correcting experimental data with the correction factor calculated using MC having no trigger condition. Additionally, experimental data without trigger condition is corrected using the correction factor calculated using MC with trigger condition. Biases from all the three studies are found to be negligible and is taken to be 0.2% for an individual case which are then added in quadrature to obtain the total trigger bias on the final observables.

5.7.4 Systematics due to event pile-up

The presence of more then one collision in a single bunch crossing can affect the measurements of Underlying Event (UE) activity significantly. Hence the track selection criteria is made very stringent and has been found to be very effective in minimizing the contributions from the pile-up events. Quantitative estimate of the effect of pile-up events on corrected UE observables is calculated by comparing the MC samples with and without pile-up. Pythia-6 Z2 tune MC with and without pile-up events is corrected using the correction factor obtained with Pythia-6 D6T tune. The effect of pile-up on the UE observables is about 1-2%.

As shown earlier in Section 5.4 , the amount of pile-up is not same in MC and experimental data. To take into account this difference a systematic uncertainty has been assigned. For this purpose, MC is reweighted to have the same amount of pile-up as that in experimental data. Figure 5.18 shows the comparison of the number of expected pile-up events in experimental data, MC with pile-up before and after re-weightning. After re-weighting the amount of pile-up in MC and experimental data has been found to be in good agreement. The effect on the UE observables due to difference in the amount of pile-up in experimental data and MC are found to be

very small.

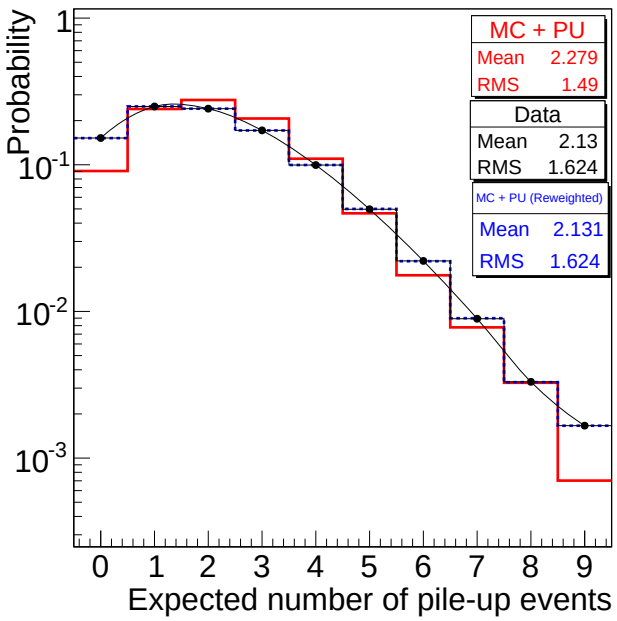

Figure 5.18: The comparison of the number of expected pile-up events in experimental data and MC with pile-up before and after the re-weightning.

5.7.5 Systematics due to lepton isolation criteria on UE variables

The Underlying Event (UE) activity and muon isolation are very much correlated. The lepton isolation efficiency is affected if the UE activity changes and by requiring the isolated muons the UE activity is biased towards lower value.. This fact is visible from the Table 5.4 which shows the muon isolation efficiency for different Pythia-6 tunes. In Drell-Yan (DY) selection, muons are required to be isolated and, by this requirement the track activity around the muon is biased towards lower value and so are the UE observables. To get the estimate of systematic bias introduced due to the isolation criteria, the UE observables for MC with and without isolation condition on muon are compared. Table 5.5 reports the effect of isolation on uncorrected UE observables for different Pythia-6 tunes.

Tune	P6 Z2	P6 D6T	P6 DW	P6 P0	P6 ProQ20
Isolation efficiency (%)	92.6	90.5	91.3	92.8	91.1

Table 5.4: The isolation efficiency(%) for various Pythia-6 tunes.

Systematic bias in UE observables due to Isolation Criteria					
Observables	Z2	D6T	DW	P0	ProQ20
$\frac{d^2\Sigma p_T}{d\eta d(\Delta\phi)}$ (towards)	1.3	2.1	2.0	1.4	1.5
$\frac{d^2\Sigma p_T}{d\eta d(\Delta\phi)}$ (transverse)	1.2	2.1	1.9	1.4	1.4
$\frac{d^2 N_{chg}}{d\eta d(\Delta\phi)}$ (towards)	1.0	1.7	1.5	1.0	1.1
$\frac{d^2 N_{chg}}{d\eta d(\Delta\phi)}$ (transverse)	0.9	1.6	1.4	0.9	1.0

Table 5.5: The systematic bias (%) due to muon isolation criteria on uncorrected UE observables for various tunes of Pythia-6.

Since the UE activity is not same in experimental data and MC, therefore correction factor for isolation, calculated from MC may not be expected to be appropriate for experimental data. To take care of this bias, Pythia-6 Z2 tune sample is corrected using Pythia-6 D6T tune with and without isolation condition and this difference between the corrected results is taken as systematics.

5.7.6 Systematics due to track selection

In order to study the systematic bias due to the track selection criteria, all the track selection variables are varied one-by-one as explained below. Then the resulting UE observables are compared with the observables obtained using optimized selection procedure.

- $\Delta R(\mu, track)$ is changed from 0.01 to 0.05 (UE25).
- $\Delta p_T/p_T^{\mu}$ is changed from 0.01 to 0.05 (UE26).
- *high purity* flag is replaced by the condition on total number of crossed layers and pixel layers (UE27).

Systematic bias in UE observables due to Track Selection Criteria						
Observable	UE27	$d_0/\sigma(d_0)$, $d_z/\sigma(d_z)$ (2, 3)	$d_0/\sigma(d_0)$, $d_z/\sigma(d_z)$ (3, 2)	ΔR,$\Delta p_T/p_T$ (0.01,0.05)	ΔR,$\Delta p_T/p_T$ (0.05,0.01)	$\sqrt{\delta^2}$
$\frac{d^2\Sigma p_T}{d\eta d(\Delta\phi)}$ *towards*	0.2 (0.2)	0.3 (0.3)	0.5 (0.7)	0.2 (0.2)	0.2 (0.2)	0.7 (0.8)
$\frac{d^2\Sigma p_T}{d\eta d(\Delta\phi)}$ *trans.*	0.2 (0.2)	0.2 (0.5)	0.5 (0.9)	0.2 (0.2)	0.2 (0.2)	0.6 (1.1)
$\frac{d^2\Sigma p_T}{d\eta d(\Delta\phi)}$ *away*	0.2 (0.2)	0.3 (0.4)	0.6 (0.6)	0.2 (0.2)	0.2 (0.2)	0.8 (0.8)
$\frac{d^2 N_{chg}}{d\eta d(\Delta\phi)}$ *towards*	0.2 (0.2)	0.4 (0.4)	0.6 (0.6)	0.2 (0.2)	0.2 (0.2)	0.8 (0.8)
$\frac{d^2 N_{chg}}{d\eta d(\Delta\phi)}$ *trans*	0.2 (0.2)	0.5 (0.5)	0.6 (0.8)	0.2 (0.2)	0.2 (0.2)	0.9 (1.0)
$\frac{d^2 N_{chg}}{d\eta d(\Delta\phi)}$ *away*	0.2 (0.2)	0.4 (0.5)	0.6 (0.6)	0.2 (0.2)	0.2 (0.2)	0.8 (0.8)

Table 5.6: The systematic uncertainties (%) due to different track selection criteria. The last column reports the combined uncertainty obtained by adding the individual contributions in quadrature. The numbers out of parentheses are for the study as a function of resultant transverse momentum ($p_T^{\mu\mu}$) of dimuon system and those in parentheses correspond to the study as a function of invariant mass ($M_{\mu\mu}$).

- $d_0/sigma(d_0)$ value changed from 3 to 2 (UE28).
- $d_z/sigma(d_z)$) value changed from 3 to 2 (UE29).

To estimate the bias on corrected distribution, experimental data with changed track selection is corrected using MC with changed track selection and then compared with experimental data corrected using MC with optimized selection. Table 5.6 summarizes the systematic uncertainty coming from different track selection conditions.

5.7.7 Systematics due to fake tracks

To estimate the effect of fake tracks on UE observables, a set of MC sample is created by reducing the fake tracks by applying ΔR matching between reconstructed tracks and primary generator level tracks. To calculate the systematic bias due to fake tracks, unfolded distribution in experimental data obtained using this new MC (after excluding fakes) is compared with unfolded experimental data distributions obtained using MC which contains all fake tracks.

Table 5.7 and 5.8 reports the total systematic bias estimated for UE variables as a function of $p_T^{\mu\mu}$ and $M_{\mu\mu}$ respectively.

5.8 Underlying Event Results and Discussion

The Underlying Event (UE) activity is quantified in terms of the average scalar sum of the transverse momenta p_T of all the charged particles per unit pseudo-rapidity and per unit $\Delta\phi$ and the average number of charged particles per unit pseudo-rapidity and per unit $\Delta\phi$. The dependence of these observables on the resultant transverse momentum ($p_T^{\mu\mu}$) and the invariant mass ($M_{\mu\mu}$) of dimuon system has been studied. While studying the UE observables as a function of invariant mass ($M_{\mu\mu}$) a maximum cut of 10 GeV/c on the $p_T^{\mu\mu}$ has been applied in order to minimize the effect of radiation.

Figure 5.19 (left column) shows the average scalar p_T sum density of the charged particles in experimental data compared to MC models, (top to bottom) in the *to-*

Observable	Trigger	Isolation	Track Sel.	Fake	Pile-up	QCD Model	bkg.
$\frac{d^2\Sigma p_T}{d\eta d(\Delta\phi)}$ (towards)	0.4	1.0	0.7	0.7	1.0	0.7	1.9
$\frac{d^2\Sigma p_T}{d\eta d(\Delta\phi)}$ (transverse)	0.4	0.8	0.6	0.7	0.9	0.4	2.0
$\frac{d^2\Sigma p_T}{d\eta d(\Delta\phi)}$ (away)	0.4	0.6	0.8	0.7	0.6	1.0	0.2
$\frac{d^2 N_{chg}}{d\eta d(\Delta\phi)}$ (towards)	0.4	0.8	0.8	0.9	1.2	0.7	0.7
$\frac{d^2 N_{chg}}{d\eta d(\Delta\phi)}$ (transverse)	0.4	0.7	0.9	0.9	1.1	0.7	0.7
$\frac{d^2 N_{chg}}{d\eta d(\Delta\phi)}$ (away)	0.4	0.5	0.8	0.9	0.7	0.7	0.2

Table 5.7: Summary of the systematic uncertainties (%) from different sources. The first three rows show the systematic uncertainties for the average scalar sum of p_T of the charged particles in the *towards*, *transverse* and *away* regions, whereas the last three rows report the systematic uncertainties for the average number of charged particles ($1/\mathrm{N}_{ev}\ \Delta^2 N_{ch}/\Delta\eta\ \Delta(\Delta\phi)$) in the *towards*, *transverse* and *away* regions. The last column reports the maximum uncertainty due to ($t\bar{t}$) background. The numbers refer to study vs. $p_T^{\mu\mu}$.

Observable	Trigger	Isolation	Track Sel.	Fake	Pile-up	QCD Model	bkg.
$\frac{d^2\Sigma p_T}{d\eta d(\Delta\phi)}$ (towards)	0.4	1.1	0.8	0.7	1.2	1.5	0.2
$\frac{d^2\Sigma p_T}{d\eta d(\Delta\phi)}$ (transverse)	0.4	1.3	1.1	0.7	1.2	1.7	0.2
$\frac{d^2\Sigma p_T}{d\eta d(\Delta\phi)}$ (away)	0.4	0.8	0.8	0.6	1.1	1.4	0.2
$\frac{d^2 N_{chg}}{d\eta d(\Delta\phi)}$ (towards)	0.4	0.9	0.8	0.8	1.5	1.0	0.2
$\frac{d^2 N_{chg}}{d\eta d(\Delta\phi)}$ (transverse)	0.4	1.1	1.0	0.8	1.4	1.1	0.2
$\frac{d^2 N_{chg}}{d\eta d(\Delta\phi)}$ (away)	0.4	0.7	0.8	0.6	1.3	1.1	0.2

Table 5.8: Summary of the systematic uncertainties (%) from different sources. The first three rows show the systematic uncertainties for the average scalar sum of p_T of the charged particles ($1/\mathrm{N}_{ev}\ \Delta^2\Sigma p_T/\Delta\eta\ \Delta(\Delta\phi)$) in the *towards*, *transverse* and *away* regions, whereas the last three rows report the systematic uncertainties for the average number of charged particles in the *towards*, *transverse* and *away* regions. The last column reports the maximum uncertainty due to ($t\bar{t}$) background. The numbers refers to the study vs. $M_{\mu\mu}$.

wards, *transverse* and *away* regions respectively. As can be observed from the figure, th activity in the *away* region increase rapidly due to increase in the recoiling hadronic activity with the increase in $p_T^{\mu\mu}$. A small but noticeable growth in the average scalar p_T sum density with the increase in $p_T^{\mu\mu}$ can be observed for *transverse* (center) and *towards* (top) regions. The minimum energy scale of the event in this analysis is set by the invariant mass of the muon pair which is 60 GeV/c^2, the scale lies well in the MultiParton Interactions (MPI) saturation region. Therefore, slow growth in the activity in *transverse* and *towards* regions mainly due to the radiation contribution. Qualitatively, activity is similar in *transverse* and *towards* regions but activity is higher in the *transverse* due to spill-over contribution from *away* side activity. The comparative description of the experimental data with the different MC models is summarized in Figure 5.19 (right column), which shows the ratio of the MC predictions to the measurements in experimental data for the average scalar p_T sum density of the charged particles, (top to bottom) in the *towards*, *transverse* and *away* regions respectively. Pythia-8 4C describes well the activity in the *away* region. Pythia-6 Z1 and DW over-estimates the activity as $p_T^{\mu\mu} \to 0$. For $p_T^{\mu\mu} \to 0$, Pythia-8 4C gives the best description of the measurements in the *transverse* and the *towards* regions whereas Pythia-6 Z1 describes the experimental results within ∼10%. At higher values of $p_T^{\mu\mu}$ (>10 GeV/c), the measurement is described well by both Pythia-6 Z1 and Pythia-6 DW, but with 15-20% discrepancy at very large value of $p_T^{\mu\mu}$ (*i.e.*> 60 GeV/c). Pythia-8 4C increasingly underestimates the activity.

Figure 5.20 (left column) shows the average charged particle density in experimental data compared to the various models of MC, (top to bottom) in the *towards*, *transverse* and *away* regions respectively. The quantitative description of the experimental data by different MC models is reported in Figure 5.20 (right column), which shows the ratio of the MC predictions and measurement in experimental data for the average charged particle density. As $p_T^{\mu\mu} \to 0$, Pythia-6 DW gives the best description of the measurements in the *transverse* and the *towards* regions, whereas Pythia-6 Z1 describes the measurements within ∼10%. At higher values of $p_T^{\mu\mu}$ (>10 GeV/c), the measurement is described well by both Pythia-6 Z1 and Pythia-6 DW. Pythia-8 4C

underestimates the UE activity upto 15-20%.

Figure 5.21 (left column) shows average scalar p_T sum density of the charged particles, and (right column) shows the ratio as a function of invariant mass ($M_{\mu\mu}$) of dimuon system of the MC predictions and measurement in experimental data for the same variable, (top to bottom) in the *towards*, *transverse* and *towards* regions respectively. Similarly, Figure 5.22 (left column) shows the average charged particle density, in the experimental data compared to various models of MC and (right column) shows the ratio as a function of invariant mass ($M_{\mu\mu}$) of dimuon system of the MC predictions and measurement in experimental data for the same variable, (top to bottom) in the *towards*, *transverse* and *towards* regions respectively. Average densities as a function of invariant mass are almost flat within statistical uncertainty. This is due to the fact that energy scale of event defined by invariant mass is quite high to lie in the MPI saturation region. Measurement of average density of scalar sum of transverse momentum is best described by Pythia-8 4C and measurements of average charge particle density are best described by Pythia-6 Z1 and Pythia-8 4C.

In this chapter we presented the measurement of the UE activity using the DY events. Detailed description of event and track selection criteria has been reported. The dependence of the UE observables on $M_{\mu\mu}$ and $p_T^{\mu\mu}$ has been studied. The UE observables have been corrected for the detector effects and selection efficiencies using bin-by-bin technique and compared with various models for soft interaction. Any of the existing model does not fully describe the measurements and required further tuning.

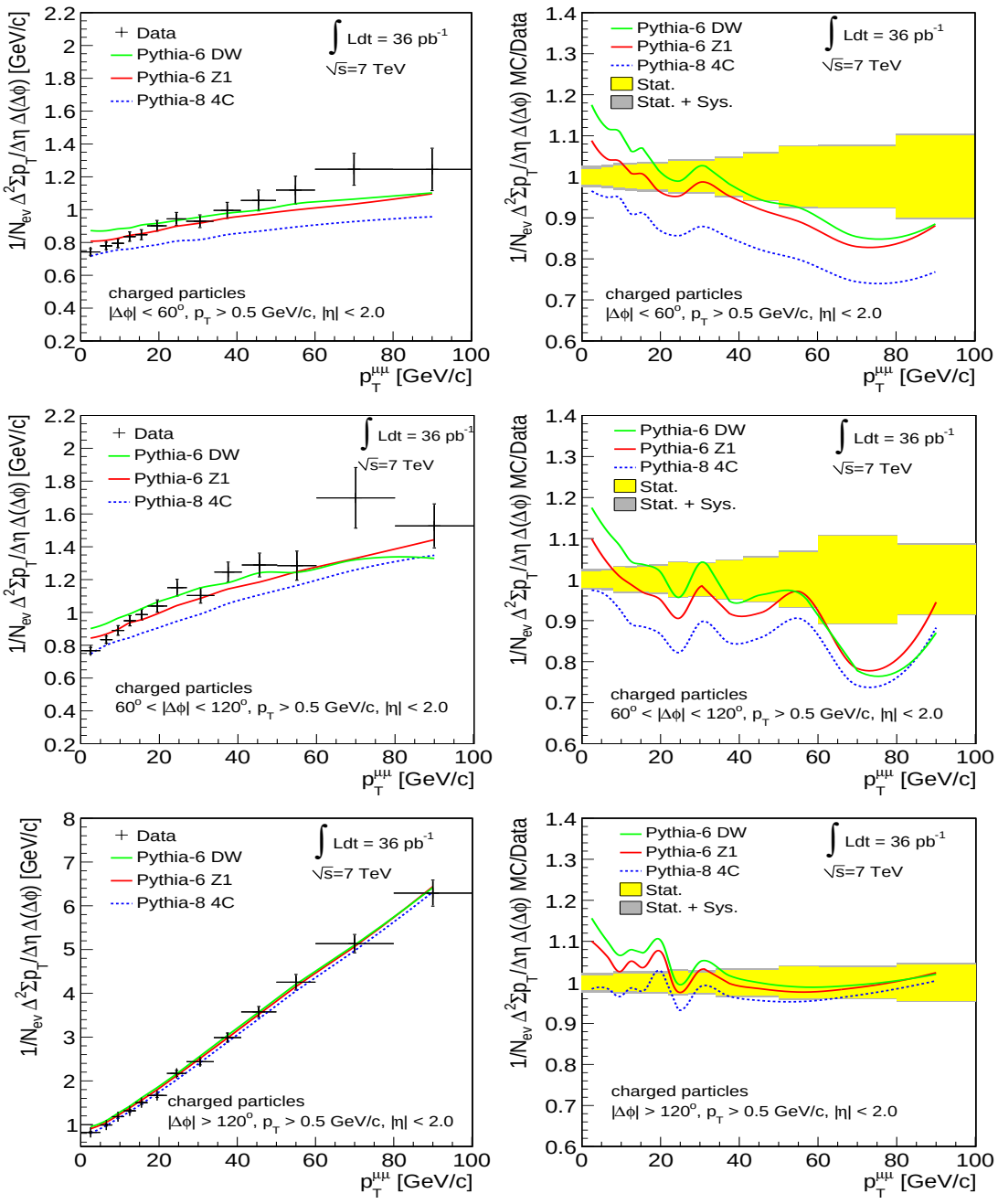

Figure 5.19: (Left column) shows the average scalar sum of p_T of the charged particles per unit pseudo-rapidity per unit $\Delta\phi$ and (right column) shows the ratio of MC prediction and measurement in experimental data for the same variable in the from (top to bottom) in *towards*, *transverse* and *away* regions respectively as a function of $p_T^{\mu\mu}$. The inner band indicates the statistical uncertainties and the outer band represent the statistical and systematic uncertainties added in quadrature.

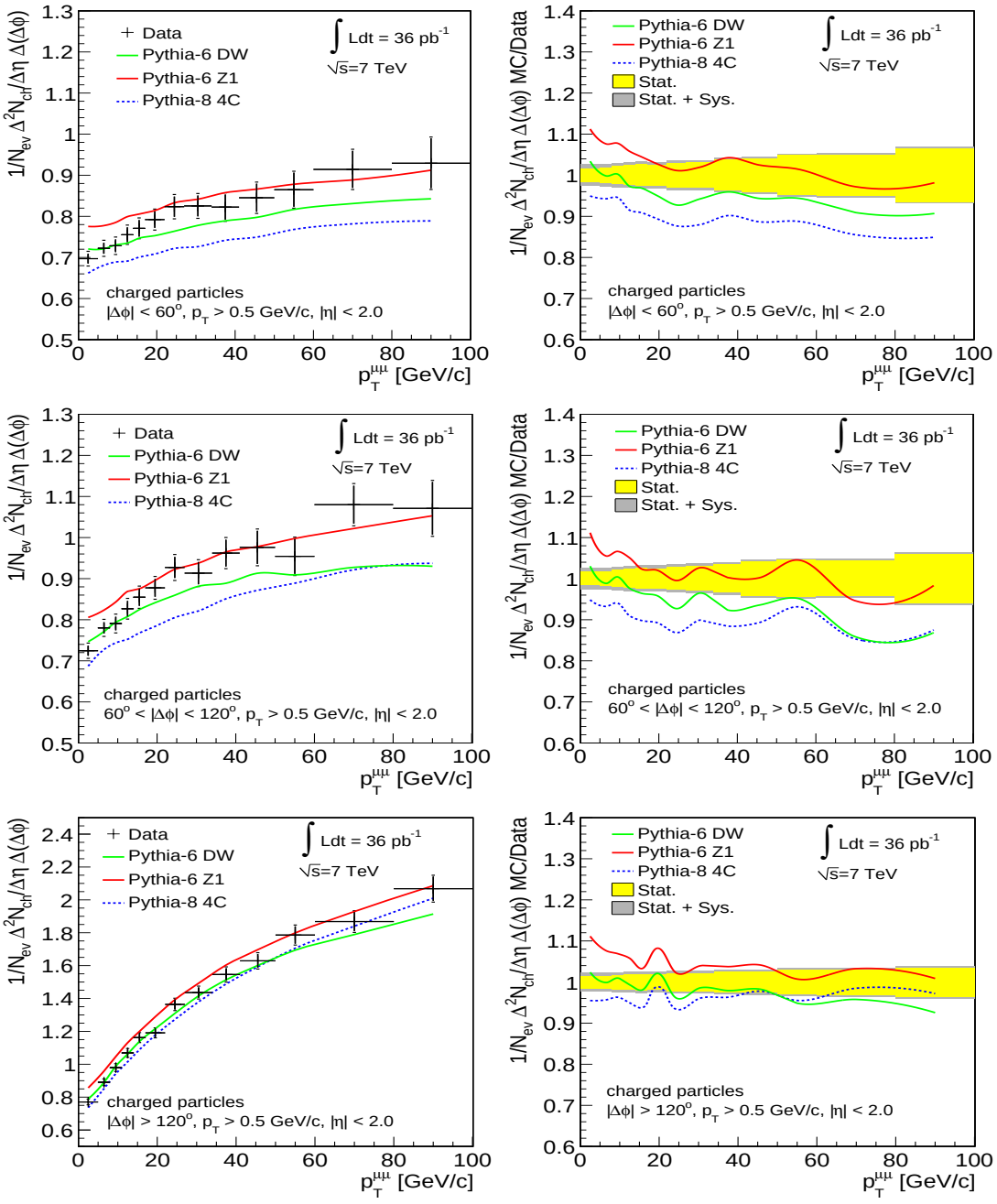

Figure 5.20: (Left column) shows the average number of charged particles per unit pseudo-rapidity per unit $\Delta\phi$ and (right column) shows the ratio of MC prediction and measurement in experimental data, from (top to bottom) in the *towards*, *transverse* and *away* regions respectively as a function of $p_T^{\mu\mu}$. The inner band indicates the statistical uncertainties and the outer band represents the statistical and the systematic uncertainties added in quadrature.

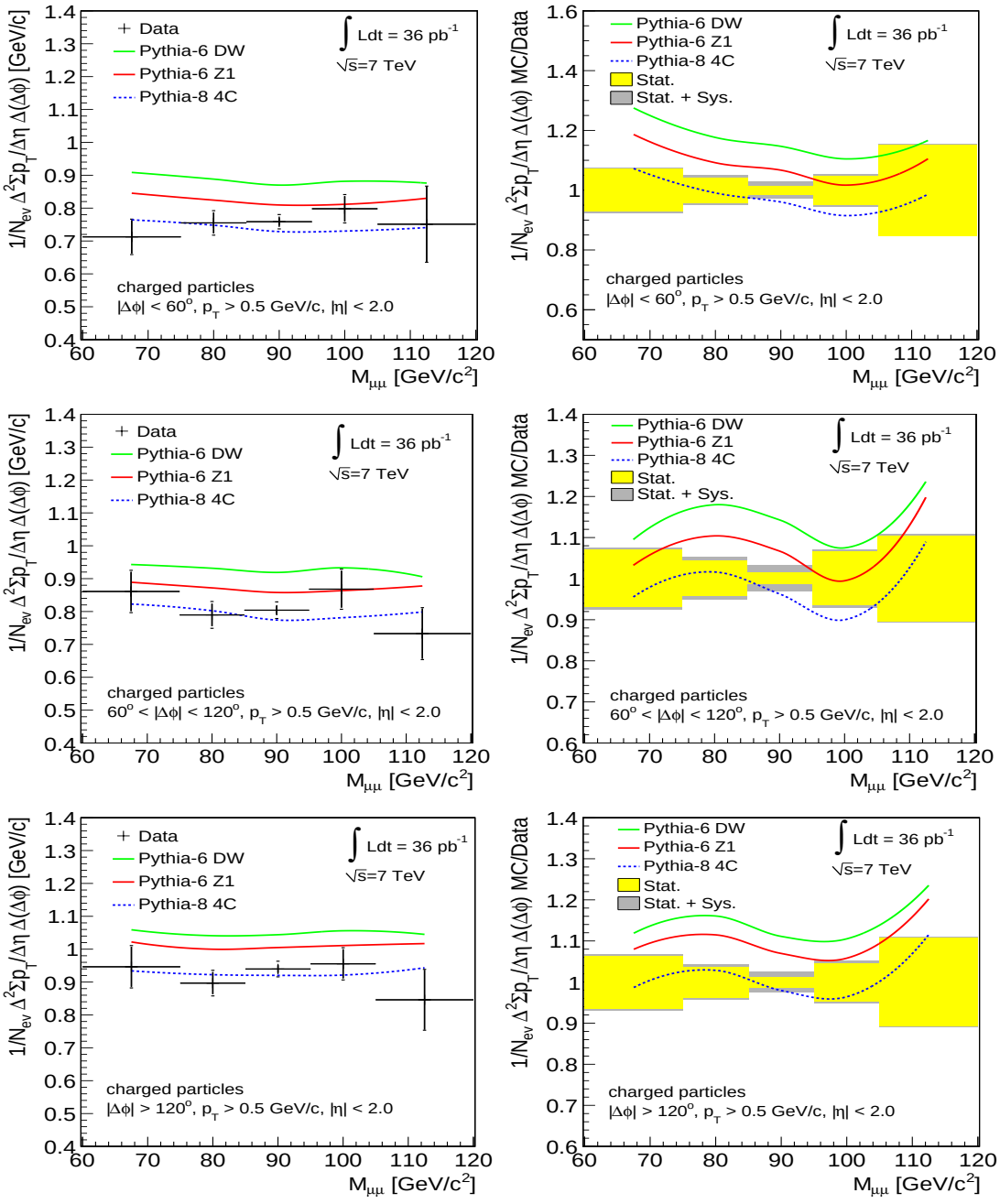

Figure 5.21: (Left column) shows the average number of charged particles per unit pseudo-rapidity per unit $\Delta\phi$ and (right column) shows the ratio of MC prediction and measurement in data, from (top to bottom) in the *towards*, *transverse* and *away* regions respectively as a function of $M_{\mu\mu}$. The inner band indicates the statistical uncertainties and the outer band represents the statistical and the systematic uncertainties added in quadrature.

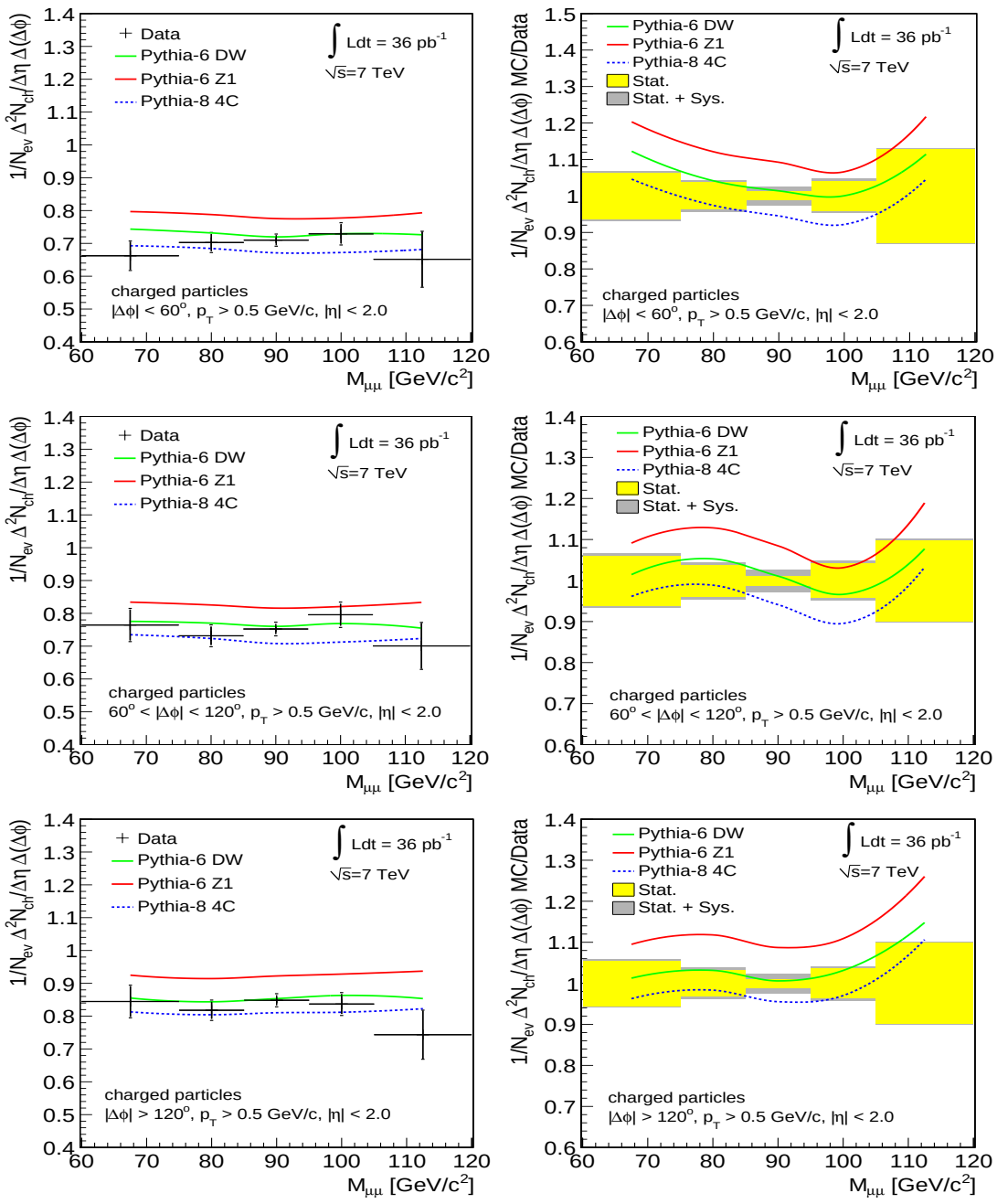

Figure 5.22: (Left column) shows the average scalar sum of p_T of the charged particles per unit pseudo-rapidity per unit $\Delta\phi$ and (right column) shows the ratio of MC prediction and measurement in experimental data for the same variable in the *away* (left), *transverse* (centre) and *towards* (right) regions as a function of $M_{\mu\mu}$. The inner error bars indicate the statistical uncertainties affecting the measurements and the outer error bars represent the statistical and systematic uncertainties added in quadrature.

6

Summary and Conclusions

The first proton-proton collisions with the center-of-mass energies of 0.9 and 2.36 TeV were observed by the CMS experiment at the Large Hadron Collider (LHC) in the year 2009. The proton-proton collisions at $E_{CM} = 7$ TeV, which is the highest energy reached so far in a particle collider, were recorded in March 2010 and marked the start up of the new era of the research in High Energy Experimental Physics. The CMS experiment at the LHC, collected data corresponding to an integrated luminosity of $\int Ldt = 36.0 \pm 1.4$ pb^{-1} during the year 2010. In this thesis work, using the data collected at CMS detector during the year 2010, we have reported the measurements of the SM processes like Drell-Yan (DY) and the understanding of the Underlying Event (UE), which are very crucial before the discovery studies at LHC.

6.1 Study of Drell-Yan process with CMS

The present analysis of the measurement of differential cross-section for the Drell-Yan (DY) production is based on the data collected using CMS experiment during the year 2010, which corresponds to an integrated luminosity of 36.0$\pm$1.4 pb^{-1}. The DY cross-section has been measured using muonic final state over the wide range of invariant mass ($M_{\mu^+\mu^-}$) of the muon pair (15-600 GeV/c^2). Events have been triggered using the single muon triggers mentioned in Section 4.3, with various thresholds on the muon transverse momentum depending on the instantaneous luminosity, with trigger

efficiency higher than 90% for the signal events. To reject the poorly reconstructed muons, cosmic muons, fake muons and the muons coming from the decay of heavy hadrons, a highly efficient and effective muon identification criteria has been used described in Section 4.3. To reduce the contribution of the jet faking as a muon and the muon coming from decay of heavy hadrons, an isolation requirement is imposed on the muons, $(\frac{I_{TH}}{p_T^\mu}) = \frac{\sum(p_T(tracks)+E_T(hcal))}{p_\mu^T} < 0.15$. The energy deposits in the electromagnetic calorimeter are not included in isolation condition, because the photons radiated from muons as Final State Radiation significantly reduce the efficiency in the Z and γ^* interference region. Event selection *i.e.* trigger, muon identification, reconstruction and isolation efficiencies are estimated using "TagAndProbe" data driven method as discussed in Section 4.5. The efficiencies measured using TagAndProbe method are found to be in good agreement with the Monte-Carlo predictions.

After all the selections, the main dominating background contribution comes from the QCD multijet process in the low mass region $\lesssim 40$ GeV/c^2, whereas $DY \to \tau\tau$ is contributing in the intermediate mass range $30 < \mathrm{M}_{\mu^+\mu^-} < 70$ GeV/c^2. In the high mass region above 90 GeV/c^2, $t\bar{t}$ and dibosons (WW, ZZ and WZ) are the dominating backgrounds. The contribution of all these background sources have been estimated using Monte-Carlo simulation, summarized in Table 4.7. However the contribution of the genuine dimuon backgrounds *i.e.* $DY \to \tau\tau$, $t\bar{t}$ and WW has also been estimated using a data driven approach, which is based on the reconstruction of an electron-muon pair in the final state in experimental data and normalizing to muon-muon final state. The $\mu^+\mu^-$ background events estimated in data using $e\mu$ method corresponds to a total of 153 $\pm$ 23 (stat) events which is in good agreement with 163 $\pm$ 13, the number of the $\mu^+\mu^-$ background events predicted by Monte-Carlo, cut-based analysis.

The experimental yield is then corrected for the detector resolution, reconstruction and selection efficiencies. The DY differential cross-section is then calculated using the equation:

$$\sigma = \frac{N_U}{A * FSR * \mathcal{L}}. \tag{6.1}$$

described in Section 4. The cross-section from experimental data is further corrected for the CMS detector acceptance and for the effects of Final State Radiation. In

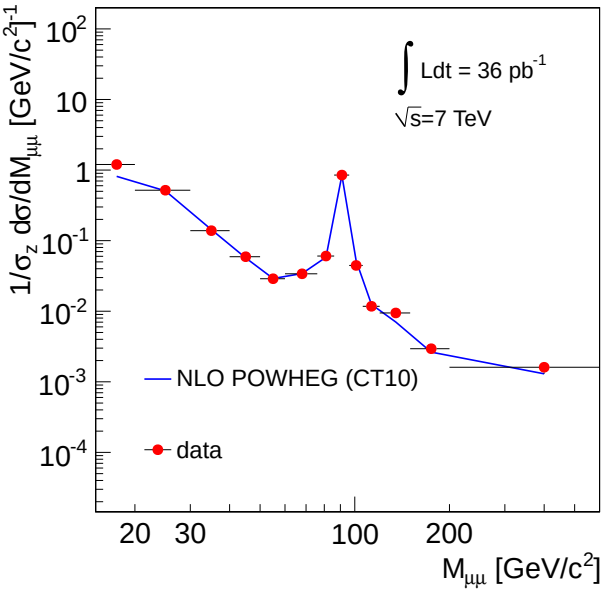

Figure 6.1: Shape of the Drell-Yan mass spectrum normalized to Z-peak compared with theory predictions at NLO with CT10 PDF set.

order to reduce the systematic uncertainty the corrected cross-section is normalized with the cross-section of the Z-mass peak region defined by 60-120 GeV/c^2 mass window. In this analysis, the cross-section of the Z-mass peak region measured is 923 ± 5 (stat) ± 6 (syst) ±4% (lumi) pb and is consistent with the CMS measurement of the Z-mass peak cross-section which is 974 ±0.7 (stat) ±0.7 (syst) ± 4% (lumi) pb. The differential cross-section is then compared bin-by-bin with the theoretical predictions at the next-to-leading order given by the POWHEG Monte-Carlo sample using CT10 [74] parton distribution function. The corrected experimental results are found to be in good agreement with the next-to-leading order theoretical predictions as shown in Figure 6.1.

6.2 Underlying Event Study using Drell-Yan

Using Drell-Yan process, we have also performed the study of the Underlying Event (UE) activity in the proton-proton collisions at the centre-of-mass energy $\sqrt{s} = 7$ TeV, using data collected with the CMS detector during the Year 2010. The DY pro-

cess with muonic final state $q\bar{q} \rightarrow \mu^+\mu^-$, provides an excellent way to study the UE activity by separating the hard interaction from the soft component and, to study the Multiparton Interactions (MPI) and Initial State Radiation contribution separately. The observables which are sensitive to the UE, the average charged particle density and the average density of the scalar sum of the transverse momentum of the charged particles, have been studied in the directions opposite to, along and transverse to the resultant direction of the muon pair, defined in the plane transverse to the beam direction. All the charged particles, excluding the pair of muons coming from Z/γ^*, with transverse momentum (p_T) above 0.5 GeV/c in the central region of the detector ($\eta < 2.0$) are considered for calculating the UE observables. Tracks are required to pass through the various quality criteria mentioned in Section 5.4, to reduce the fake, pile-up and secondaries coming from the decay of long lived particles or photon conversion. For the comparison with the predictions of various models of soft interaction, measurements are corrected for the detector effects and selection using bin-by-bin correction technique. The systematic uncertainty has been calculated in Section 5.7 for the various effects and is found to be 1-2%.

The UE activity is observed to be independent of the dimuon invariant mass in the region between 60 and 120 GeV/c^2 (after requiring $p_T^{\mu\mu} < 10$ GeV/c) as shown in Figure 5.21 and 5.22, implying a saturation of the Multiparton Interaction (MPI) at these energy scales. As shown in Figure 5.19 and 5.20 the UE observables in the *away* region show fast rise with transverse momentum of muon pair and is dominated by hard parton-parton interaction. A slow growth of the UE activity is observed in the *transverse* and *towards* region with increasing transverse momentum of the muon pair. The UE activity is observed to show the similar behaviour in the *transverse* and the *towards* regions, however the slightly higher activity in the *transverse* region is due to the spill-over contribution from *away* side recoiling activity. The dependence of the UE activity on the energy scale (invariant mass of muon pair) is well described by Pythia-6 Z2 and Pythia-8 4C, but these models fail to describe the $p_T^{\mu\mu}$ dependence. Any existing model of soft interactions does not fully describe all the features of the UE activity and requires further tuning as is shown by our study. Further, this

work shows that DY process is a powerful handle to study the UE activity in the proton-proton collisions at the LHC.

Bibliography

[1] M. Herraro, *"The Standard Model", arXiv:9812242v1 (1998).*

[2] L. Anchordoqui, *et al., "Lessons in Particle Physics", arXiv:0906:1271v1 (2009).*

[3] M. K. Gaillard, *et al., "Standard Model of Particle Physics", arXiv:9812285v1 (1998).*

[4] S. Bethke, *"Experimental tests of Asymptotic Freedom", arXiv:0606035v2 (2006).*

[5] S. L. Glashow, *"Partial-symmetries of weak interactions", Nucl. Phys. 22, 579 (1961); doi:10.1016/0029-5582(61)90469-2.*

[6] S. L. Weinberg, *"A Model of Leptons", Phys. Rev. Lett. 19, 1264 (1967); doi:10.1103/PhysRevLett.19.1264*

[7] A. Salam, *"Proc.* 8^{th} *Nobel Symposium", Stockholm, ed. N. Svartholm (Almqvist and Wiksells, Stockholm 1968) p. 367. (1968)*

[8] J. Ellis, *et al., "Radiative corrections to the masses of supersymmetric Higgs bosons", Phys Lett. B, Volume 257, p. 83-91, doi:10.1016/0370-2693(91)90863-L (1991).*

[9] G.A. Blair, *"Precision SUSY and the GUT Scale", 33rd SLAC Summer Institute on Particle Physics (SSI 2005), 25 July-5 August 2005.*

[10] Y. Ashie, *et al., "Evidence for an oscillatory signature in atmospheric neutrino oscillation", arXiv:0404034v1 (2004).*

[11] J. H. Christenson, *et al., "Observation of Massive Muon Pairs in Hadron Collisions", Phys. Rev. Lett. 25, 1523 (1970) and "Observation of Muon Pairs in High-Energy Hadron Collisions", Phys. Rev. Lett. 25, 1523 (1970).*

[12] P. E. Reimer, *et al., "Exploring the partonic structure of hadrons through Drell-Yan process", arXiv:0704.3621v2 (2007).*

[13] J. J. Aubert, *et al., "Experimental Observation of a Heavy Particle", Phys. Rev. Lett. 33, 1404 (1974).*

[14] S. D. Drell, *et al., "Massive Lepton-Pair Production in Hadron-Hadron Collisions at High Energies", Phys. Rev. Lett. 25, 316 (1970) and Ann. Phys. (N.Y.), 66, 578 (1971).*

[15] J. D. Bjorken, *et al., "Inelastic Electron-Proton and γ-Proton Scattering and the Structure of the Nucleon", Phys. Rev. 185, 1975 (1969).*

[16] R. P. Feynman, *"Very High-Energy Collisions of Hadrons", Phys. Rev. Lett. 23, 1415 (1969).*

[17] U. Baur, *et al., "Electroweak radiative corrections to neutral-current Drell-Yan processes at hadron colliders", Phys. Rev. D 65 (2002); doi:10.1103/PhysRevD.65.033007.*

[18] A. Martin, *et al., "Parton Distributions for the LHC", Eur.Phys.J. C63 189, arXiv:0901.0002 (2009).*

[19] Y. K. Kim, *et al., "Initial state gluon radiation studies on Drell-Yan data for top-pair production in hadron collider", CDF/PHYS/CDFR/6804 (2004).*

[20] S. Haywood, *et al., "ElectroWeak Physics", arXiv:0003275 (2000).*

[21] H. Schellman, *"Practical Aspects of Collider Physics, Institute of Advanced Studies", Princeton, NJ. http://www.sns.ias.edu/pitp/index2005.html (2005).*

[22] The CDF Collaboration, *"Studying the underlying event in Drell-Yan and high transverse momentum jet production at the Tevatron", arXiv:1003.3146 (2010).*

[23] The CMS Collaboration, *"The CERN Large Hadron Collider:Accelerator and Experiments", JINST 0803 S08001 (2008).*

[24] The CMS Collaboration, *"The CMS experiment at the CERN LHC", JINST 0803 S08004 (2008).*

[25] The CMS Collaboration, *"The ATLAS Experiment at the CERN Large Hadron Collider", JINST 0803 S08003 (2008).*

[26] The CMS Collaboration, *"The LHCb Detector at the LHC", JINST 0803 S08005 (2008).*

[27] The CMS Collaboration, *"The TOTEM Experiment at the CERN Large Hadron Collider", JINST 0803 S08007 (2008).*

[28] The CMS Collaboration, *"The ALICE experiment at the CERN LHC", 2008 JINST 0803 S08002 (2008).*

[29] The CMS Collaboration, *"Tracking and Primary Vertex Results in First 7TeV Collisions", CMS Physics Analysis Summary TRK-10-005 (2010).*

[30] A. A. Annenkov, *et al., "Lead tungstate scintillation material", Nucl. Instrum. Meth. A 490 30 (2002).*

[31] The CMS Collaboration, *"Energy resolution of the barrel of the CMS electromagnetic calorimeter", JINST 2 P04004 (2007).*

[32] The CMS Collaboration, *et al., "Design, performance and calibration of the CMS hadron-outer calorimeter", Eur. Phys. J. C 57: 653663 (2008); doi 10.1140/epjc/s10052-008-0756-6.*

[33] The CMS Collaboration, *et al., "The CMS muon project, technical design report", CERN-LHCC-97-032, http://cdsweb.cern.ch/record/343814 (1997).*

[34] The CMS Collaboration, *et al., "Performance of the CMS drift tube chambers with cosmic rays", JINST 5 T03015 (2010).*

[35] The CMS Collaboration, *et al., "Performance of the CMS cathode strip chambers with cosmic rays", JINST 5 T03018 (2010).*

[36] The CMS Collaboration, *et al., "Performance study of the CMS barrel resistive plate chambers with cosmic rays", JINST 5 T03017 (2010).*

[37] R. Santonico, *et al., "Development of resistive plate counters", Nucl. Instrum. Meth. 187 (1981) 377.*

[38] R. Cardarelli, *et al., "Performance of a resistive plate chamber operating with pure CF_3Br", Nucl. Instrum. Meth. A 333 99 (1993).*

[39] The CMS Collaboration, *"Measurement of Momentum Scale and Resolution using Low-mass Resonances and Cosmic Ray Muons", CMS Physics Analysis Summary TRK-10-004 (2010).*

[40] The CMS Collaboration, *"The TriDAS project, technical design report. Volume 1: The level-1 trigger", CERN-LHCC-2000-038, http://cdsweb.cern.ch/record/706847 (2000).*

[41] The CMS Collaboration, *"The TriDAS project, technical design report. Volume 2: Data acquisition and high-level trigger technical design report", CERN-LHCC-2002-026, http://cdsweb.cern.ch/record/578006 (2002).*

[42] T. Sjöstrand, *et al., "Multiple parton-parton interactions in an impact parameter picture", Phys. Lett. B188 149 (1987).*

[43] T. Sjöstrand, *et al., "PYTHIA 6.2 physics and manual", arXiv:0108264v1 (2001).*

[44] T. Sjöstrand, *et al., "PYTHIA 6.4 physics and manual", JHEP 05 (2006) 026, arXiv:0603175.*

[45] T. Sjöstrand, *et al., "A Brief Introduction to PYTHIA 8.1", Comput. Phys. Commun. 178 (2008) 852; doi:10.1016/j.cpc.2008.01.036.*

[46] R. Corke, *"Multiple Interactions in Pythia 8", arXiv:0901.2852 (2009).*

[47] B. Andersson, *et al., "General Model For Jet Fragmentation", Z. Phys. C 20, 317 (1983).*

[48] T. Affolder, *et al., " Charged jet evolution and the underlying event in proton-antiproton collisions at 1.8 TeV", Phys. Rev. D65, 092002 (2002).*

[49] R. Field, *"Studying the underlying event at CDF and the LHC", arXiv:1003.4220 (2008).*

[50] The CDF Collaboration, *"Studying the underlying event in Drell-Yan and high transverse momentum jet production at the Tevatron", arXiv:1003.3146 (2010).*

[51] D. Acosta, *et al., "Underlying event in hard interactions at the Fermilab Tevatron $p\bar{p}$ collider", Phys. Rev. D70, 072002 (2004).*

[52] The CMS Collaboration, *"Measurement of the Underlying Event Activity at the LHC with $\sqrt{s}$=7 TeV and Comparison with $\sqrt{s}$ = 0.9 TeV", arXiv:1107.0330 (2011).*

[53] H.L. Lai, *et al., "Global QCD Analysis of Parton Structure of the Nucleon: CTEQ5 Parton Distributions", arXiv:9903282 (1999).*

[54] J.Pumplin, *et al.,"New Generation of Parton Distributions with Uncertainties from Global QCD Analysis", arXiv:0201195v3 (2008).*

[55] R. Field, *et al., "Physics at the Tevatron", Acta Phys. Polon. B 39 2611 (2008).*

[56] A. Buckley, *et al., "Systematic event generator tuning for the LHC", Eur. Phys. J. C 65 331, arXiv:0907.2973 (2010); doi:10.1140/epjc/s10052-009-1196-7.*

[57] The ATLAS Collaboration, *et al., "Charged-particle multiplicities in pp interactions measured with the ATLAS detector at the LHC", arXiv:1012.5104 (2010).*

[58] R.Corke, *et al.,"Interleaved Parton Showers and Tuning Prospects", arXiv:1011:1759v1 (2010).*

[59] G. Corcella, *et. al., "HERWIG 6: an event generator for hadron emission reactions with interfering gluons (including supersymmetric processes)", JHEP 01 (2001) 010, arXiv:0011363.*

[60] S. Frixione, *et al., "Matching NLO QCD computations with Parton Shower simulations: the POWHEG method", JHEP 11 (2007) 070, doi:10.1088/1126-6708/2007/11/070.*

[61] E. Boos, *et. al., "Generic user process interface for event generators", arXiv:0109068 (2001).*

[62] Z.Was, *"TAUOLA the library for tau lepton decay and KKMC/KORALB/KORALZ/... status report", arXiv:0011305v1 (2000).*

[63] S.Agostinelli, *et al., "Nuclear Instruments and Methods in Physics Research", A 506, 250 (2003).*

[64] *http://lcgapp.cern.ch/project/simu/HepMC/20400/HepMC2_user_manual.pdf*

[65] T.Miao, *et al.,"Beam Spot determination using tracks", CMS Analysis Note, CMS-AN-2007/021, (2007).*

[66] R. Fruewirth, *et al., "Adaptive Vertex Fitting",CMS Analysis Note, CMS-AN-2007/008 (2008).*

[67] D'Hondt, *et.al, "Sensitivity of Robust Vertex Fitting Algorithms", CMS Analysis Note, CMS-AN-2004/002 (2004).*

[68] W. Adam, *et al., "Track reconstruction in the CMS tracker", CMS Analysis Note, CMS-AN-2006/04 (2006).*

[69] S. Cucciarelli, *et al., "Track reconstruction, primary vertex finding and seed genneration with the Pixel Detector", CMS Analysis Note, CMS-AN-2006/026 (2006).*

[70] G. Abbiendi, *et al., "Muon Reconstruction in the CMS detector", CMS Analysis Note CMS-AN-2008/097 (2008).*

[71] G. Bruno, *et al., "Local reconstruction in the muon detectors", CMS Analysi Note CMS-AN-2002/043 (2002).*

[72] R. Frühwirth, *et al., "Application of Kalman Filtering to Track and Vertex Fitting", Nucl.Instrum. and Methods A262 (1987) 444; doi:10.1016/0168-9002(87)90887-4.*

[73] V. Innocente, *et al., "GEANE: Average Tracking and Error Propagation Package", CERN Program Library, IT-ASD W5013-E (1991).*

[74] H. Lai, *et al., "New parton distributions for collider physics", Phys. Rev. D82 (2010) 074024; doi:10.1103/PhysRevD.82.074024.*

[75] A. Ryd, *et al., "EvtGen: A Monte Carlo Generator for B-Physics", BAD 522 V6 (2004).*

[76] S. D. Drell, *et al., "Massive Lepton-Pair Production in Hadron-Hadron Collisions at High Energies", Phys. Rev. Lett. 25, 316 (1970) and Ann. Phys. (N.Y.), 66, 578 (1971).*

[77] S.Haywood, *et al., "ELECTROWEAK PHYSICS",arXiv:0003275 (2000).*

[78] R. Gavin, *et al., "FEWZ 2.0: A code for hadronic Z production at 986 next-to-next-to-leading order", arXiv:1011.3540v1 (2010).*

[79] The CMS Collaboration, *"Measurements of Inclusive W and Z Cross Sections in pp Collisions at $\sqrt{s}$ = 7 TeV", arXiv:1012.2466v2 (2010).*

[80] N. Adam, *et al., "Generic Tag and Probe Tool for Measuring Efficiency at CMS with Early Data", CMS Analysis Note CMS-AN-2009/111 (2009).*

[81] A. Juodagalvis, *et al., "Drell-Yan Differential Cross Section Measurement at 7 TeV in the Electron Channel", CMS-Analysis Note, CMS-AN-2011/011 (2011).*

[82] T. Adye, *"Unfolding algorithms and tests using RooUnfold", arXiv:1105.1160v1 (2011).*

[83] D. Bourilkov, *et al., "LHAPDF: PDF use from the Tevatron to the LHC", arXiv:0605240 (2006).*

[84] A. Kubik, *et al., "Studies of Final State Radiation in the Drell-Yan Di-Muon Channel", CMS Analysis Note, CMS-AN-2011/044 (2011).*

[85] The CMS Collaboration, *"Measurement of the Inclusive W and Z Production Cross Sections in pp Collisions at $\sqrt{s}$ = 7 TeV", arXiv:1107.4789v1 (2011).*

[86] The CMS Collaboration, *"Performance of muon identification in pp collisions at $\sqrt{s}$ = 7 TeV", CMS Physics Analysis Summary MUO-10-002 (2010).*

[87] The CMS Collaboration, *"Tracking and Vertexing Results from First Collisions", CMS Physics Analysis Summary TRK-10-001 (2010).*

Publications/Conferences

Publications/CMS Public Notes

1. Monika Jindal, J.B.Singh, *et al., "Drell-Yan process at Large Hadron Collider", Pramana-Journal of Physics, Vol.76, No.3, pp. 421-430 (2011).*

2. Monika Jindal, J.B.Singh, *et al., "Estimation of level-1 trigger efficiency of RPC detectors in CMS experiment using cosmic muon data", Nuclear Inst. and Methods in Physics Research,A, doi:10.1016/j.nima.2010.08.098, (2010).*

3. The CMS Collaboration, *"Measurement of the Underlying Event Activity in the Drell-Yan process in proton-proton collisions at* $\sqrt{s}$ *= 7 TeV", CMS Physics Analysis Summary, QCD-10-040 (2011).*

4. The CMS Collaboration, *"Measurement of the Drell-Yan Cross Section in pp Collisions at* $\sqrt{s}$ *= 7 TeV", arXiv:1108.0566v1, submitted to J. High Energy Phys.*

5. Monika Jindal, J.B.Singh, *et al., "Estimation of level-1 trigger efficiency of RPC detectors in CMS experiment using cosmic muon data", CMS conference Report, CMS CR-2010/060 (2010).*

CMS Analysis Notes

1. Monika Jindal, J.B. Singh, *et.al, "Measurement of the Underlying Event Activity using Drell-Yan process at the LHC with* $\sqrt{s}$*= 7 TeV", CMS Analysis Note CMS AN-2011/384 (2011).*

2. Monika Jindal, J.B. Singh, *et al., "Drell-Yan Differential Cross Section Measurement at 7 TeV in the Muon Channel", CMS Analysis Note CMS AN-2011/013 (2011)*

3. Monika Jindal, J.B. Singh, *et al., "Study of Underlying Events in Drell-Yan process", CMS Analysis Note CMS AN-2010/355 (2010).*

4. Monika Jindal, J.B.Singh, *et al., "Towards a Measurement of the Drell-Yan Production Cross Sections in pp Collisions at* $\sqrt{s}$*= 10 TeV with Di-muons in CMS", CMS Analysis Note CMS AN-2009/151 (2009).*

5. Monika Jindal, J.B.Singh, *et al., "Study of the Drell-Yan Process using Horace Event Generator", CMS Analysis Note CMS AN-2009/113 (2009).*

Papers presented in the Conferences

1. M. Jindal, J.B. Singh, *et al., "Measurement of the Drell-Yan differential cross-section* $d\sigma/dM$ *at* $\sqrt{s}$ *= 7 TeV", XXV International Symposium On Lepton Photon Interactions at High Energies, August 22-27, 2011, TIFR, Mumbai, INDIA.*

2. M. Jindal, J.B. Singh, *et al., "Measurement of the Underlying Event using the Drell-Yan process at the LHC with* $\sqrt{s}$ *= 7 TeV", XXV International Symposium On Lepton Photon Interactions at High Energies, August 22-27, 2011, TIFR, Mumbai, INDIA.*

3. M. Jindal, J.B. Singh, *et al., "Estimation of level-1 trigger efficiency of RPC detectors in CMS experiment using cosmic muon data", X Workshop on Resistive Plate Chambers and Related Detectors, Darmstadt, Germany (2010).*

CMS Publications

1. The CMS Collaboration, *"Measurement of the Production Cross Section of Pairs of Isolated Photons in pp collisions at sqrt(s)=7 TeV", http://cdsweb.cern.ch/record/1394260.*

2. The CMS Collaboration, *"Measurement of the Rapidity and Transverse Momentum Distributions of Z Bosons in pp Collisions at $\sqrt{s}$=7 TeV", http://arxiv.org/abs/1110.4973, Phys. Rev. D.*

3. The CMS Collaboration, *"Jet Production Rates in Association with W and Z Bosons in pp Collisions at $\sqrt{s}$ = 7 TeV", http://arxiv.org/abs/1110.3226, J. High Energy Phys.*

4. The CMS Collaboration, *"Measurement of the weak mixing angle with the Drell-Yan process in proton-proton collisions at the LHC", http://arxiv.org/abs/1110.2682, Phys. Rev. D.*

5. The CMS Collaboration, *"Measurement of energy flow at large pseudorapidities in pp collisions at $\sqrt{s}$ = 0.9 and 7 TeV", http://arxiv.org/abs/1110.0211, J. High Energy Phys.*

6. The CMS Collaboration, *"Forward Energy Flow, Central Charged-Particle Multiplicities, and Pseudorapidity Gaps in W and Z Boson Events from pp Collisions at $\sqrt{s}$ = 7 TeV", http://arxiv.org/abs/1110.0181, Eur. Phys. J. C.*

7. The CMS Collaboration, *"Search for a Vector-like Quark with Charge 2/3 in t + Z Events from pp Collisions at $\sqrt{s}$ = 7 TeV", http://arxiv.org/abs/1109.4985, Phys. Rev. Lett.*

8. The CMS Collaboration, *"Search for Supersymmetry at the LHC in Events with Jets and Missing Transverse Energy", http://arxiv.org/abs/1109.2352, Phys. Rev. Lett.*

9. The CMS Collaboration, *"Measurement of the $t\bar{t}$ Production Cross Section in pp Collisions at 7 TeV in Lepton + Jets Events Using b-quark Jet Identification", http://arxiv.org/abs/1108.3773.*

10. The CMS Collaboration, *"Measurement of the Differential Cross Section for*

Isolated Prompt Photon Production in pp Collisions at 7 TeV",
http://arxiv.org/abs/1108.2044, Phys. Rev. D, 84: 052011, 2011.

11. The CMS Collaboration, *"Measurement of the Drell-Yan Cross Section in pp Collisions at* $\sqrt{s}$ *= 7 TeV",*
http://arxiv.org/abs/1108.0566, J. High Energy Phys.

12. The CMS Collaboration, *"Search for* $B_s^0 \to \mu^+\mu^-$ *and* $B^0 \to \mu^+\mu^-$ *decays in pp collisions at* $\sqrt{s}$ *= 7 TeV",*
http://arxiv.org/abs/1107.5834, Phys. Rev. Lett.

13. The CMS Collaboration, *"Dependence on pseudorapidity and on centrality of charged hadron production in PbPb collisions at* $\sqrt{s_{NN}}$ *= 2.76 TeV",*
http://arxiv.org/abs/1107.4800, J. High Energy Phys., 08: 141, 2011.

14. The CMS Collaboration, *"Search for Resonances in the Dijet Mass Spectrum from 7 TeV pp Collisions at CMS",*
http://arxiv.org/abs/1107.4771, Phys. Lett. B, 704: 123-142, 2011.

15. The CMS Collaboration, *"Measurement of the Inclusive W and Z Production Cross Sections in pp Collisions at* $\sqrt{s}$ *= 7 TeV",*
http://arxiv.org/abs/1107.4789, J. High Energy Phys.

16. The CMS Collaboration, *"Search for Three-Jet Resonances in pp Collisions at* $\sqrt{s}$ *= 7 TeV",*
http://arxiv.org/abs/1107.3084, Phys. Rev. Lett., 107: 101801, 2011.

17. The CMS Collaboration, *"Search for supersymmetry in pp collisions at* $\sqrt{s}$*=7 TeV in events with a single lepton, jets, and missing transverse momentum",*
http://arxiv.org/abs/1107.1870, J. High Energy Phys., 08: 156, 2011.

18. The CMS Collaboration, *"A search for excited leptons in pp Collisions at* $\sqrt{s}$ *= 7 TeV",*
http://arxiv.org/abs/1107.1773, Phys. Lett. B, 704: 143-162, 2011.

19. The CMS Collaboration, *"Inclusive search for squarks and gluinos in pp collisions at $\sqrt{s}$ = 7 TeV"*, *http://arxiv.org/abs/1107.1279, Phys. Rev. D.*

20. The CMS Collaboration, *"Measurement of the Underlying Event Activity at the LHC with $\sqrt{s}$ = 7 TeV and Comparison with $\sqrt{s}$ = 0.9 TeV"*, *http://arxiv.org/abs/1107.0330, J. High Energy Phys., 09: 109, 2011.*

21. The CMS Collaboration, *"Search for New Physics with a Mono-Jet and Missing Transverse Energy in pp Collisions at $\sqrt{s}$ = 7 TeV"*, *http://arxiv.org/abs/1106.4775, Phys. Rev. Lett.*

22. The CMS Collaboration, *"Search for New Physics with Jets and Missing Transverse Momentum in pp collisions at $\sqrt{s}$ = 7 TeV"*, *http://arxiv.org/abs/1106.4503, J. High Energy Phys., 08: 155, 2011.*

23. The CMS Collaboration, *"Measurement of the B_s^0 Production Cross Section with $B_s^0 \to J/\psi\phi$ Decays in pp Collisions at $\sqrt{s}$ = 7 TeV"*, *http://arxiv.org/abs/1106.4048, Phys. Rev. D, 84: 052008, 2011.*

24. The CMS Collaboration, *"Search for Supersymmetry in Events with b Jets and Missing Transverse Momentum at the LHC"*, *http://arxiv.org/abs/1106.3272, J. High Energy Phys., 07: 113, 2011.*

25. The CMS Collaboration, *"Measurement of the t-channel single top quark production cross section in pp collisions at $\sqrt{s}$ = 7 TeV"*, *http://arxiv.org/abs/1106.3052, Phys. Rev. Lett., 107: 091802, 2011.*

26. The CMS Collaboration, *"Search for Light Resonances Decaying into Pairs of Muons as a Signal of New Physics"*, *http://arxiv.org/abs/1106.2375, J. High Energy Phys., 07: 098, 2011.*

27. The CMS Collaboration, *"Search for Same-Sign Top-Quark Pair Production at $\sqrt{s}$ = 7 TeV and Limits on Flavour Changing Neutral Currents in the Top*

Sector",
http://arxiv.org/abs/1106.2142, J. High Energy Phys., 08: 005, 2011.

28. The CMS Collaboration, *"Search for Physics Beyond the Standard Model Using Multilepton Signatures in pp Collisions at $\sqrt{s}$ =7 TeV",*
http://arxiv.org/abs/1106.0933, Phys. Lett. B, 704: 411-433, 2011.

29. The CMS Collaboration, *"Measurement of the $t\bar{t}$ Production Cross Section in pp Collisions at $\sqrt{s}$=7 TeV using the Kinematic Properties of Events with Leptons and Jets",*
http://arxiv.org/abs/1106.0902, Eur. Phys. J. C, 71: 1721, 2011.

30. The CMS Collaboration, *"Measurement of the Ratio of the 3-jet to 2-jet Cross Sections in pp Collisions at $\sqrt{s}$ = 7 TeV",*
http://arxiv.org/abs/1106.0647, Phys. Lett. B, 702: 336-354, 2011.

31. The CMS Collaboration, *"Measurement of the Inclusive Jet Cross Section in pp Collisions at $\sqrt{s}$ = 7 TeV",*
http://arxiv.org/abs/1106.0208, Phys. Rev. Lett., 107: 132001, 2011.

32. The CMS Collaboration, *"Measurement of the $t\bar{t}$ production cross section and the top quark mass in the dilepton channel in pp collisions at $\sqrt{s}$ =7 TeV",*
http://arxiv.org/abs/1105.5661, J. High Energy Phys., 07: 049, 2011.

33. The CMS Collaboration, *"Search for First Generation Scalar Leptoquarks in the $e\nu jj$ Channel in pp Collisions at $\sqrt{s}$ = 7 TeV",*
http://arxiv.org/abs/1105.5237, Phys. Lett. B, 703: 246-266, 2011.

34. The CMS Collaboration, *"Indications of Suppression of Excited Υ States in Pb-Pb Collisions at $\sqrt{s_{NN}}$ = 2.76 TeV",*
http://arxiv.org/abs/1105.4894, Phys. Rev. Lett., 107: 052302, 2011.

35. The CMS Collaboration, *"Measurement of $W\gamma$ and $Z\gamma$ production in pp collisions at $\sqrt{s}$ = 7 TeV",*
http://arxiv.org/abs/1105.2758, Phys. Lett. B, 701: 535555, 2011.

36. The CMS Collaboration, *"Long-range and short-range dihadron angular correlations in central PbPb collisions at $\sqrt{s_{NN}}$ = 2.76 TeV", http://arxiv.org/abs/1105.2438, J. High Energy Phys., 07: 076, 2011.*

37. The CMS Collaboration, *"Search for supersymmetry in events with a lepton, a photon, and large missing transverse energy in pp collisions at $\sqrt{s}$ = 7 TeV", http://arxiv.org/abs/1105.3152, J. High Energy Phys., 06: 093, 2011.*

38. The CMS Collaboration, *"Measurement of the Polarization of W Bosons with Large Transverse Momenta in W+Jets Events at the LHC", http://arxiv.org/abs/1104.3829, Phys. Rev. Lett., 107: 021802, 2011.*

39. The CMS Collaboration, *"Charged particle transverse momentum spectra in pp collisions at $\sqrt{s}$ = 0.9 and 7 TeV", http://arxiv.org/abs/1104.3547, J. High Energy Phys., 08: 086, 2011.*

40. The CMS Collaboration, *"Search for new physics with same-sign isolated dilepton events with jets and missing transverse energy at the LHC", http://arxiv.org/abs/1104.3168, J. High Energy Phys., 06: 077, 2011.*

41. The CMS Collaboration, *"Measurement of the B^0 Production Cross Section in pp Collisions at $\sqrt{s}$ = 7 TeV", http://arxiv.org/abs/1104.2892, Phys. Rev. Lett., 106: 252001, 2011.*

42. The CMS Collaboration, *"Measurement of the differential dijet production cross section in proton-proton collisions at $\sqrt{s}$=7 TeV", http://arxiv.org/abs/1104.1693, Phys. Lett. B, 700: 187206, 2011.*

43. The CMS Collaboration, *"Search for Neutral Minimal Supersymmetric Standard Model Higgs Bosons Decaying to Tau Pairs in pp Collisions at $\sqrt{s}$=7 TeV", http://arxiv.org/abs/1104.1619, Phys. Rev. Lett., 106: 231801, 2011.*

44. The CMS Collaboration, *"Measurement of the Inclusive Z Cross Section via Decays to Tau Pairs in pp Collisions at $\sqrt{s}$ = 7 TeV", http://arxiv.org/abs/1104.1617, J. High Energy Phys., 08: 117, 2011.*

45. The CMS Collaboration, *"Search for Large Extra Dimensions in the Diphoton Final State at the Large Hadron Collider"*, *http://arxiv.org/abs/1103.4279, J. High Energy Phys., 05: 085, 2011.*

46. The CMS Collaboration, *"Measurement of the lepton charge asymmetry in inclusive W production in pp collisions at $\sqrt{s}$ = 7 TeV"*, *http://arxiv.org/abs/1103.3470, J. High Energy Phys., 04: 050, 2011.*

47. The CMS Collaboration, *"Search for Physics Beyond the Standard Model in Opposite-sign Dilepton Events in pp Collisions at $\sqrt{s}$ = 7 TeV"*, *http://arxiv.org/abs/1103.1348, J. High Energy Phys., 06: 026, 2011.*

48. The CMS Collaboration, *"Search for Resonances in the Dilepton Mass Distribution in pp Collisions at $\sqrt{s}$ = 7 TeV"*, *http://arxiv.org/abs/1103.0981, J. High Energy Phys., 05: 093, 2011.*

49. The CMS Collaboration, *"Search for Supersymmetry in pp Collisions at $\sqrt{s}$ = 7 TeV in Events with Two Photons and Missing Transverse Energy"*, *http://arxiv.org/abs/1103.0953, Phys. Rev. Lett., 106: 211802, 2011.*

50. The CMS Collaboration, *"Search for a W' boson decaying to a muon and a neutrino in pp collisions at $\sqrt{s}$ = 7 TeV"*, *http://arxiv.org/abs/1103.0030, Phys. Lett. B, 701: 160179, 2011.*

51. The CMS Collaboration, *"Study of Z boson production in PbPb collisions at $\sqrt{s_{NN}}$ = 2.76 TeV"*, *http://arxiv.org/abs/1102.5435, Phys. Rev. Lett., 106: 212301, 2011.*

52. The CMS Collaboration, *"Measurement of W^+W^- Production and Search for the Higgs Boson in pp Collisions at $\sqrt{s}$ = 7 TeV"*, *http://arxiv.org/abs/1102.5429, Phys. Lett. B, 699: 25-47, 2011.*

53. The CMS Collaboration, *"Search for a Heavy Bottom-like Quark in pp Collisions at $\sqrt{s}$ = 7 TeV"*, *http://arxiv.org/abs/1102.4746, Phys. Lett. B, 701: 204223, 2011.*

54. The CMS Collaboration, *"Strange Particle Production in pp collisions at $\sqrt{s}$ = 0.9 and 7 TeV"*,
http://arxiv.org/abs/1102.4282, J. High Energy Phys., 05: 064, 2011.

55. The CMS Collaboration, *"Measurement of $B\overline{B}$ angular correlations based on secondary vertex reconstruction at $\sqrt{s}$=7 TeV"*,
http://arxiv.org/abs/1102.3194, J. High Energy Phys., 03: 136, 2011.

56. The CMS Collaboration, *"Measurement of Dijet Angular Distributions and Search for Quark Compositeness in pp Collisions at $\sqrt{s}$ = 7 TeV"*,
http://arxiv.org/abs/1102.2020, Phys. Rev. Lett., 106: 201804, 2011.

57. The CMS Collaboration, *"Observation and studies of jet quenching in PbPb collisions at $\sqrt{s_{NN}}$ = 2.76 TeV"*,
http://arxiv.org/abs/1102.1957, Phys. Rev. C, 84: 024906, 2011.

58. The CMS Collaboration, *"First Measurement of Hadronic Event Shapes in pp Collisions at $\sqrt{s}$=7 TeV"*,
http://arxiv.org/abs/1102.0068, Phys. Lett. B, 699: 48-67, 2011.

59. The CMS Collaboration, *"Dijet Azimuthal Decorrelations in pp Collisions at $\sqrt{s}$ = 7 TeV"*,
http://arxiv.org/abs/1101.5029, Phys. Rev. Lett., 106: 122003, 2011.

60. The CMS Collaboration, *"Measurement of BoseEinstein Correlations in pp Collisions at $\sqrt{s}$ = 0.9 and 7 TeV"*,
http://arxiv.org/abs/1101.3518, J. High Energy Phys., 05: 029, 2011.

61. The CMS Collaboration, *"Inclusive b-hadron production cross section with muons in pp collisions at $\sqrt{s}$ = 7 TeV"*,
http://arxiv.org/abs/1101.3512, J. High Energy Phys., 03: 090, 2011.

62. The CMS Collaboration, *"Search for Heavy Stable Charged Particles in pp collisions at $\sqrt{s}$ = 7 TeV"*,
http://arxiv.org/abs/1101.1645, J. High Energy Phys., 03: 024, 2011.

63. The CMS Collaboration, *"Search for Supersymmetry in pp Collisions at 7 TeV in Events with Jets and Missing Transverse Energy"*, *http://arxiv.org/abs/1101.1628, Phys. Lett. B, 698: 196218, 2011.*

64. The CMS Collaboration, *"Measurement of the B^+ Production Cross Section in pp Collisions at $\sqrt{s}$ = 7 TeV"*, *http://arxiv.org/abs/1101.0131, Phys. Rev. Lett., 106: 112001, 2011.*

65. The CMS Collaboration, *"Search for a heavy gauge boson W' in the final state with an electron and large missing transverse energy in pp collisions at $\sqrt{s}$ = 7 TeV"*, *http://arxiv.org/abs/1012.5945, Phys. Lett. B, 698: 21-39, 2011.*

66. The CMS Collaboration, *"Upsilon production cross section in pp collisions at $\sqrt{s}$ = 7 TeV"*, *http://arxiv.org/abs/1012.5545, Phys. Rev. D, 83: 112004, 2011.*

67. The CMS Collaboration, *"Search for Pair Production of Second-Generation Scalar Leptoquarks in pp Collisions at $\sqrt{s}$ = 7 TeV"*, *http://arxiv.org/abs/1012.4033, Phys. Rev. Lett., 106: 201803, 2011.*

68. The CMS Collaboration, *"Search for Pair Production of First-Generation Scalar Leptoquarks in pp Collisions at $\sqrt{s}$= 7 TeV"*, *http://arxiv.org/abs/1012.4031, Phys. Rev. Lett., 106: 201802, 2011.*

69. The CMS Collaboration, *"Search for Microscopic Black Hole Signatures at the Large Hadron Collider"*, *http://arxiv.org/abs/1012.3375, Phys. Lett. B, 697: 434-453, 2011.*

70. The CMS Collaboration, *"Measurements of Inclusive W and Z Cross Sections in pp Collisions at $\sqrt{s}$ = 7 TeV"*, *http://arxiv.org/abs/1012.2466, J. High Energy Phys., 01: 080, 2011.*

71. The CMS Collaboration, *"Measurement of the Isolated Prompt Photon Production Cross Section in pp Collisions at $\sqrt{s}$ = 7 TeV"*,

http://arxiv.org/abs/1012.0799, Phys. Rev. Lett., 106: 082001, 2011.

72. The CMS Collaboration, *"Search for Stopped Gluinos in pp collisions at $\sqrt{s}$ = 7 TeV",*
http://arxiv.org/abs/1011.5861, Phys. Rev. Lett., 106: 011801, 2011.

73. The CMS Collaboration, *"Charged particle multiplicities in pp interactions at $\sqrt{s}$ = 0.9, 2.36, and 7 TeV",*
http://arxiv.org/abs/1011.5531, J. High Energy Phys., 01: 079, 2011.

74. The CMS Collaboration, *"Prompt and non-prompt J/ψ production in pp collisions at $\sqrt{s}$ = 7 TeV",*
http://arxiv.org/abs/1011.4193, Eur. Phys. J. C, 71: 1575, 2011.

Conferences/Schools/Workshops Attended

1. 22-27 August 2011, **XXV International Symposium On Lepton Photon Interactions at High Energies, TIFR, Mumbai, INDIA**

2. 8-17 June 2011, **The 2011 Hadron Collider Physics Summer School, CERN, Geneva.**

3. 9-12 February 2010, **X Workshop on Resistive Plate Chambers and Related Detectors, Darmstadt, Germany.**

4. 21-27 October 2009, **LHC Physics WorkShop, TIFR, Mumbai, India.**

5. 17-23 August 2009, **Third Linear Collider Physics School, Ambleside, UK.**

6. 9-27 February 2009, **VII SERC school on Experimental High Energy, IIT Mumbai,India**.

7. 8-16 August 2008, **CTEQ - MCnet Summer School on QCD Phenomenology and Monte Carlo Event Generators, Debrecen, Hungary**.

8. 26-29 March, 2008, **LHC08: Early Physics at LHC with CMS Detector, TIFR, Mumbai, INDIA**.

9. 12-16 February, 2008, **The International Workshop on Physics and Analysis of Hot Dense and Matter , University of Jammu, Jammu, INDIA**.